Integrating sensors into total hip replacements

Oliver George Vickers

Submitted in accordance with the requirements for the degree of
PhD and Master of Science

The University of Leeds
School of Mechanical Engineering
September 2023

Declaration

The candidate confirms that the work submitted is his own, except where work which has formed part of jointly authored publications has been included. The contribution of the candidate and the other authors to this work has been explicitly indicated below. The candidate confirms that appropriate credit has been given within the thesis where reference has been made to the work of others.

The paper contributing to this thesis:

Vickers, O.G., Culmer, P.R., Isaac, G.H., Kay, R.W., Shuttleworth, M.P., Board, T. and Williams, S. 2021. **Is in vivo sensing in a total hip replacement a possibility? A review on past systems and future challenges.** Progress in Biomedical Engineering. 3(4), p.42004. A full copy of this publication can be found in the Appendix.

The primary author completed all literature searching and reviewing, and preparation of the publication. All remaining authors contributed to proofreading the article before publication.

Acknowledgements

I would like to acknowledge the Engineering and Physical Science Research Council for the funding for this project via the Tissue Engineering and Regenerative Medicine Centre for Doctoral Training.

I would like to thank the technical staff and administrative staff within the School of Mechanical Engineering for the help during my project.

I would like to thank my supervisors, Sophie Williams, Robert Kay, Peter Culmer and Graham Isaac for their endless support and guidance throughout this project. I could not have asked for a better supervisory team. I would also like to thank Tim Board as the clinical advisor to this project whose insight was very valuable.

I would like to thank all my friends and family for their support throughout my life and during my studies.

A huge thank you to my partner Selena for keeping me sane and motivated to the very end.

I would like to dedicate this thesis to my father, his words of encouragement kept me working hard through everything.

Abstract

Total hip replacement (THR) is a successful intervention for late-stage osteoarthritis. The NJR reported in 2022, that 100,000 total hip replacement (THR) surgeries were performed in England, Wales and N.Ireland. Use of THR is increasing and younger patients are receiving THRs. Implants need to be reliable, have good survivorship, be cost effective and enable surgeons to provide a high level of patient care to reduce the growing burden on clinicians, healthcare providers and the economy.

Instrumented implants capable of in-vivo sensing would allow for the continuous monitoring of patients post operatively. Data collected from the implant could provide insight into the function of the implant in-vivo and track the recovery of the patients.

Previous work on integrating sensing systems into THRs has focused on measuring joint reaction forces and component loosening. Tracking joint kinematics would allow the collection of metrics such as joint range of motion and step count which are commonly used to track post-operative recovery. Furthermore, measuring the components relative position and orientation could enable the detection of adverse events and so give early indications of component damage or the need for clinical intervention.

The aim of this thesis was to develop a sensing system for use within a THR to measure the relative kinematics of the components. The chosen sensing method utilised a three-axis magnetic field sensor and a permanent magnet. The method has been shown to track the relative position and orientation of the components and detect adverse motions unique to THRs including component impingement and impingement driven subluxation.

This thesis has resulted in a validated engineering prototype. With further development this sensing method could feature within an instrumented THR implant and be used to measure the kinematics of the components in-vivo. Metrics such as joint range of motion, step count and risk of component impingement or impingement driven subluxation could be extracted and used to guide post operative care.

Conference Proceedings

Chapter 5 of this thesis is based on the publication at the Orthopaedic Research Society 2022 Conference titled: **Development of a non-contact real-time method of tracking position and orientation of total hip replacement components**.

Chapter 6 of this thesis is based on the publications at the Wrightington John Charnley Gold Medal Research Day 2022 and the International Society for Technology in Arthroplasty 2022 Conference titled: **A non-contact method for measuring separation during subluxation events in total hip replacements**.

Copies of the full abstracts submitted as a part of the above conference proceedings can be found in the Appendix.

List of Abbreviations

CoCrMo – Cobalt chromium metal alloy

CTS – Camera tracking system

DoF – Degrees-of-Freedom

IMD – Implantable medical device

MPO – Magnetic position and orientation

NIMA - Numerical inversion of magnetic field approximations

THA – Total hip arthroplasty

THR – Total Hip Replacement

TKR – Total Knee Replacement

Table of contents

List of figures

List of tables

Chapter 1 Introduction, aims and objectives

1.1 Background on total hip replacements

Total hip arthroplasty (THA) can be considered as one of the most successful interventions for dealing with osteoarthritis (Knight et al., 2011) and is often touted as the operation of the century (Learmonth et al., 2007). Osteoarthritis is the progressive degeneration of a joints protective cartilage resulting in loss of function joint stiffness and debilitating pain (NHS, 2023), is the most common sole reason for a patient to receive a total hip replacement (THR) at 88% of primary THR cases (NJR, 2022). Other common reasons include trauma and avascular necrosis. The hip is a six degrees-of-freedom ball-and-socket joint and is the largest joint in the body. The human hip can experience loads of 2.5X body weight when walking (Damm et al., 2013) and up to 8.7X body weight when stumbling (Bergmann et al., 1993). It is not uncommon for a person to make 10,000 steps a day which culminates to millions of cycles over a lifetime. A THR aims to return function back to the patients hip by restoring the joint's natural centre of rotation, weight bearing capability and ball-and-socket mobility. During THA surgery the body's damaged tissue is replaced with artificial components. A THR consists of metal stem positioned in the central canal of the femur with an affixed femoral head i.e. the ball. A metal shell component is fixed within the acetabulum of the pelvis, and typically a liner made from a high wear resistant material (e.g. polyethylene) is positioned within the acetabular shell thus replicating a socket. A diagram of a THR implanted within a human hip is shown in Figure 1.

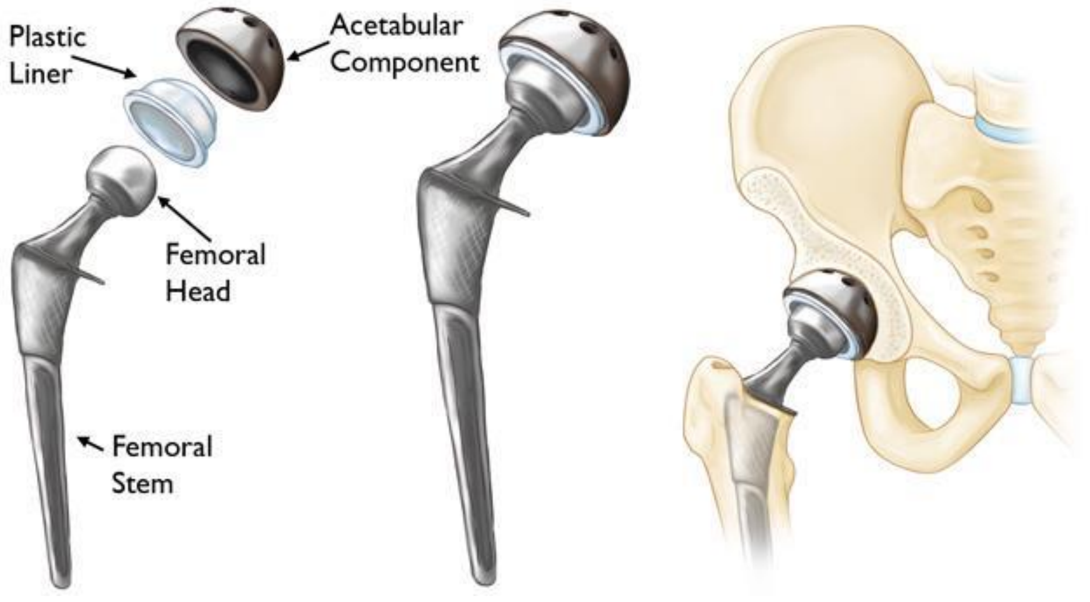

Figure 1 - Diagram of a total hip replacement components and a total hip replacement prosthesis implanted within a human hip. Reproduced with permission from OrthoInfo. © American Academy of Orthopaedic Surgeons. https://orthoinfo.org/.

National joint registries (SHAR, 2017; NJR, 2018; CIHI, 2018; AOA, 2018) have all shown consistent increase in the use of THA and projections are estimating further growth in the demand for procedures (Singh et al., 2019; Matharu et al., 2022). Therefore, to ease the burden on Governments, medical institutions and clinicians, implants need to be reliable, have good survivorship and enable clinicians to provide high levels of patient care. Sensor enabled total hip replacements and a robust telehealth system could improve the convenience and quality of patient care by collecting data to inform post operative decision making. Smart instrumented implants could enable the early detection to recommend the need for a change of patient behaviour or clinical intervention thus reducing revision rates. It is apparent that the future of total hip replacement use will feature embedded sensors capable of in-vivo sensing.

1.2 Rationale and long-term vision of the research: Why is it desirable to have telemetry in an instrumented hip implant?

An implanted medical device (IMD) with sensing capabilities and telemetric link could provide a means of continuous monitoring as oppose to traditional episodic monitoring (Baumann et al., 2020). This would enable clinicians to track the post-operative recovery process, better guide personalised postoperative care (Soares dos Santos et al., 2014; Ledet et al., 2018; Cushner et al., 2022) and empowers patients with the ability to review and manage the health of their implant. Additionally, the system could provide alerts on the occurrence of adverse events to give an early indication of the need for further investigation, or modification in activities.[1]

Increased availability of cheaper, smaller and more powerful integrated circuits and semiconductors has led to huge technological advances in electronics, sensing and communications. These advances and increased adoption of technology in healthcare has meant that smart IMDs are becoming a reality and are commonly used across healthcare. For example, the Freestyle Libre continuous glucose monitor (Abbott, Ill, US) offers an alternative to traditional finger prick blood glucose tests. The Freestyle Libre offers a pain free method for continuously measuring blood glucose levels and information on the direction blood glucose levels are trending. This demonstrates an example of how the advent of technology has improved both the convenience and quality of the care.[1]

The data gathered by an instrumented implant could inform the healthcare professional during their diagnostic decisions. In the case of a THR this data could include (for example) metrics on the performance of the implant or activity of an individual patient such as daily steps, range of motion, and condition of the bone-implant bond or wear of the bearing surfaces. Furthermore, this data would also be valuable to researchers to gain a better understanding of the overall use and performance of THRs across a patient population. Ultimately this research could be used to refine the design and surgical placement of existing implants to give enhanced performance and increased longevity. If these improvements were achieved, they would be of benefit patients and clinicians; and providers (healthcare systems) and financiers (governments and insurance companies).[1]

Additionally, experimental hip simulators have been used successfully to assess the performance of THRs with a variety of bearing materials and whilst

---

[1] *Work in this section was published on 16 September 2021 by the author as a topical review. The author was the primary contributor to the work.*

under both normal and adverse scenarios (Williams et al., 2003; McKellop and D'Lima, 2008; Ali et al., 2016; Hadley et al., 2018; O'Dwyer Lancaster-Jones et al., 2018). However, test protocols don't allow for a line-of-sight view of the bearing and assessments of the bearing's performance must be made at intervals or once the test has been completed. Therefore, there is a need for real time sensing within hip simulators and condition monitoring of parameters relating to the bearing's performance for example occurrence of impingement, relative motions of the components, excessive wear etc.

If successful, an instrumented hip implant will be a valuable tool for researchers to use, to gain a better understanding of the performance of the bearing during in-vitro testing. Designers could use what is found by the system to improve the design of existing implants and thus improve their performance and longevity. If a better understanding of existing implants is achieved and if improvements in the designs of THRs can be made, surgeons and patients will benefit from improved outcomes and success rates. Furthermore, this work aims to be the first stage in achieving a fully instrumented implant for clinical use. If this is reached, then it could enable surgeons to track the performance and healing of implanted THRs and thus guide postoperative care (Soares dos Santos et al., 2014; Ledet et al., 2018; Cushner et al., 2022). Demonstrating the function of an embedded sensing system in an in-vitro hip simulator would be the first stage of developing an instrumented implant for clinical use.

1.3 Research Proposal

1.3.1 Aim

The aim of this project is to integrate a sensing system into clinically available hip implant components to provide clinically relevant indicators of performance. This is early-stage development of an engineering mechanical prototype to demonstrate functionality and act as a proof-of-concept.

1.3.2 Objectives

1. Identify what physical or mechanical phenomena that occur within the environment of a THR are useful to measure, technically achievable within the scope of this project and practical from a regulatory point of view.
2. Develop a bespoke test rig to mimic the motion and adverse events of a hip replacement e.g. ball and socket joint and mimic adverse motions such as impingement and subluxation. This will provide a more flexible approach to prototyping and testing a sensor system.
3. Formulate design specifications for an instrumented hip implant (for use within an experimental hip simulator) that is capable of condition monitoring.
4. Produce initial sensor system design concepts using known sensing methods and evaluate their potential for providing the most useful output, by developing proof of concept prototypes.
5. Finalise sensor system design and integrate into a clinically available implant components. Use the test rig developed in objective 2. to characterise the capability and accuracy of the developed sensing system.
6. Make recommendations on future work i.e. further testing, progression of technology readiness level and the pathway for clinical translation.

1.4 Contributions

This thesis is the first body of work to use a magnetic position and orientation sensing system within a THR to measure the motion of the components. This thesis describes a novel method for tracking the occurrence and location of a component-component impingement in THRs. This thesis describes a novel method to detect THR bearing surface separation during impingement driven subluxation.

1.5 Thesis outline and graphical abstract

A graphical abstract detailing the structure of this thesis is shown in Figure 2.This thesis begins with a literature review that examines the common indications for the need for revision THR surgery and continues with a comprehensive review of past instrumented hip implants and challenges associated with their clinical adoption. This review was published by the author as a Topical Review (Vickers et al., 2021).

Chapter 3 details development and selection of a hip simulation test rig. This includes the design requirements, design specifications and development of a hip simulation test rig, and the justification for the selection of a robot arm as the final hip simulation solution.

Chapter 4 presents the generated design requirements and design specifications for a sensing system that can be integrated into a THR. There is then a discussion on the selected sensing method and the concept of a magnetic position and orientation sensing system is introduced. A description of the parameters of the system is given which are determined by the dimensions of the implant, the design requirements and the design specifications. Chapter 5 continues with a description of the magnetic field simulation methodology and a comparison of the output of the simulation with that of the selected magnetometer sensor.

Chapter 5 and 6 present the concept development work required to produce a prototype sensing system. Both Chapters include details of the design optimisation of the prototype and selection of the optimal method of calibrating the output of the sensor to the orientation and position of the components of the implant (magnet). The output of the prototype is characterised and validate using the robot arm hip simulation model and the performance is evaluated against the sensing system design specifications.

This thesis is concluded with a discussion (Chapter 7) The limitations and outcomes of the project are highlighted and discussed in the context of the project objectives and recommendations for future work are given.

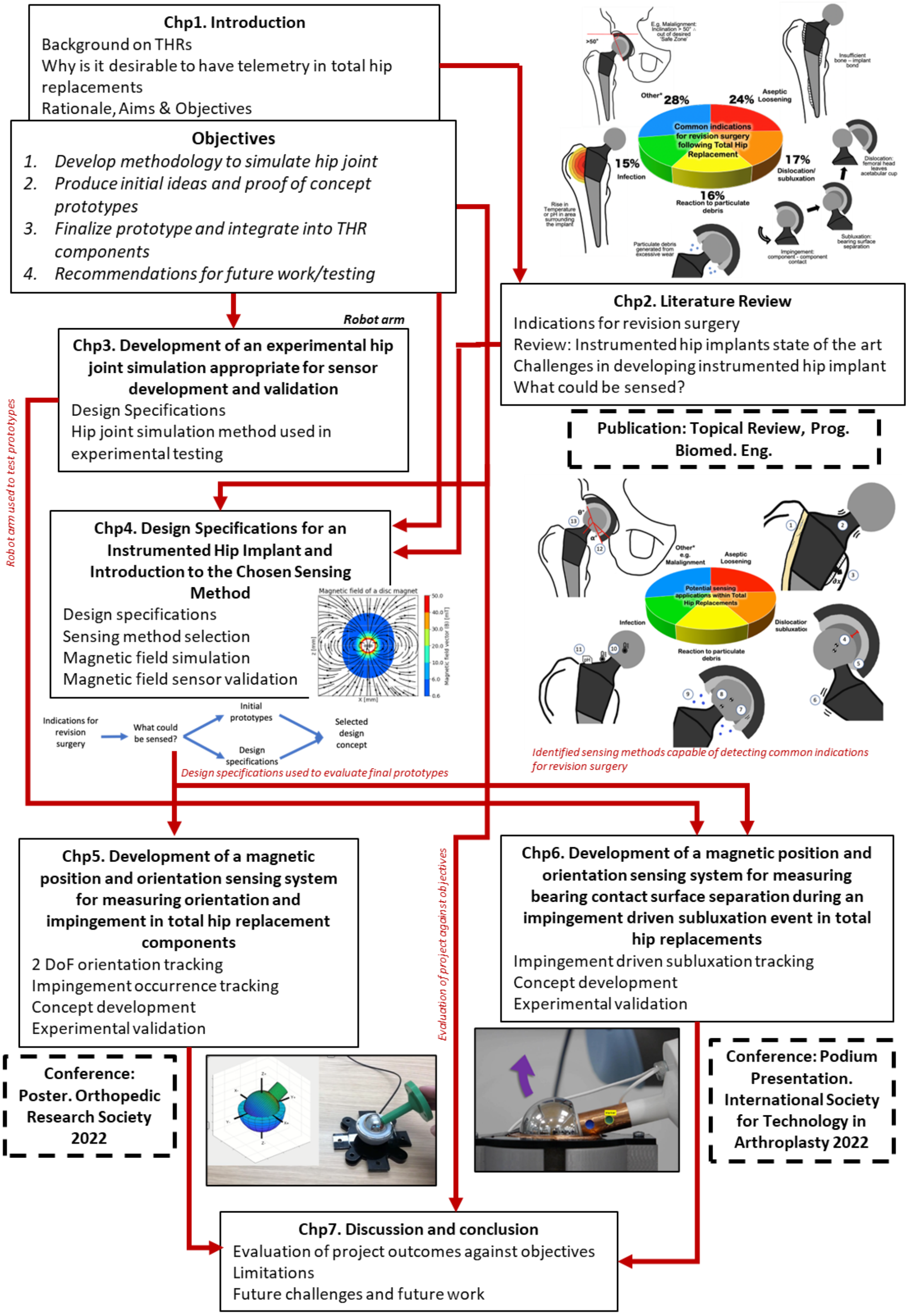

Chp1. Introduction
Background on THRs
Why is it desirable to have telemetry in total hip replacements
Rationale, Aims & Objectives

Objectives
1. *Develop methodology to simulate hip joint*
2. *Produce initial ideas and proof of concept prototypes*
3. *Finalize prototype and integrate into THR components*
4. *Recommendations for future work/testing*

Chp2. Literature Review
Indications for revision surgery
Review: Instrumented hip implants state of the art
Challenges in developing instrumented hip implant
What could be sensed?

Publication: Topical Review, Prog. Biomed. Eng.

Chp3. Development of an experimental hip joint simulation appropriate for sensor development and validation
Design Specifications
Hip joint simulation method used in experimental testing

Chp4. Design Specifications for an Instrumented Hip Implant and Introduction to the Chosen Sensing Method
Design specifications
Sensing method selection
Magnetic field simulation
Magnetic field sensor validation

Chp5. Development of a magnetic position and orientation sensing system for measuring orientation and impingement in total hip replacement components
2 DoF orientation tracking
Impingement occurrence tracking
Concept development
Experimental validation

Conference: Poster. Orthopedic Research Society 2022

Chp6. Development of a magnetic position and orientation sensing system for measuring bearing contact surface separation during an impingement driven subluxation event in total hip replacements
Impingement driven subluxation tracking
Concept development
Experimental validation

Conference: Podium Presentation. International Society for Technology in Arthroplasty 2022

Chp7. Discussion and conclusion
Evaluation of project outcomes against objectives
Limitations
Future challenges and future work

Figure 2 - Graphical abstract detailing the structure of the thesis. Elements adapted from O G Vickers et al 2021 Prog. Biomed. Eng. 3 042004. DOI 10.1088/2516-1091/ac1b7f. © 2021 The Author(s). Published by IOP Publishing Ltd.

Chapter 2 Literature Review

This literature review includes an examination into how total hip replacements fail and the common indication associated with the need for revision surgery. Following on from this is a review of past instrumented systems to assess the previous developments in the field. Finally, there will be a discussion on the challenges that need to be overcome for in-vivo sensing to be a possibility including choice of sensor, biocompatibility and integration within the implant, power, communication, and regulatory considerations.

Some work in this Chapter was published on 16 September 2021 by the author as a topical review. Specifically this includes Figure 3, Section 2.2, Section 2.3 and Section 2.5. The author was the primary contributor to the work. The full citation is:

Vickers, O.G., Culmer, P.R., Isaac, G.H., Kay, R.W., Shuttleworth, M.P., Board, T. and Williams, S., 2021. Is in vivo sensing in a total hip replacement a possibility? A review on past systems and future challenges. Progress in Biomedical Engineering, 3(4), p.042004.

2.1 Indications for revision surgery

To address survivorship, one must look at why hip implants are failing, a useful indication is reviewing the reasons for revision surgery. In 2018 the NJR report (NJR, 2018) that there were a total of 27,600 primary revisions and the most common indications were aseptic loosening at just over 24%, dislocation/subluxation at around 17%, reaction to wear particulates at around 17%, pain at just over 16%, and infection at 14% (Figure 3). Pain was not normally reported as the sole indication for revision; around 70% of cases were reported along with one or more other indications. Other indications of note include malalignment, implant wear and implant fracture. Although, in the short term, namely less than one year since primary hip replacement, the most common indications were dislocation/subluxation, peri-prosthetic fracture, infection and aseptic loosening with failures per 1000 prosthesis-years of 2.39, 1.69, 1.63 and 1.11 respectively. Clearly pain cannot be detected by means of an instrumented implant however there is scope for the other listed indications to be detected in-vivo and during in-vitro hip simulator tests. To further understand the reasons for revision these common indications will be discussed together with their prevalence and current diagnostic methods.

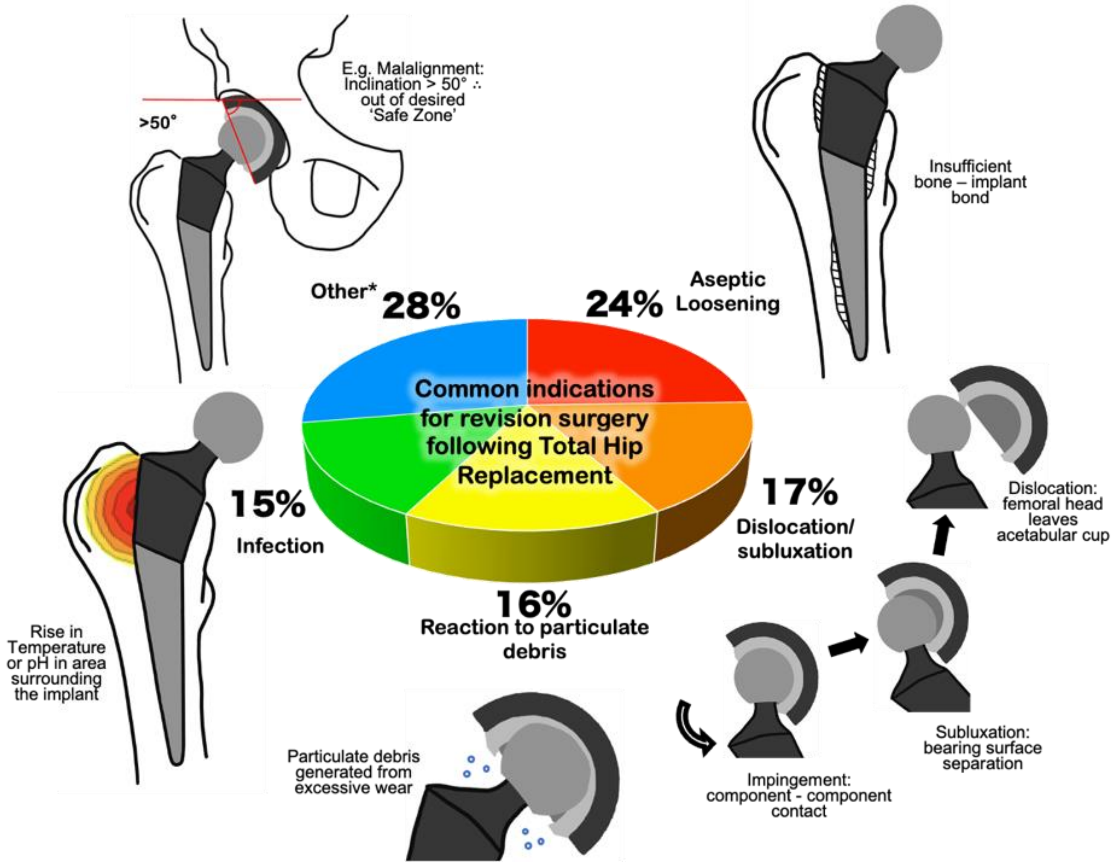

Figure 3 - Common indications for primary revision following primary revision surgery as reported by the 17th Annual Report of the National Joint Registry (National Joint Registry, 2020). *Other indications of note include malalignment, implant wear and implant fracture. Citation: O G Vickers et al 2021 Prog. Biomed. Eng. 3 042004. DOI 10.1088/2516-1091/ac1b7f. © 2021 The Author(s). Published by IOP Publishing Ltd.

2.1.1 Loosening

Aseptic loosening is the most common reason for orthopaedic implant revision and is defined as a failure of the implant – bone bond, in the absence of infection. Aseptic loosening can cause high levels of pain and if it is diagnosed too late, can lead to a destruction of bone stock which can create issues when implanting a new revision implant (Ewald et al., 2011). The initiation and progression of aseptic loosening is multifactorial with theories including: resultant adverse biological reaction from cement, polyethylene, metal or ceramic particles, micromotion, stress shielding, high fluid pressure, endotoxin or individual and genetic variations (Sundfeldt et al., 2006).

Adequate fixation of the components is critical to the success of the total hip replacement. However, there is still debate over cemented or cementless fixation as to which is the optimal technique (Abdulkarim et al., 2013). Cemented fixation uses polymethylmethacrylate (PMMA) bone cement to bind the cancellous bone and prosthesis. Cementless stem fixation is achieved by maximising initial mechanical fixation and encouraging biological fixation or osseointegration namely bone ingrowth or bone ongrowth (Kim and Yoo, 2016). Ingrowth is encouraged by creating microscopic pores over the surface of the implant through the use of sintered beads, fibre mesh and porous metals (Kim and Yoo, 2016; Maggs and Wilson, 2017).

The standard modalities for diagnosing aseptic loosening are plain radiographs, arthrography and scintigraphy (Rowlands et al., 2008; Ruther et al., 2012). Radiograph X-rays are taken of the joint and loosening is represented by lucencies at the bone-cement or bone implant interfaces (Varga and Wolter, 2014). Arthrography requires the joint space to be injected with a dye such as iodide, to act as a positive contrast agent, or air, to act as a negative contrast agent (Deyle, 2005). An X-ray is then taken and smaller radiolucencies that would not have been picked up by a plain radiograph can be visualised due to the penetration of the contrast material (Rowlands et al., 2008). Scintigraphy involves the injection of a radioactive material (e.g. radioactive metals Technetium 99 m, Gallium 76 and Indium 111) (Rowlands et al., 2008), into the bloodstream, which is attracted to regions of high bone metabolism such as bone fracture or bone repair (Parvizi et al., 2010). A loose prosthesis can then be characterised by an increase in bone metabolism around the implant which will be visible on a bone scan taken two to three hours after the isotope has been injected (Rowlands et al., 2008). Following an extensive meta-analysis of 32 articles published between January 1975 and June 2004, Temmerman et al (2005) found that there was no significant difference in the sensitivity of the three techniques which ranged from 86%-82% and sensitivity from 85%-72%. They concluded that plain radiography and bone scintigraphy were preferred methods because of their efficacy and lower risk of patient morbidity.

2.1.2 The occurrence and mechanisms of impingement, subluxation and dislocation

Dislocation of a total hip replacement is a separation of the bearing contact surfaces in which an intervention is required to relocate the joint (Padgett and Warashina, 2004). The 2018 National Joint Registry (NJR, 2018) report that dislocation and subluxation was the second most common indication for revision, at 4,663 (16.9%) cases and the most common cause of early failure (<1yr) requiring revision. Dislocation is a traumatic event for the patient, increases medical costs and can result in the patient losing confidence in their implant and surgeon (Jaramaz et al., 1997; Brown and Callaghan, 2008; Liu et al., 2019).

Even though the negative effects and burden of dislocation have long been known, yet the causation is disputed. The two main reasons for this lack of understanding are that there has been limited biomechanical studies (Scifert et al., 1999; Brown and Callaghan, 2008) and that dislocation is a multifactorial event with some indications more prevalent in some patients than others (Jaramaz et al., 1997; Shon et al., 2005). Those who have tried to define the mechanisms of dislocation come to the same conclusions in that the three most common modalities are: 1.) Malpositioning or loosening of the components, 2.) impingement be it primary (implant on implant), secondary (bone on bone) or hybrid (implant on bone) and 3.) hyperlaxity due to muscular or soft tissue insufficiency (Dorr et al., 1983; Dargel et al., 2014; Liu et al., 2019). Other causes include post traumatic THR, neuromuscular disorders, osteonecrosis of the femoral head, surgical approach and early postoperative compliance (Padgett and Warashina, 2004; Liu et al., 2019). There is agreement that primary impingement is the most common cause of dislocation (Shon et al., 2005; Brown and Callaghan, 2008; Ghaffari et al., 2012).

Impingement is contact between the neck of the femoral stem and the rim of the acetabular cup (Figure 4). If the leg is moved further out of the allowable range of motion (ROM), the femoral head can be levered out of the cup with the cup's rim acting as a fulcrum (Usrey et al., 2006). This separation of the bearing contact surfaces is known as subluxation and if the legs movement continues, and the external moment applied to the femoral component is high enough to overcome the resisting moment of the hip joint (Scifert et al., 1999), full dislocation can occur. The mechanism of impingement was first described in the mid-1970s by (1975) who elucidated how impingement can lead to an increased risk of dislocation. Since then, further issues have been associated with impingement including component loosening. When there is an impingement, a torque is applied to the acetabular cup. This may not displace the cup straight away however repeated contacts could result in loosening (Murray, 1992). Accelerated wear can also be a consequence of impingement; not only does contact between the components cause the release of wear particles but separation of the bearing through subluxation can cause a greater inflow of abrasive particulates (Shon et al., 2005). Furthermore, as the femoral head is levered out of the cup it begins to climb up the wall of the cup. This can generate egress site stresses on the opposing side of the cup which can be equal to or even higher than the stresses generated at the impingement site (Brown and Callaghan, 2008). Again, this leads to the generation of wear debris and elevated stresses causing fatigue type failure, and poses the risk of component fracture (Brown and Callaghan, 2008).

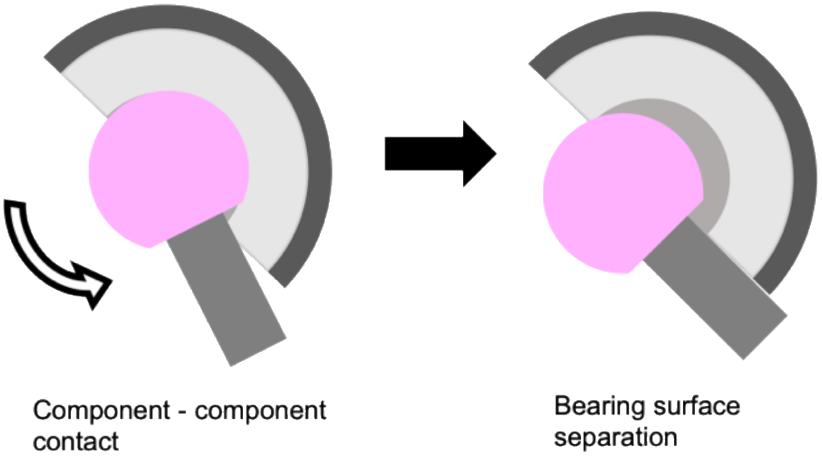

Figure 4 - Diagram of total hip replacement components during impingement and subluxation mechanism.

Impingement events are difficult to detect with traditional clinical evaluations and radiographs (Malik et al., 2007). As such, it’s rarely seen to be the sole reason for revision (Marchetti et al., 2011). Most of what is known about impingement has been learned from retrieval studies. Shon et al. (Shon et al.,

2005) used stereomicroscopic examination to inspect 170 implants for evidence of impingement. Severity of the impingement was subjectively graded on a scale of 1 – 4 from little evidence of impingement to damage extending more than 2mm into the rim. Thirty-six components were given a grade 1 and 40 were judged to be grade 2. More severe impingement was seen in the 10 components given grade 3 and the remaining 10 given grade 4. Radiographs were available for 124 of the implants and were used to assess the positioning of the implants. Ninety-four of these implants were implanted within the acceptable ranges of 30° to 50° inclination and 5° to 25° anteversion. Of these 94, 54 (57%) showed evidence of impingement suggesting that the previously reported optimal ranges may be narrower or that impingement will occur regardless. Usrey et al. (Usrey et al., 2006) examined 113 acetabular components for signs of impingement and wear. They found evidence of impingement in 60% of the cups and 32% were found to have moderate or severe damage to the rim. Of the cups with moderate or severe impingement damage the average wear rate was 159 ± 42 mm3/y compared to 70 ± 21 mm3/y which was seen in cups with no or mild impingement damage. Marchetti and colleagues conducted the largest continuous retrieval study with 416 acetabular cups assessed. Evidence of impingement was found in 214 (51.4%) of the cups and severe damage (notch > 1mm) was seen in 130 (31.3%) of the cups.

2.1.3 Wear

Reducing wear has been a primary focus for improving total hip replacement design since the introduction of the low friction prostheses by Sir John Charnley in the 1960s. Wear can occur through five predominant modes (Figure 5) they include : 1) sliding between the bearing contact surfaces; 2) wear from contact between a bearing surface and non-bearing surface, for example during a subluxation event when contact occurs between the femoral head and edge of the rim; 3) Third-body wear which is a form of abrasive wear that occurs when hard particles e.g. metal, ceramic or bone particles, become embedded within the softer surface; 4) wear occurring between two non-bearing surfaces, such as during an impingement event or from backside wear which is wear between the liner and acetabular shell (McKellop, 2007).

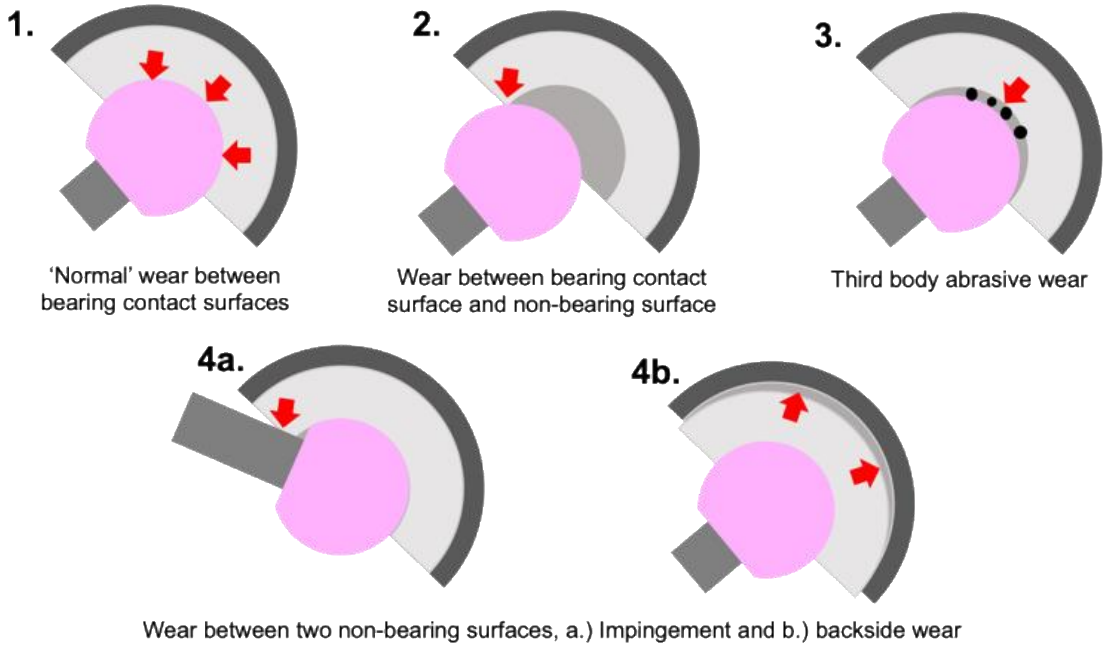

Figure 5 - Five modalities of wear: 1) normal wear between the bearing contact surfaces; 2) wear between bearing contact surface and non-bearing contact surface; 3) Third body abrasive wear; 4) Wear between two non-bearing surfaces, a.) Impingement and b.) backside wear. Adapted from: (McKellop, 2007).

There are multiple factors leading to increased wear rates furthermore, the consequences of high wear levels have a significant impact on the functionality and longevity of the implant, these are described in Figure 6.

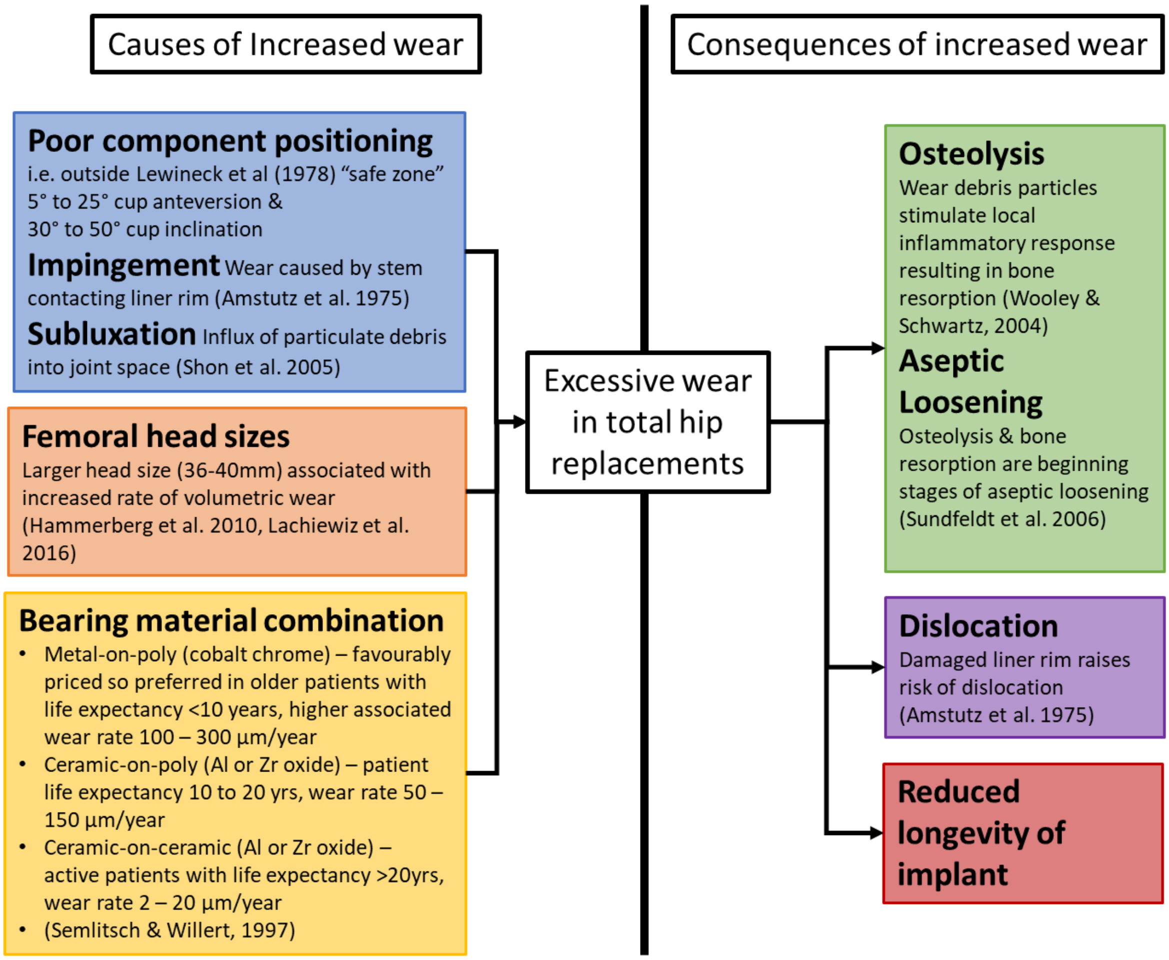

Poor component positioning i.e. outside Lewineck et al (1978) “safe zone” 5° to 25° cup anteversion & 30° to 50° cup inclination

Impingement Wear caused by stem contacting liner rim (Amstutz et al. 1975)

Subluxation Influx of particulate debris into joint space (Shon et al. 2005)

Femoral head sizes Larger head size (36-40mm) associated with increased rate of volumetric wear (Hammerberg et al. 2010, Lachiewiz et al. 2016)

Bearing material combination

- Metal-on-poly (cobalt chrome) – favourably priced so preferred in older patients with life expectancy <10 years, higher associated wear rate 100 – 300 µm/year
- Ceramic-on-poly (Al or Zr oxide) – patient life expectancy 10 to 20 yrs, wear rate 50 – 150 µm/year
- Ceramic-on-ceramic (Al or Zr oxide) – active patients with life expectancy >20yrs, wear rate 2 – 20 µm/year
- (Semlitsch & Willert, 1997)

Osteolysis Wear debris particles stimulate local inflammatory response resulting in bone resorption (Wooley & Schwartz, 2004)

Aseptic Loosening Osteolysis & bone resorption are beginning stages of aseptic loosening (Sundfeldt et al. 2006)

Dislocation Damaged liner rim raises risk of dislocation (Amstutz et al. 1975)

Reduced longevity of implant

Figure 6 - The causes and consequences of excessive wear in total hip replacements (Amstutz et al., 1975; Lewinnek et al., 1978; Semlitsch and Willert, 1997; Wooley and Schwarz, 2004; Shon et al., 2005; Sundfeldt et al., 2006; Hammerberg et al., 2010; Lachiewicz et al., 2016).

The most common method of clinically measuring wear following total hip arthroplasty is using plain serial radiographs. This requires x-rays to be taken immediately after surgery and then at subsequent follow ups. Femoral head penetration into the acetabular socket can then be evaluated manually or computational edge detection techniques can be used as a more accurate approach (McCalden et al., 2005). Radiography is the preferred method for clinically assessing levels of wear as it is widely accepted and cost effective however, there are some limitations such as not being able to distinguish linear wear from creep or plastic deformation, it’s a two-dimensional (2D) analysis and the method assumes the centre of the femoral head and the acetabular cup coincide (Grillini and Affatato, 2013). Additionally, as wear rates have reduced, the amount to be measured is similar to the accuracy limits of the technique. An alternative technique is using radiostereometric analysis (RSA) which, because of its high precision and accuracy, is considered the ’Gold Standard’ for measuring wear following joint replacement (Teeter et al., 2016). RSA involves radiographs being taken simultaneously from multiple views. The x-ray images are then aligned using radiopaque tantalum beads, which are inserted intra-operatively into bone segments surrounding the implant and into the implant. This allows for an accurate measurement of the relative displacement of the components and so implant migration and wear can be inferred. However, the limitations are that when compared to plain radiograph analysis it is far more costly, requires beads to be added to the prosthesis and is therefore harder to adopt as a routine procedure (Grillini and Affatato, 2013).

2.1.4 Malalignment

Alignment of the acetabular component is crucial to the success of THA. Malalignment has a significant influence on dislocation, impingement, pelvic osteolysis, acetabular migration and wear (Kennedy et al., 1998). Ali at al. (2017) conducted a study to investigate the effect variations in component positioning (different levels of medial-lateral translational mismatch at standard and steep cup inclination angles) have on the severity of edge loading, dynamic separation and wear of size 36 mm metal-on-polyethylene hip bearings in an electromechanical hip joint simulator. They found that as cup inclination and medial-lateral translational mismatch increased, so did dynamic separation, severity of edge loading and, wear and deformation of the polyethylene.

Component orientation is defined by the angles of operative anteversion, the angle between the longitudinal axis of the patient and the acetabular axis as projected on to the sagittal plane (akin to hip flexion), and operative inclination the angle between the acetabular axis and the sagittal plane or the abduction of the acetabular axis (akin to hip abduction) (Murray, 1993), operative anteversion and inclination are described in Figure 7. Lewinnek et al. (1978) has previously described a “safe zone” as the optimal orientation of acetabulum cup as 5° to 25° of cup anteversion and 30° to 50° of cup inclination.

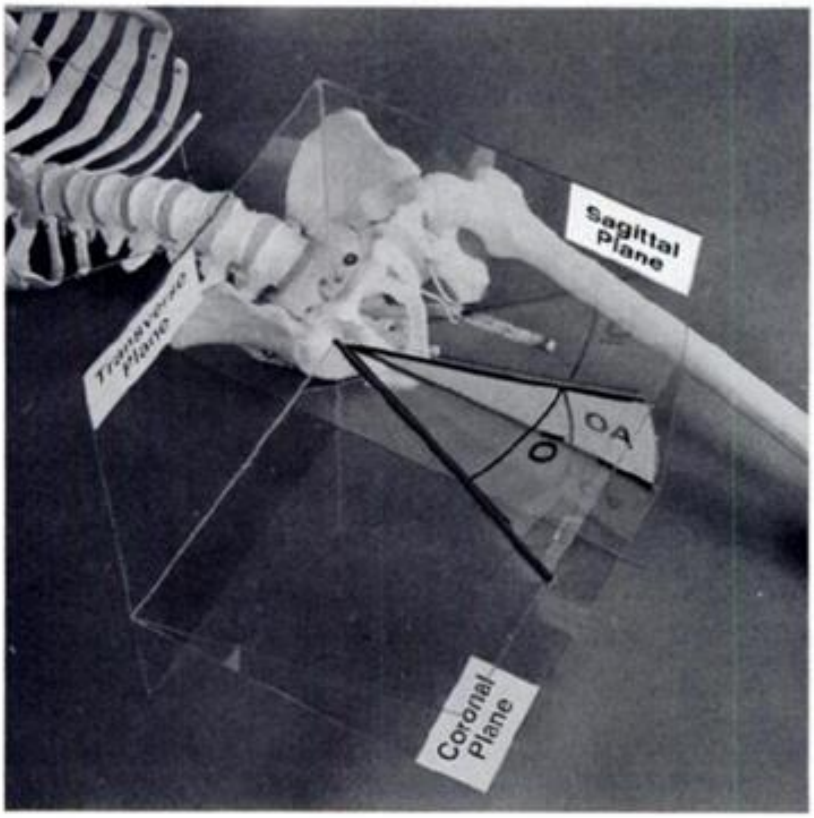

Figure 7 - Diagram of the operative anteversion and operative inclination angles in relation to the human pelvis with annotated sagittal plane, coronal plane and transverse plane. Reprinted from (Murray, 1993) , Copyright (1993), with permission from The Journal of Bone & Joint Surgery British Volume.

The relevance of the Lewinnek “safe zone” (1978) is still being debated (Rittmeister and Callitsis, 2006). However, a more pressing issue is that surgeons are struggling to position the acetabular component within their target range (Hassan et al., 1998; DiGioia III et al., 2002; Bosker et al., 2007). These groups are concluding that freehand positioning is not a reliable method (Bosker et al., 2007) and that a method for accurately measuring cup orientation within the operating room is required (Hassan et al., 1998).

2.2 Past instrumented hip implant systems

This review gives an overview of the previous work conducted in the field of instrumented hip implants with the aim of addressing the following research questions:

1. What sensors have been used within instrumented hip implants and what parameters were monitored?
2. Where have the sensors, and accompanying electronics, been packaged within the instrumented hip implants?
3. What is the current stage of the technology? (with regards to clinical use)

The findings are reported in sections relating to the indication for revision or main phenomena that the study was looking to detect or monitor; (i.e. biomechanics and aseptic loosening).

2.2.1 Biomechanics

In terms of instrumented hip implants, most of the focus has been on studying the biomechanics of THRs and function in an in-vivo environment. Strain gauges, piezoelectric transducers and temperature sensors have been used to measure forces, pressures, moments and temperatures in-vivo. The data collected in these studies has been important in validating computational and cadaveric models, and inform designers and surgeons thus improving implant design and surgical technique.

Early Work on Measuring Hip Joint Force In-Vivo

The first use of sensors in an instrumented implant, for in-vivo use, was that of Rydell et al (1966) who positioned strain gauges within the neck of the femoral prosthesis. The prosthesis was implanted successfully in two patients successfully and six months later a second surgery passed lead wires out of the skin to allow for data collection. After a week these lead wires were designed to be cut free by a sharp edge at the junction with the prosthesis however this method failed, and a separate operation had of be conducted to remove the leads. Results (in terms of measured load) were recorded from two patients (Table 1).

Convenience, improved patient comfort and reduced risk of infection led to the use of wireless connections in future developments. An approach, first described by English and Kilvington (1979) and later in Kilvington and Goodman

(1981), was to use battery power and a FM transmitter chip (Sandev SNlO2F) operating at 102.3 MHz. Their implant consisted of a sealed piston with four strain gauges thus forming a load cell capable of measuring the axial compressive load transmitted through the neck of the femoral component. A cable was passed out of the implant stem and led to an implanted Perspex box where the transmitter and accompanying electronics were housed, the cable and box were encapsulated within silicone rubber. The system had an operational battery life of approx. 70 hours and with the use of sub miniature magnet controlled reed switches, recordings could be made up to 43 days post-op (English and Kilvington, 1979). Results (load from walking and one-legged stance) from a single patient were collected (Table 1).

Other early work measured contact pressures at the joint surface, Carlson et al (1974) developed a prototype prosthesis to measure the magnitude and distribution of pressure generated over the inner surface of a natural human hip socket. The implant featured 14 pressure transducers covering the outer surface of the femoral head, and a 16-channel telemetry system located within the femoral head. The power and data transfer induction coil were located at the distal end of the implant, allowing the implant to be powered by an external power coil. A similar approach was adopted by Otake et al (2005) who developed a modified femoral head with eight sub-miniature pressure sensors embedded over the surface and covered with a spherical ABS plastic surface to reduce friction. The device was limited in that it was only intended to measure intraoperative pressures at the bearing contact surfaces.

3D Force Measurements Acting on the Femoral Stem

In 1979 Georg Bergmann developed a new method for measuring force distributed over a femoral head termed the matrix method (Orthload, 2019). The method required only one sensor for each load component and so meant that 3D force measurements could be made on the femoral head with the use of only three strain gauges positioned within the femoral neck (on the inner surface). Bergmann then developed his own instrumented hip implant that he initially tested in sheep (Bergmann et al., 1987). A functional telemeterised hip for in-vivo human use was first described and implanted in 1988 (Bergmann et al., 1988). The implant, (Figure 8a), included three semiconductor strain gauges positioned on the inner wall of the hollow neck. The remaining electronics, including the power coil and RF transmitter, were placed on both sides of a 15mm X 7mm wide substrate and housed in an 8mm X 25mm cylinder. The top plate of the cylinder had two lead throughs that connect to the RF transmitter antenna which was fitted into the cavity of a ceramic head (Graichen and Bergmann, 1991). Two patients received the instrumented hips, firstly in 1988 a bilateral procedure (both hips) was performed on an 82 year-old male with height 168cm and bodyweight (BW) 650N, and then in 1990 in the right hip of a 69 year-old female of height 160cm and BW 470N. Results recorded (peak loads in walking and stumbling) from the two patients are shown in Table 1.

In the 1990s Bergmann's group developed a further endoprosthesis which measured the force components experienced by the head and also the temperature distribution across the full length of the femoral stem (Graichen et al., 1999). The implant, (Figure 8b) was based on the hollow shaft hip endoprosthesis CENOS (ARTOS, Berlin, Germany) and featured three semiconductor strain gauges and two temperature sensors (TS1 & TS2 Figure 8b) glued to the inner surface of the hollow neck along with an additional six temperature sensors (TS3 - TS8 Figure 8b) positioned along the shaft of the stem. The power coil and two telemetry units were positioned within the hollow shaft, which was sealed by a top plate. The top plate was welded to the top of the implant neck, and featured two lead throughs that allowed connection to the antenna that occupied the cavity of the ceramic head, (Graichen et al., 1999) similar to the previous endoprosthesis (Graichen and Bergmann, 1991).

In 2001 Bergmann and colleagues published the results of two studies conducted using these new endoprosthesis (G. Bergmann et al., 2001; G Bergmann et al., 2001). Firstly, contact forces were reported from four patients', age range 51 – 76 years and BW range of 702N – 980N. Hip contact force results collected from these four patients are shown in Table 1. In the second study temperature measurements were made in seven patients', age range 51 – 82 years. Peak temperature of implants with a polyethylene liner was measured at 43.18°C after an hour of walking and was observed in sensor TS1 which was positioned at the top of the neck (G. Bergmann et al., 2001), (Figure 8b).

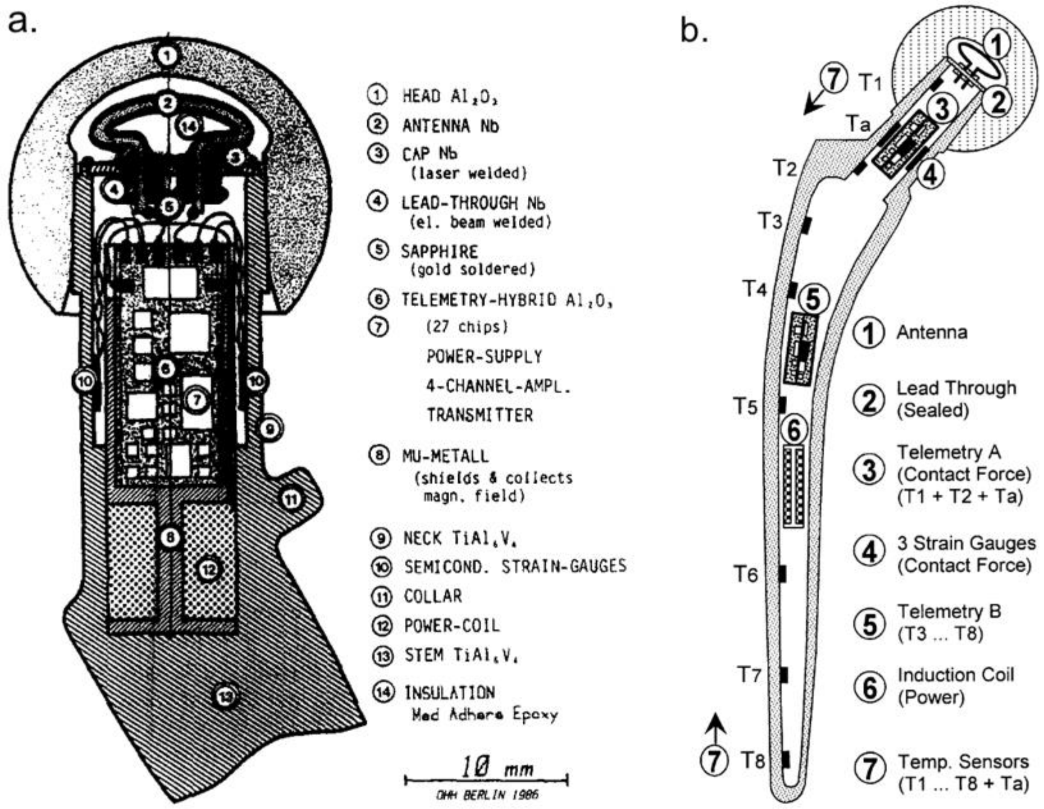

Figure 8a – Cross section of Bergmann's first hip endoprosthesis for force measurements. Reprinted from (Bergmann et al., 1988) Copyright (1988), with permission from Elsevier. b – Bergmann's hollow shaft smart prosthesis capable of force measurement and temperature measurement along the full length of the stem. Reprinted from (Graichen et al., 1999) Copyright (1999), with permission from Elsevier.

The third iteration of Bergmann's instrumented hip prosthesis (Damm et al., 2010) was based on a "Cementless Tapered Wedge" (CTW) prosthesis (Merete Medical GmbH, Berlin, Germany). This allowed for the measurement of forces and moments acting in the joint. Three custom-made twin semiconductor strain gauges were positioned inside the hollow neck along with a nine-channel telemetry transmitter and an internal induction coil. A cut-out model of the prosthesis is shown in Figure 9a. The prosthesis had a transmission range of 50cm (Damm et al., 2010). In 2013 Damm and colleagues (2013) reported in-vivo friction measurements using Bergmann's modified CTW prosthesis. Results at 3 months post-op from eight subjects, age range 50 – 69 years and BW range of 754N – 899N and are shown in Table 1.

Table 1– Summary of studies reporting in-vivo loads measured through hip joint

Study	Method	Patients	Stance/Activity	Measured load through joint normalised to body weight
Rydell (1966)	Six strain gauges in stem	2	One-legged stance	2.3X (peak patient 1) 2.9X (peak patient 2)
			Walking 1.3m/s (patient 1) & 1.4m/s (patient 2)	1.8X (peak patient 1) & 3.3X (peak patient 2)
Kilvington & Goodman (1981)	Load cell piston	1	One-legged stance	2.8X (12 days post-op) & 2.2X (40 days post-op)
			Walking	2.0X (12 days post-op) & 1.9X (40 days post-op)
Davy (1988)	Three strain gauges matrix method	1	One-legged stance (31 days post-op)	2.1X
			Walking	2.6X to 2.8X (range)
			Stair climbing	2.6X
Kotzar (1991)	Three strain gauges matrix method	2	One-legged stance (23 days post-op)	2.1X to 2.8X (range)
			Walking	2.8X to 3.6X (range)
Bergmann et al. (1993)	Three strain gauges matrix method	2	Walking 0.3m/s (patient 1) & 1.4m/s (patient 2)	2.8X (peak patient 1) & 4.8X (peak patient 2)
			Stumbling	7.2X (peak patient 1) & 8.7X (peak patient 2)
Bergmann et al. (2001)	Three strain gauges matrix method	4	One-legged stance	2.3X (mean from 4 patients)
			Walking (1.1m/s)	2.4X (mean from 4 patients)
Damm et al. (2013)	Three strain gauges matrix method	8	Walking (3 months post-op)	2.5X (mean from 8 patients)

Bergmann et al (2012) also developed a further prosthesis based on the CTW design solely for in-vivo temperature measurements. This had a 6.2mm diameter X 50mm long bore in the neck for the thermistor and accompanying electronics, (Figure 9b). Bergmann's previous implants had all featured internal power coils and an external niobium antenna. The new prosthesis however, had a combined power and data coil positioned within a hermetically sealed chamber instead of being positioned in the recess of the femoral head and encapsulated in silicone. The justification being that the plastic encapsulation of electronics should only be used for non-permanent implants (Bergmann et al., 2012). To date no study has been reported from this prosthesis however, Bergmann et al. (2012) state that a clinical study on temperature rise in hip implants was planned in 100 patients.

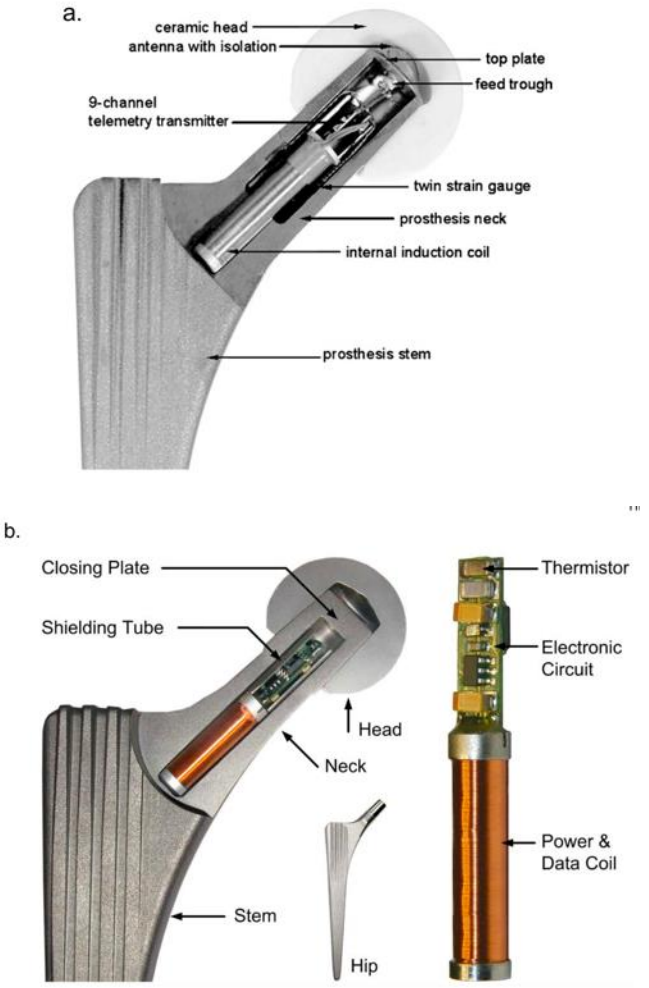

Figure 9a – Bergmann's first CTW implant with three twin semiconductor strain gauges, internal power coils and an external niobium antenna. Reprinted from (Damm et al., 2010) Copyright (2010), with permission from Elsevier. b – The latest of Bergmann's smart implants and the first to feature a combined power and data transfer coil. Reproduced from (Bergmann et al., 2012) CC By 4.0.

2.2.2 Implant Loosening

Aseptic loosening is failure of the implant – bone bond in the absence of infection. It is the most common reason for orthopaedic implant revision. Aseptic loosening can cause pain and if it is diagnosed too late, can lead to a destruction of bone stock which can create issues when implanting a new revision implant (Ewald et al., 2011). The initiation and progression of aseptic loosening is multifactorial, this includes: resultant adverse biological reactions to cement, polyethylene, metal or ceramic particles, micromotion at the interface, stress shielding, high fluid pressure, endotoxin or individual and genetic variations (Sundfeldt et al., 2006).

Vibration Analysis

Vibration analysis (VA) relies on measuring the ambient vibrations and frequencies of a system or the vibration response following a mechanical excitation from an external source e.g. a shaker. A structural change or degradation within the system, for example an imbalance, worn and broken components or torque variations, will give rise to distinct features in the output signals. An abnormal vibration response can be more easily identified if an original or typical vibration response is known (Jantara, 2020). The frequency response of a linear system will show the excitation (input) oscillating at the same frequency as the output. Whereas the output of a nonlinear system will contain multiple harmonics. In the case of a THR, a well-fixed prosthesis can be considered as a linear system whereas an unstable or loose implant will behave like a nonlinear system, Figure 10.

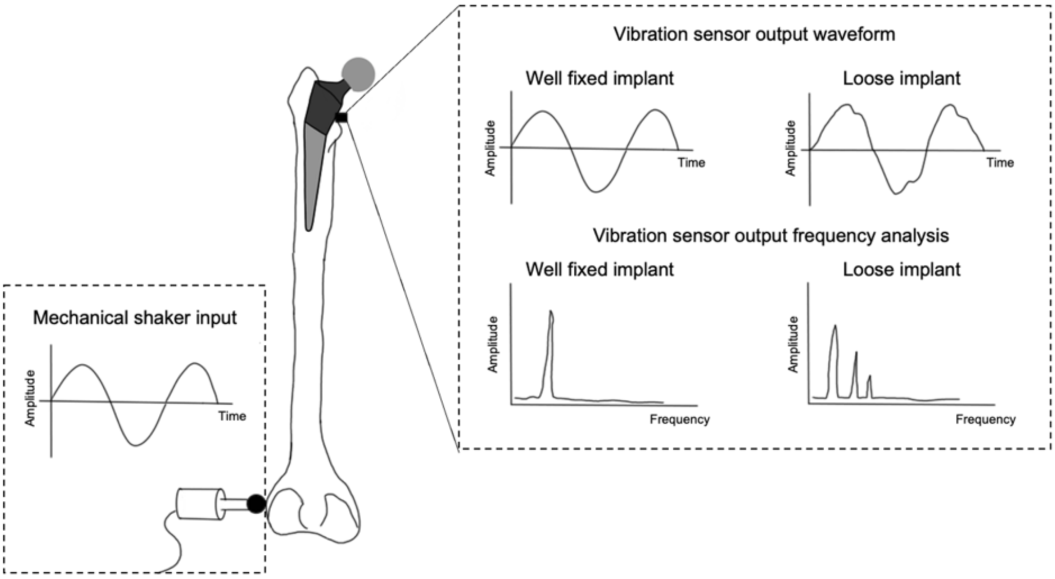

Figure 10 – Conceptual diagram of vibration analysis being performed on a femur and implanted stem. The output waveform of a well-fixed implant will match the sinusoidal nature of the input excitation and frequency analysis will reveal one major frequency. Conversely a loose implant will have a distorted output waveform and multiple harmonics will be present. Adapted from (Rosenstein et al., 1989).

Chung et al (1979) first suggested the use of VA as a diagnostic technique to assess THR fixation. They described the technique as safe and non-invasive because only a small mechanical excitation was required; that the method could be used on pre-existing implant designs and previously implanted prostheses and allow for the real time monitoring of levels of osseointegration. The in-vitro experimental setup included a mechanical shaker applying an excitation to the implant–bone system and accelerometer(s) attached to the bone, measuring the vibration response. Several studies report similar findings to Chung et al (1979) using a femoral stem implanted in a femur (Rosenstein et al., 1989; Li et al., 1996; Çelik and Kisioglu, 2019), acetabular cup implanted in a Sawbone block (Alshuhri et al., 2015) and complete THR system implanted in a Sawbone femur and pelvis (Rieger et al., 2013). Results demonstrate that an implant–bone interface with a loosened implant, gave a distorted output waveform, increased numbers of resonance peaks and a reduction in the magnitude of the fundamental frequency.

Rosenstein et al (1989) and Georgiou and Cunningham (2001) further developed this concept by conducting in-vivo trials using VA to detect THR loosening in-vivo. In both studies, a single accelerometer was positioned over the greater trochanter and a vibrator applied excitation to the lateral epicondyle of the femur. Rosenstein et al (1989) found that in five patients where the VA test was positive for loosening, it was also observed in revision surgery. Additionally, Georgiou and Cunningham (2001) reported their VA method had a sensitivity of 80% and a specificity of 89%, and when compared to the standard radiographic method was 20% more sensitive and able to diagnose 13% more patients. There were however, limitations in the in-vivo method; firstly, the technique is unsuitable for patients who could not lie on their side or who experience pain and discomfort induced by the vibrator, in Georgiou and Cunningham's study this accounted for 10% of the patients. Secondly, although the authors took care to position the sensor and shaker with "good bony contact" variations in patient soft tissue can greatly affect the propagation of the vibrations to the body's surface and so affect the diagnostic capabilities (Rowlands et al., 2008).

Using an implant with telemetry presents an alternative method that would allow for ongoing VA assessment of the THR component loosening. Puers et al (2000) propose a concept that included a capacitive accelerometer sealed in a titanium can and placed into a recess made in the femoral head (Figure 11). The inductive power and data coils were fed through the lid of the titanium can and coil around the superior portion of the neck stem. Puers et al. (2000) state that having the sensing system within the implant will provide far better results when compared to previous VA methods. One limitation of this integration method is that the required recess incurs significant modification to the femoral head which would affect the bearing function at the articulating interface. Additionally, the coils are within the operating space of the ball and socket joint and are thus vulnerable to damage if primary impingement (contact between the cup and stem) occurred.

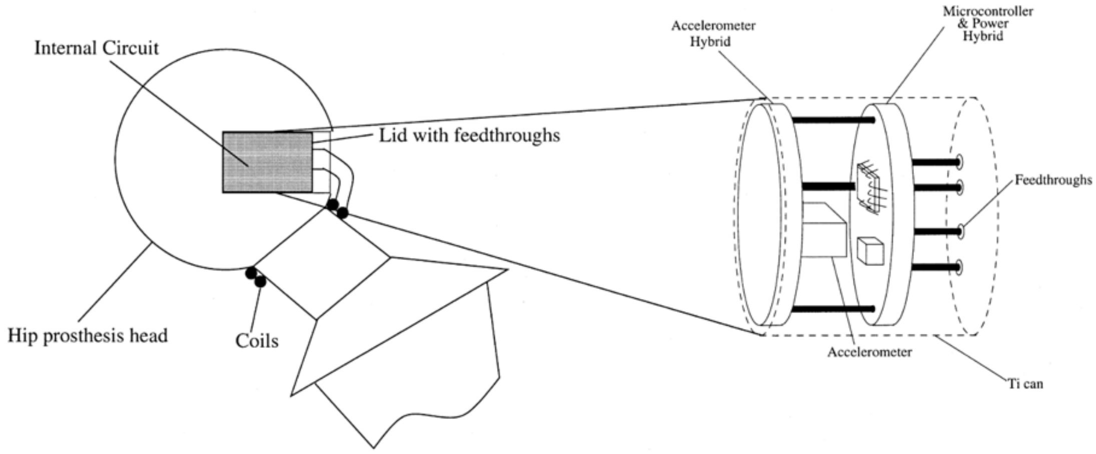

Figure 11 - Method of packaging showing the location of the recess in the femoral head and positioning of the transmission coils. Reprinted from (Puers et al., 2000) Copyright (2000), with permission from Elsevier.

Marschener et al (2009) developed a system with a custom transponder chip and an accelerometer complete with a lock-in amplifier, which filtered out signal noise generated by the in-vivo environment. The system also featured onboard storage, that could include patient and prosthesis manufacturer data as well as reference data sets for loosening trend analysis. The chosen integration solution was to screw the coil and electronics housing to the distal end of the prosthesis this ensured vibration coupling to the implant and meant that there was no metal surrounding the transponder coil (2009).

Sauer et al (2013) positioned a sensor system in the femoral head. The rationale for the approach was that firstly, when compared with the manufacturing process of stem, modifying the femoral head would be far simpler and cheaper. Secondly, the micro-porous surface coating on their stem required a gamma sterilisation process that would have a detrimental effect on integrated hardware. Finally, there were less femoral head design options compared with the number of stem sizes so using the femoral head would reduce the number of required variations. Their system included a three-axis acceleration sensor, lock-in amplifier and inductively coupled data transmission and power supply working at 125Hz. The first integration concept was to put the sensor system within the cone of a ceramic head, (Figure 12). To secure the sensing apparatus a low consistency silicone was selected to provide a durable fixation and no electromagnetic disturbance or shielding of the telemetry coils. However, it was noted that the titanium acetabular cup would interfere with the electromagnetic field of the transponder coils and so an alternative approach was devised. In this approach, the sensor system was encapsulated within the titanium sleeve and the coils, connected by lead throughs, were wound on a polyether ether ketone (PEEK) element and mounted on the sleeve, as shown in Figure 13.

.

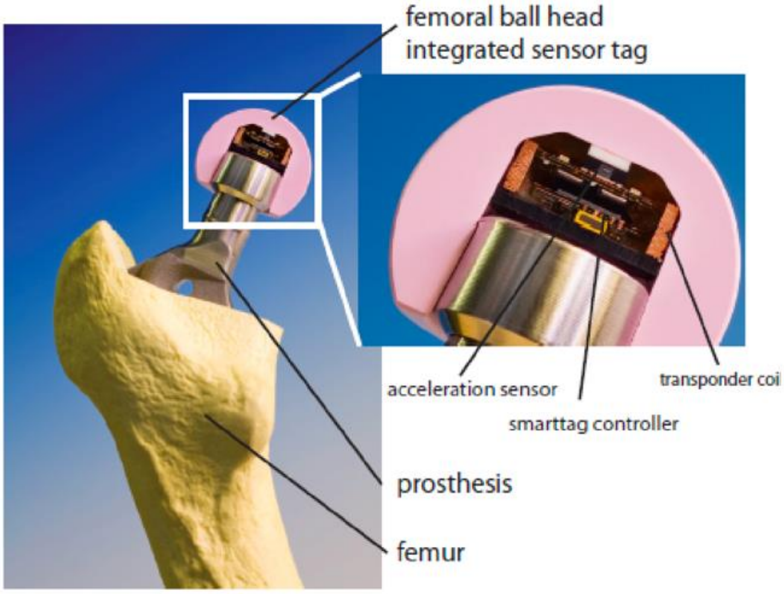

Figure 12 - THR sensing system to measure vibration potted in the femoral head. Reprinted form (Sauer et al., 2013). Copyright (2013) with permission from IFSA publishing.

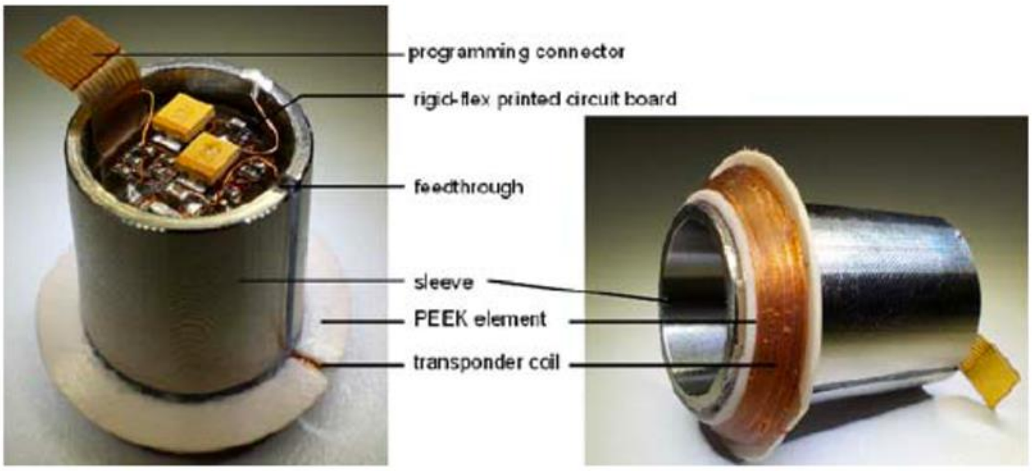

Figure 13 - THR sensing system to measure vibration showing the sensing system positioned within a titanium sleeve and the transponder coil wrapped around a PEEK element. Reprinted from (Sauer et al., 2013). Copyright (2013) with permission from IFSA publishing.

All three research groups (Puers et al., 2000; Marschner et al., 2009; Sauer et al., 2013) that investigated telemetric VA were able to verify their sensing systems and produced similar vibrational response data to (Chung et al., 1979; Rosenstein et al., 1989; Li et al., 1996; Rieger et al., 2013; Alshuhri et al., 2015; Çelik and Kisioglu, 2019).

Acoustic Emissions

Acoustic emission (AE) is the phenomenon of energy release, in the form of acoustic (elastic) waves, as a result of a solid material undergoing irreversible changes in its internal structure such as crack propagation, phase changes and dislocations within the material (Wevers and Surgeon, 2000). The stress waves generated propagate to the materials surface (Figure 14) where they can be recorded by sensors, typically piezoelectric. Key parameters can then be derived including rise time, maximum signal amplitude, signal duration, signal energy and peak counts. If multiple sensors are present the timings of the waves arrival at the materials surface can be used to triangulate the point of origin and hence the location of the defect.

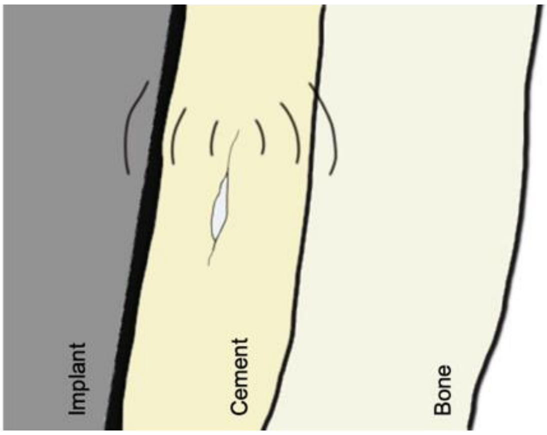

Figure 14 – Crack propagation in the bone cement will release acoustic waves which will travel to the surface of the bone or implant and can then be detected.

One of the earliest examples of using AE to determine the occurrence of implant loosening was conducted in 1989 by Sugiyama et al (1989). They used an AE technique to investigate the effect torsional load has on femoral stem loosening and compared three cementing techniques including combinations of canal irrigation, manual insertion, and vacuum mixing combined with pressure injection. They concluded that the most successful cementing technique (as measured by reduced AEs) was pressure injection and vacuum mixing of the cement, however some AEs were still detected suggesting that even the best cementing technique was prone to failure when torsional loading was applied (Sugiyama et al., 1989).

Other studies (Davies et al., 1996; Roques et al., 2004; Mavrogordato et al., 2011) have also assessed whether AE can be related to cement-bone debonding. These studies used a similar approach; placing piezoelectric transducers positioned on the surface of, or embedded into, the femoral stem. All noted the discontinuous nature of the cumulative AE events and attributed this to the propagation of a crack or coalescence between a main crack and a microcrack. Additionally, AE waveforms related to cement cracking have higher energy, longer signal duration and shorter rise times. Furthermore, work conducted by Rowland et al. (2004) demonstrated that AE monitoring could be used for the detection of excessive wear. They had two AE sensors positioned on the top and bottom fixtures of a five-station wear rig and noted that one of the stations showed two repeating signals of 57dB and 66dB amplitude. This was associated with higher volumetric wear and a subsequent inspection of the implant components showed evidence of wear that was not seen in the other stations.

Ruther et al (2010) developed a novel detection technique they termed magnetic oscillator, that uses elements of AE sensing. The sensing process begins with an external coil exciting the ferrous head of the oscillator. The oscillator then hits the membrane inside the implant and the impulse generated by this contact is dependent on the material adjacent to the membrane. For example, close bone contact, indicative of successful osseointegration, would mean there would be a lower deformation energy and reduced spring dampening. This could be measured by a second external detection coil measuring the velocity of the oscillator or by recording the resulting AE generated by the oscillator contacting the membrane. A mock-up of how the system could be used clinically, a cross section of an instrumented implant and magnified views of the oscillator, is shown in Figure 15.

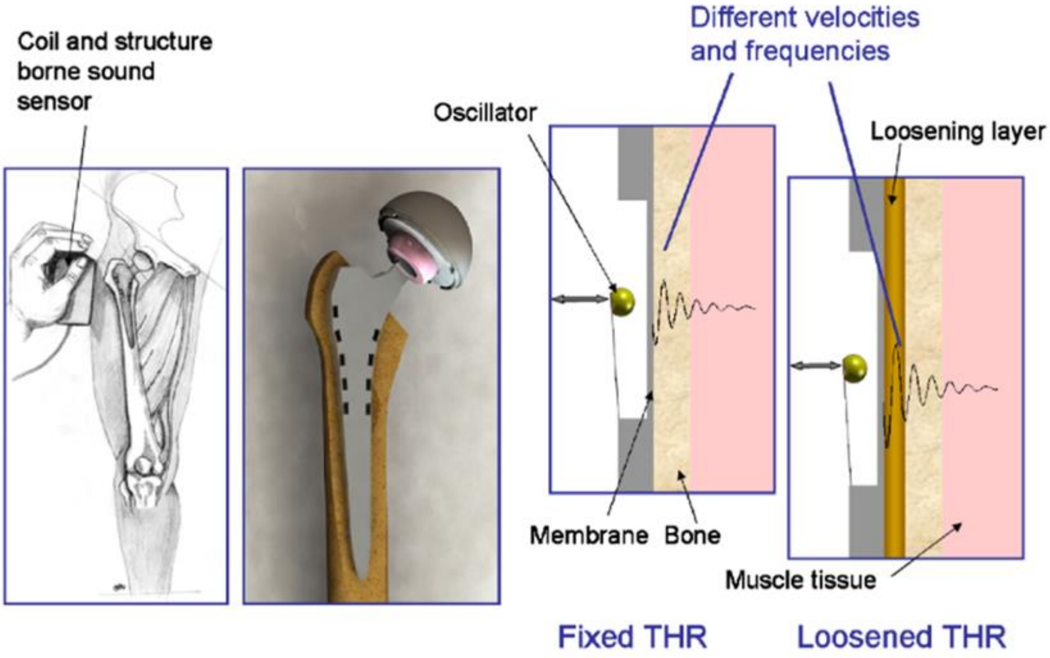

Figure 15 - Mock-up of how the novel magnetic oscillator system could be used clinically, a cross section of an instrumented implant and magnified views of the oscillator. Reprinted from (Ewald et al., 2011). 10.1109/ICSENS.2011.6127166. Copyright (2011) IEEE.

Ruther et al (2014) assessed this concept in an in-vivo rabbit model. Three different implant surfaces were used to induce various levels of osseointegration. Over the 4 weeks of implantation the AE changed with loosening of the implants (defined by the low axial pull-out strength of the implant) showing a continuous increase in central frequency. Ruther et al propose a novel solution for a non-destructive in-vivo assessment of implant loosening, this required no embedded electronics or telemetry systems and has the potential to provide localised measurement of osseointegration. However, to cover the full surface of the implant the concept would likely require extensive modification to the prosthesis and the addition of the oscillators would potentially complicate the manufacturing process.

Eddy Current

An Eddy current sensor uses a sensing coil supplied with an alternating current to create a magnetic field (primary field). If a conductive material intersects the primary field, a magnetic field will then be induced within the conductive material (secondary field), causing a change in the impedance of the coil. This change in impedance can then be detected and related to the distance between the sensing coil and conductive material.

Khoke et al (2018) examined the efficacy of implanting Eddy current sensors within the positioning holes left after total knee arthroplasty with the aim of detecting tibial component micromotions. Mohammadbagherpoor et al (2019) assessed the use of an Eddy current proximity sensor with a 10mm diameter solenoid coil. Their simulated and experimental work showed that they were able to detect the micromotions of a 10mm CoCr rod with a 100µm resolution at a distance of 20mm. Although, an Eddy current sensing coil would enable noncontact sensing of micromotions, it remains relatively under-developed and there are potential concerns of factors such as sensor migration over time with any changes in bone morphology.

2.3 Challenges in developing a telemetry system for an instrumented hip implant

The following section will discuss the challenges that need to be overcome to enable an effective in-vivo sensing system for use within a THR. These include choice of sensor, biocompatibility and integration within the implant, power, communication, and regulatory considerations.

2.3.1 Choice of Sensor

The choice of sensor is a key challenge in developing a telemetry system for an instrumented implant. Sensor choice is clearly a complex challenge, but most simply should primarily be driven by the cause or causes of revision for which data is being collected and accordingly the type and complexity of the system required. There are however several additional considerations. Firstly, the implant is likely to be in situ and functional for over ten years. So, the information collected upon implantation may well be needed to address questions formulated 10-15 years in the future. So wherever possible the system needs to be future-proofed. Secondly as more data is collected on implant performance it may be that hitherto unknown associations or ‘surrogate’ measures may be found to link a data output with impending revision. For example, could reduction in activity be a pre-cursor to failure caused by loosening?

Thirdly, the outcomes outlined in Figure 3 are binary in that they focus on revision as an endpoint. It is likely that as more data is collected there will be a more nuanced measure of failure such as degradation of activity or reduced range of motion. These additional factors may modify the primary driver for sensor choice to what sensors or combination of sensors would give the most comprehensive output data.

2.3.2 Biocompatibility and integration within the implant

Integration of sensing system within an implantable medical device (IMD) such as a total hip replacement has the potential to be beneficial however, it is important that the system does not impede the normal function of the implant nor cause an adverse biological response. This will require miniaturisation of the components to fit the size constraints of the implants as well as careful selection of materials and the mounting, embedding or encapsulation method. The assessment of biocompatibility should require biological evaluation including cytotoxicity testing, examination of the immunological and pathological effect on surrounding tissue and characterisation of the expected degradation of the implant’s material over the lifetime of the implant as per the recommendations of ISO 10993 or other such standards. Furthermore, conventional consumer electronics are designed for a lifetime of 2 – 5 years whereas the lifetime of an orthopaedic implant is longer 10-15 years and so this is a factor that will need to be considered by medical device manufacturers (MDMs).

Typically, electronic components require protection and shielding from dust, debris, moisture, temperature and salinity that could interrupt their function or cause a degradation in their performance. Electronics implanted in humans must be protected from inner body elements such as cells, proteins, platelets, and chemical gases (Joung, 2013). Furthermore, electronic components and the substances for the building up of integrated circuits, circuit boards, packaging materials and communication cables are not suitable for implantation. Printed circuit boards (PCB) consist predominantly of fiberglass and copper foil which are not biocompatible (Uhlemann et al., 2005;

Beshchasna et al., 2006), additionally PCB manufacture requires toxic chemical treatments.

Conventional electronics can be used within IMDs but will require encapsulation within a polymer or in a hermetically sealed chamber. Low consistency silicone has been shown to have favourable water absorption, water solubility and surface characteristics for long term implantation when compared to epoxy resin or polyurethane (Kirsten et al., 2012). Chambers or recesses can be manufactured within the bulk material of the implant be it metal, polymer, glass or ceramic and welded or bonded to create a hermetic seal (Joung, 2013). The hermeticity of the device would need to be assessed before medical device approval.

2.3.3 Power delivery system

Power supply is vital for the telemetry system of an IMD and the selection affects the proper function of the circuitry and the longevity of the working system. To date, only batteries and inductive power coupling have been used in untethered instrumented hip implants. Power supply still remains one of the most limiting factors of IMDs with the most significant constraints being size and demands of high capacity/lifespan (Joung, 2013; Amar et al., 2015).

Sensing systems can be classified as active or passive; active systems require an internal power supply to drive active components such as a microcontroller unit and transducers. Conversely, passive systems don’t receive power internally but instead by an external interrogator, whereby, a signal is generated by the interrogator’s excitation circuit and sent at radiofrequency to the sensor (Nelson et al., 2020). A sensing system can include active sensors but have a passive power supply unit such as an inductive charging link.

Batteries can supply consistent levels of electrical energy that is stored in the form of chemical energy. The first use of a battery within an instrumented hip implant was English and Kilvington (1979) and then Davy (1988). Many widely accepted IMDs use batteries. Examples are drug pumps, cochlear implants and pacemakers which can have a lifespan of 8 – 10 years (British Heart Foundation, 2020).

Lithium ion batteries are preferred owing to their high energy density which can range from 210 mWh/g to 440 mWh/g (Bock et al., 2012; Amar et al., 2015). A rechargeable system would satisfy the requirements of an IMD including longevity and power supplied. However, during the process of recharging battery cells temperature can increase significantly and energy capacity is decreased with every recharge cycle. Recharging options are limited, one option would be an ultrasonic source. Ultrasonic transcutaneous power transfer begins with an external transmitter converting electrical energy into acoustic or vibration waves which propagate through the tissue gap to the internal receiver. The piezoelectric receiver then converts the acoustic or vibration energy back to electrical energy (Ozeri and Shmilovitz, 2010). Awal et al. (2016) conducted an empirical review on the use of acoustic energy transfer for IMDs and found that such systems can reach an efficiency of 45% over a range of 400mm and typically operated over a frequency range of 35kHz to 30MHz with a maximum power level being found to be 5.4W. Although, charging capabilities require additional circuitry (Soares dos Santos et al., 2013) thus straining the size constraints of IMDs.

Another option for powering an instrumented hip implant is inductive charging which was first used by Carlson et al. (1974) an later by other groups (Bergmann et al., 1988; Graichen et al., 1999; Puers et al., 2000; Marschner et al., 2009; Damm et al., 2010; Bergmann et al., 2012; Sauer et al., 2013). An inductive coupling system has been the preferred method of power transfer likely since data can also be transferred inductively.

In the early 1830s, Michael Faraday first discovered the concept of electromagnetic induction, the theory behind the wireless transfer of electrical energy. Inductive power transfer works by passing an alternating current through an “external” transmitter coil which generates an electromagnetic field which induces a voltage within an “internal” receiver coil (Amar et al., 2015; Wageningen and Waffenschmidt, 2018). The voltage can then be converted to direct current through a voltage rectifier and then be used to power a circuit or charge an inbuilt battery or storage capacitor for use at a later time. Factors that can affect wireless inductive power efficiency include resonance/operating frequency, distance, coil alignment, size and number of turns (Cao et al., 2012;

Wageningen and Waffenschmidt, 2018). Inductive power can satisfy the size and energy requirements for an instrumented implant. Theoretically an inductive link power system can be used for an infinite amount of time after surgery thus making them an attractive option for a long term IMD. However, exposure to high levels of electromagnetic fields can be dangerous for patients (Soares dos Santos et al., 2013) and if the coils are not properly aligned power transfer efficiency is significantly reduced (Shadid and Noghanian, 2018). Wearing the transmitter coil system can be uncomfortable for patients, possibly limiting their ability to complete activities of daily living and limits the acquisition of data over prolonged periods of time (Almouahed et al., 2011; Soares dos Santos et al., 2013).

A promising alternative technology is the use of energy harvesting to convert the mechanical energy from joint motion into electrical energy for powering implants. The concern is whether the joints low frequency movement (typically <1Hz whilst walking) would be sufficient to generate the required power. Unlike conventional sources of mechanical energy, movements can be infrequent and inconsistent and so traditional power management and battery charging systems will be unsuitable. Silva et al. (2013) developed a hip prosthesis with three separate power generators including a translation and rotation based electromagnetic generator and a piezoelectric generator powered by a ceramic diaphragm located in the hollow femoral head, shown in Figure 16. Each generator had an individual power conditioning circuit that fed into the main ultracapacitor energy reservoir, so the implant could function once the generators begin to produce enough energy, or the energy can be stored. Once a predetermined voltage had been reached within the ultracapacitor the energy stored within was delivered to the IMDs telemetry circuit. Other attempts at developing energy harvesting systems for a THR have similarly used a linear electromagnetic generator (Pancharoen et al., 2014) and piezoelectric transducers (Lange et al., 2020).

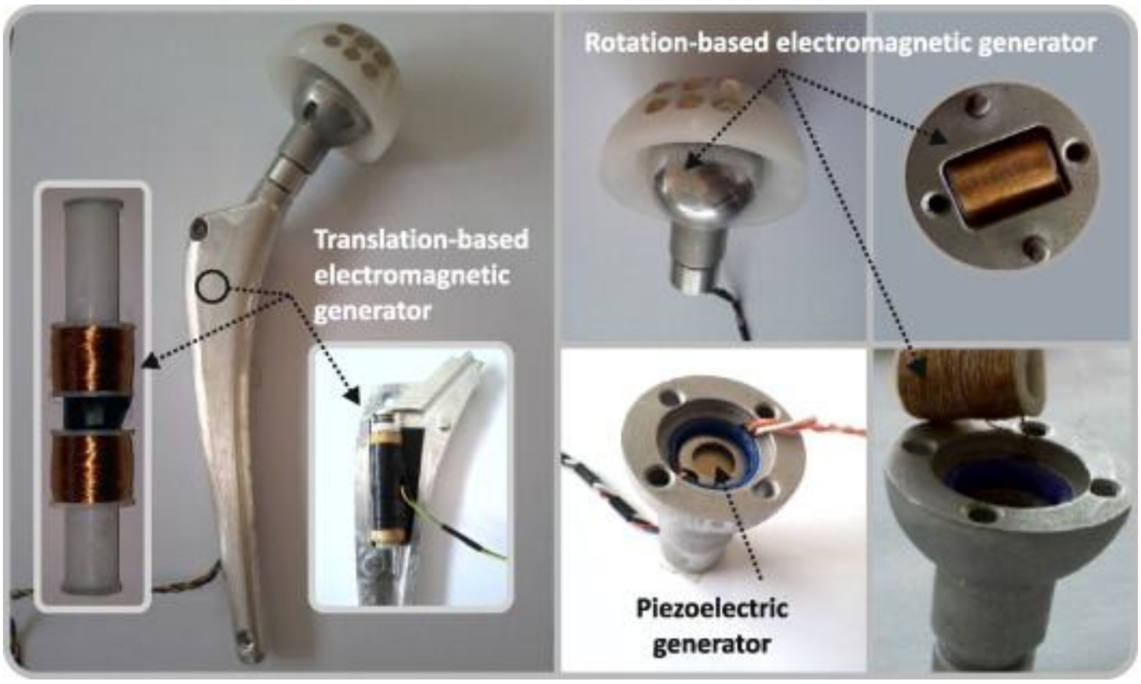

Figure 16 – Hip prosthesis with three independent power generating systems. Reprinted from (Silva et al., 2013). Copyright (2013), with permission from Elsevier.

2.3.4 Data transfer system

Wireless communication would be a necessity for the telemetry system of an implantable medical device, particularly in a deeply implanted orthopaedic implant. Wired communications were used in the first iterations of instrumented implants but are not a viable option as they would induce unnecessary pain or discomfort to the patient and pose an infection risk. A wireless connection would also better enable continuous data collection without causing inconvenience to patients. In which case designers will have to consider data transfer rate, range, permittivity through human tissue and the additional size and power consumption constraints.

The choice of the wireless communication system will depend on what data needs to be transferred to or from the implant, and when. If the system's output only involves small amounts of data (e.g. identity of the patient and implant or single measurement of blood glucose or temperature) or if the frequency of measurement is low (e.g. 1 sample per hour) this places lower demands on a real time data transfer system. Similarly, if the collected data can be stored or processed locally (in the implant), it can be uploaded at the convenience of the user, without requiring a continuous telemetry system in place. One such low capacity yet versatile data transfer method could be radio frequency identification (RFID), which is being used in warehouse inventory tracking, pet identification, contactless payments and tracking marathon runner times.

A RFID system consists of a transponder or tag, a reader or interrogator, accompanying antennas to enable communication through radio frequency and software that controls the system and manages the data (Asif and Munir, 2005). The tags will have a chip that stores the identification data or electronic product code (EPC). Tags can be active, powered by a battery and favoured for their increased range, or passive, powered by the reader’s signal and favoured for their low cost (<10 cents) (Souto et al., 2019).

RFID technology is used to track items and store low levels of data so, could be used to identify medical devices once they have been implanted and include data on the make and model of the implant, reasons for the intervention, the surgeon who completed the procedure and details of the surgical approach. One such company addressing this is Ortho-tag in collaboration with the University of Pittsburgh. Ortho-tag was developed to provide a non-invasive, battery less and wireless method of identifying an implanted orthopaedic device. The system consists of a RFID chip embedded within an implantable tag and a ‘touch probe’ that uses transcutaneous near field communication to power and communicate with the tag from outside the body (Sejdić et al., 2013). Orthotag claim their system is capable of storing information on an implanted medical device, information which could include X-rays and patient medical records (Ortho-tag, 2020).

An enhancement to a RFID system, that could be beneficial in orthopaedic devices, is passive or battery-less sensing capabilities, such systems are known as computational RFIDs (CRFID) (Souto et al., 2019). Sample et al. (2008) achieved this with their wireless identification and sensing platform (WISP) which could both receive power and communicate data to a wireless RFID reader. They showed the efficacy of their WISP by integrating sensors such as temperature, ambient light, rectified voltage, and orientation. Other groups have looked at the possibility of using CRFID systems within IMDs including pressure sensors for orthopaedic implants (Vena et al., 2015) and blood glucose sensors for continuous blood glucose monitoring (Xiao et al., 2015). Ortho-tag suggest that their system can feature sensors for the in-vivo measurement of pH and temperature to indicate infection in the tissue surrounding an implant (Ortho-tag, 2020).

In past in-vivo sensing systems have been used to record real time load and vibration data at frequencies >1Hz which required data transfer systems with higher data transfer rates. The predominant method used in the majority of past instrumented hip implants has been inductive data transfer with (Puers et al., 2000; Marschner et al., 2009; Bergmann et al., 2012; Sauer et al., 2013) all using inductive coupling data transfer and Bergmann (2012) having a combined power and data coil. Nikola Tesla was the first to realise that electrical energy, and so data, could be transmitted wirelessly between two inductively resonant coils (Tesla, 1900). Inductive power transfer can reach a data transfer rate of up to 100 Mbps at a range of 6cm outside the body (Islam and Yuce, 2016). However, as well as the aforementioned limitations of using inductive coupling for power transfer, when being used for data transfer an inductively coupled system is susceptible to interference from nearby electromagnetic fields (Joung, 2013; Islam and Yuce, 2016).

These limitations lead many medical device companies to use, antenna based, radio frequency (RF) transceivers for wireless communications between an IMD and external unit. The IMD is equipped with an antenna that when fed with a signal radiates electromagnetic waves through the body to an external receiver (Teshome et al., 2018). The radio frequency spectrum ranges from 3KHz to 300GHz; between 30MHz and 400MHz is the human body’s resonance range where specific absorption rate is at its highest (WHO, 1993) meaning that RF waves can penetrate the furthest into the body. Therefore, a transceiver operating around this frequency range would be desirable for a deeply implanted medical device.

In 1999, the increased use of RF systems in IMDs lead the Federal Communications Commission (FCC) standardising the Medical Implant Communication Service (MICS), to the RF band 402 – 405 MHz. In 2009 the FCC upgraded the MICS to the Medradio service which included two additional “wing bands” thus extending the band to 401 – 406 MHz (Bradley, 2011; Islam and Yuce, 2016; Teshome et al., 2018). Global medical device companies have manufactured their own remote monitoring systems using MICS: Biotronik Home Monitoring® (FDA approval 2001), Medtronic Carelink® Network (FDA approval 2005) and Merlin.net® Patient Care Network (FDA approval 2007) (Guevara-Valdivia and Torres, 2011).

Another option for wireless communication is Bluetooth or Bluetooth low energy (BLE). Bluetooth is a standard for wireless exchange of data operating at a radio frequency of 2.45GHz. At this frequency the radio waves will have a penetration depth of approx. <4cm in fat and <2cm in skin and muscle (Gabriel et al., 1996; Melia, 2013) however, the higher frequency means that BLE has a far higher data transfer rate, up to 2Mbps (Bluetooth.com, 2020).

To date Bluetooth has not been used in an instrumented hip implant but has seen use in other IMDs. The Confirm Rx ICM (Abbott, Ill, US) is the first Bluetooth enabled and smartphone compatible implantable cardiac monitor to have received FDA approval in Oct 2017 (Abbott, 2017). In July 2018 the world’s first pacemaker with Bluetooth technology (Azure Bluesync pacemaker, Medtronic, Db, Ireland) was implanted (Southampton, 2018). Bluetooth is widely used within consumer electronics with many personal devices being Bluetooth enabled. Based on the early adoption of Bluetooth enabled IMDs it is reasonable to assume that devices of a similar nature will become more widespread throughout the medical sector. However, for application within the hip joint the low penetration of 2.4GHz RF waves will make Bluetooth an unfeasible option. An alternate solution to this is a dual band radio repeater that can receive radio signals at one frequency and retransmit at another. Kiourti et al. (2014) configured an on-body antenna to receive transmissions from an IMD in the MedRadio band 401 – 406 MHz and retransmit the received data to an external device in the ISM band, 2400 – 2480 MHz. This approach would also improve energy efficiency as transmitting low frequency waves is far more energy efficient therefore reducing the power consumption of the IMD’s telemetry system.

2.3.5 Regulatory considerations – Medical device approval

Europe and the US are the largest global markets for medical devices. To market their devices within these territories MDMs need to comply with the regulations laid out by the European Commission in their Medical Devices Regulation (MDR) to achieve a CE mark or be approved by the U.S. Food and Drug Administration (FDA), respectively.

An in-vivo sensing system for use within a THR will be a class III (implanted) medical device and so will require extensive pre-clinical and clinical testing to provide evidence of its efficacy and safety before it can be approved. The same will be required when following the FDA's pre-market approval (PMA) pathway for new medical devices when entering the US market.

If integration of the telemetry system has required modification of the implant, then new approval will be required for the implant. These additional regulatory hurdles will mean further costs, risks and inconvenience for the MDM. Whereas, if the sensing system is able to integrate with the implant without changing function or geometry then approval requirements may be more easily met. Furthermore, the safety of the in-vivo sensing system, and accompanying telemetry, should not be considered in isolation and interactions with the implant should also be considered. Attaching or embedding the sensing system could lead to corrosion, generation of wear particles and there is the risk that the system will move from the intended position or become separated from the implant. These implications should also be considered for the entire lifetime of the implant even if the telemetry system becomes inactive or stops working.

In a 2018 FDA public workshop (Baumann et al., 2020) it was highlighted that care should be taken to go beyond physical characteristics associated with pre-clinical testing, such as biocompatibility, sterilisation, electrical and mechanical performance, and sensor accuracy and repeatability. For in-vivo sensing systems, regulatory considerations should also encompass validation of the metrics produced and the level of evidence required should be dependent on how the data will be used, for example if the sensor is delivering a treatment or providing a diagnosis of a potentially life-threatening condition. In either scenario the wrong result would cause harm to the patient or be life threatening.

2.3.6 Regulatory considerations - Cybersecurity

In 2017, the global WannaCry cyber-attack was estimated to have cost the NHS £92m, £19m lost output and £73m in IT costs the majority being spent in the aftermath (DHSC, 2018). A study conducted by Clearswift revealed that in the UK, 67% of healthcare organisations suffered a cybersecurity incident in 2019 (Clearswift, 2020). The risk of cybersecurity related incidents within healthcare are increasing as more medical devices have wireless connectivity and are joining the internet of things.

In the past there was concern over malicious cyberhackers gaining unlawful access to a patient's implanted medical device (IMD) and causing harm to the patient. In a 2013 interview, Former Vice President Dick Cheney revealed that in 2007 he had the wireless connectivity of his pacemaker disabled to avoid the possibility of an assassination attempt (Cheney, 2013). Halperin et al. (2008) were the first research group to show that an IMD could be infiltrated and patient data and safety put at risk. In 2011, amateur hacker Barnaby Jack demonstrated live on stage, at the Hacker Halted conference in Miami, how he could hack into an insulin pump and deliver a fatal dose to the user (Goodin, 2011; Burns et al., 2016). The following year Jack performed a similar live demonstration in which he hacked into a pacemaker and commanded the device to deliver a deadly voltage surge of 830V (Gray, 2012; Burns et al., 2016). Although theoretically possible it is highly unlikely that attacks like these would ever occur. Dick Cheney's unique public figure status meant that he was at a high risk and so every precaution was taken to guard him against possible attacks. Additionally, hacking into a user's pacemaker would require the attacker holding 'suspicious' specialised electronic equipment close to the user for an extended period of time therefore making it hard for the attack process to be scaled and in general there are far easier, more effective and profitable ways to cause harm or steal a person's data (Domas, 2019). To-date there is no evidence of cases where a patient's IMD has been hacked with malicious intent. Though there have been device recalls (FDA, 2015a; FDA, 2018c) and safety communications issued by the FDA (FDA, 2015b; FDA, 2018b; FDA, 2019; FDA, 2020) where cybersecurity vulnerabilities were cited.

Cardiac and drug delivery devices, such as pacemakers and insulin pumps, carry higher levels of risk whereas, a non-active in-vivo sensing system will carry less risk as it only provides diagnostic capabilities so cannot have a 'physical effect' on the patient or user. However, if a smart implant capable of in-vivo sensing is realised, and intended to be used clinically, it is likely that the device would include or even require functionality to store data on the patient and their medical history. This data could be a potential target for malicious cyber hackers as medical records are worth more than a credit card number or bank details when sold on the dark web (Conaty-Buck, 2017; Yao, 2017). Although there will be an inherent risk of an IMD being hacked, this is not the only component of cybersecurity that should concern MDMs and regulatory bodies instead, the majority of medical device cybersecurity should be preventing accidental cyber harm and, making sure the system is robust to the unknown and unexpected (Domas, 2016).

In 2013, the FDA released a safety communication that warned MDMs, hospitals and users that cybersecurity breaches could affect the proper function of an IMD (FDA, 2013). Building upon this the FDA issued the "Content of Premarket Submissions for Management of Cybersecurity in Medical Devices" guidance document (FDA, 2014), and updated in 2018 (FDA, 2018a). The guidance encourages MDMs to consider cybersecurity measures during the entire lifecycle of the device and provides details on the documentation required for the PMA submission with regards to cybersecurity. Additionally, in 2019, the Medical Device Coordination Group (MDCG) released "Guidance on Cybersecurity for medical devices" (MDCG, 2019) which provides recommendations to MDMs on how to satisfy the requirements laid out in the MDD that relate to cybersecurity.

2.4 What physical or mechanical phenomena that occur within the environment of a total hip replacement could be sensed?

The potential sensing applications that have been formulated around the common indications for revision surgery of a THR (as shown Figure 3), are summarised in Figure 17. The aim being to develop a system that could continuously provide useful data on the performance of the implant and occurrence, or progression of the phenomena associated with the indications for revision surgery. These potential sensing methods are further explained and expanded upon in Table 2 which includes the common indications for revision THR surgery and the associated key physical phenomena along with suggestions of the aspects of these phenomena that could be detected by an instrumented implant. Table 2 also includes “Implant failure” which does not appear on Figure 17 but falls under the category of “other” common indications.

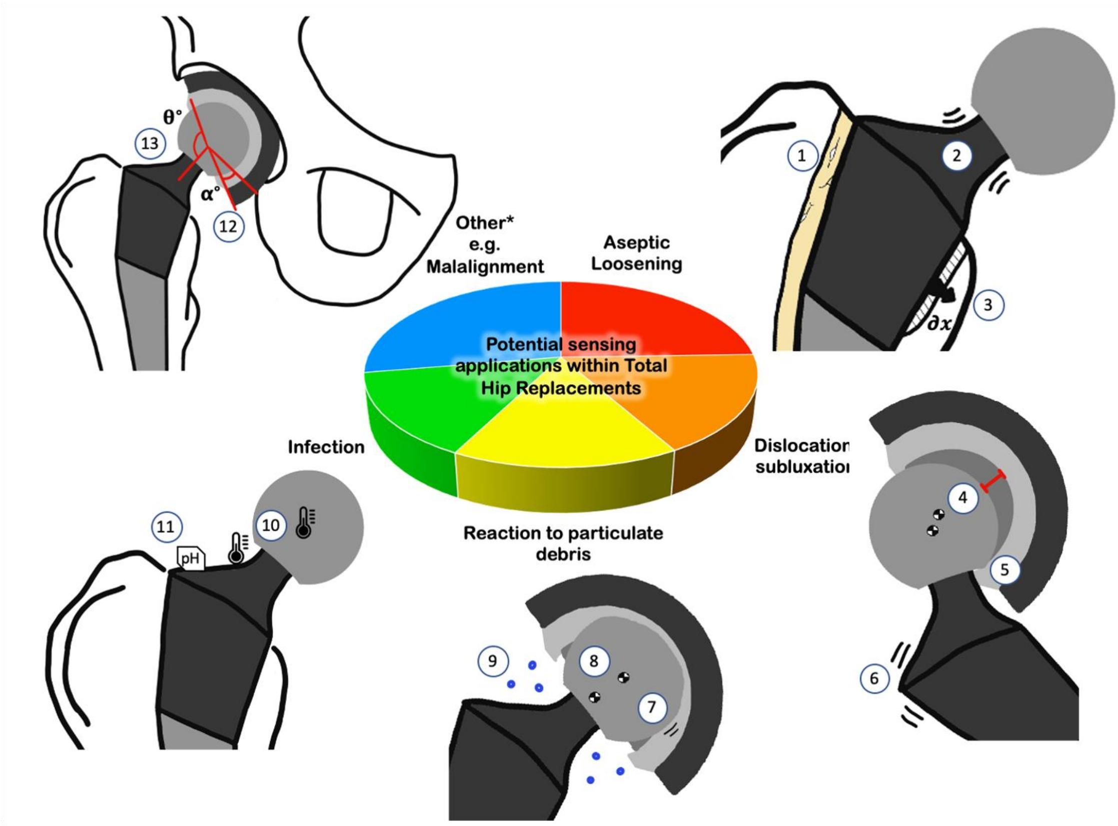

Aseptic Loosening	
1.	Acoustic Emission sensing to monitor the integrity of the bone cement
2.	Vibration sensing can be used to compare vibrational response of well-fixed and loose implant bone system
3.	Measuring the displacement of the implant components relative to the bone and so the magnitude of the micromotions(dx)
Dislocation/Subluxation	
4.	Measuring relative displacement of components to show if bearing surfaces separate
5.	Force or pressure sensors at the cup’s rim to sense force form femoral stem contact
6.	Vibration sensing could detect torque generated when components contact
Reaction to particulate debris	
7.	Vibration sensing could show changes in friction as bearing surfaces become worn/rough
8.	Measuring relative displacement of components to show if head position in cup has changed due to excessive wear
9.	Directly measure wear particle concentration at the implant sight or in patients’ blood
Infection	
10.	Measuring the temperature of components or the tissue surrounding the components
11.	pH sensing the tissue surrounding the components
Malalignment	
12.	Measuring the relative angles of the components relative to the bones to show if they are positioned in the “Gold Standard” range intra or post-op
13	Measuring the relative angles of the components to show if they are positioned in the “Gold Standard” range intra or post-op

Figure 17 - Graphical representations of potential sensing methods within a THR addressing the common indications for THR revision surgery. *Other indications of note include malalignment, implant wear and implant fracture. Citation: O G Vickers et al 2021 Prog. Biomed. Eng. 3 042004. DOI 10.1088/2516-1091/ac1b7f. © 2021 The Author(s). Published by IOP Publishing Ltd.

Table 2 - Common Indications for revision surgery, their associated physical phenomena and what features could be detected/sensed/monitored.

Indication for Revision Surgery	**Key Physical Phenomena**	**What could be detected?**
Aseptic Loosening	• Acoustic emissions and vibration response will differ between well fixed and loose component • Micromotions/ component recession • Stress shielding	1. Measure acoustic/vibration response when implant or femur is excited/vibrated 2. Relative motions/position of components with respect to the bone 3. Force/pressure imbalance could predict risk of stress shielding and subsequent loosening
Dislocation/ Subluxation	• Primary Impingement: contact between cup and stem • Subluxation: separation of bearing contact surfaces • Dislocation: complete separation of bearing contact surfaces	1. Relative motions/position of components could show when at the extremes of ROM and so if impingement will occur or if bearing surfaces have separated 2. Sense if contact between the femoral stem and rim of the liner has occurred 3. Force of contact could indicate if impingement contact or full subluxation event has occurred 4. Impingement contact could generate a vibrational response within components
Wear	• Increase in friction as rough surfaces created by wear • Decrease in liner thickness/head size • Increase in particulate wear debris	1. Vibration response will change as bearing surfaces become worn/rough 2. Relative motions/position of components can be used to see if heads position in cup has changed due to excessive wear 3. Directly measure wear particles at the implant sight or in patients' blood
Infection	• Temperature rise of the implant or surrounding area • Rise in pH in the area surrounding the implant	1. Temperature sensor embedded within or on the surface of the components 2. pH sensor on the surface of the components
Malalignment	• "Gold standard" implantation range	1. Relative motions/position of components could show if they are positioned in "gold standard" range intra or post-op.
Implant Failure	• Stress fracture within implant	1. Strain gauges could be used to detect regions of high stress concentrations and so at risk of failure

The table shows that monitoring the kinematics of the components would provide the opportunity to monitor the most of the considered physical phenomena occurring within a THR. To date no previous work has been done using integrated sensors to measure the angles or positions of hip implant components. This could enable the identification and characterisation of complex mechanical motions such as impingement and subluxation. In the past these have been hard to identify during in-vitro testing of THRs. If THR component kinematic data is gathered in-vivo then it could be used to quantify the patient’s gait be extracting metrics such as number of steps, cadence and joint range of motion. These are common metrics used to track recovery following THR surgery.

Measuring the load transmitted through the joint or through the components has been extensively explored in the past. As previously stated, the data gathered from these implants was extremely useful in understanding how THRs function in-vivo. Datasets have also been made available by the research group (Orthload, 2019). Yet force and moment data alone is currently not sufficient to identify the occurrence of mechanical phenomena associated with common indications for implant failure.

There is potential that load transmitted through the joint could give an indication of walking speed, the number of steps taken and if the patient is able to put their full weight through their joint. However, this would only likely be the case when under ideal conditions and would require a large set of training and verification data. Whereas, if the kinematics of the implant components (i.e. relative orientations and positions of the components) can be accurately measured it would provide a better way of obtaining other clinically useful measures that are more often used as outcome measures when evaluating the performance of the surgery and tracking the recovery of the patient. These can include joint range of motion, cadence, and potentially monitoring motion of the components during activities of daily living i.e. sit to stand or tying shoelaces.

Vibration analysis and tracking the acoustic emissions of the components has been widely reported in literature. Although, it is believed that there is the potential for a far wider range of indications or phenomena to be detected from examining the vibration response of an implant system. Nevertheless, some features may not produce a signal strong enough to be detected and it may be hard to distinguish between the different signals especially as there will likely be significant background noise generated by an experimental hip simulator and when in an in-vivo environment. However, improvements in data acquisition and processing techniques and advancements in artificial intelligence and machine learning could provide scope for the data gathered from a vibration response of a hip implant system to be processed and features accurately identified.

Although infection is a common complication associated with total hip arthroplasty, biological methods of detecting infection will not be considered in this work and instead the sensing of physical and mechanical phenomena will be the focus of this work. However, physical factors such as temperature or pH can be indicative of infection and so would be useful outputs to monitor in vivo and during experimental tests. Additionally, as temperature sensors are readily available and relatively simplistic to integrate within circuitry the inclusion of temperatures sensor will not be a burden or pose a significant engineering challenge.

2.5 Review Conclusion

The number of total hip replacements implanted are increasing, complication and revision rates whilst low are still at undesirable levels. An in-vivo sensing system with telemetric capabilities would be beneficial as a means of gathering valuable data on the implant's function and the condition of the surrounding tissue. This data could be used to verify in-silico and in-vitro studies, inform improvements in implant design and surgical technique, and guide postoperative care. If real time condition monitoring is achieved along with intelligent recognition of adverse events and deviations from a patient's normal function, then such systems could provide advantages including remote patient monitoring, improved accessibility to healthcare and continuous as opposed to episodic and largely unnecessary assessment and early detection of problems.

Total hip replacements are a successful late-stage intervention for osteoarthritis however revision surgeries, which have higher associated costs and poorer outcomes, are still a cause for concern and possess a high burden on society and medical institutes. The indications show that there are a variety of ways an implant can fail all of which present the symptoms of patient pain making them hard to diagnose through clinical observations. The current methods of diagnosing need for revision are commonly conducted in a clinical setting and so are subjective, costly and can have long turnarounds and thus lead to a late diagnosis. Therefore, an instrumented hip implant capable of real time condition monitoring of an implant’s performance and early detection of indications for revision would be beneficial for patients and surgeons alike.

Since the implantation of the first instrumented hip implant in the 1960s less than 100 patients have received an instrumented implant capable of in-vivo sensing. These implants have measured biomechanical metrics, including force and moments and temperature. The data gathered has helped progress understanding of how a THR functions in-vivo and so informed improvements in implant design and surgical technique. However, force, moments and temperature measurements are currently not sufficient to deduce early indications for revision surgery. However, they are important metrics and may still be required in a sensing system for use in a smart THR capable of condition monitoring and intelligent feature recognition. Other experimental work has looked at measuring levels of implant loosening presumably because loosening is the most common indication for revision surgery in THR and indeed other orthopaedic implants. This work has shown potential but until it can be shown that the diagnostic accuracy and reliability is matched to standard radiographic methods then, clinical translation will not be a possibility.

Widespread adoption of smart instrumented THRs and IMDs will not be realised until several key challenges have been overcome these include: what sensing method is used, biocompatibility and integration within the implant, power delivery, communication, and regulatory considerations. Additionally, product liability is also a limiting factor within the field of IMDs as MDMs will not want to take on the additional risks associated with developing and marketing such technology without measurable benefits either in improved outcomes or reduced costs but also to the wider healthcare system. Also, the expected lifetime of a THR is >15 years whereas the lifetime of common consumer electronics such as a smartphone is <5 years (whilst also receiving regular software updates). This will need to be considered by MDMs when designing the hardware and software of the IMD. Smart implantable medical devices, such as pacemakers and insulin pumps, are becoming more accepted and widely used as clinical interventions. Furthermore, advances in technology such as wireless power and telemetry systems, suggests that the development and eventual adoption of an instrumented hip implant, capable of real time condition monitoring, is imminent.

The successful introduction of technology outlined in this review would not only benefit the patient, but it would also enable clinicians to base decisions on more objective quantitative data This would potentially obviate the need for follow-up clinics for all patients thereby reducing hospital workload and hence costs which would benefit the payer whether they are a government or an insurance company.

There is an apparent lack of work conducted on sensing relative motions/positions of hip implant components using an integrated sensing system. It is hypothesised that tracking the component position and orientation would be more beneficial for condition monitoring of an implant and detect a wider range of early indications for revision surgery and other clinically useful metrics. Therefore, the focus of this work going forward will be to develop an instrumented hip implant with integrated sensors that can measure the relative motions and positions of the implant components and so address the apparent gap in the field of work.

Chapter 3 Development of an experimental hip joint simulation appropriate for sensor development and validation

This Chapter presents the design specifications, selection of a hip joint simulation model and the novel methods developed and used for the work in this thesis including detection of an impingement occurrence and measuring femoral head translation during an impingement driven subluxation event.

Experimental hip simulators previously used in (Pryce, 2019; Pryce et al., 2021; Williams, 2022) were available during this PhD. However, they were not appropriate for the development and validation of a prototype sensing system for the following reasons:

- The simulators are costly and in low supply.
- Limited achievable range of motion.
- Require specialist permanent fixation using PMMA bone cement.
- The architecture of the simulators provides limited access to the components.
- The simulators are complex to set up and run.

A bespoke test rig that could simulate hip joint motion was necessary in this application to allow for a convenient method of testing prototype sensing systems. The hip joint simulation model needed to be simple to operate, provide easy access to all the hip implant components, provide external validation of the sensing system output parameters (e.g. angle or position of the components) to a clinically relevant degree of accuracy and mimic the motion of a hip joint. An important part of this development was to define the motions to be sensed in a THR and this was used to establish the design requirements of the hip joint simulation and the prototype sensing system.

This chapter will, firstly describe the motions to be sensed within a THR and provide a rationale, then the design requirements and design specifications of the hip joint simulation test rig will be discussed. The details of hip joint simulation design iteration are then presented, and the design is discussed and evaluated with respect to the design requirements and specifications.

3.1 Design specifications for an experimental hip joint simulation

The design specifications have been developed from information in the literature review and the design requirements. The design specifications are presented in Table 3. The table includes the need or the design requirement, the justification behind the requirement and the final specification. The final specifications have been given a pass/fail grade or split into a red/green classification system to aid final assessment of the design's performance or function. They are as follows:

Red – Acceptable, the design is able function or operate adequately however the performance is not optimal and so could be improved.

Green – Good/Exceptional, the design meets or exceeds the criteria established in the requirements.

Table 3 – Hip simulation test rig design specifications including the need or the design requirement, the justification behind the requirement and the final specification.

Item No.	Requirement	Justification	Specification
1	Mimic clinically relevant motion of a total hip replacement	A THR aims to restore function to a hip joint i.e. a ball and socket joint. So simulator should replicate motion of a ball and socket joint to three degrees-of-freedom to cover full working range of motion of a THR.	**Red** – Manipulate components in two planes (orientation to two DoF) **Green** – Manipulate the components in three planes (orientation to three DoF) **Pass/fail –** Manipulate the THR components through their full working range of motion.
2		Speed of the rig should match the top speed of the hip during walking. Mentiplay et al (2018). measured peak joint angular motion to be 67°/s at walking speed of 0.40 to 59 m/s and 220°/s at walking speed of 1.40 to 1.60 m/s. Although the latter were measured in healthy patients so is unlikely to be reached by a patient following THR	**Red** – achieved angular speed 67° to 220°/s **Green** – achieved angular speed >220°/s
3	Mimic adverse events experienced in a THR	Impingement & impingement driven subluxation Impingement being contact between the neck of the femoral stem and the rim of the acetabular cup (Amstutz et al., 1975) Subluxation being when the femoral head is levered out of the cup with the cup's rim acting as a fulcrum (Usrey et al., 2006)	**Pass/fail –** Produce impingement event
4			**Pass/fail –** Produce subluxation event with bearing contact surfaces being separated and head centre of rotation being displaced by >1mm
5		Malignment of acetabulum component referring to cup anteversion and cup inclination	**Pass/fail –** Acetabulum can be positioned beyond typical implantation angle of 15° anteversion and 45° inclination by ±20°
6	Provide angular measurements of the implant components (ball & socket joint)	Real time measurement of the angular position of the implant components will be required to assess the sensing system's ability to measure the positions of the components. Maximum encoder resolution of the experimental hip simulator used in (Pryce, 2019; Williams, 2022) was 0.09° however, unrealistic to achieve this level of resolution. Upon consultation with industry experts and practicing orthopaedic surgeons the minimum required resolution and accuracy was set as 1°.	**Red –** Resolution >=1° **Green –** Resolution <0.1°
7			**Red –** Accuracy >=1° **Green –** Accuracy <0.1°
8	Take positional measurements of the actuated component	Real time measurement of the position of the actuated implant components will be required to assess the sensing system's ability to measure the positions of the components. Positional measurements will be needed when replicating adverse mechanical motions e.g. joint separation, edge loading and subluxation. Upon consultation with industry experts and practising orthopaedic surgeons the minimum required resolution and accuracy was set as <1mm.	**Red -** Resolution >=1mm **Green –** Resolution <1mm
9			**Red -** Accuracy >=1mm **Green –** Accuracy <1mm
10	Data acquisition and presentation	Early-stage development of a sensing system requires proof of concept work where the sensors have not been properly calibrated and so real time data presentation is very useful for the developer when investigating a sensors response and assessing its viability.	**Red** – Data requires external post-processing to get angular position etc. and delay in data presentation **Green** – Real time presentation of component angle presented as Tilt Angle & Azimuthal Angle

11	Lab use	To enable easy lab use the rig should be a manageable size and more importantly allow for clear access to implant components. The rig should also run off standard lab power supply and be controlled by a PC.	**Pass/fail –** Requires power supply of 24v
12			**Pass/fail -** Bench top mounted
13			**Pass/fail -** Space allows easy access to implant components/sensor system
14			**Pass/fail –** Controlled by a PC
15	Accepts variety of implant sizes	Implant head sizes range from 22mm to 50mm in diameter, therefore it is important for the simulator to a range of head sizes as the sensing system need to work in all implant sizes	**Red –** Can only accept 1 implant size and sectioning or adaptation of the components required **Green** – can accept implants from minimum (22mm) to maximum (50mm) head size
16		Easily interchange between different component sizes	**Red** – Interchanging implant component requires rig component interchanging **Green** – Fixtures and fittings allow for implant component interchanging

3.2 Experimental hip joint simulation model

3.2.1 Typical experimental setup

The UR3 (Universal Robots, Odense, Denmark) is a robotic arm with six rotating joints and a maximum reach of 500mm. All the actuated joints have ranges of ± 360° except for the tool flange which has unlimited rotary range of motion. This makes the robot highly flexible and ideally suited to actuating the ball and socket joint of a hip joint model. The UR3 has a pose repeatability of ±0.1mm and was configured to record position and orientation of the tool centre point at a maximum frequency of 150 Hz.

An image of the test set up used with the robot arm is shown in Figure 18. The robot arm was mounted on a custom aluminium extrusion base frame. A stem component was 3D printed and matched the geometry of a clinically available stem taper (as mentioned in Section 4.6.1) and included an extruded pocket, on the face of the stem taper, to house the 8X2mm permanent disc magnet, as shown in Figure 19. The stem’s neck feature was extended and included a flat base to allow secure mounting to the robot tool flange. A clinically available femoral head component (as mentioned in section 4.6.1) was then pressed onto the stem fully so that the top face of the magnet was coincident to the head taper face. An acetabular shell component was held in a 3D printed mount with a hemispherical recess the same dimension as the outer diameter of the shell component (approx. 56mm). An acyclic sheet with a through hole smaller than the diameter of the face of the shell component but larger than the diameter of the face of the liner component was screwed in place on top of the mount and used to clamp the shell and liner into the mount. An image of this mount assembly is shown in Figure 20. The experimental setup was not intended to undergo anatomical loading and so it was deemed acceptable to manufacture the stem component from 3D printed PLA.

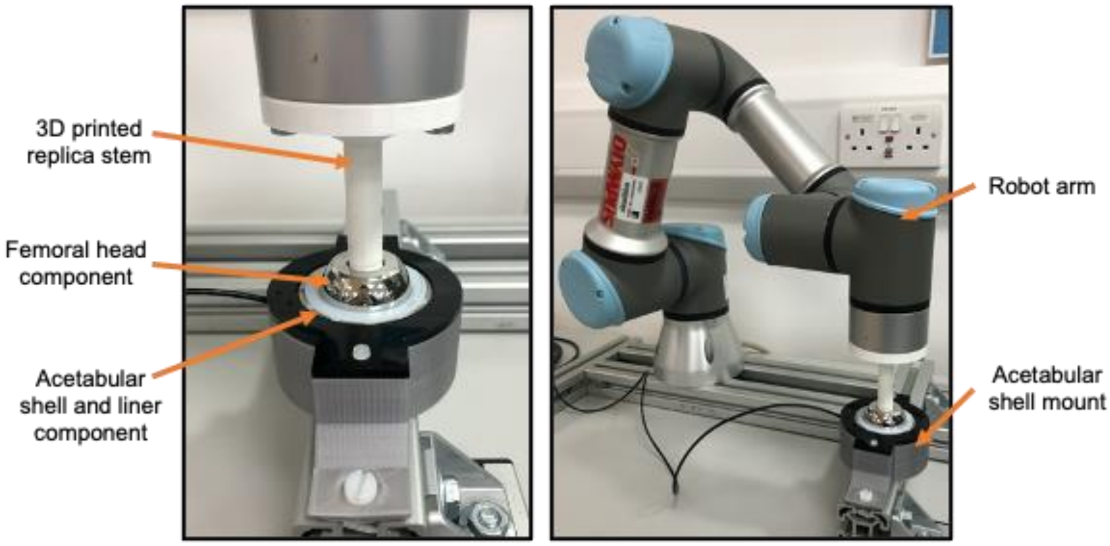

Figure 18 - Experimental set up using the UR3 showing stem/femoral head positioned in the acetabular liner in the 'neutral position'.

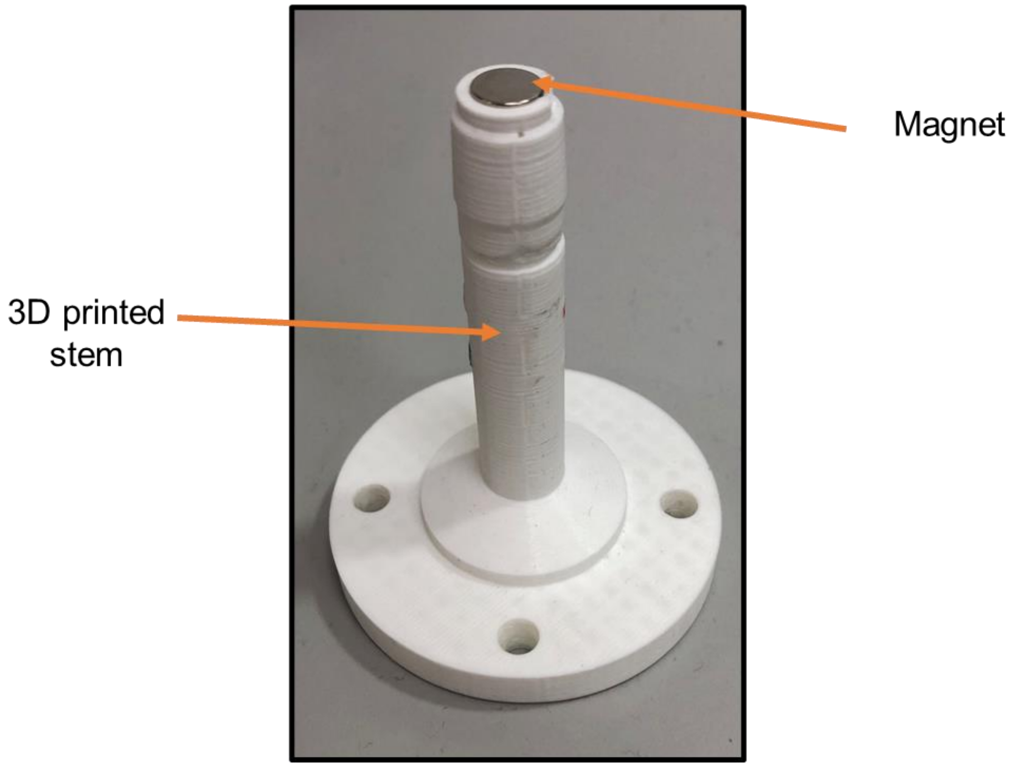

Figure 19 - 3D printed replica stem component fitted with magnet.

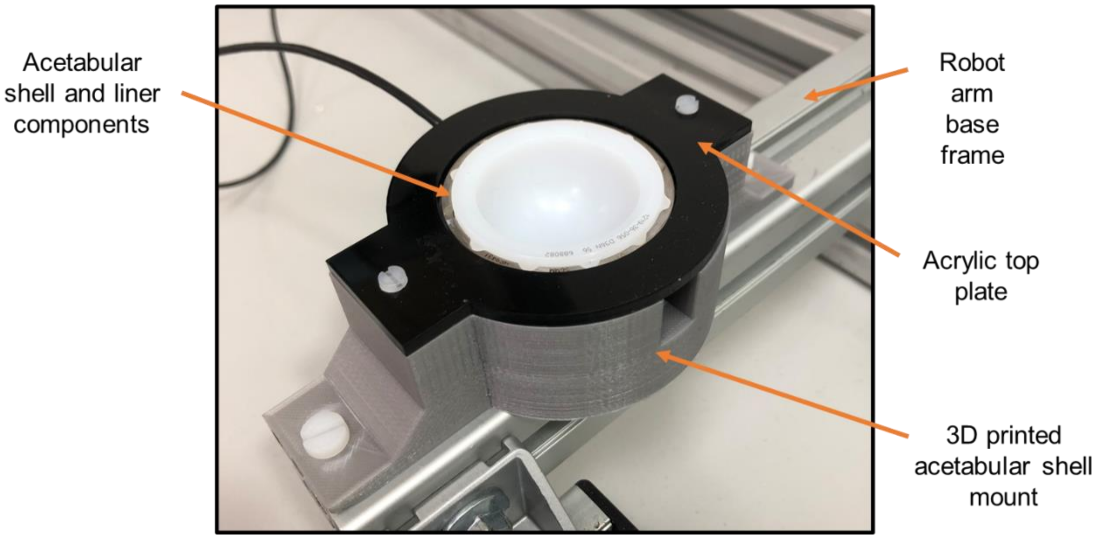

Figure 20 - 3D printed polymer acetabular shell mount and acrylic top plate mounting acetabular shell and liner components to robot arm base frame.

The head was positioned manually in the liner with the UR3 in Freedrive mode. The Freedrive mode is an in-built feature of the UR3 where "while the Freedrive button is held down, it is possible to physically grab the robot arm and pull it to where you want it to be" [UR3 user manual]. Once the femoral head was located into the liner the robot was then commanded to align the stem vertically (and so perpendicular to the face of the shell and liner) whilst keeping position constant ensuring the femoral head remained located in the liner. This was defined as the stem in the neutral position and was recorded onto the UR3 controller to keep component positioning consistent throughout testing. An image of the femoral head position in the liner is shown in Figure 18.

The robot arm could be programmed to rotate the stem whilst the femoral head was located in the liner component thus replicating the motion of a ball and socket joint. Additionally, the robot could translate the stem component causing the femoral head to translate out of the liner component thus causing the bearing surfaces to separate. This set up allowed for the maximum range of motion in all axes of the cup component. Further details of the specific motion protocols followed during the experimental work of this thesis, can be found in Sections 4.7.2, 5.6.2, 5.7.1, and 6.3.

Robot recorded orientation data as rotation vectors which was converted to Euler anglers using rv2RPY function (Appendix a) and then the Euler angles were converted to Azimuth and Tilt using the azinc function (Appendix a). The

UR3 has a pose repeatability of ±0.1mm [UR3 user manual]. The tilt angle orientation error resulting from the robot tool flange being positioned incorrectly by 0.1mm was evaluated to estimate the impact this would have on the effective resolution and accuracy of the robot in terms of orientation of the components. Circle segment theorem was used (see Appendix b) for calculations where the effective orientation resolution was evaluated as 0.08° in tilt angle and 0.9° in azimuth.

3.2.2 Experimental method to measure the occurrence of a component-component impingement point in total hip replacement components

Component-component impingement occurs at the point when the femoral stem contacts the rim of the liner component, a schematic of THR component impingement is shown in Figure 21.

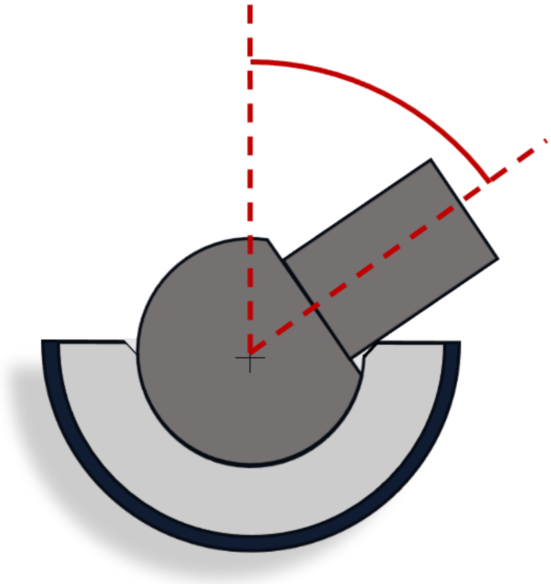

Figure 21 – Diagram of a component-component impingement event occurring between total hip replacement components.

Copper foil was wrapped around the 3D printed stem component and positioned around the region of the liner's rim where the stem would contact if component impingement occurred, as shown in Figure 22. Wires were soldered to the two pieces of copper foil, and one was connected to a digital input pin (DI_pin) and the second was connected to the power pin of the robot arm controller. This formed a continuity switch where contact between the copper foil on stem and on the rim of the liner completed the electrical circuit sending DI_pin high. When DI_pin was high a subprogram in the robot program pulses an analogue output pin of the robot arm controller from 3.3v to 0v. The analogue output is connected to the digital read pin of the microcontroller along with the ground which ensured the two devices shared a common ground. When the logic state changed from a high to low on the digital read pin of the microcontroller a Boolean variable was changed from 0 to 1 (0 = no impingement, 1 = impingement) and during the experimental tests was recorded by the microcontroller along with the timestamp.

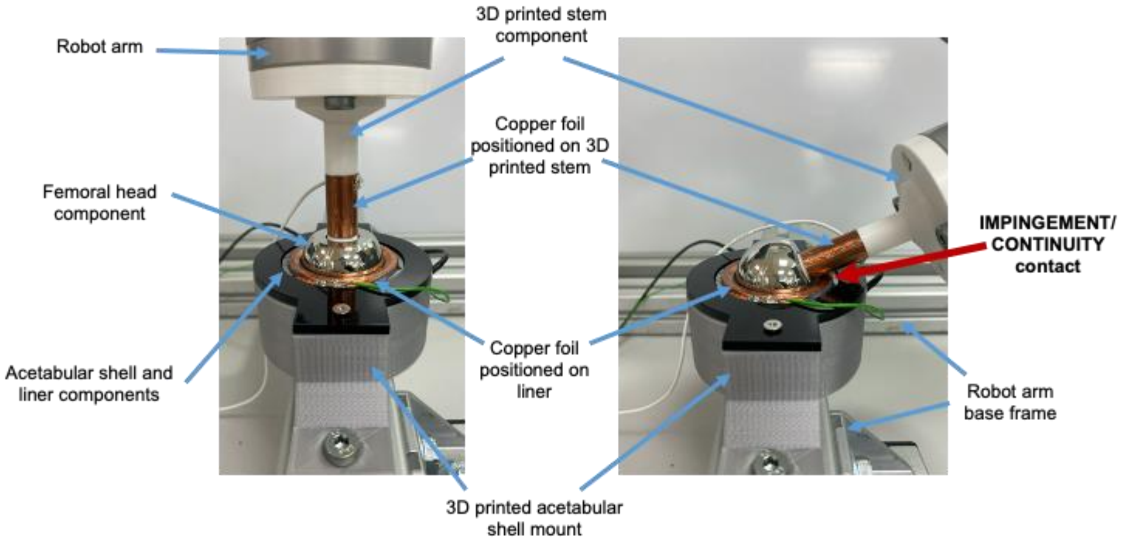

Figure 22 - Images showing the experimental setup used in the impingement detection study including copper foil positioned on the THR components at the location of a component-component impingement.

This method only measures the occurrence and location of an impingement event and force of the impingement contact was not measured. Force factors into the severity of an impingement event yet the focus of this work was to track the components kinematics and so force was not an output of interest in this methodology. The UR3 was capable of outputting force data yet the fidelity was not sufficient to derive an impingement contact occurrence nor the force of the impingement contact. To clarify, this method is only suitable for in-vitro dry use. This method could not be translated to use within patients nor to experimental hip simulation methodologies that use joint lubrication.

This copper continuity method was developed in collaboration with M.Shuttleworth as part of a wider project in the research group. M.Shuttleworth, Research Fellow, Faculty of Engineering, University of Leeds m.p.shuttleworth@leeds.ac.uk.

3.2.3 Experimental method to measure bearing contact surface separation during an impingement driven subluxation event

An impingement driven subluxation is caused when the femoral head is levered out of the liner component with the component-component impingement point acting as the fulcrum of the lever, a schematic of THR component impingement driven subluxation is shown in Figure 23. This causes the centre of the femoral head to be displaced from the joint centre of rotation and the bearing contact surfaces to separate. Impingement driven subluxation can lead to liner damage, cause patient pain and discomfort and be a precursor to dislocation (McGrory et al., 2010; Brown et al., 2014). There is a need to further investigate the mechanics of impingement driven subluxation in-vitro using experimental hip simulators. However, current methods of assessing impingement driven subluxation in-vitro require a line-of-sight view of the joint which is not always possible during experimental testing. Therefore, a sensing system that can be integrated into THR components and record the occurrence, location and severity of a impingement driven subluxation event would be a useful tool for a researcher to use when investigating subluxation in THRs in-vitro.

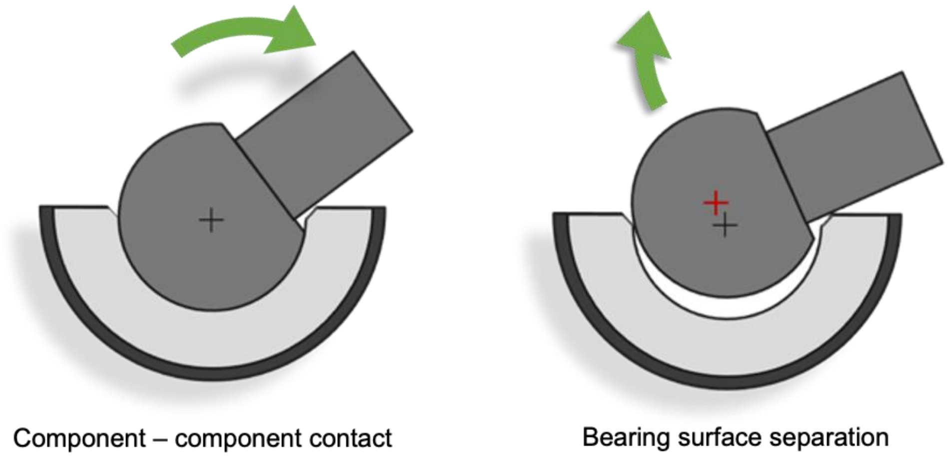

Figure 23 - Diagram of component - component impingement event leading onto THR component impingement driven subluxation which results in the centre of the femoral head to be displaced from the joint centre of rotation and the bearing contact surfaces to separate.

Justification of the chosen bearing surface separation verification method – a custom camera tracking system

During a pilot study it was found that the robot recorded pose during an impingement driven subluxation event was not the true position of the 3D printed stem and femoral head component. This was likely due to the flex in the 3D printed stem component and how it was bolted to the tool flange of the UR3. Therefore, an alternate method of measuring the position of the centre of the femoral head as it is displaced out of the liner component was needed. This method needed to:

- Measure centre of the femoral head component position (with respect to the acetabular component) to an accuracy and resolution of 0.1mm in two axes (X and Z).
- Integrate with the robot arm model and current experimental protocol.

Direct methods of linear displacement sensing for example linear variable differential transformer (LVDT) or a linear micrometre, were ruled out first. Although the precision of these methods is sufficient (<0.1mm) the integration into the current test setup would be challenging. Firstly, ensuring the probe is consistently positioned in line with the central axes of the femoral head (to ensure accurate derivation of the position of the centre of the femoral head) would be unreliable. Secondly, the device themselves and accompanying mounting fixtures may limit the functional range of motion of the robot and hinder the operator’s workflow.

Image processing systems are commonly used for gait analysis (Muro-De-La-Herran et al., 2014) with systems such as OptiTrak and Vicon being considered the gold standard motion capture systems (Nagymáté and Kiss, 2018; Panero et al., 2018; Albert et al., 2020). Both commercially available stereophotogrammetric systems use reflective markers and often multiple cameras to track the coordinates of objects in 3D space. However, these systems are very costly requiring significant upfront investment and use proprietary software and would not have been available to the investigator throughout the duration of the project.

Pounds (2023) developed a camera tracking system in their thesis to measure the displacement of the meniscus and tibia during natural knee joint simulation. They used an off the shelf Raspberry Pi camera, the MATLAB Image Processing and Computer Vision toolbox and coloured markers attached to the biological tissue. In a validation study on the system's reliability, a knee simulator (loaded with dummy components including a Delrin tibial base, a metal femur and a Delrin floating meniscus) produced anterior-posterior sinusoidal displacement at magnitudes of +/- 1 mm, +/- 2 mm, +/- 4mm, +/- 6 mm. They reported a maximum absolute position error of 0.18mm. This method developed by Pounds (2023) was shown to have the desired level of precision, was simplistic to implement and could be achieved with a non-specialist camera and software available during this project (MATLAB Image Processing and Computer Vision toolbox). Therefore, this method was chosen to be adapted and further developed to enable the position and orientation tracking of the centre of a THR femoral head during a subluxation motion.

Method of verifying bearing surface separation using a custom camera tracking system

An impingement driven subluxation event was recreated using the robot arm to rotate the stem to an extreme angle beyond the normal working range of motion of the components thus causing the components to impinge and the femoral head to lever out of the liner. Images of the components at the point of an impingement driven subluxation event are shown in Figure 24. The continuity trigger, previously described in Section 3.2.2, was used to determine when impingement first occurred and so when a subluxation event began. The stem would then return from the extreme angle and the continuity connection would break thus indicating that the stem had returned to within the normal working range of motion of the components and that the subluxation event had ended. The experimental setup featured a digital camera (Panasonic Lumix DMC-GF6K Panasonic, Osaka, Japan) which was used to record the position of the femoral head during the impingement driven subluxation motion so that the femoral head displacement could be measured. The camera tracking system was used to measure the true displacement of the femoral head out of the liner component. An image of the experimental setup is shown in Figure 25.

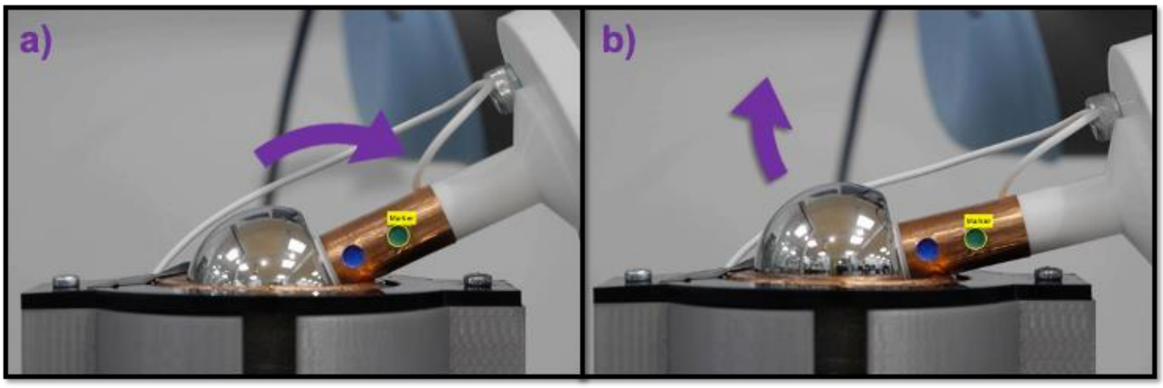

Figure 24 - a) Image of the THR components recorded by the digital camera at the moment of initial component – component impingement, b) Image of the THR components recorded by the digital camera at the moment of maximum bearing surface separation during a subluxation event.

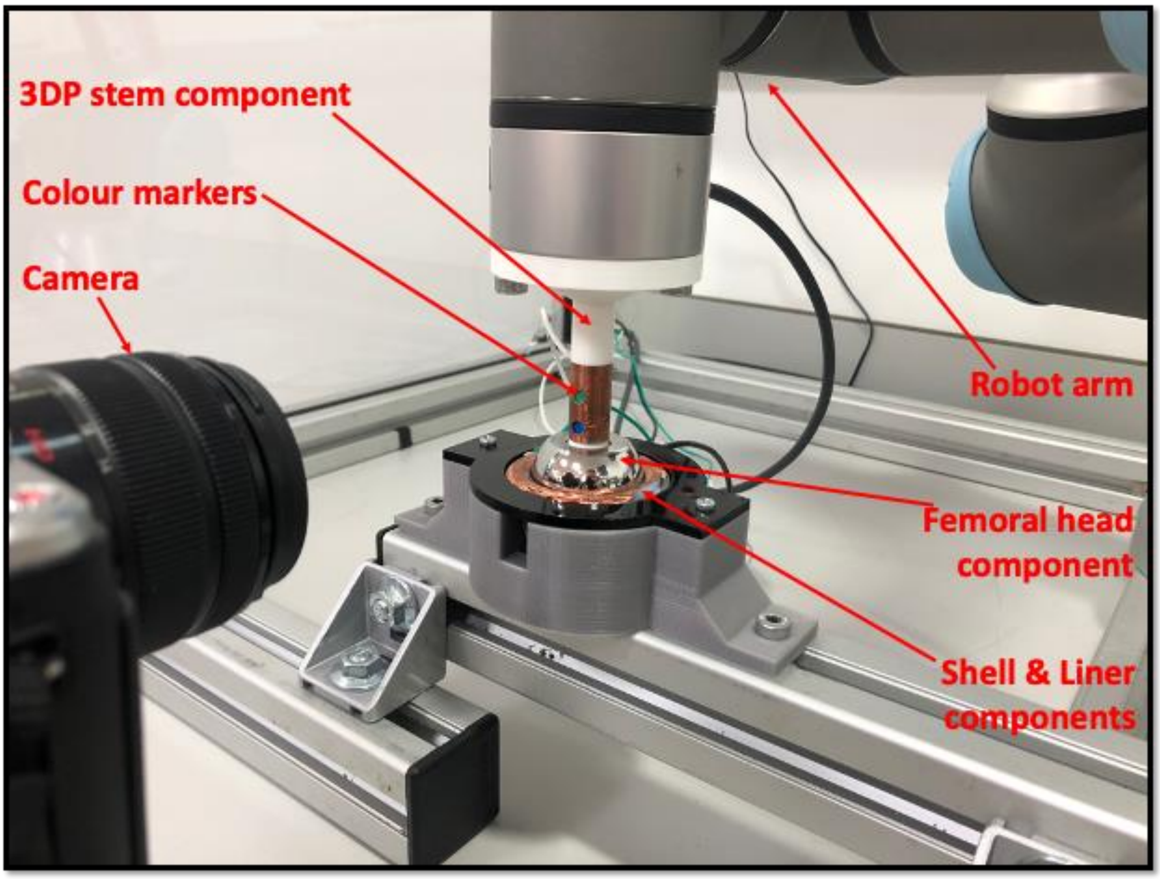

Figure 25 - Annotated image of the test setup used for the bearing contact surface separation study.

Two colour markers were drawn on to the 3D printed stem component using a paint pen. Two circular recesses were designed into the 3D printed stem component these were completely filled with the coloured pen paint. This method was initially chosen as it would result in accurate positioning of the two markers which was crucial for calibrating the system and post-processing the coordinate data. The colours were selected to contrast with the components and the background of the scene. The MATLAB Image Processing and Computer Vision toolbox was then used to compute the position of the two markers over the course of the impingement driven subluxation motion. The Color Thresholder tool was used to identify the pixels of the marker within the video frames, the Blob Analysis tool was then used to calculate the centroid pixel of the marker region throughout the video. To return 2D space coordinate data the pixel coordinate data was multiplied by a pixel calibration factor. The pixel calibration factor was calculated by dividing a known reference length (in mm) by the reference length in pixels seen in the video frame. For this study the known reference length was the distance between the centroids of the two markers namely, 10mm. Images of the components at the point of a subluxation event are shown in Figure 24. This image was from the recording made by the digital camera and shows the marker annotation the MATLAB post processing puts on the image.

The two markers were positioned along the central Z axis of the stem at a known distance from the combined centre of rotation of the 3D printed stem and femoral head components. Therefore, the angle between the two centroid coordinates were equal to the orientation of the stem. The 2D space coordinate data of the markers and the angle of the stem could then be used to calculate the location of the shared centre of rotation of the stem and femoral head component, and the position and orientation of the magnet. A diagram of the femoral stem showing the location of the two markers, the centre of rotation and the location of the magnet, and a sample graph of the position of the two markers, the shared centre of rotation of the stem and femoral head component and the magnet during a subluxation event, is shown in Figure 26.

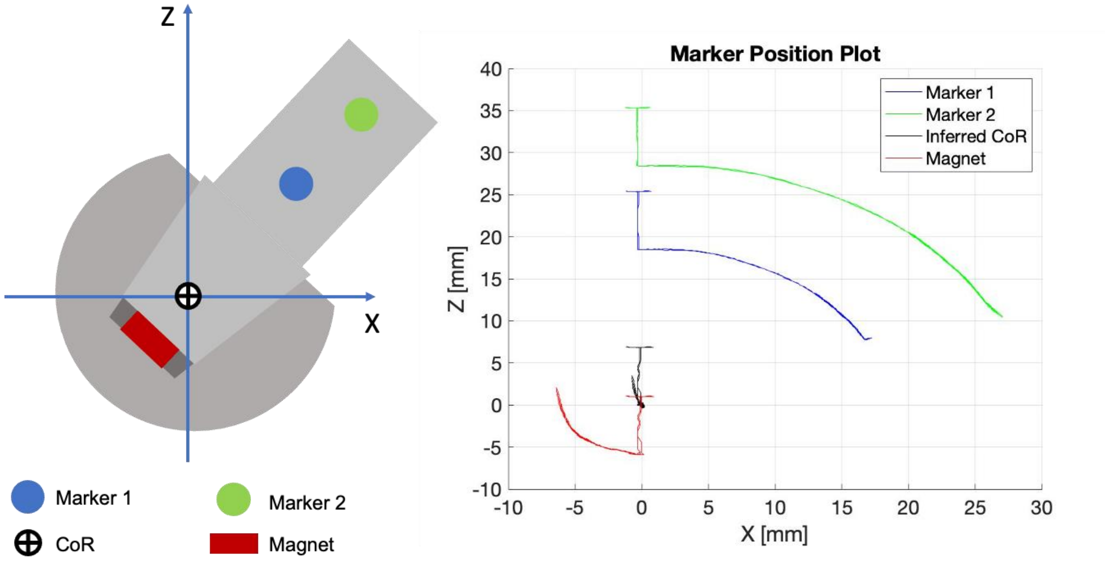

Figure 26 - Diagram of the femoral stem showing the location of the two markers, the centre of rotation and the location of the magnet, and a sample graph of the position of the two markers, the inferred centre of rotation and the magnet during a subluxation motion protocol. Where (0,0) is the location of the centre of rotation of the joint.

This camera tracking method was adapted from work produced by Genevieve Pounds as part of their PhD project. Development of a Novel Motion-Capture Methodology to Assess Medial Meniscus Displacement during Cadaveric Gait Simulation [IN PRINT] (Pounds, 2023), PhD Student, Institute of Medical and Biological Engineering, Faculty of Engineering, University of Leeds sp13gp@leeds.ac.uk.

Validation of the performance of the camera tracking system

At the start of each impingement driven subluxation motion protocol the stem began in a vertical position the robot arm then translated the stem in the Z direction out of the liner by 7mm. The stem was then translated to +1mm and then to -1mm location along the X axis and then returned to in line with the Z axis and finally back down to a located position within the liner. The movement in the X and Z direction was then used to validate the position accuracy of the output of the camera tracking system (CTS) against the robot arm (ground truth). The CTS reported position in the X and Z direction over the first 10 seconds of the test were compared to that recorded by the robot. The first 10 seconds of the test included the planned verification movements and didn’t include any femoral head motion resulting from subluxation as this could not be validated against the robot arm.

The plots of the centre of the femoral head position in the X and Z direction during the impingement driven subluxation motion protocol as recorded by the robot arm and the camera tracking system (n = 3) are shown in Figure 27 and Figure 28 respectively. The error between the robot reported position and CTS recorded position is also show for each repeat of the impingement driven subluxation motion protocol. The RMSE ± standard deviation of the error between the robot arm reported position (expected) and the camera tracking system reported position (observed) across all three repeats of the impingement driven subluxation motion protocol were 0.26mm ± 0.24mm and 0.24mm ± 0.23mm in the X and Z direction respectively. Peak error occurred when the robot was in motion during the verification movements. Errors are also greater after 2.76 seconds which is the time the robot arm began to rotate the stem. The peak errors are more likely to be a result of timestamp mismatch between the robot and the CTS systems as they are prominent when the robot is moving the fastest and there is some expected discrepancy due to the difference in sampling frequency between the robot and CTS. The latter can be explained as being caused by precision rounding errors when using trigonometry function to infer the location of the centre of the femoral head from the location of the two coloured markers. Additionally, there will also have been discrepancies in the theoretical intended centre of rotation of the femoral head and the actual centre of rotation realised during the experiment. These could be a result of the inaccuracies in the 3D printed components and mounting of the components in the experimental setup. Nevertheless, this level of error was deemed acceptable for this application.

The level of error was greater than that evaluated by Pounds (2023) who reported a maximum absolute position error of 0.18mm. For the present study max absolute position error in the X and Z direction was 0.67mm and 0.91mm respectively. These discrepancies could be due to several differences between the methodologies firstly, the difference in camera. Pounds (2023) used Raspberry Pi cameras specifically selected for their low fisheye distortion. The present study used a regular digital camera (Panasonic Lumix DMC-GF6K Panasonic, Osaka, Japan). Pounds (2023) used a light source to illuminate the marker and highlighted that greater error were seen when the marker moved into darker regions of the frame as there was less contrast with the background. The present method relied on the ambient lighting of the lab which was well lit but not focussed on the working area. Finally, they used coloured beads as their markers whereas the present method used circular recesses filled with pen paint. Although, the present method ensured accurate positioning of the markers the manual aspect of colouring the markers meant that the resultant shapes were not perfect circles. It was not investigated but it is believed that inconsistency of the marker shape would have introduced errors as the MATLAB function would struggle with attachment of the boundary box to the marker pixels. The use of the circular stickers could be a consideration for future work as designing in features on the stem for the stickers to be positioned on (similar to that of designing recess to be coloured in) would still ensure accurate marker positioning on the stem component.

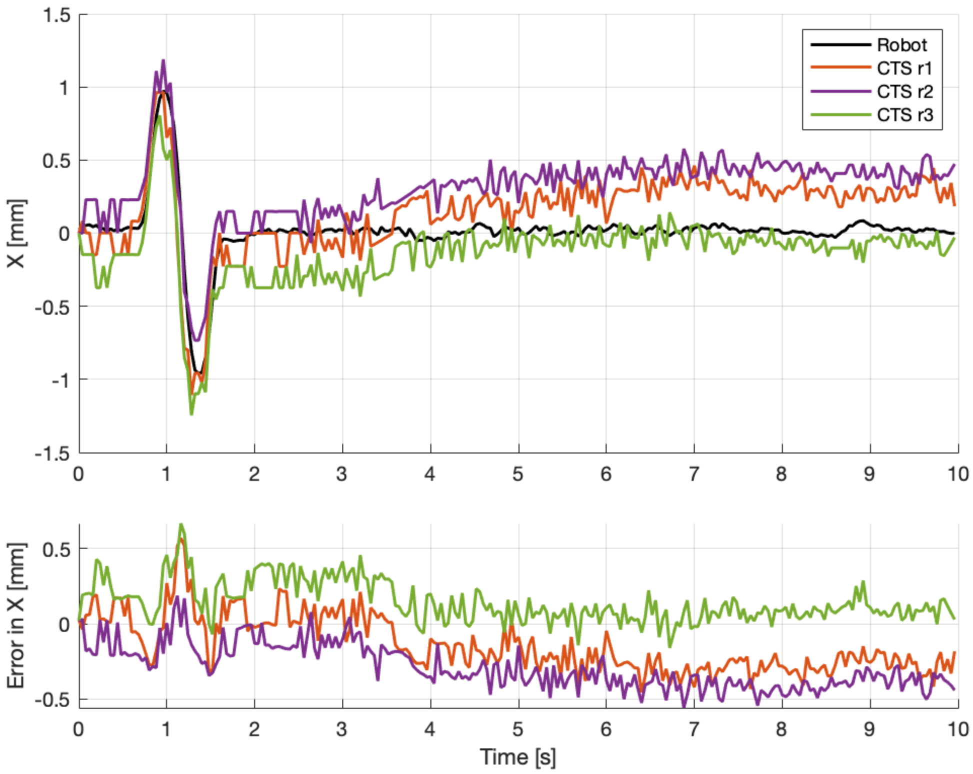

Figure 27 - Robot arm and the camera tracking system (n = 3) recorded position of the centre of the femoral head in the X direction and the error between the robot reported position and CTS recorded position during the initial 10 seconds of the subluxation motion protocol. The peaks of +1mm and -1mm are the planned verification movements in the X direction.

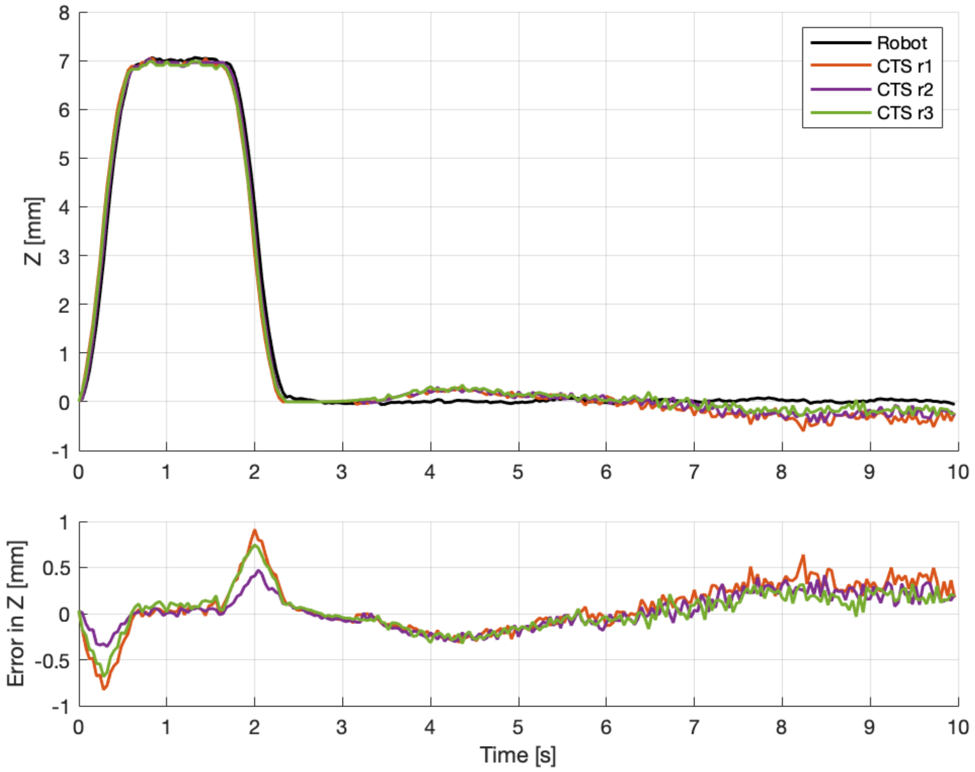

Figure 28 - Robot arm and the camera tracking system (n = 3) recorded position of the centre of the femoral head in the Z direction and the error between the robot reported position and CTS recorded position during the initial 10 seconds of the subluxation motion protocol. The peak levelled of peak at 7mm is the planned verification movement in the Z direction.

3.2.4 Evaluation of the experimental hip joint simulation model

The design specification evaluation for the robot arm hip simulator is shown in Table 4. The robot arm satisfied all the design specifications except for specification 5 which required the angle and position of the tool centre point of the robot (and so the position and orientation of the THR components) to be displayed in real time. Upon reflection this was not an inconvenience to the investigator as the motion of the robot was pre-programmed and repeatable so a live read out of the robot’s position and orientation was not needed.

Table 4 - Robot arm hip joint simulator design specification evaluation

Item No.	Specification	Evaluation
1	**Red** – Manipulate components in two planes (orientation to two DoF) **Green** – Manipulate the components in three planes (orientation to three DoF) **Pass/fail –** Manipulate the THR components through their full working range of motion.	**Green & Pass –** An unconventional orientation notation was used to define the orientation of the components this is clarified in Chapter 4
2	**Red** – achieved angular speed 67º to 220º/s **Green** – achieved angular speed >220º/s	Not assessed yet the joints providing the majority of the motion can achieve maximum speed of 180 º/s??
3	**Pass/fail –** Produce impingement event	**Pass** – Robot arm was able to manipulate the stem beyond the normal working range of the components causing the components to impinge and the bearing contact surfaces separate thus replicating an impingement driven subluxation event.
4	**Pass/fail –** Produce subluxation event with bearing contact surfaces being separated and head centre of rotation being displaced by >1mm	
5	**Pass/fail –** Acetabulum can be positioned beyond typical implantation angle of 15º anteversion and 45º inclination by ±20º	Not assessed as cup component was fixed to base frame with the face of the liner facing upwards. However, alternate cup component mounts could be manufactured to hold the cup in any position.
6	**Red –** Resolution >=1º **Green –** Resolution <0.1º	**Green** - Effective orientation resolution (Appendix b) was evaluated as 0.08° for tilt angle direction. **Red** - 0.9° for azimuth angle direction, so did not make Green specification but was deemed acceptable for this work.
7	**Red –** Accuracy >=1º **Green –** Accuracy <0.1º	
8	**Red -** Resolution >=1mm **Green –** Resolution <1mm	**Green** - Pose repeatability of ±0.1mm.
9	**Red -** Accuracy >=1mm **Green –** Accuracy <1mm	
10	**Red** – Data requires external post-processing to get angular position etc. and delay in data presentation **Green** – Real time presentation of component angle presented as Tilt Angle & Azimuthal Angle	**Red – .**csv file exported once test was completed and post-processing was required to report angles as Rotation angle, Azimuthal angle and Tilt angle.
11	**Pass/fail –** Requires power supply of 24v	**Pass**
12	**Pass/fail -** Bench top mounted	**Pass**
13	**Pass/fail -** Space allows easy access to implant components/sensor system	**Pass**
14	**Pass/fail –** Controlled by a PC	**Pass**
15	**Red –** Can only accept 1 implant size and sectioning or adaptation of the components required **Green** – can accept implants from minimum (22mm) to maximum (50mm) head size	**Green** - The rig had the space to accept all femoral head and acetabular shell sizes. However, a 3D printed stem was used as a mounting point for the femoral head.
16	**Red** – Interchanging implant component requires rig component interchanging **Green** – Fixtures and fittings allow for implant component interchanging	**Green** - Acetabular cup components could be easily interchanged as the 3D printed mount secured the component with a bolted on top plate and alternate femoral head components could be swapped as they were pressed onto the shaft. However, to test components of different sizes alternate 3D printed mounting fixtures would be required.

3.3 Summary

The aim of this chapter was to define the motion to be sensed within a total hip replacement and formulate design specifications for a hip joint simulation solution. A UR3 robot arm was chosen as the final hip joint simulation model and provided a flexible and convenient method of prototyping, developing, calibrating and testing the novel sensing system technology. The advantage of using the robot arm to simulate the motion a hip joint was the convenience, flexibility, and repeatability of the system. The UR3 has a pose repeatability of ±0.1mm and could actuate the stem component over the complete desired testing ROM and position sensing zone of the THR components. Myriad motion profiles could be performed using the same test set up and mounting components. This allowed for the performance of the sensing system to be fully characterised as well as allowing for more complex motions to be investigated for example, motions that mimic THR impingement and impingement driven subluxation. See Sections 4.7.2, 5.6.2, 5.7.1 and 6.3 for where these test setups developed in this chapter are used in this work.

Chapter 4 Design Specifications for an Instrumented Hip Implant and Introduction to the Chosen Sensing Method

This Chapter presents the design specifications for the prototype sensing system developed in this work, this included defining the physical kinematic parameters to be measured and defining the physical parameters of the system. This Chapter then introduces the chosen sensing method which was a magnetic position and orientation sensing system. This includes verification of the magnetic field simulation method and validation of the selected magnetic field sensor used in the prototype development presented in this thesis. A flow chart detailing the work presented in this chapter is shown in Figure 29.

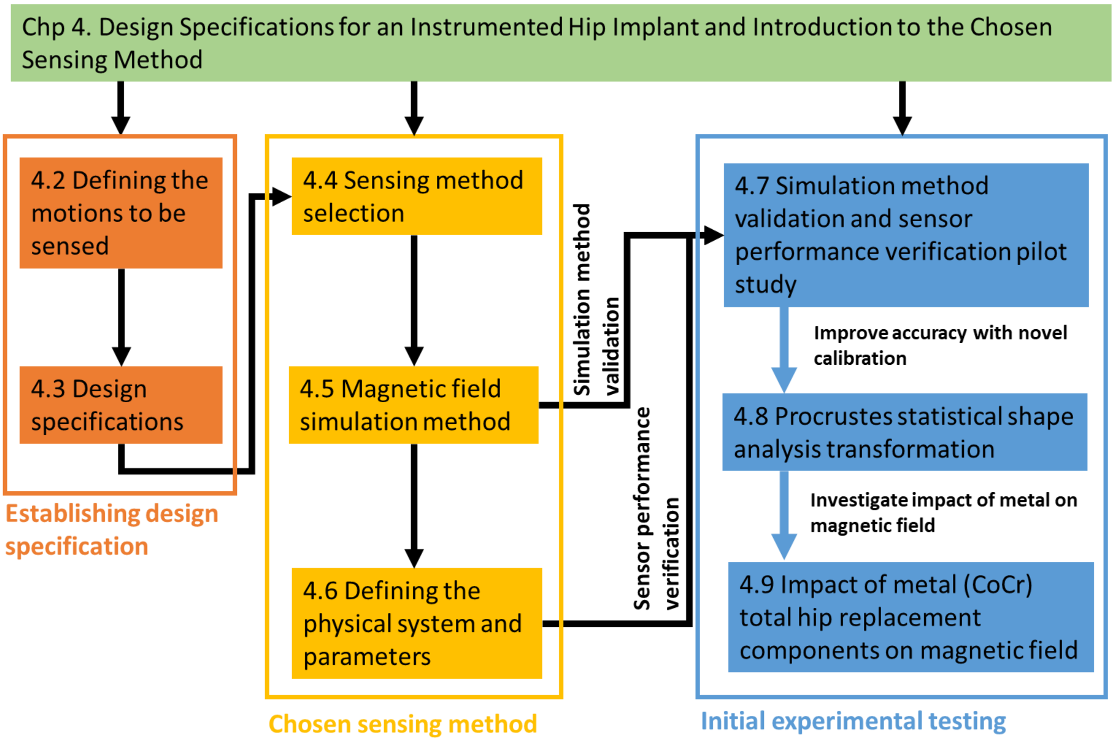

Figure 29 - Flowchart of the work presented in chapter 4 showing the interconnections between the individual pieces of work.

4.1 Chapter 4 Objectives

The objectives of this chapter were:

1. To define the kinematic parameters of a THR to be measured.
2. To develop design specifications for an instrumented THR.
3. To define the physical parameters of the system to be used in simulation and optimisation work.
4. To validate a method of generating simulated magnetic field data representative of the position of a magnet as it is translated due to changing stem angle or position.
5. To verify the performance of the selected magnetic field sensor when compared to the generated simulated data.
6. To verify the consistency of the magnetic fields generated by the multiple samples of the selected magnet and multiple sensor boards.
7. To investigate whether the metallic components of a THR impact the magnetic field of a magnet or influence the readings of a magnetometer.

4.2 Defining the motions to be sensed within a Total Hip Replacement

4.2.1 Total hip replacement neck orientation

A hip is a ball and socket joint with motion in three planes with six degrees of freedom (DoF) a THR intends to restore and mimic this motion. The orientation of a ball and socket joint can be defined by three angles i.e. rotation angle [φ], tilt angle [θ] and azimuthal angle [ψ], a schematic showing these three angles that define the head orientation is shown in Figure 30. This orientation notation is the same as the ZYZ Euler angle notation which is commonly used in robotics. This is an unconventional method of defining the orientation of a hip joint however, it was the preferred notation for describing orientation of neck of a THR with respect to the acetabular component it was a more intuitive notation method when:

- Describing a THR as a ball and socket joint sectioned at the neck of the femoral stem.
- Orientation can only be described to two degrees of freedom.
- Visualising and describing phenomena unique to THRs including impingement and impingement driven subluxation see Sections 5.7 and 6.3.

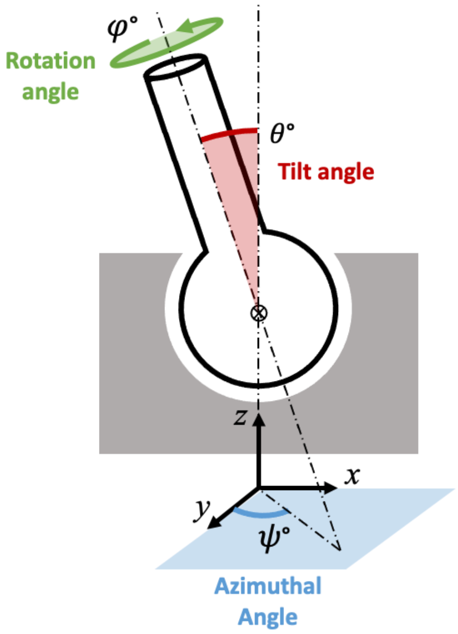

Figure 30 - Diagram illustrating the three angles that define the orientation of a ball and socket joint namely rotation angle [φ], tilt angle [θ] and azimuthal angle [ψ]. Adapted from: (Malagò et al., 2020)

Rotation of the human hip joint is typically described as rotations in the planes of the body namely sagittal plane flexion/extension (FE), coronal plane abduction/adduction (AA) and transverse plane internal and external rotation (IE) which is the same as Euler XYZ. Euler ZYZ can be converted to Euler XYZ and so FE/AA/IE convention using rotation matrices see appendix c). Therefore if all three angles [φ,θ,ψ] are known/can be derived then the orientation of the THR and so orientation of the hip joint can be described using the FE/AA/IE convention. However, if only two angles are known/can be derived then a conversion is not possible. This would mean the orientation of the THR, and so hip joint could not be expressed as the recognised convention. Therefore, to achieve the most clinical utility the sensing system should be capable of measuring orientation to 3 DoF.

Evaluation of CAD files from clinically available THR components provided the working ROM of that particular set of components (56mm outer diameter & 36mm femoral head). The maximum tilt angle of the stem before the stem impinged on the liner rim, was 66° from the vertical central axis perpendicular to the face of the cup. A diagram illustrating the maximum tilt angle of the stem at rim impingement is shown in Figure 31. Furthermore, in some circumstances the stem can reach a tilt angle greater than 66°. This can occur following an impingement event in which the femoral head is levered out of the cup namely, termed impingement driven subluxation. Therefore, the sensing system should be able to cover a range greater than ±66° in the tilt angle direction. Additionally, it would be desirable for the sensing system to operate within the full range of the Azimuthal angle and Rotation angle ranges (0° to 360°).

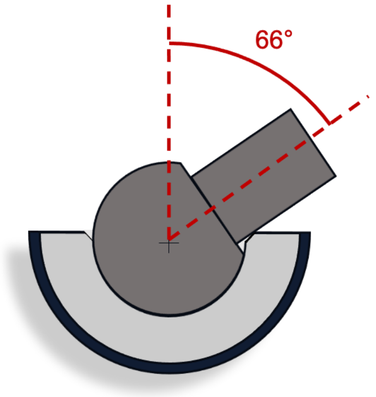

Figure 31 - Diagram illustrating the maximum tilt angle of the stem component when component impingement first occurs.

4.2.2 Translation of the femoral head with respect to the liner resulting from adverse events in the hip joint

It was initially hypothesised measuring the translation of the femoral head with respect to the acetabular component could be used to track wear in THR components. The penetration of the femoral head into the liner could be recorded in the three axes and used to estimate the linear and volumetric wear (Geerdink et al., 2008; Grillini and Affatato, 2013). US Patent (US7195645B2) (Disilvestro et al., 2007) outlines a similar methodology. The patent specifies a device that uses magnets and magnetic sensors to make in-vivo measurements of the joint space of a THR and so determine the extent of implant component wear at the articulating surfaces. Clinically, methods used to assess wear after THR surgery rely on using radiographs to quantify femoral head penetration and estimate linear and volumetric wear rates. Wear assessment is ongoing and periodic estimations are made by comparing the most recent radiograph to the earlier ones taken (paired analysis) or from a single radiograph in which head penetration is measured assuming the femoral head and acetabular component are concentric, and any deviation is a result of the bearing surfaces wearing (single analysis) (Geerdink et al., 2008). Therefore, instead of a lengthy and costly clinic visit a patient could be routinely required to stand or lie still whilst a measurement is automatically taken, and a report sent direct to their physician. This would greatly improve patient care and reduce the cost and workload required by the healthcare provider to treat the patient. Although, current wear rates can vary from 0.003mm/yr to 0.22mm/yr (Engh Jr et al., 2012; Glyn-Jones et al., 2015) and current in-vivo methods of characterising wear typically have a resolution of <0.1mm (Glyn-Jones et al., 2015). However, this level of resolution and accuracy is unlikely to be achievable with the sensing system developed in this work.

The femoral head of a THR can also translate out of the acetabular component and the bearing contact surfaces can separate for a variety of reasons for example during the swing phase of the gait cycle (Komistek et al., 2002) or during other activities where there is no load translated through the hip joint for example when lying down either prone, lateral or supine. Furthermore, impingement driven subluxation can occur levering the femoral head out of the cup (Usrey et al., 2006). THR joint separation is where the centre of rotation of the head and centre of rotation of the acetabular cup, migrate away from each other. Lombardi et al (2000) and Komistek et al (2002) defined 0.75mm as a threshold value in their study examining the amount of femoral head separation from the acetabular component during normal gait. They were comparing metal-on-metal components with metal-on-polyethylene to see if there was any difference in the level of separation.

Therefore, the sensing system is also required to measure the position of the femoral head component with respect to the acetabular cup component. Following consultation with industry experts and surgeons, the target accuracy and resolution were set as 1mm. The justification being that this would be the expected accuracy and resolution of a clinically representative measurement.

4.3 Design specifications for an instrumented hip implant prototype

The design specification is presented in Table 5, which includes the need or the design requirement, the rationale for the requirement and the final specification. The final specifications included a pass/fail grade or split into a red/green classification system which indicates the assessed importance of each criterion associated with that specification, this format is like the one described in Section 3.1. The instrumented implant was not intended for use in-vivo or within an experimental hip simulator (like that used in (Williams et al., 2003; Ali et al., 2016; Hadley et al., 2018; O’Dwyer Lancaster-Jones et al., 2018) as this was outside the scope of this PhD therefore the design specifications only cover the intended use as a proof-of-concept prototype.

Table 5 -- Instrumented hip implant prototype design specifications

Requirement	Justification	Specification
Integration within implants	Excessive modifications to implant will affect its function	**Red** – Significant changes to implant geometry or bearing contact surface **Green** – No change to implant geometry
	Adaptable to various implant designs, bearing surfaces and sizes	**Red** – Functional in one type of bearing surface **Green** – Functional in all bearing surfaces (Metal-on-Polymer, Ceramic-on-Polymer & Ceramic-on-Ceramic)
		Red – Functional in only one implant size **Green** – Functional in all implant head/cup sizes minimum (22mm) to maximum (50mm) head size and femoral stem of length up to 275mm
Power and data transfer	Wired connection	**Red** – Excessive wiring or positioning of the tether disrupts normal function of the implants **Green** – Tether has no impact on the function of the components
	Source of power	**Red –** Requires additional power supply **Green –** Can run on power supplied from PC or laptop
	Frequency of data collection	**Red** - Standardised gait cycle is 101 discrete data points per cycle so 50Hz to 101Hz would match monitoring 0.5cycle/s. **Green** - Standardised gait cycle is 101 discrete data points per cycle so 101Hz would match monitoring 1cycle/s.
Ability to measure the angle of the femoral stem relative to the acetabulum cup	Normal working ROM of components is a tilt angle of ±66º however, this can be exceeded because of impingement driven subluxation. Required range in Azimuthal angle direction is 0º to 360º. Required range in Rotation angle direction is 0º to 360º.	**Red** – Can measure orientation over full angle range for one of the defined angle directions **Green** – Can measure orientation over full angle range in all three defined angle directions
	The angular measurement of the components can give an indication of impingement, malalignment and tracking patient activities such as No. steps, types of motion, range of motion, adverse events etc. Upon consultation with industry experts and practising orthopaedic surgeons the target accuracy and resolution was set as 1º as a sensible outcome.	**Red -** Resolution 5º to 1º **Green –** Resolution <1º
		Red - Accuracy 5º to 1º **Green –** Accuracy <1º
Measure component centre of rotation translation/separation of bearing contact surfaces	Relative displacement of the implant's components can give indications of wear and subluxation. Upon consultation with industry experts and practising orthopaedic surgeons the target accuracy and resolution was set as 1mm as a sensible outcome.	**Red** – Determine displacement of components to resolution >1mm **Green** - Determine displacement of components to resolution <1mm
		Red - Accuracy 2mm to 1mm **Green –** Accuracy <1mm

4.4 Sensing method selection

A magnetic position and orientation system and an inertial measurement unit were the two methods considered as having potential to measure the motion of THR components. The applicability of these two sensing methods is discussed further in the following section.

Permanent magnets coupled with a magnetic field sensor can provide a contact free method for position, proximity, and angle measurement. Magnetic position and orientation (MPO) systems have been used previously to measure the position of a joystick (Ermakova et al., 2018; Lutz. and Foletto., 2019; Lumetti et al., 2020; Malagò et al., 2020). These sensing systems work by correlating or matching the measured magnetic field to the position and orientation of a permanent magnetic. The similarity of magnetic field propagation through biological tissue and air, make the response of a magnetic field sensor predictable and repeatable. Furthermore, magnetic sensors are typically low-cost, have a small form factor, low power consumption and sufficient sensing frequency and resolution. This sensing method is achieved through non-contact means, and the sensor and magnet would not need to be positioned near the bearing contact surfaces and so integration of the system would have little to no effect on the function or geometry of the implant.

If a magnetic field sensor and reference magnet are integrated into a total hip replacement, relative displacement of the components could be measured. If magnetic field strength is measured in multiple axes the orientation and position of the magnet (and thus the implant components) can be determined. This may mean achieving full 6DoF position and orientation tracking is too challenging and would likely require multiple three-axis magnetic field sensors thus complicating the system.

There have been previous attempts at integrating magnetic sensing into orthopaedic implants. US Patent (US7195645B2) (Disilvestro et al., 2007) described a hip prosthesis with a magnet and magnetic sensor affixed either side of the joint space (i.e. the magnet or sensor positioned on the femoral stem component or acetabular component). Changes in the in-vivo sensor measurements correlate to changes in joint space distance and so could determine the extent of implant component wear at the articulating surfaces.

However, the patent gave no mention of determining orientation of the components using magnetic sensor readings. Arami et al,. (2011; 2013; 2014) developed an instrumented knee implant which featured three three-axis anisotropic magnetoresistance sensor embedded within the polyethylene knee insert and a permanent magnet positioned in the femoral component of the knee replacement. They calibrated their system to predict 15 orientation states of combined flexion/extension and abduction/adduction rotation (sagittal plane angle range 138º to 192º and coronal angle range -8º to 4º). They reported a root mean squared error and maximum absolute error of 2.35º and 5.4º in flexion/extension angle and 0.31 º and 0.93º in abduction/adduction angle. To the authors knowledge no instrumented orthopaedic device featuring magnetic sensing has been used in-vivo. This early work has shown promise and demonstrated utility. The concept of a magnetic sensing system for use in orthopaedic implants needs further development in particular improving accuracy and sensing range of the outputs before in-vivo use can be realistically considered. Additionally, the integration of a magnet into an implanted THR may be hazardous to the patient if the patient comes into the proximity of a high-powered magnet e.g. MRI scanner.

Nine-axis inertial measurement units (IMUs) are composed of a three-axis accelerometer (measuring acceleration/change in velocity), a three-axis gyroscope (measuring angular rate/angular velocity) and three-axis magnetometer (measuring local or earth’s magnetic field). With a sensor fusion algorithm an IMU can give motion, orientation, and heading. An IMU would be a very attractive approach for this application; the sensor chips are relatively cheap, small (typically < 5X5X1mm) and low power therefore would be well suited to integration within an instrumented implant. Furthermore, accelerometers can also be configured to operate as vibration sensors and so there could be scope to also record the vibration response of the implant which has been done previously to determine component fixation.

IMUs are being widely used in wearables which are increasingly used to track human biomechanics. Devices specific to patient monitoring following orthopaedic surgery are now being used clinically e.g., TrackPatch (TrackPatch Health Sacramento, CA, USA) or MotionSense (Stryker, Kalamazoo, MI, USA). These devices are positioned on the surface of the skin so soft tissue artifacts will result in decreasing the accuracy and precision of the measurements (Arami et al., 2011). The Persona IQ (Zimmer Biomet, Warsaw, IN, USA) is the first example of a clinically available instrumented total knee prosthesis. The device uses an IMU and can report metrics including walking speed, cadence, and functional range of motion. Several systems intended to aid surgeon in guiding implantation of acetabular shell use IMUs including the Navbit Sprint (Navbit, Sydney, Australia) and Naviswiss (Naviswiss AG, Brugg Switzerland). To the authors knowledge no clinically available instrumented THR featuring an IMU sensor have been used in-vivo.

The disadvantage of using an IMU are they report orientation and heading with respect to gravity therefore, to record the relative orientation of the implant components (i.e. the orientation of the femoral stem component with respect to the liner component) an IMU sensor would need to be positioned on each component. This would mean each component would need to be sensor enabled and the two circuits would need to be linked (wire tether or wireless enabled) to synchronously record data thus increasing the complexity of the system. Furthermore, an IMU based system cannot be used to measure the relative position or displacement of the components i.e. if the bearing surfaces separate. Additionally, IMUs suffer from integration drift resulting in the accumulation of errors over time (Siciliano et al., 2008).

In conclusion, a magnetic field sensing system was the most favourable of the two sensing methods considered and was the concept chosen to progress to further design development. The aim of further design development was to explore integrating a magnetic field sensing system into clinically available implant components. The remainder of this chapter presents the validation of the simulation method that was used to simulate the magnetic fields of moving magnets and how the simulation output was used to verify the performance of the chosen magnetometer sensor.

4.5 Magnetic field simulation method

Simulations of a magnet’s motion and magnetic field were produced based on the defined physical parameters of the system. The results of the simulations were used to develop the magnetic position and orientation sensing system methods, verify the theoretical accuracy, and optimise the performance of the system. Development of the magnetic position and orientation sensing system is presented in Chapter 5 and Chapter 6.

The simulation software used was Magpylib Python package (Version: 4.0.0b2, Author: Michael Ortner). The library includes methods for translating and rotating magnet features and a sensor class that returns the magnetic field vector at a specified location in the format [Bx By Bz]mT, the same output format to that of the mlx90393 3-axis magnetometer. Magpylib was developed by Michael Ortner who has used the package in the development of a magnetic sensor enabled joystick (Ermakova et al., 2018; Lumetti et al., 2020; Malagò et al., 2020). The computation is vectorised improving computation performance and use of the Python scipy.spatial.transform.Rotation package (Virtanen et al., 2020) to conveniently apply rotations to objects, makes it an attractive choice when developing a magnetic position and orientation sensing system.

The Magpylib library uses accepted analytical equations and theory to compute magnetic fields of permanent magnets which results in <1% error (Malagò et al., 2020). One of the featured equations (Equation 1) was first presented by Camacho and Sosa (2013) and is an analytical calculation for cylindrically symmetrical magnets to evaluate the magnetic field at a discrete point located of the surface of the magnet along the central axis. Where B_r is magnetic remanence (material dependent), R is radius of cylinder, h is height of cylinder and z is distance along the central axis from the base of the cylinder, an illustration of a cylindrical magnet demonstrating this principle is shown in Figure 32.

$$B(z) = \frac{B_r}{2}\left(\frac{z}{\sqrt{z^2 + R^2}} - \frac{z-h}{\sqrt{(z-h)^2 + R^2}}\right)$$

Equation 1

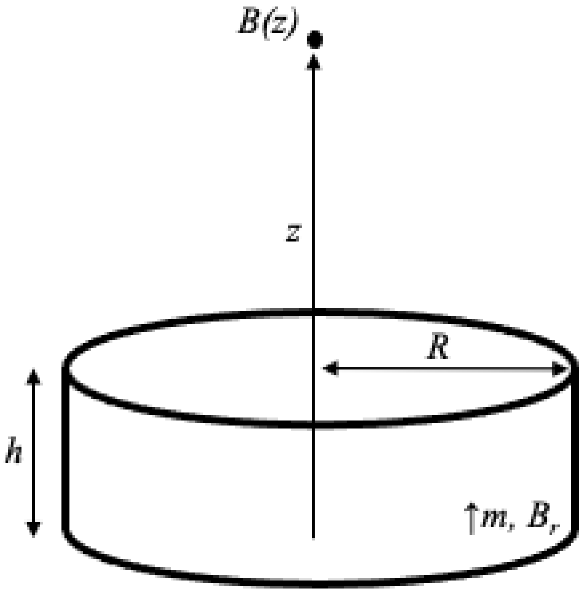

Figure 32 – Diagram of a disk magnet magnetised along the central axis. The annotated parameters are those need to calculate magnetic field at a discrete location from the surface of the magnet where ↑m is magnetization direction, B_r is magnetic remanence (material dependent), R is radius of cylinder, h is height of cylinder and z is distance along the central axis from the base of the cylinder.

For example, an 8X2mm neodymium disc magnet grade N42 with Br of 1300microT with a sensing node positioned 20mm from the centre of the magnet (so $z = 20 + \frac{h}{2} = 21mm$). Equation 1 gives magnetic field to be B = 2463microT. The same scenario simulated using Magpylib (Figure 33 shows the graphic output of the simulation) also returns the magnetic field to be B = 2463microT.

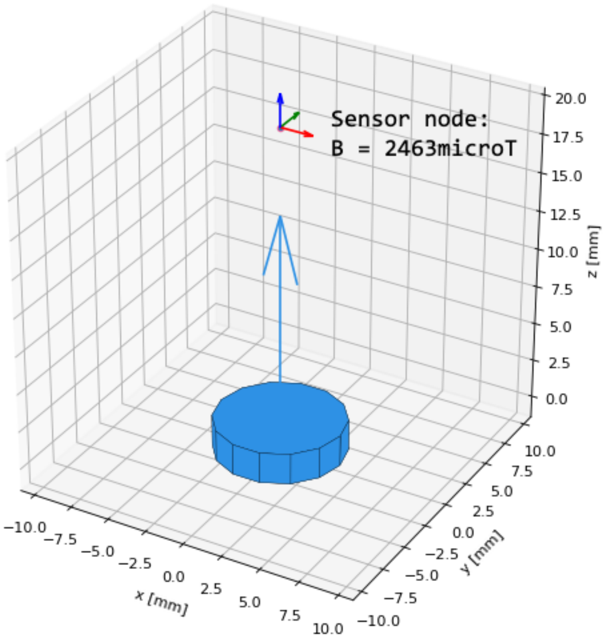

Figure 33 – Graphic output produced by Magpylib simulating a 8X2mm neodymium disc magnet grade N42 with Br of 1300microT returning the value of the magnetic field read at a sensing node positioned 20mm from the centre of the magnet.

4.6 Defining the physical system and parameters required for the simulation and optimisation of the magnetic position and orientation sensing system

The system parameters needed for the simulation and optimisation work included the:

- Geometry of the THR components, in particular where the sensing system components (sensor and magnet) could be located.
- The shape and material of the magnet.
- The chosen sensor in particular, the working range.
- The component motions to be sensed.

As previously stated in Section 4.6.1, the component motions to be sensed are 0° to 360° in the rotation angle [φ] direction, 0° to 66° in the tilt angle [θ] direction and 0° to 360° in the azimuthal angle [ψ] direction, as summarised in Figure 30

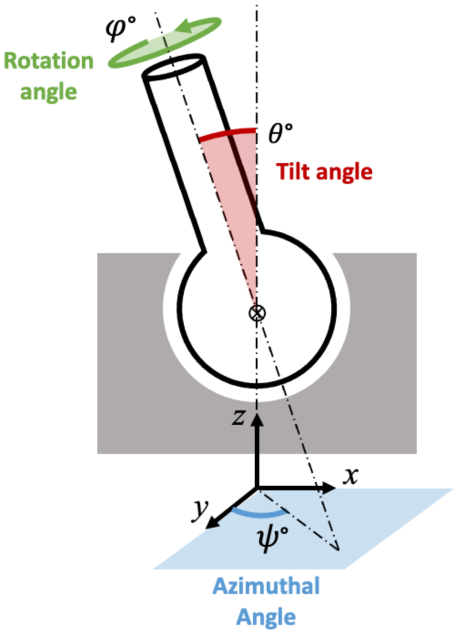

Repeat of: Figure 30 - Diagram illustrating the three angles that define the orientation of a ball and socket joint namely rotation angle [φ], tilt angle [θ] and azimuthal angle [ψ]. Adapted from: (Malagò et al., 2020).

4.6.1 Description of physical system

A cross section diagram of a typical total hip replacement is shown in Figure 34. A THR is a ball and socket joint with the centre of rotation located at the middle of the femoral head. Two annotated zones have been identified as possible sensor or magnet locations are shown in Figure 34. These include the region between the taper face and the femoral head face. The distance between these two faces can vary as it is dependent on how far the head is pushed onto the stem during surgery but is typically less than 4mm and in this example the minimum diameter of the head’s hole is approximately 12mm. The second region is within the introducer hole and backside region of the THR shell. The introducer hole (approximately 10mm diameter and 3mm height) is a feature used during surgery and is how the introducer is attached to the shell during placement of the component. However, following surgery the hole is either occupied with cap or left empty. These two regions have been identified as potential sensor or magnet locations for the following reasons:

- Non load bearing or comparatively low internal stress and regions are far from bearing contact surface.

- Regions are made from or surrounded by ‘hard’ material namely not the ‘soft’ polyethylene liner.
- The identified regions offer the possibility of small profile components without the need to modify the geometry of the THR components.

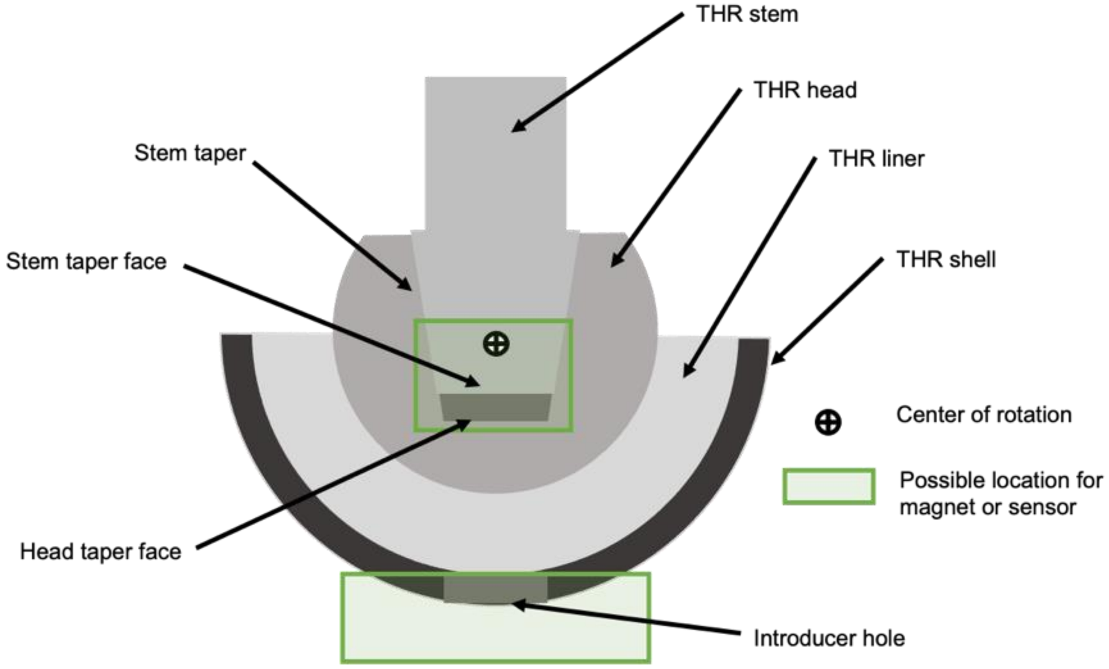

Figure 34 - Cut through diagram of a typical total hip replacement with annotated centre of rotation and possible regions for sensor or magnet locations.

For a 36mm femoral head and liner, and a 56mm outer diameter acetabular shell, the distance from the introducer hole to the centre of rotation was approximately 26.5mm and the distance between the head taper face and the centre of rotation is approximately 6mm. Therefore, the following key dimensions can be extracted, and are shown in Figure 35:

- Magnet to sensor sensing range 20.5 to 26.5mm
- Maximum space for magnet cylindrical region (Diameter = 12mm Height = 4mm)
- Maximum space for sensor cylindrical region (Diameter = 10mm Height = 3mm)

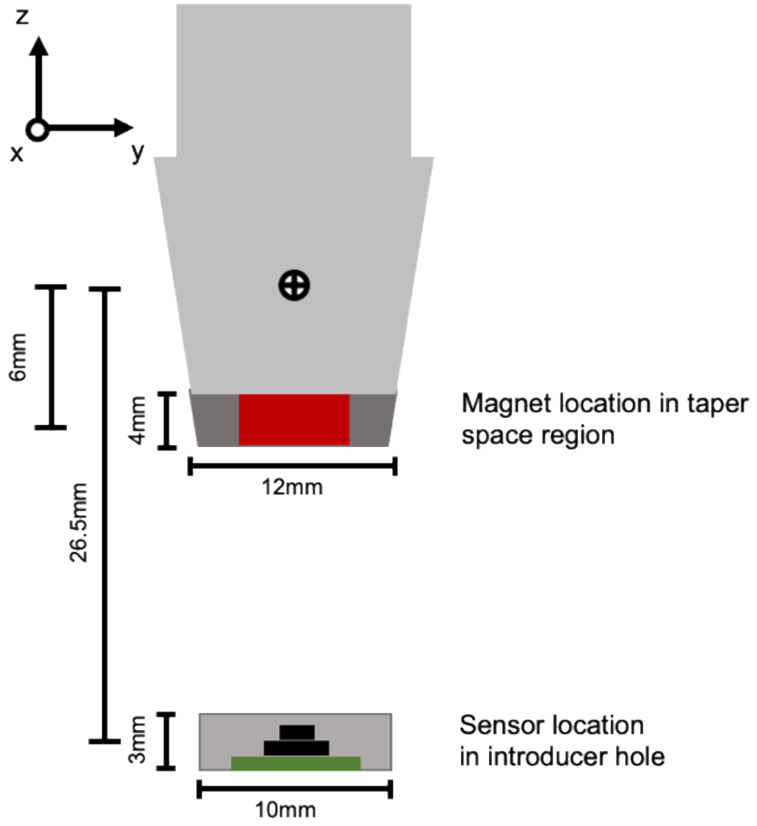

Figure 35 - Annotated technical drawing of possible regions for sensor and magnet location

The material of the metallic THR components used in this work was CoCr which is inherently non-ferrous. Cobalt chromium metal alloy is non-ferrous therefore should not induce an unexpected magnetic field onto the components or impact the reading of the sensor. Arami et al, (2013) confirmed that the material had negligible effect on the magnetic flux of a permanent magnet which they had integrated into total knee replacement components. A preliminary study was performed to show if the addition of a metal (CoCr) femoral head component, would influence the magnetic field of the magnet thus changing the output of the sensor, an overview of this study is presented in Section 4.9.

4.6.2 Magnetoresistive sensor selection and calibration

The selected sensor was a Melexis mlx90393 Triaxis magnetometer. At the time of research this was the only commercially available multi axis system in small form factor package. The sensor is low power 3.3v and available in the miniature QFN package 3X3mm and has a minimum sensitivity in BxBy of 0.150µT and Bz of 0.242 µT and maximum frequency of 717Hz. The sensor chips were soldered onto custom PCBs (6mmX6.8mm) with accompanying passive components as per the manufacturers recommended application diagram, an image of the soldered board is shown in Figure 36 and a schematic is shown in Appendix d). The boards were wired to an Arduino Uno/Teensy 4.0 microcontroller and the sensor data was read in via an I2C serial connection. A dedicated library (Adafruit_MLX90393 library, Adadruit Industries) was used to configure the sensor (for more details on the configuration of the sensor see Appendix e)) these parameters were kept constant through all use of the magnetic field sensor. This resulted in the sensor reporting magnetic field values at a measured frequency of 49Hz and at an approximate sensitivity of 6.01µT in the X and Y direction, and 9.68 µT in the Z direction.

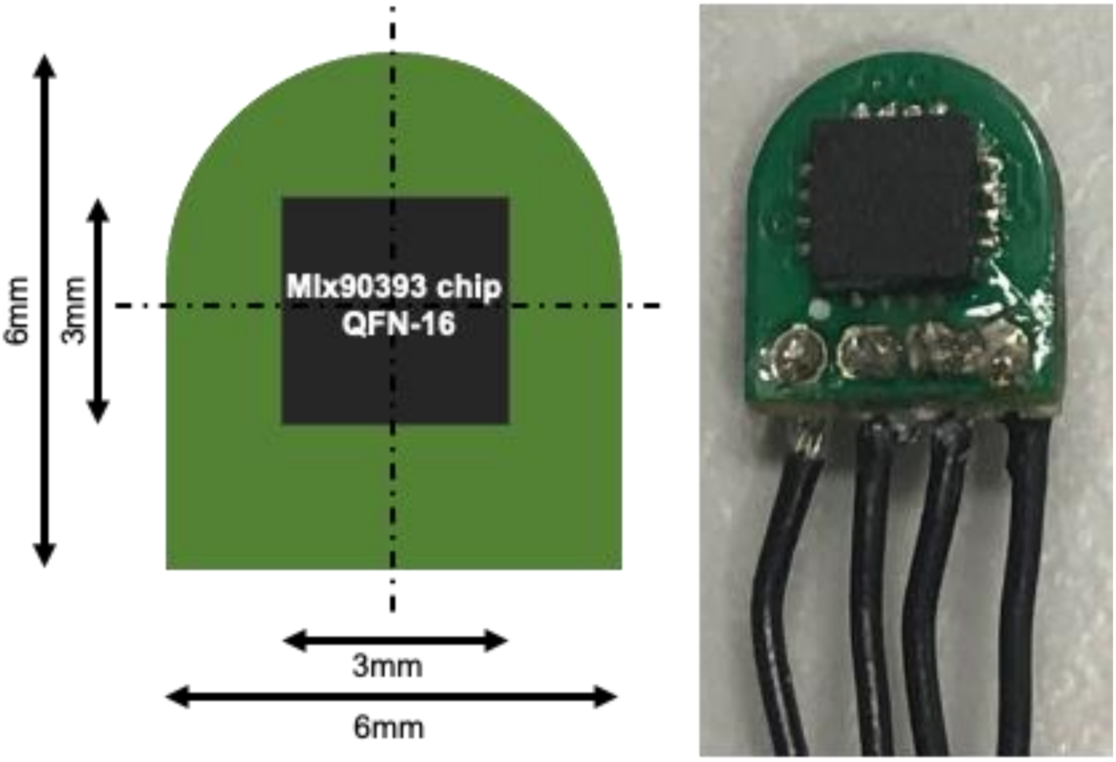

Figure 36 - Melexis mlx90393 Triaxis magnetometer sensor soldered to a custom PCB (6mmX6.8mm)

Errors can occur in magnetoresistive sensors as a result of bias, scale factor error and install alignment error however, distortion as a result of the hard and soft iron effect is likely to be the biggest contributor to error (Guo 2008). Hard iron offset is a result of interfering magnetic fields from sources that have permanent magnetic fields whereas the soft iron effect is interference from induced magnetic field on otherwise unmagnified ferromagnetic material (Ozyagcilar 2012). Sources of hard and soft iron interference are often near the sensor such as components on the PCB or the surrounding installation environment. Ideal data gathered from a magnetometer when it has been subjected to a full array of 3D rotations and there is no hard or soft iron interference, should resemble a perfect sphere centred on the origin. Hard and soft iron effect results in distortion and displacement to the sphere as shown in Figure 37 A. & B.

2D diagram of the impact of soft-iron and hard-iron effect on magnetic field data

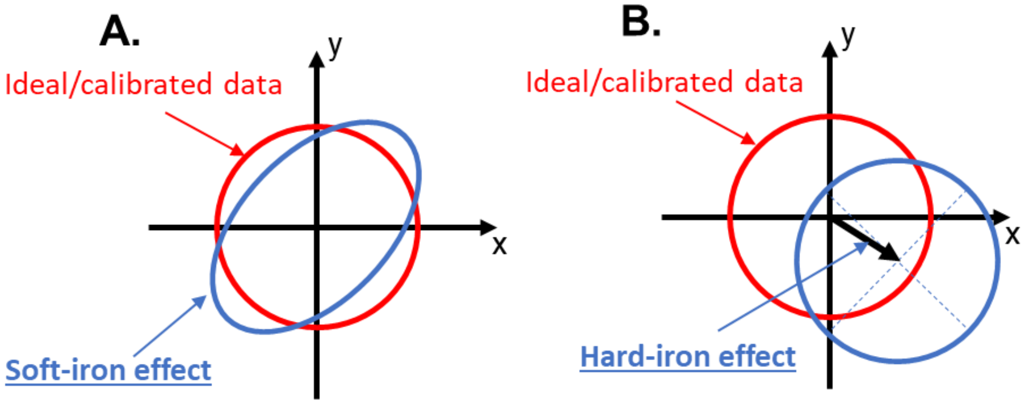

3D scatter plot of magnetic field data before & after soft-iron & hard-iron calibration

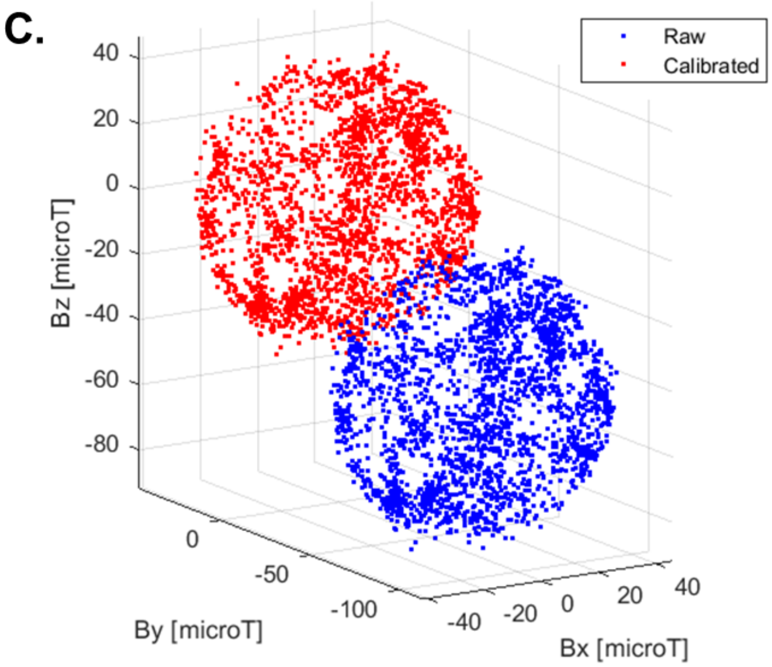

Figure 37 – Diagram showing the impact of the hard-iron (A.) and soft-iron (B.) effect on magnetic field data. Adapted from: (MathWorks, 2019) **(C.) 3D scatter plot of a sample dataset of uncalibrated magnetic field data gathered by an mlx90393 sensor and the calibrated magnetic field data resulting from the application of the hard and soft iron calibration.**

An algorithm described by (Ozyagcilar, 2012) and implemented using the magcal function (Matlab, Mathworks) is able to produce a transformation matrix (A) that re-shapes the ellipsoid to a sphere and a translation vector (c) that is able to centre the data about the origin. The hard and soft iron coefficients are then applied to the raw magnetic field data B_{raw} in real time to as:

$$B_{calibrated} = (B_{raw} - c) \times A$$

Prior to use of the selected magnetic field sensor, the sensor was rotated to cover the full range of movement available in all axes at the working location until a representative ellipsoid of magnetic field data was recorded (this equated to approximately 3000 samples). The magcal algorithm was then used to produce the hard and soft iron coefficients which were saved and then applied to the magnetic field gathered by that particular sensor during that experimental session. A sample dataset of B_{raw} along with the resulting $B_{calibrated}$ is shown in Figure 37 C. and demonstrates the impact of hard and soft iron correction i.e. the calibrated data is now better centred around the origin so the hard-iron effect has been corrected (in this instance there was not noticeable soft-iron distortion as the shape of the data was apparently spherical).

4.6.3 Initial Magnet selection

The size and shape of the magnetic field of a permanent magnet is dependent on the size, shape, material and magnetisation direction of the magnet. A disc magnet was considered as the stem taper and the taper hole of the femoral head is cylindrical which would allow the greatest volume of magnetic material to fit within in the void thus increasing the effective strength of the field reaching the sensor. The magnetic field and magnetic field vector lines of a typical disc magnet (magnetised axially in the positive Z direction) is shown in Figure 38.

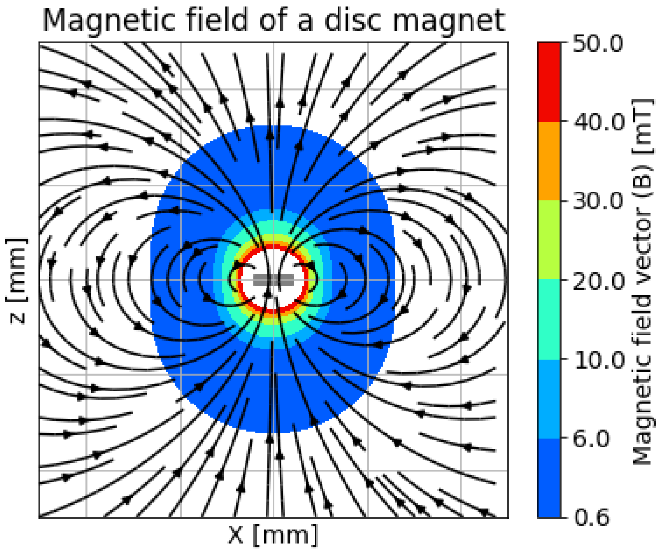

Figure 38 - Typical magnetic field and magnetic field vector lines of a disc magnet

It was vital that the reference magnet was positioned within the sensor's effective working range over the entire range of the possible orientations namely when the stem tilt angle is at the maximum of 66°. The upper bound of the working range is 50mT as this is the saturation onset of the magnetic field sensor. The lower bound had been established as 0.6mT this is 10 times the value of the earths latent magnetic field, this ensured that errors and noise caused by the earth's magnetic field were reduced.

Simulations were performed using a neodymium disc magnet grade N42 with remanence (Br) of 1300mT (supplied by first4magnets.com) magnetised axially in the positive Z direction. The range of magnet shape dimensions selected were the same as those commercially available and within the size constraint of the system namely radius of disc magnet 3mm to 5mm and height of disc magnet 1mm to 4mm.

The magnet is positioned -6.5mm (in the Z direction) from the origin/centre of rotation (0,0) thus replicating the magnet being positioned on the stem taper face. A simulated sensor was positioned at -26.5mm (in the Z direction) thus replicating the sensor being positioned in the introducer hole of the acetabular component. The simulation was first performed with the stem in the neutral position so a tilt angle of 0°. The simulation was then repeated with the magnet rotated by 66° about the origin thus replicating a stem tilt angle of 66°.

Representative 2D axisymmetric magnetic field plots (shown in Figure 39) were produced to compare both simulation conditions for the nine magnets investigated. The appropriate magnet had to be able to produce a magnetic field greater than 0.6mT at the location of the sensor (0,0,-26.5mm) shown as the black dot in Figure 39. Furthermore, it was preferred that the magnet was as small as possible to minimise the impact of mounting/embedding it to the femoral stem.

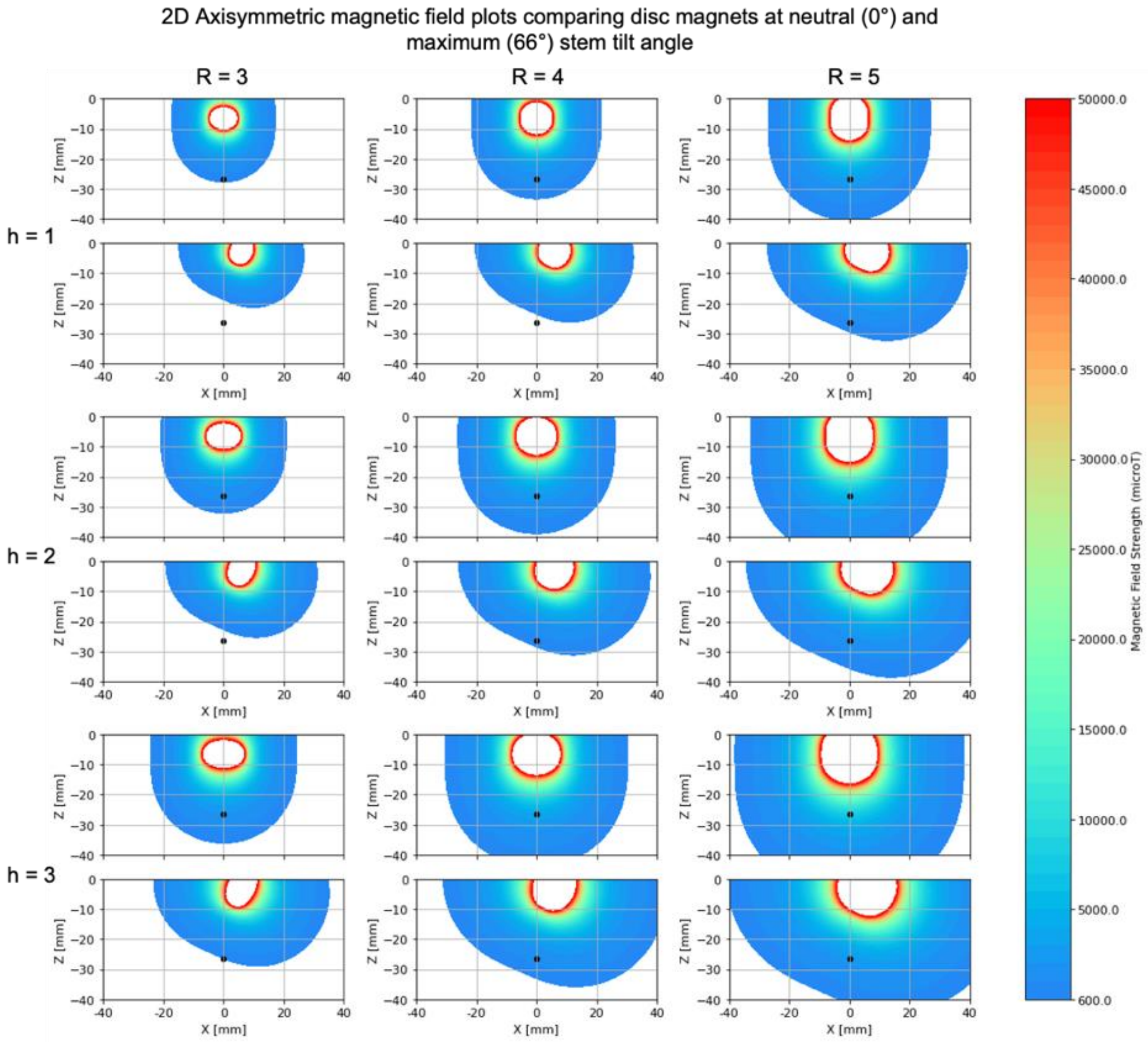

Figure 39 - 2D axisymmetric magnetic field colour plots showing the effect of changing radius (R) and height (h) [measured in mm] of a neodymium N42 disc magnet, the black dot represents the location of the sensor (0,0,-26.5mm).

Increasing the radius of the disc magnet had a greater impact on increasing the strength of the magnetic field. The magnet size [h = 2mm, R = 4mm] is the smallest magnet in which the magnetic field at the location of the sensor (0,0,26.5mm) is greater than the defined minimum of 600microT. Therefore, for this application an 8X2mm disc magnet was selected as this left clearance space all around the magnet making it the best suited to being integrated within the region between the stem taper face and the head taper face.

Other grades of neodymium are available for example N35 (Br = 1195mT) and the higher grade N52 (Br = 1455mT) (supplied by first4magntes.com) however, the higher grades are typically rarer. The effect of changing the neodymium magnet grade of an 8X2mm disc magnet is shown in Figure 40. As can be seen from Figure 40 changing the grade has a minimal impact on the magnetic field and hence the use of a N42 magnet was deemed sufficient.

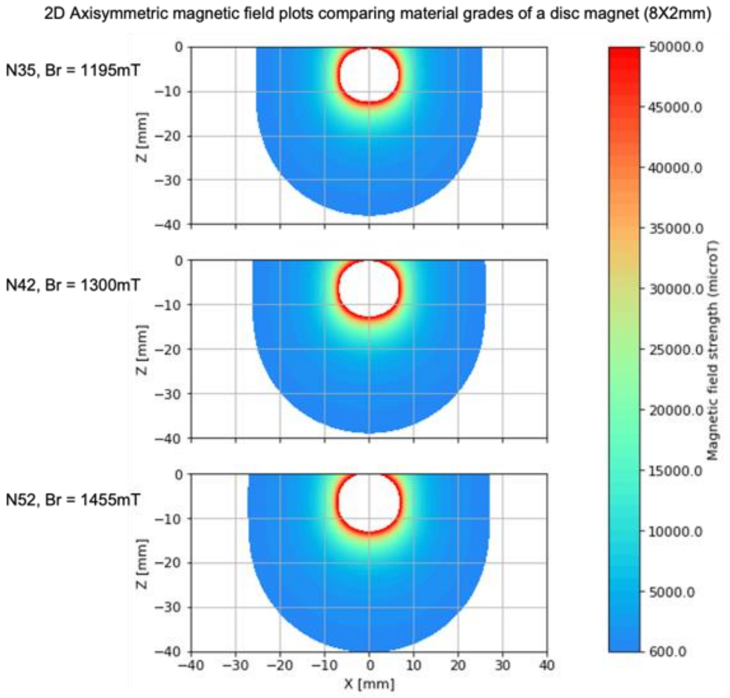

Figure 40 - 2D axisymmetric magnetic field colour plots showing the effect of changing Neodymium magnet material grade of an 8X2mm disc magnet.

4.6.4 Proposed layout of a magnetic position and orientation sensing system within total hip replacement components

A diagram of the selected magnet and sensor positioned within the THR is shown in Figure 41. The top views of the stem taper face and head taper face shown that both the magnet and sensor were centred on the vertical Z axis. The same 8X2mm N42 Neodymium magnet selected and used in the experimental verification was chosen. This magnet fits the size constraints of the system and when positioned in the configuration shown in Figure 41 the magnetic field reaching the sensor was within the working range of the selected sensor.

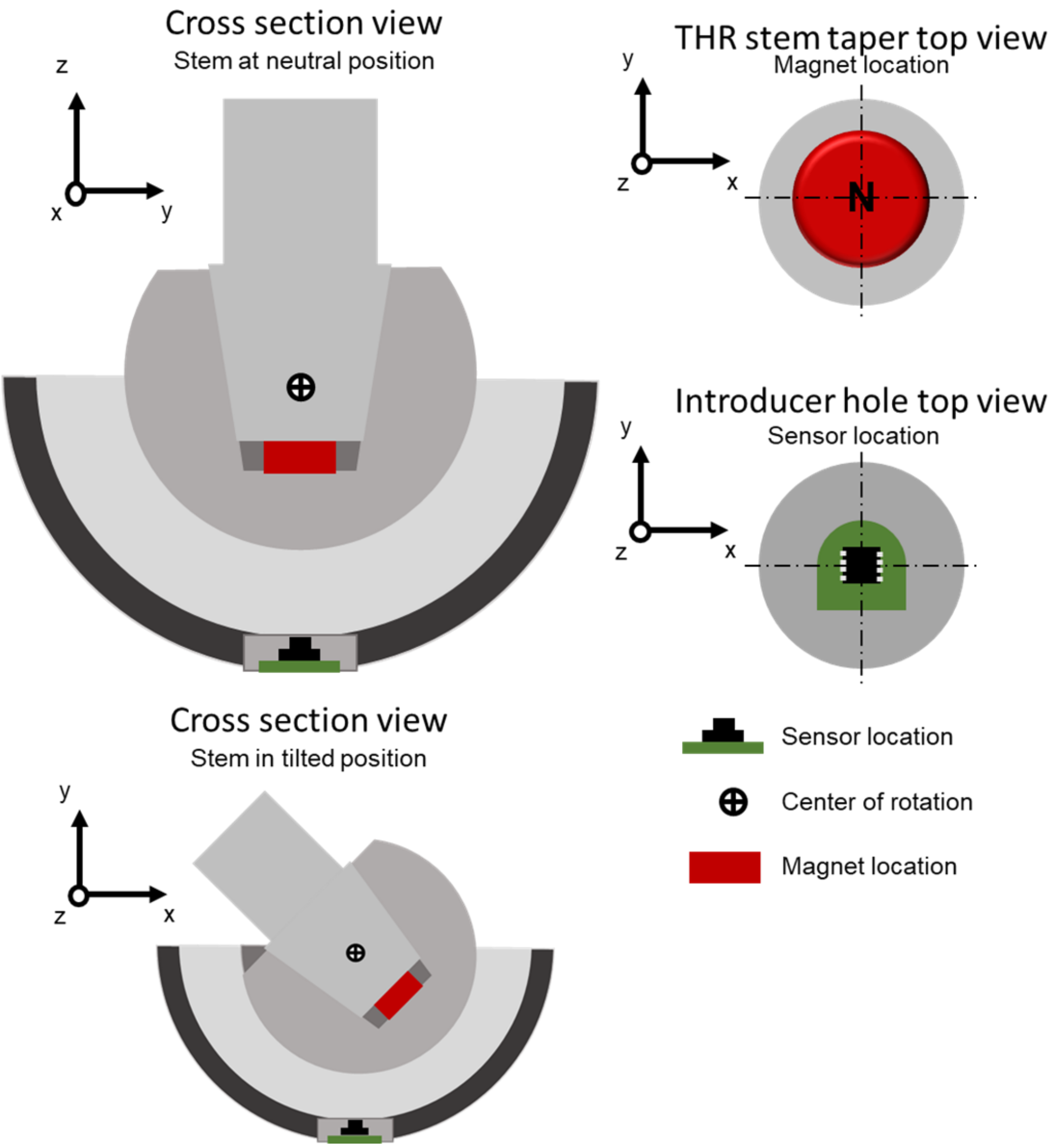

Figure 41 - Diagram of a 3axis magnetic field sensor board and 8X2mm Neodymium permanent magnet positioned in the components of a total hip replacement.

4.7 Simulation method validation and sensor performance verification pilot study

4.7.1 Aim

The aim of this pilot study was to validate the output of the magnetic field simulations and characterise the performance of the magnetic field sensor. The simulated and experimental data will be compared, and the levels of error determined. Experimental data from different magnets and sensors will be gathered so that comparisons can be made on their variability. The research questions to be answered include:

1. Is the simulated magnetic field data comparable to the data gathered experimentally by the magnetic field sensor?
2. Is there variation in the magnetic fields of the magnets (inter magnet variability)?
3. Is there variation in the output data of the sensors (inter sensor variability)?

4.7.2 Methods

The sensor board was pushed into a 3D printed mount that was held in place by an acrylic mount plate that was fixed to the robot support frame. The location of the sensor was defined as the origin (0,0,0)mm. An 8X2mm N42 Neodymium magnet (first4magnets.com) was mounted within a 3D printed replica stem at 79mm from the robot tool face. The magnet start location was positioned directly above the sensor at a distance of 28mm making the start location (0,0,28)mm. This location was found by positioning the robot so that the stem component contacted the inner edges of the circular hole of the acrylic mount plate. This was done along the diameter of the circle in the X and Y directions. The centre point of these locations (relative to the robot) was then used as the X and Y position of the central axis of the test set up (as the sensor mount was designed to position the sensor die within the centre of the acrylic mount plate). The stem component was then positioned to contact the top face of the acrylic mount plate and the location (relative to the robot) was recorded to give the robot a reference to the position of the mount plate in the Z direction. Images of the experimental method are shown in Figure 42. The robot arm was used to translate a magnet axially by ±10mm in the X.Y & Z axes in turn, beginning at the defined magnet start location.

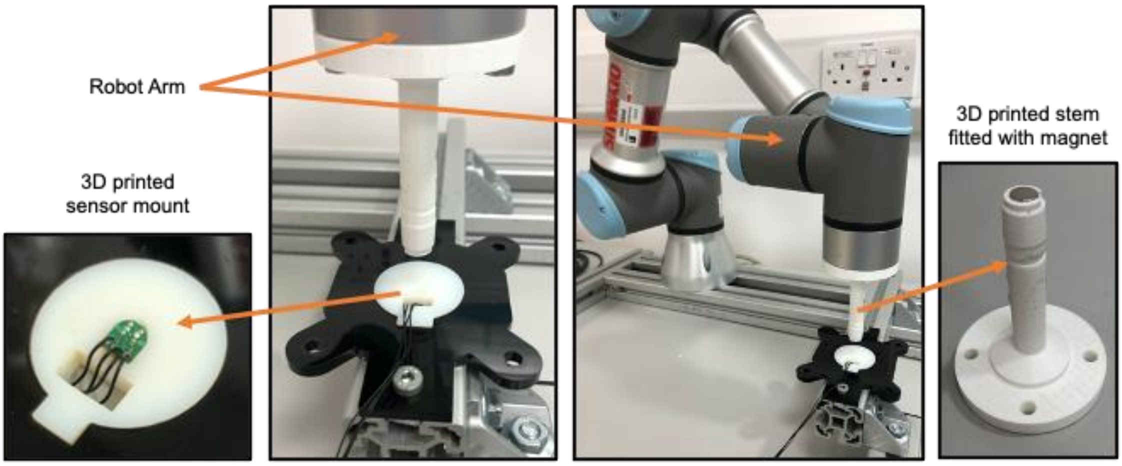

Figure 42 - Pilot study experimental set up including a 3D printed stem component (with fitted magnet) mounted to a UR3 robot arm position above a triaxis magnetometer sensor (mlx90393) held in a 3D printed mount.

The magnetic field output of the sensor (Bx,By,Bz) was recorded throughout the motion of the magnet and the robot arm recorded magnet position (ground truth measurement) at their maximum sampling rates of 50Hz and 125Hz respectively. At the start of each test run the robot sent a trigger signal to a microcontroller which meant the data from the two sources could be synched. To obtain datasets of the same size for statistical analysis timestamps of the sensor data were matched to the closest timestamp of the robot data. The remaining robot data was omitted leaving datasets of the same size.

During the experimental trial four different magnets (mag1 to mag4) and four different magnetic field sensor boards (C,D,E & F corresponding to the hexadecimal character of the I2C address) were tested. This allowed for the magnets to be compared to show if there was any variation in their magnetic field (inter magnet variability). The different boards were also compared to assess the consistency of their output and to verify if they had been correctly manufactured and soldered. And finally, magnetic field data recorded by the sensors could be compared to the theoretical simulated data to validate the simulation method. The translation routine was performed 5 times for each magnet and sensor configuration which resulted in a total of $4 \times 4 \times 5 = 80$ experimental runs.

The robot recorded magnet position data was inputted into the Magpylib simulation to generate simulated magnetic field data specific to each experimental run of the test. A sample scatter plot of the position coordinates of the magnet, a plot of the position of the magnet in the X, Y and Z direction (mm) over time and the corresponding magnetic field strength Bx, By and Bz over the duration of the sensor verification motion, is shown in Figure 43. Horizontal movement of the magnet away from the defined origin decreases the measured magnetic field in the Z direction Bz from 928µT to 647.6µT. Absolute measured magnetic field in the corresponding horizontal direction i.e. Bx or By increases from -365 to 365µT depending on the direction. Vertical movement away from the sensor decreases the magnetic field in the Z direction exponentially from 3323.4µT to 375.4µT. When there is no movement in the horizontal axes direction there is no measured magnetic field in Bx or By.

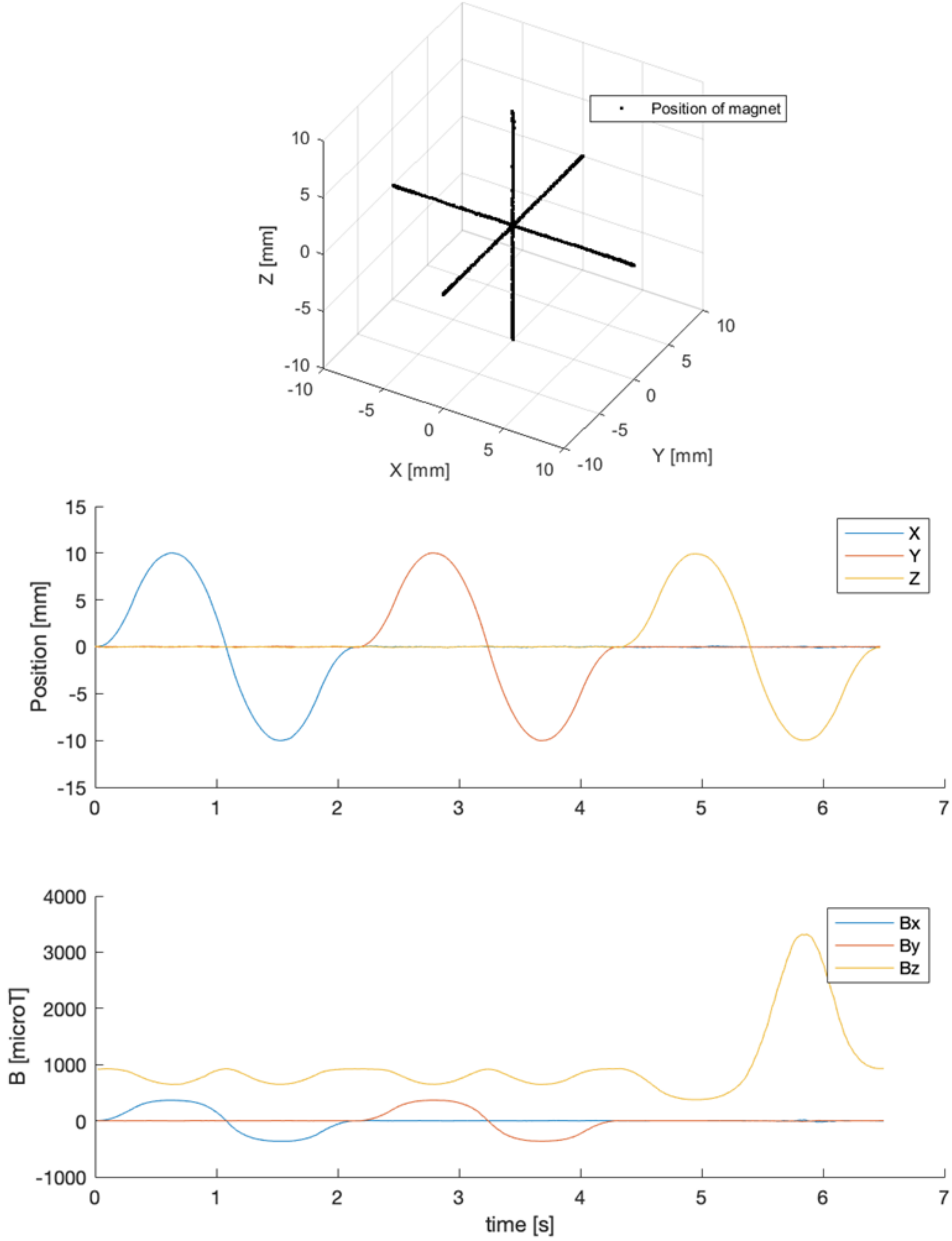

Figure 43 – Scatter plot of the position of the magnet in 3D space during the sensor verification motion experiment. Plot of the position of the magnet in the X, Y and Z direction (mm) over time and the corresponding simulated magnetic field strength Bx, By and Bz over the duration of the sensor verification motion experiment.

To compare the simulated (expected) and the sensor recorded magnetic field data (observed) the root mean squared error RMSE (Equation 2 & $RMSE = \sqrt{mean(Error^2)}$

Equation 3), standard deviation (SD) and minimum and maximum error were computed. The metrics were evaluated for all the data across the four repeats of each magnet and sensor condition, and then for each specific magnet and sensor.

$$Error = Observed\ Value - Expected\ Value$$

Equation 2

$$RMSE = \sqrt{mean(Error^2)}$$

Equation 3

4.7.3 Results

Overall results

The values of the RMSE ± standard deviation between the sensor recorded magnetic field vector and the simulated magnetic field vector across all magnet and sensor configurations (80 experimental runs) was 74.4 microT ± 73.3 microT and the range was -566.0 microT to 579.4 microT. As percentages of the maximum simulated magnetic field value (3328 microT) RMSE ± standard deviation was 2.24% ± 2.2% and the range was -17.0% to 17.4%. A sample plot of the sensor recorded magnetic field response and the simulated magnetic field response during the fifth experimental run repeat of sensor F and magnet four, is shown in Figure 44. Plots of the error recorded by the magnetic field sensor in the X, Y and Z direction, are shown in Figure 45, Figure 46 & Figure 47 respectively. The plots of the position of the magnet in the X, Y and Z direction (mm) and the corresponding simulated magnetic field strength (Bx, By or Bz) over the duration of the sensor verification motion, are also shown in Figure 45, Figure 46 & Figure 47 respectively.

The key findings of this study are:

1. The experimental data recorded from the four magnets and the four sensors is accurate when compared to the simulated magnetic field vector values as RMSE is 74.4 microT.
2. The experimental values are not precise as the standard deviation was 73.3 microT and range was -566.0 microT to 579.4 microT, showing variation in the values.

3. Figure 44 shows that the shape of the simulated and experimental magnetic field data responses (i.e. shape of the field) is comparable, yet the datasets appear to be offset and misaligned from each other.

4. Figure 45 and Figure 46 showed that error in the Bx and By were greatest when the magnet is closest to the sensor (i.e. moved to the -Z position).

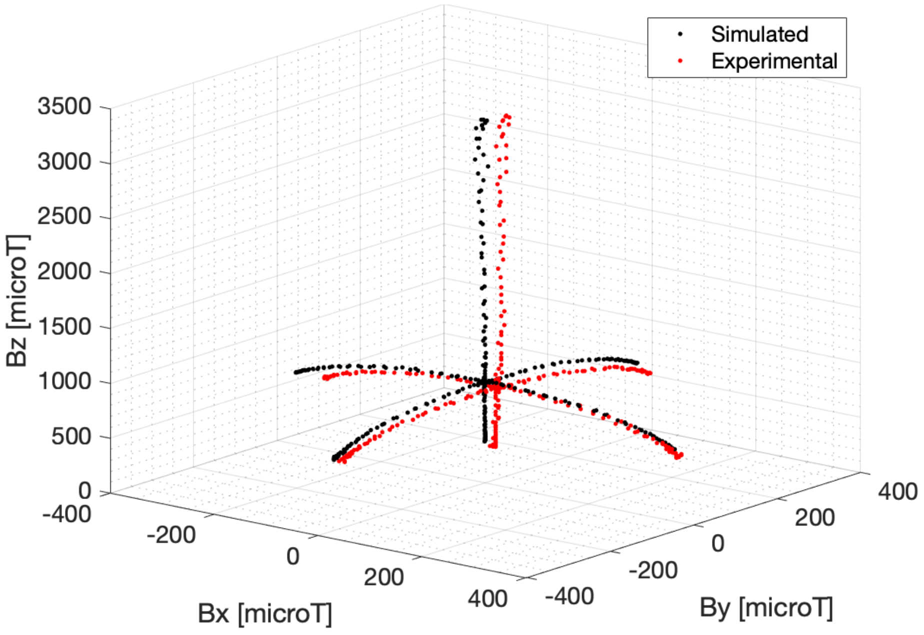

Figure 44 - Scatter of the magnetic field data Bx, By & Bz recorded by the sensor experimentally and produced by the simulation when the magnet is displaced by ±10mm from defined magnet start position.

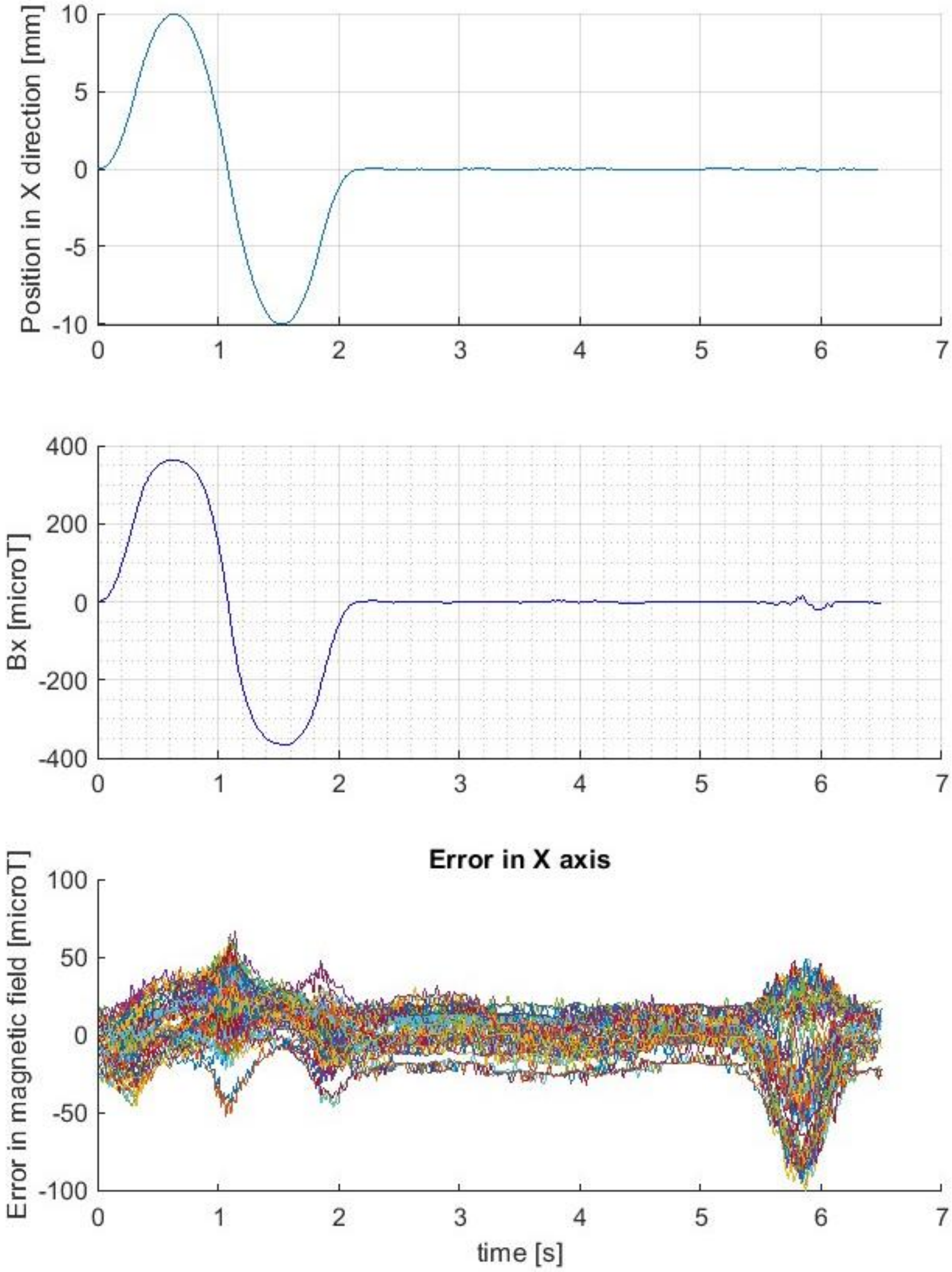

Figure 45 - Error recorded by the magnetic field sensor in the X direction (Bx) (for all 80 experimental runs) and the position of the magnet in the X, Y and Z direction (mm) and the corresponding simulated magnetic field strength Bx over the duration of the sensor verification motion experiment. The magnet was translated by ±10mm from the magnet starting position (0,0,28)mm whilst the sensor was positioned at the origin (0,0,0)mm. SensorC_mag1 refers to sensor C out of the four possible [C, D, E & F] and mag1 refers to the first magnet out of the four tested.

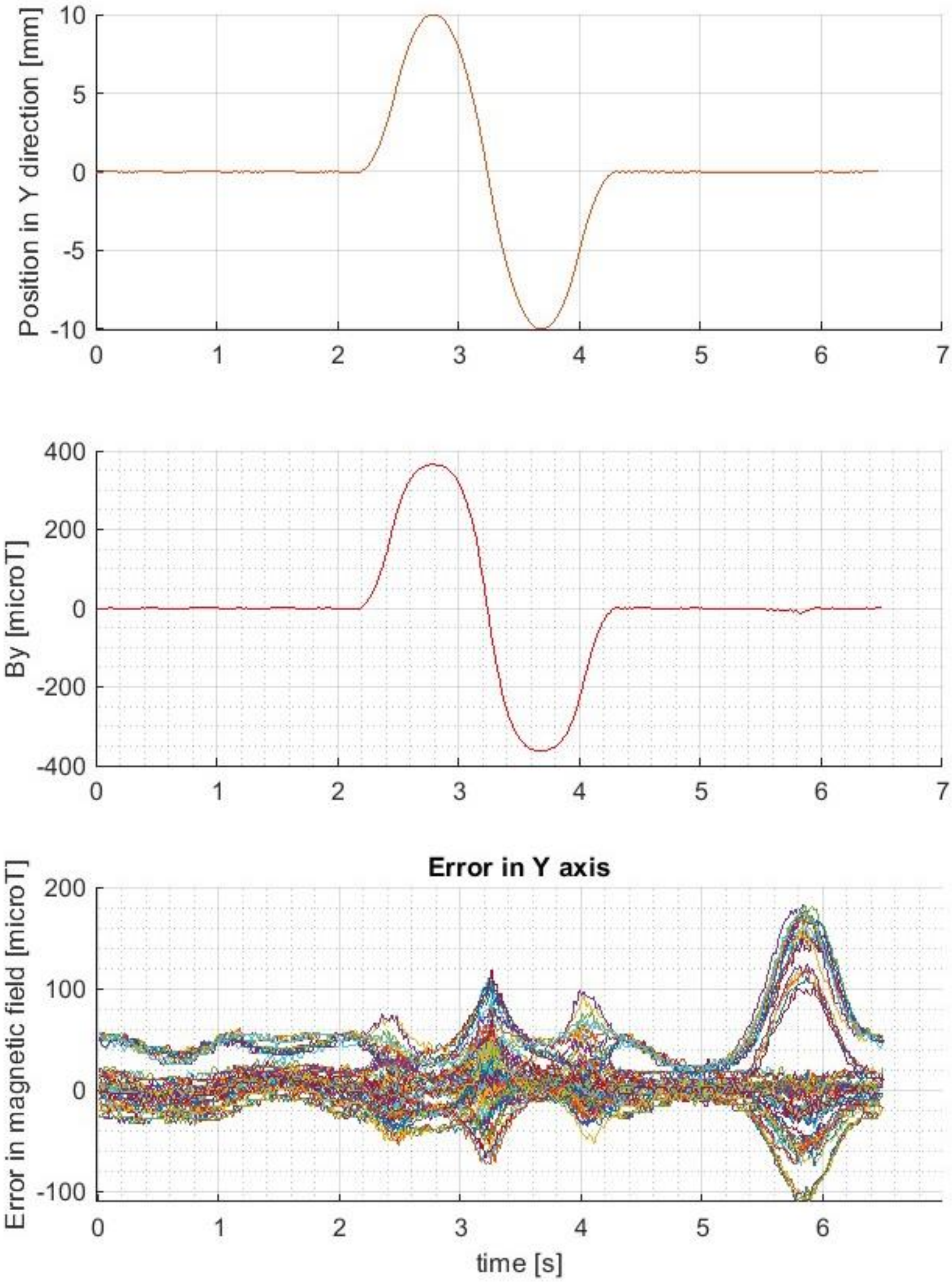

Figure 46 - Error recorded by the magnetic field sensor in the Y direction (By) (for all 80 experimental runs) and the position of the magnet in the X, Y and Z direction (mm) and the corresponding simulated magnetic field strength By over the duration of the sensor verification motion experiment. The magnet was translated by ±10mm from the magnet starting position (0,0,28)mm whilst the sensor was positioned at the origin (0,0,0)mm. SensorC_mag1 refers to sensor C out of the four possible [C, D, E & F] and mag1 refers to the first magnet out of the four tested.

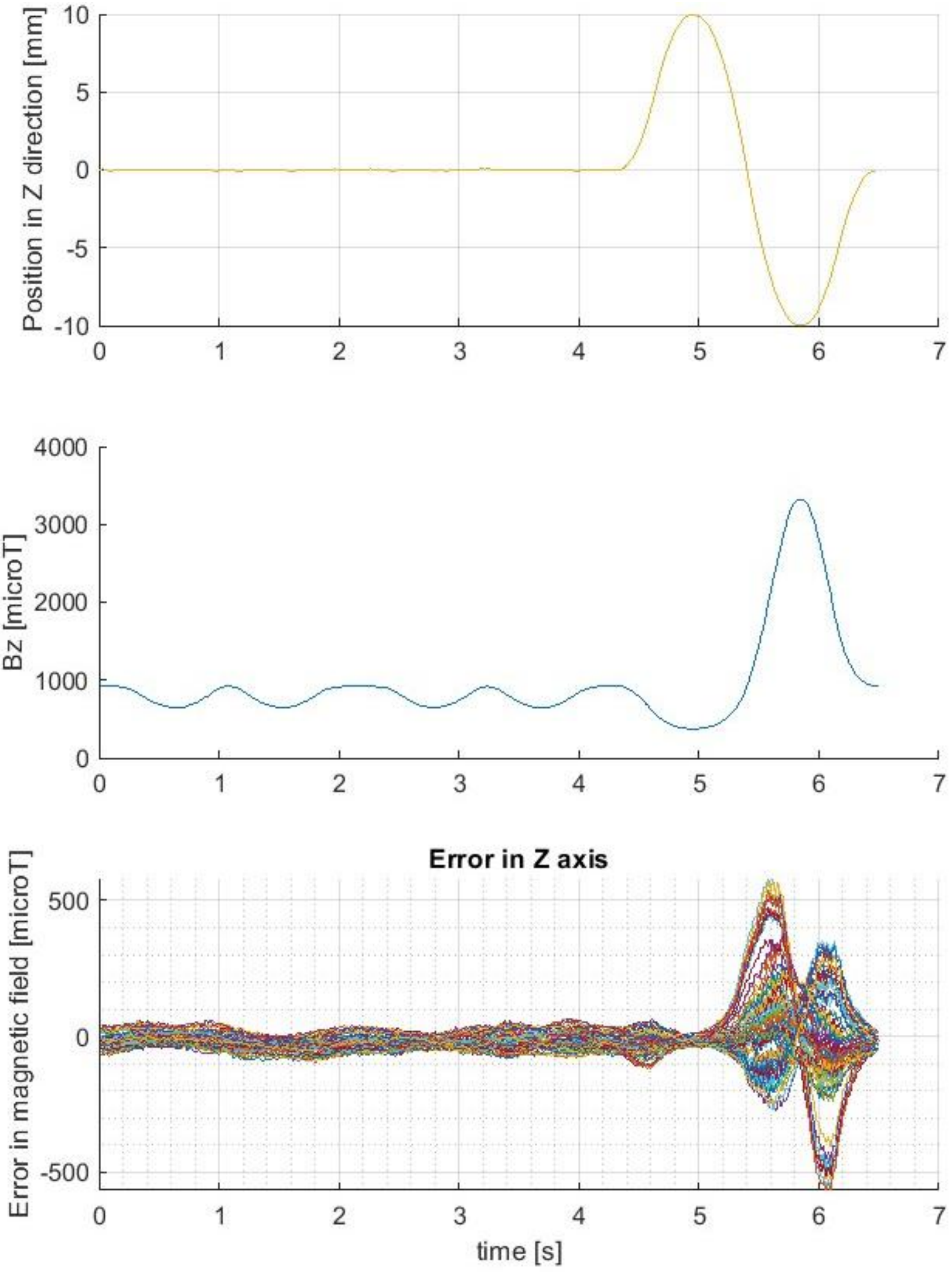

Figure 47 - Error recorded by the magnetic field sensor in the Z direction (Bz) (for all 80 experimental runs) and the position of the magnet in the X, Y and Z direction (mm) and the corresponding simulated magnetic field strength Bz over the duration of the sensor verification motion experiment. The magnet was translated by ±10mm from the magnet starting position (0,0,28)mm whilst the sensor was positioned at the origin (0,0,0)mm. SensorC_mag1 refers to sensor C out of the four possible [C, D, E & F] and mag1 refers to the first magnet out of the four tested.

Comparison of magnets and sensors results

Figure 48 & Figure 49 show the Box plots of the error between the sensor recorded magnetic field vector and the simulated magnetic field vector for each of the magnet and sensor configuration grouped to show comparison between the magnets (Figure 48) and sensors (Figure 49) respectively. The median error is random across both plots showing that there is no trend or pattern dependent on the specific magnet or sensor configurations. Table 6 shows the RMSE ± standard deviation for each of the four sensors and each of the four magnets. The standard deviation values overlap showing that there is no significant difference in the error reported between different magnets or sensors.

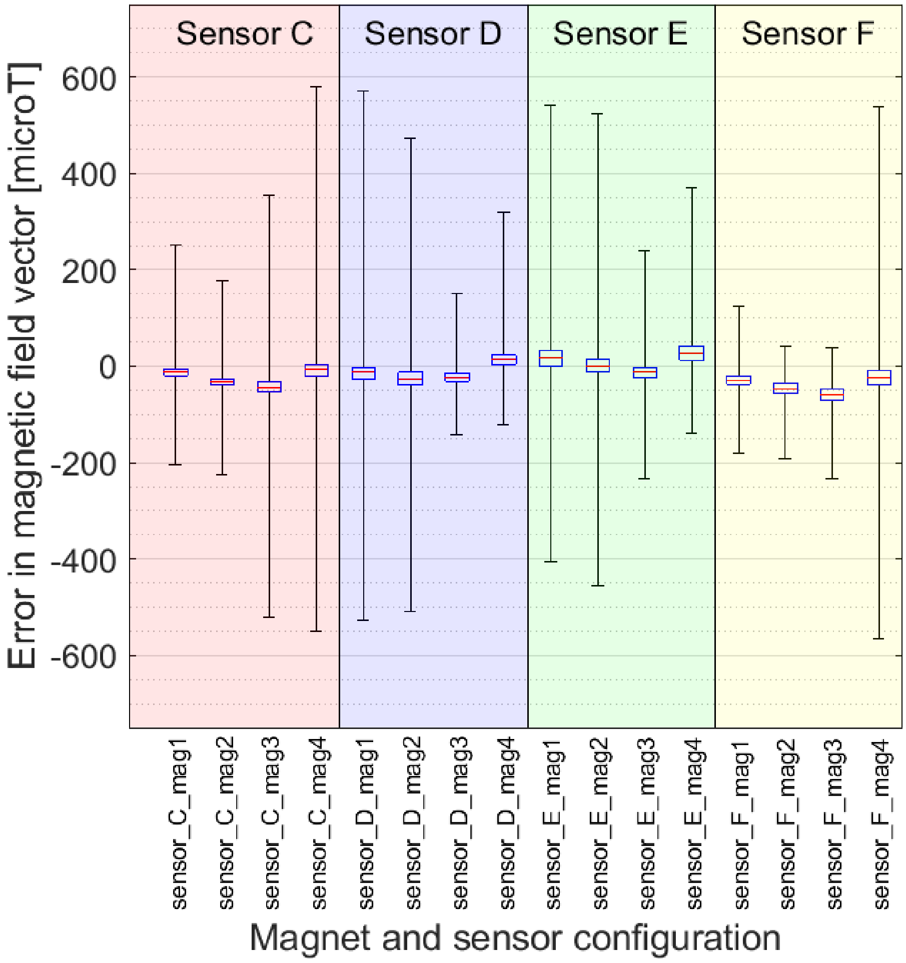

Figure 48 - Error in the magnetic field vector recorded by the sensor when compared to the simulated magnetic field vector when the magnet was translated by ±10mm from the magnet starting position (0,0,28)mm whilst the sensor was positioned at the origin (0,0,0)mm. SensorC_mag1 refers to sensor C out of the four possible [C, D, E & F] and mag1 refers to the first magnet out of the four tested. The boxplots have been grouped to show comparison between the MAGNETS.

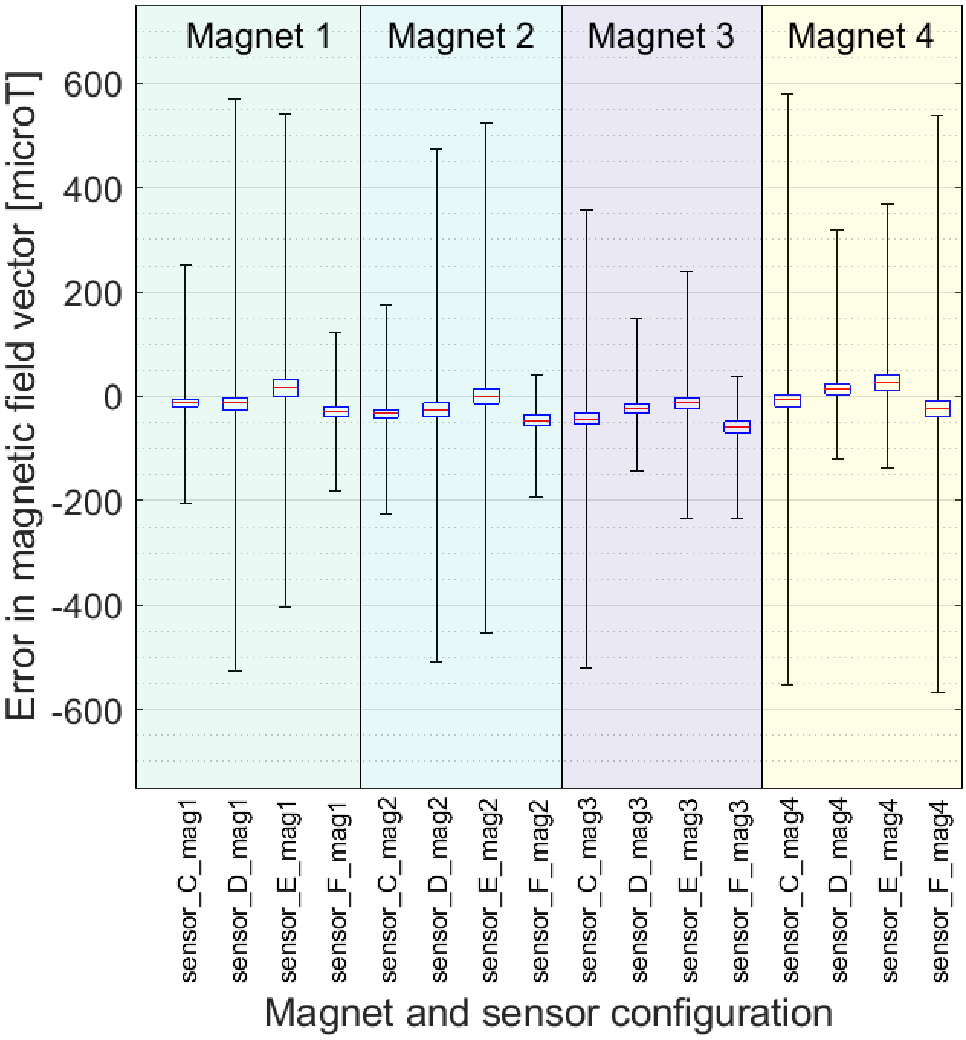

Figure 49 - Error in the magnetic field vector recorded by the sensor when compared to the simulated magnetic field vector when the magnet was translated by ±10mm from the magnet starting position (0,0,28)mm whilst the sensor was positioned at the origin (0,0,0)mm. SensorC_mag1 refers to sensor C out of the four possible [C, D, E & F] and mag1 refers to the first magnet out of the four tested. The boxplots have been grouped to show comparison between the SENSORS.

Table 6 - Mean percentage error ± standard deviation for each of the four sensors and each of the four magnets. Where mean percentage error for Sensor C is the mean percentage error for the sensor_C_mag1, mag2, mag3 and mag4 configurations.

Sensors	Sensor C	Sensor D	Sensor E	Sensor F
RMSE ± standard deviation	72.9 microT ± 69.9 microT	75.7 microT ± 75.5 microT	73.2 microT ± 71.7 microT	75.7 microT ± 65.0 microT
Magnets	Magnet 1	Magnet 2	Magnet 3	Magnet 4
RMSE ± standard deviation	69.7 microT ± 69.6 microT	73.0 microT ± 69.2 microT	60.8 microT ± 50.5 microT	90.8 microT ± 90.2 microT

4.7.4 Discussion

The aim of this study was to validate the accuracy of the magnetic field data produced by the simulation against the output of a 3-axis magnetometer to see if the two were comparable. The increased error in Bx and By when the magnet is closest to the sensor can be explained by the margin of error being greater when the magnet is closer to the sensor. Consequently, when the simulated magnet is at the defined origin (0, 0, 28)mm displacement of the magnet by 1mm in the X or Y axis will result in an error in Bx or By of 48.3µT (5.2% of magnetic field vector) and when the magnet is closest to the sensor i.e. (0, 0, 18)mm the same displacement of 1mm would incur an error in Bx or By of 264.1µT (8.0% of magnetic field vector). The high error in Bx and By is also suggestive of component misalignment.

The high level of error can be explained by the apparent misalignment of the datasets which indicates that the central axes of the sensor and magnet were not properly aligned above each other, which suggest that the system is very sensitive to errors in the positioning of the magnet. Therefore, variations seen are not variations in the magnets or the sensors but instead were most likely due to errors in the mechanical positioning of the robot arm with respect to the sensor mounted to the base frame.

Positioning the robot arm directly above the sensor and verifying that positioning was correct, was challenging. The aluminium base frame was readily available and made prototyping and adapting the test setup convenient, yet the fixtures and fittings made positioning the components (with respect to the robot) to the required precision <1mm inherently hard. The contacting method which essentially used the robot arm to measure component position (with respect to the robot) was an improvement. However, this method was still flawed as judging component contact was subjective and the size difference between the 3D printed stem component and the circular hole of the acrylic mount plate meant there was a high margin for error when judging the circular hole’s diameter that was aligned to the X or Y axis of the robot. Additionally, the stem and sensor mount were 3D printed and so there would have been errors and imperfections in these components. Therefore, a more robust method of mechanically aligning the components is needed or an additional calibration step is required to reduce the impact of these random errors.

The magnet manufacturer (first4magnets.com) quote the Remanence magnetism (Br) of the N42 magnet grade as a range (1280-1320μT). For the simulations the median of this range was used (1300μT) however, the exact value of the Br of the magnet was not assessed in this work. As previously stated, simulated magnetic field when the magnet is positioned when the magnet is directly above the sensor in neutral position and when simulated Br = 1300μT was returned as 1996.8μT. When the Br of the simulated magnet was decreased to 1280μT and increased to 1320μT, simulated magnetic field was returned as 1966.0μT and 2027.5μT respectively. This equates to a percentage decrease of 1.5% and percentage increase of 1.5% when compared to the original simulated magnetic field value. This maximum potential percentage error is less than the maximum percentage error seen in the experiment. So, errors resulting from deviations in magnet material, will have had an impact on the experimental error but were not the only contributing factor.

4.8 Procrustes statistical shape analysis transformation of magnetic field to account for errors in the mechanical positioning of the sensor and magnet

Procrustes analysis is a form of statistical shape analysis that compares the points of two shapes. The Procrustes function (Matlab, Mathworks) evaluates the rigid transform that best superimposes shape A onto shape B. The returned transformation consists of a translation, rotation and scaling in the form of:

$$C = s * A * r + t$$

Where A is a matrix of the coordinates describing shape A, s is the scaling component, r is the rotation or reflection matrix, t is the translation component and C is the resulting transformed shape that best superimposes shape A onto shape B. Procrustes analysis is an ideal solution to correct the offset and misalignment present between the simulated and experimental magnetic field data that is present due to mechanical errors in the positioning of the sensor and magnet. This is because it will produce the most optimal transformation function that rotates and translates the magnetic field dataset whilst best preserving the original shape of the response.

4.8.1 Aim

The aim of this study was to see if Procrustes statistical shape analysis could be used to calibrate experimental magnetic field data to improve the accuracy and precision when compared to simulated magnetic field data.

4.8.2 Methods

Procrustes analysis was performed on the simulated and experimental magnetic field data of the first four repeats for each of the magnet and sensor configurations gathered in the sensor performance verification pilot study. The resulting transformation function was then used to transform the sensor recorded magnetic field data of the final fifth repeat. The transformed magnetic field data of the fifth repeat was then compared to the corresponding fifth repeat of the simulated data produced from the magnet position data recorded by the robot.

4.8.3 Results

The RMSE ± standard deviation between the sensor recorded magnetic field vector and the simulated magnetic field vector for the experimental fifth repeat across all magnet and sensor configurations was -83.5 microT ± 82.7 microT and the range was -551.6 microT to 579.4 microT, and 73.6 microT ± 73.7 microT and the range was -583.9 microT to 517.2 microT for the transformed magnetic field data. A sample plot of the sensor recorded magnetic field response, the transformed sensor recorded magnetic field response and the simulated magnetic field response during the fifth experimental run repeat of sensor F and magnet four, is shown in Figure 50. Box plots of the error between the simulated magnetic field vector and the original and transformed sensor recorded magnetic field vector for each of the magnet and sensor configuration, are shown in Figure 51. Each box and whisker represent the distribution of the error gathered during the fifth experimental run that was performed for each of the magnet and sensor configurations. The red boxplots correspond to the original experimental data and the blue boxplots correspond to the transformed experimental data. Table 7 shows the RMSE ± standard deviation for the original magnetic field data and the transformed magnetic field data of the fifth experimental repeat.

The aim of this study was to see if Procrustes statistical shape analysis could be used to calibrate experimental magnetic field data to improve the accuracy and precision when compared to simulated magnetic field data. The results show that performing the Procrustes calibration has reduced the RMSE between the sensor recorded magnetic field vector and the simulated magnetic field vector. Figure 50 shows the Procrustes transformation has better aligned the experimental magnetic field data to the simulated magnetic field data and so improved the accuracy of the experimental data when compared to the simulated values.

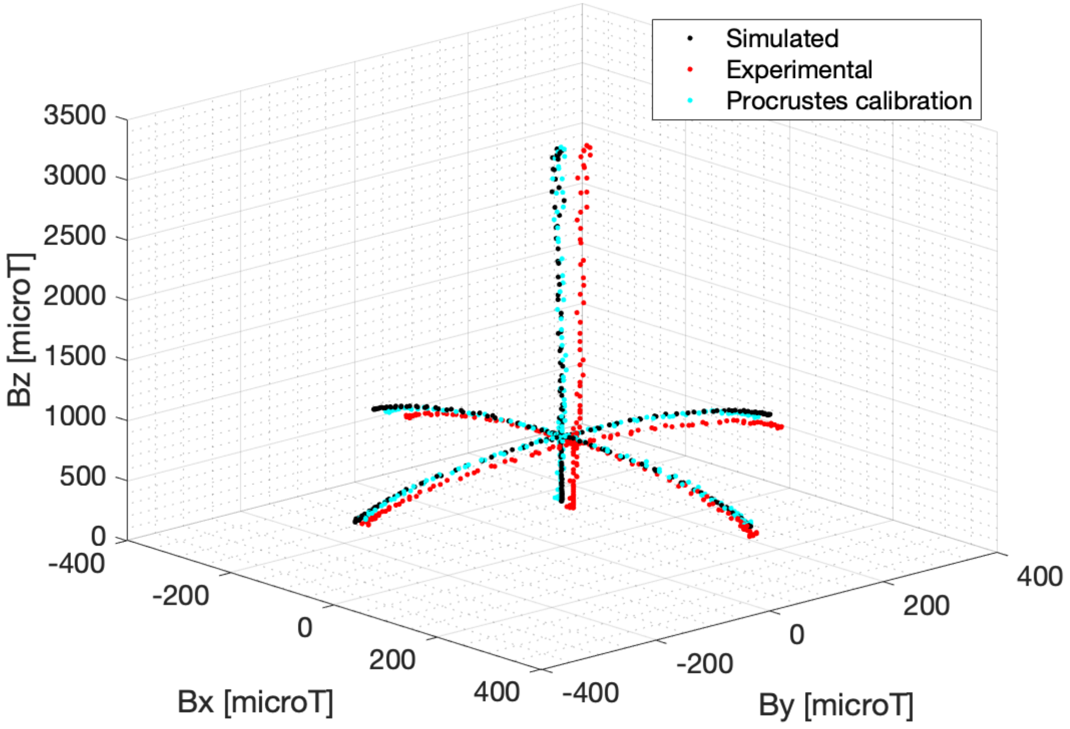

Figure 50 - Three-dimensional scatter plot of the magnetic field data Bx, By & Bz recorded by the sensor experimentally, the sensor recorded magnetic field following the Procrustes transformation and the magnetic field data produced by the simulation when the magnet is displaced by ±10mm from defined magnet start position.

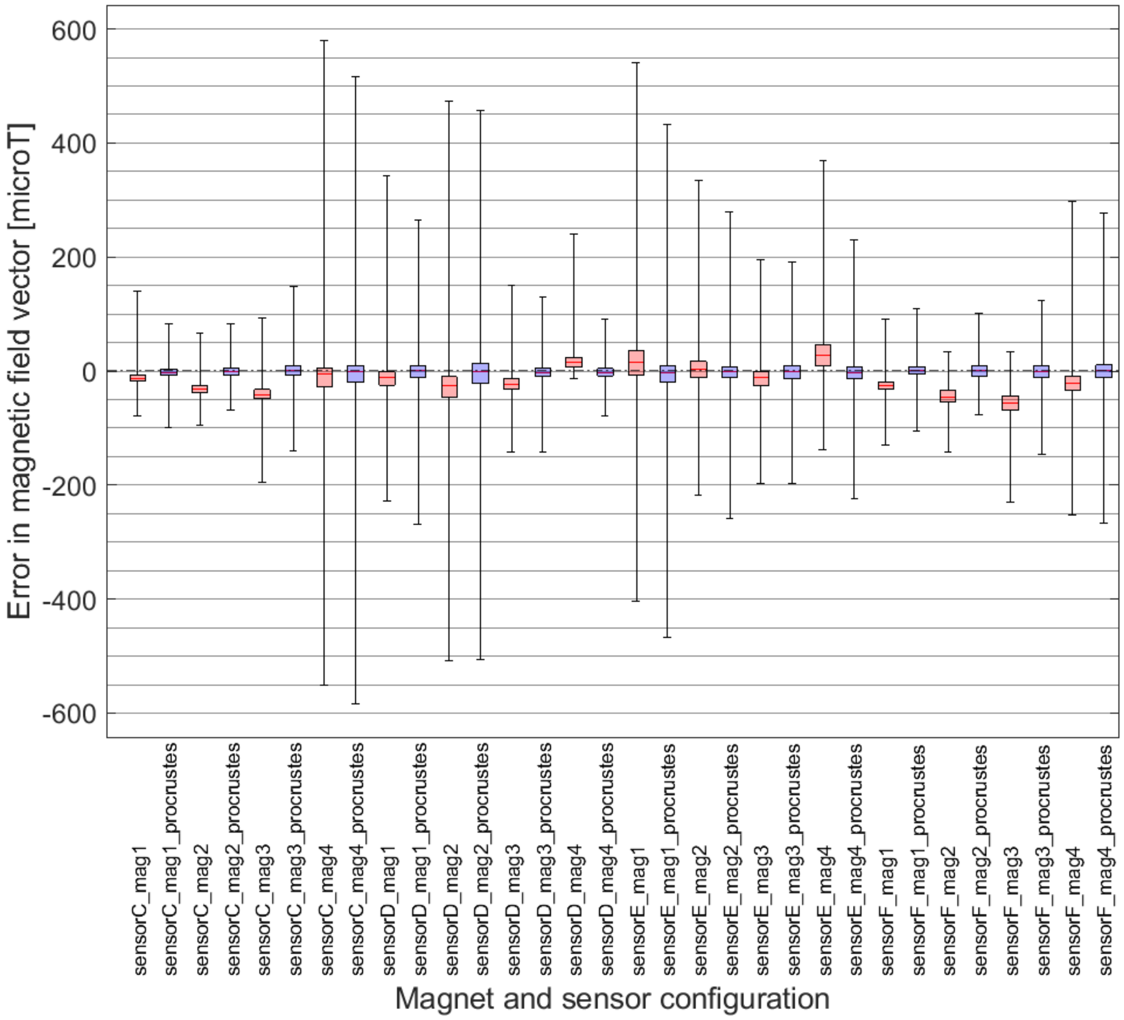

Figure 51 – Error in the sensor recorded transformed magnetic field vector when compared to the simulated magnetic field data when the magnet was translated by ±10mm from the magnet starting position (0,0,28)mm whilst the sensor was positioned at the origin (0,0,0)mm SensorC_mag1-procrustes refers to sensor C out of the four possible [C, D, E & F] and mag1 refers to the first magnet out of the four possible and _procrustes means the Procrustes transformation has been applied to the sensor recorded magnetic field data. The red shaded boxplot denotes the error in experimental magnetic field data of the fifth experimental run and the blue shaded boxplot denotes the error in the transformed magnetic field data of the fifth experimental run.

Table 7 - RMSE ± standard deviation for original magnetic field data and the transformed magnetic field data of the fifth experimental repeat.

Sensors	**Sensor C**	**Sensor D**	**Sensor E**	**Sensor F**
Original data RMSE ± standard deviation	82.7 microT ± 82.7 microT	86.5 microT ± 83.6 microT	56.2 microT ± 46.0 microT	102.1 microT ± 101.5 microT
Transformed data RMSE ± standard deviation	74.5 microT ± 74.5 microT	78.3 microT ± 78.4 microT	40.1 microT ± 40.1 microT	91.7 microT ± 91.7 microT
Magnets	**Magnet 1**	**Magnet 2**	**Magnet 3**	**Magnet 4**
Original data RMSE ± standard deviation	88.2 microT ± 85.9 microT	88..6 microT ± 88.6 microT	92.8 microT ± 91.6 microT	60.4 microT ± 48.1 microT
Transformed data RMSE ± standard deviation	81.5 microT ± 81.5 microT	80.2 microT ± 80.2 microT	82.5 microT ± 82.5 microT	42.8 microT ± 42.8 microT

4.9 Impact of metal (CoCr) total hip replacement components on magnetic field

The material of the metallic THR components used in this work was CoCr which is inherently non-ferrous. Arami et al, (2013) confirmed that the material had negligible effect on the magnetic flux of a permanent magnet which they had integrated into total knee replacement components. However, it was important to confirm experimentally if the presence of a magnet would induce an unexpected magnetic field onto the components or impact the reading of the sensor by some other means. The aim of this study was to show if the addition of a metal (CoCr) femoral head component, would influence the magnetic field of the magnet thus changing the output of the sensor.

4.9.1 Methods

The experimental method described in sections 4.7 and 4.8 was repeated with a metal (CoCrMo alloy) femoral head component pressed onto the 3D printed stem. This meant the magnet was located at the taper hole face of the femoral head and so surrounded by CoCrMo material. The experiment was performed using a single sensor and magnet configuration (Sensor C and Magnet 1). The magnetic field data gathered was then compared to the data gathered from the corresponding magnet and sensor configuration from the previous experiment presented in sections 4.7 and 4.8 where the magnet was exposed. Figure 52 shows the previous experimental setup presented (in sections 4.7 and 4.8) and the experimental setup with the addition of the metal (CoCrMo) femoral head.

Figure 52 – Sensor verification experimental original setup (LEFT) including a 3D printed stem component (with fitted magnet) mounted to a UR3 robot arm position above an mlx90393 Triaxis magnetometer sensor held in a 3D printed mount and the same setup fitted with a metal femoral head (RIGHT).

4.9.2 Results

Box plots of the error between the simulated magnetic field vector and the transformed sensor recorded magnetic field vector for the exposed magnet and the magnet within the femoral head, are shown in Figure 53. Each box and whisker represent the distribution of the error gathered during the fifth experimental run that was performed for each of the experiments.

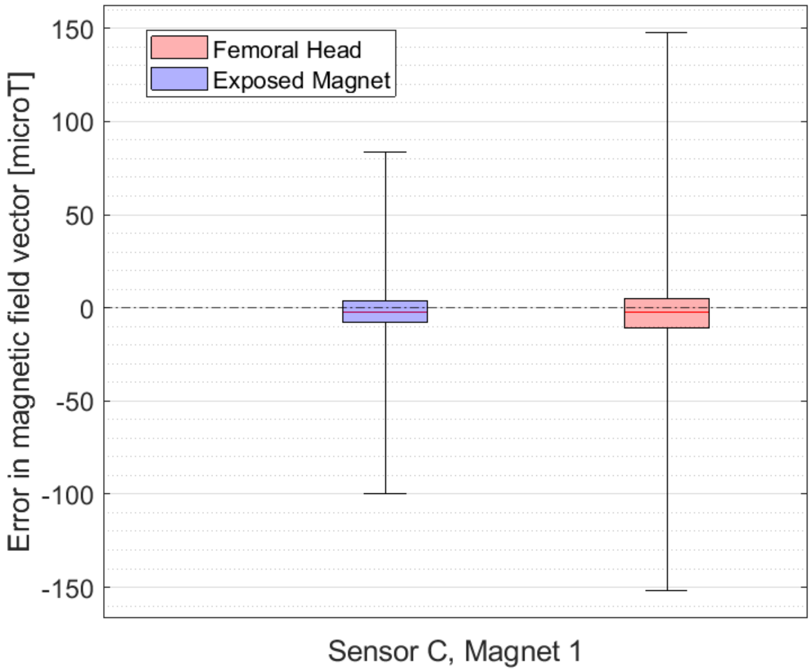

Figure 53 - Error in the sensor recorded transformed magnetic field vector when compared to the simulated magnetic field data for the exposed magnet and magnet within the femoral head. The magnet was translated by ±10mm from the magnet starting position (0,0,28)mm whilst the sensor was positioned at the origin (0,0,0)mm SensorC_mag1 refers to sensor C out of the four possible [C, D, E & F] and mag1 refers to the first magnet out of the four.

4.9.3 Discussion

The aim of this study was to show if the addition of a metal (CoCrMo) femoral head component, would influence the magnetic field of the magnet thus changing the output of the sensor. The results show that the magnetic field response produced by the sensor when the magnet was exposed and when the magnet was within the femoral head are comparable.

The outcome of sections 4.7 and 4.8 showed that the experimental setup was very sensitive to the positioning of the components when they were swapped out between magnet and sensor testing conditions. Although, this experiment used the same magnet (Magnet 1) and same sensor (Sensor C) for the tested conditions they were not performed immediately after each other. Hence, the tolerances of the 3D printed components could have resulted in errors in the positioning of the components when the magnet and sensors were loaded and re-loaded into the 3D printed components thus explaining the level of variance. Therefore, it was deemed that the level of variance was acceptable for this work and that it should be assumed that the presence of the metal (CoCrMo) femoral head has no impact on the magnetic field of the magnet. However, to prove this conclusively a more accurate and reliable method of measuring magnetic field would be needed.

4.10 Summary

The aim of this Chapter was to explore a method of simulating magnetic field data, develop calibration routine for a magnetometer and validating the simulated data produced against the output of a 3-axis magnetometer. It can be concluded that the simulations can produce valid and accurate data representing the magnetic field of a magnet. Therefore, it is sufficient as a method for generating reference datasets for use in a numerical inversion of magnetic field approximations tracking method. Furthermore, the selected magnetic field sensor produces accurate magnetic field data and the selected N42 neodymium magnets have an acceptable level of variation in their magnetic field which is also not impacted by the presence of the metal (CoCrMo) THR components. However, this study has highlighted the need for a two-stage calibration routine. Firstly, correcting for soft and hard iron influences and secondly using Procrustes transformation to account for mechanical errors in the positioning and alignment of the magnet, the sensor and the associated components. The Earth's latent magnetic field (approx. 40-60µT) was not included in any of the simulation work or accounted for during development and testing of the MPO sensing system. The sensor was stationary throughout testing and the output zeroed before every experimental test. Therefore, the Earth's latent magnetic field didn't have any impact on the results presented in this thesis.

Chapter 5 Development of a magnetic position and orientation sensing system for measuring orientation and impingement in total hip replacement components

A magnetic position and orientation (MPO) sensing system typically includes a permanent magnet and magnetic field sensor. The magnet can move independently to the magnetic field sensor and the change in relative magnet position changes the magnetic field at the location of the sensor. If configured appropriately each defined magnet position or orientation of interest (state) exerts a unique magnetic field on the sensor. A function is then used to “invert” the sensor read magnetic field data into the desired output namely, the position and orientation state of the magnet. MPO sensing systems have been used to measure linear displacement (Ortner et al., 2018), one degree of freedom (DoF) orientation (Melexis, 2021), two DoF orientation (Lutz. and Foletto., 2019), three DoF orientation (Ermakova et al., 2018; Lumetti et al., 2020; Malagò et al., 2020) and a three DoF tactile force sensor (Jones et al., 2020). US Patent (US7195645B2) refers to a MPO sensing system enabled THR implant which could measure changes in the joint space and so be used to determine the progression of implant bearing component wear. Arami et al,. (2011) developed an instrumented knee implant which featured three three-axis anisotropic magnetoresistance sensor embedded within the polyethylene insert and a permanent magnet positioned in the femoral component of the knee replacement. They used a neural network to map the sensor recorded magnetic field data to the 15 orientation states of combined flexion/extension and abduction/adduction rotation (sagittal plane angle range 138º to 192º and coronal angle range -8º to 4º). They reported a root mean squared error and maximum absolute error of 2.35º and 5.4º in flexion/extension angle and 0.31 º and 0.93º in abduction/adduction angle. A generalised summary of the applicable magnetic position and orientation sensing systems discussed in this thesis is shown in Table 8.

Matching magnetic field sensor output to the position and orientation of a permanent magnet can be achieved by solving inverse magneto static problems yet the complexity of these equations would make their use in real-time sensing applications unfeasible (Balaban et al., 2018; Malagò et al., 2020). At present, if the MPO consists of more than two DoF or complex magnet motions then numerical inversion of magnetic field approximations (NIMA) remain the more computationally and time efficient solution, and could be realised with the use of look up tables and predictive models based on pre-computed values (Malagò et al., 2020). Examples of tracking methods used in conjunction with MPO sensing systems include look-up tables (Ermakova et al., 2018; Lumetti et al., 2020; Malagò et al., 2020), ratio responsivity tracking (Lutz. and Foletto., 2019), trigonometric functions to measure heading and orientation (Melexis, 2021), trigonometric functions to measure linear displacement (Ortner et al., 2018) and neural networks (Arami et al., 2011; Jones et al., 2020).

Each position or orientation state of the reference magnet must exert a unique magnetic field on to the magnetic field sensor. This would make the system complete in that each magnet position leads to a unique output from the magnetic field sensor and so allowing each magnet state to be identified and differentiated. As such the fidelity of a NIMA method is dependent on the minimal magnetic field difference ΔB between the system's defined position and orientation states. This now becomes an optimisation problem based on the constrained and variable systems parameters (geometry of the THR components and size, shape, and material of the magnet) and the required range and resolution of the mechanical motion. Therefore, development of a MPO requires selection of tracking method and choosing optimal layout/configuration of the system judged on factors such as accuracy, reliability and computational efficiency.

Table 8 – Generalised summation of magnetic position and orientation sensing systems discussed throughout this thesis.

Authors, Application & source.	**Position or Orientation measured & Sensing range and total states/conditions**	**Notes**
Ortner et al. (2018) Linear displacement Simulation & Experimental study.	Linear position in a single axis 100mm range, continuous	Used atan2 trigonometric function to match linear position of array of arranged magnets to 3 axis mag field senor readings.
Melexis (2021) Rotary position sensor Application note.	Absolute rotary position about central z axis 0° to 360°, continuous.	Suggest using atan2 function to evaluate the magnetic field vector's heading angle (and so magnet's heading angle) using the sensor read Bx and By components.
Lutz and Foletto (2019) Joystick Application note & simulations.	Orientation to 2 DoF Tilt range 0° to 25°, continuous.	Described MPO system for measuring joystick stem tilt angle using responsivity function and presented results of simulated optimisation studies.
Research group lead by Michael Ortner including publications: *1.) Ermakova et al.* (2018) *2.) Lumetti et al.* (2020) *3.) Malago et al.* (2020) All developing multimedia control element/joystick All simulation and experimental studies.	1.) Orientation to 3 DoF 5 tilt states & 28 rotation states over 360° range so total 140 states. 5° max tilt and 360°/28 = 12.85° in rotation. 2.) Similar configuration as 1.) 5 tilt states & 180 rotation states over 360° range so total 900 states. 10° max tilt and 360°/180 = 2° in rotation. 3.) Rotation range -30° to 30° step size 2.5°, tilt angle 2° to 15° step size 1° and azimuth angle 0° to 360° step size 8°. So total states 16,200.	Described MPO sensing system for measuring joystick orientation to 3DoF using look-up table function and presented results of simulated optimisation studies.
Jones et al. (2020) 3 DoF tactile force sensor Simulation & experimental study.	Position of magnet to 3 DoF in XYZ direction. Z direction 0 to 0.8mm & XY −0.8 to 0.8mm at increments of 0.05 mm..	Magnet embedded within elastomer material positioned above 3-axis magnetic field sensor. Force applied to elastomer displaced magnet thus change in recorded magnetic field was equated (using neural network) to applied force. Resulting prototype had a pressure sensing range of up to 45KPa normal and 6KPa shear.
US Patent (US7195645B2) (2007)	Joint space of a hip prothesis (I.e. Linear position in a single axis)	Magnet and sensor positioned separately on either side of the joint and used to measure changes in the joint space to determine penetration of femoral head into liner component and indicate wear rate of bearing surfaces.
Arami et al (2011; 2013; 2014) Sensor enabled total knee replacement Experimental studies.	Orientation to 2 DoF of total knee replacement Sagittal plane angle range 138º to 192º and coronal angle range -8º to 4º with 15 total orientation states..	Positioned 3 three-axis anisotropic magnetoresistance sensor embedded within the polyethylene insert of total knee replacement and magnet in the femoral component. Used a neural network to associate magnetic field values to orientation of the components in 2 planes i.e. flexion/extension & abduction/adduction.

MPO systems are increasingly being used to track the motion of “joysticks” for use as user interface and multimedia control elements (Ermakova et al., 2018; Lutz. and Foletto., 2019; Malagò et al., 2020). The motion of a joystick is comparable to that of a ball and socket joint and so comparable to the motion of a THR assuming perfect spherical motion and no component translation. Using the same notation described in Section 4.2.1 the desired sensing range of the THR components are 0° to 360° in the rotation angle [φ] direction, 0° to 66° in the tilt angle [θ] direction (66° is the maximum stem tilt angle at which component contact occurs and so is the working tilt angle range of the components) and 0° to 360° in the azimuthal angle [ψ] direction, as summarised in Figure 30

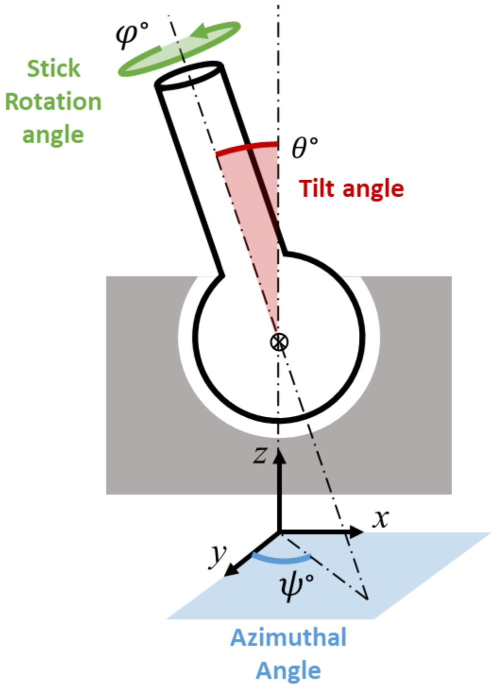

Repeat of: Figure 30 - Orientation defining angles of a joystick: stick rotation angle [φ], tilt angle [θ] and azimuthal angle [ψ]. Adapted form: (Malagò et al., 2020a).

The MPO developed in this work used a single three axis magnetic field sensor, the same as used in Section 4.6.2. This significantly simplified the system furthermore, the introducer hole (which typically appears once per implant) identified as a favourable location for a sensor was limited in size and only one of the chosen sensor boards available during this work could fit. Examples of single sensor, single magnet sensing systems include (Ermakova et al., 2018; Lutz. and Foletto., 2019; Jones et al., 2020; Malagò et al., 2020). The selected magnetic field sensor is limited to three DoF (giving magnetic field as [Bx, By, Bz]) therefore output of the MPO sensing system will be constrained to three DoF or less. Determination of two DoF orientation is an achievable outcome when using a single three DoF magnetic field sensor and requires an assumption to be made. When orientation of the stem (magnet) is being measured it will be assumed that the motion is spherical, and the centre of rotation of the femoral head and acetabular cup remain aligned. Only measuring orientation to two DoF will mean the orientation of the components cannot be determined however, it will still be worthwhile to know the orientation of the stem to two DoF. For example, if the measured stem angle exceeds that of the normal working range of the components, then it can be inferred that impingement has occurred and that the stem has contacted the rim of the liner. This could be incorporated as a subprogram in the software of the tracking system as a means of measuring the occurrence of an impingement event.

This chapter presents development of a MPO for two DoF orientation tracking of THR components. The work required exploring different methods of matching the sensor read magnetic field data to orientation and position of the stem component. Different configurations of magnet shape and location were simulated and evaluated in order to select which implementation would give optimal sensing performance. A final prototype was manufactured from a clinically available implant component and the performance of the MPO sensing system was validated experimentally.

5.1 Objectives

1. Investigate MPO tracking methods for converting magnetic field into the desired output values (THR component orientation).
2. Optimise the layout of the MPO sensing system for improved THR component **orientation** sensing performance.
3. Experimentally characterise the performance of the MPO sensing system when measuring the two DoF orientation of the stem component.

5.2 Magnetic field responsivity to magnet tilt and trigonometry for two degrees of freedom orientation tracking

Typically, in a magnetic sensor enabled joystick a magnet is positioned at the lower end of the stick (below the pivot point or centre of rotation) with a sensor positioned in the base of the joystick beneath the sensor, as shown in Figure 54. As the stick is tilted away from the central axis the magnet is translated in the XY plane which in turn changes the magnetic field at the site of the magnetic field sensor. This increases the sensed signal in the XY plane and correspondingly decreases the sensed signal in the Z direction. This relationship of magnetic field responsivity to magnet tilt angle has been used by Lutz and Foletto (2019) to track the tilt angle of the joystick using direct and ratio tracking methods which will be discussed and investigated in the following section.

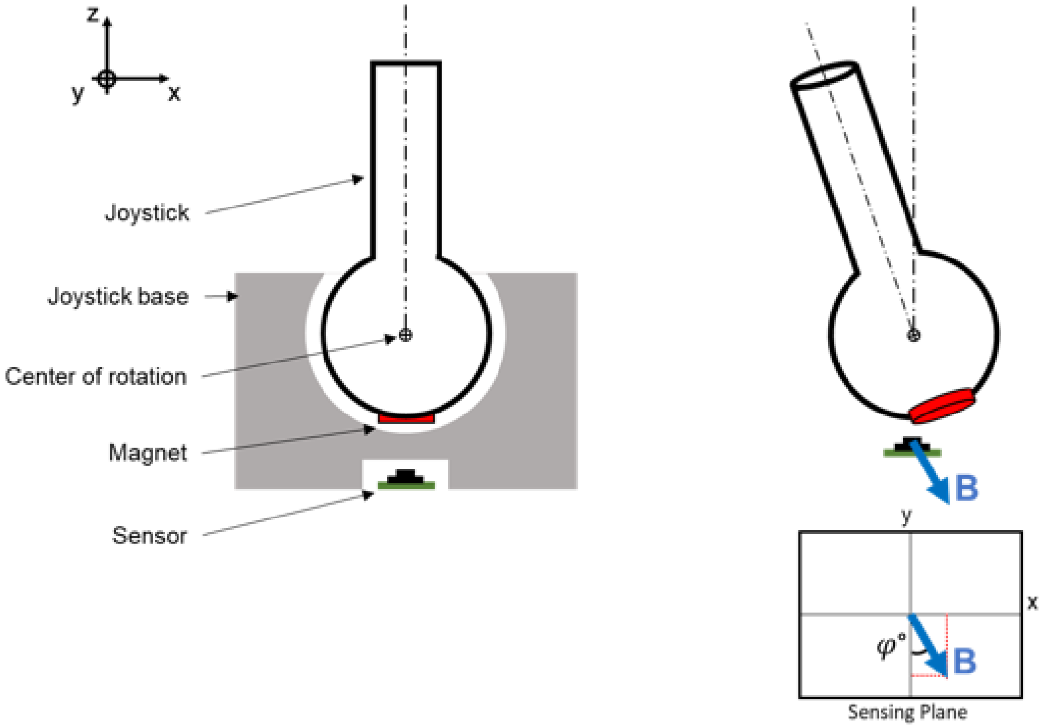

Figure 54 - Typical implementation of a magnetic sensing system in a joystick. In which increased stick tilt angle increases magnitude of sensed signal in the XY sensing plane and projection of the sensed magnetic field vector in the XY sensing plane is indicative of the azimuthal angle of the stem. Adapted form: (Lutz. and Foletto., 2019).

As shown in Figure 54, the projection of the magnetic field vector on the XY sensing plane reflects the azimuthal angle of the joystick. Therefore, the azimuthal angle can be calculated as follows:

$$Azimuthal\ Angle\ (\psi) = arctan(B_y, B_x)$$

Where if the stem azimuthal angle is 0° it is aligned with the positive X axis and when it is 90° it is aligned with the positive Y axis, as represented in the diagram shown in Figure 55. The inverse tangent function has been suggested by Melexis (the manufacturer of the selected 3 axis magnetometer mlx90393) for tracking the rotary position and heading of a magnet in a position sensor application (Melexis, 2021). Use of trigonometric functions is advantageous as they are simplistic to implement using in-built functions, requires minimal memory on an embedded system and are faster compared to look up table functions (Ortner et al., 2018).

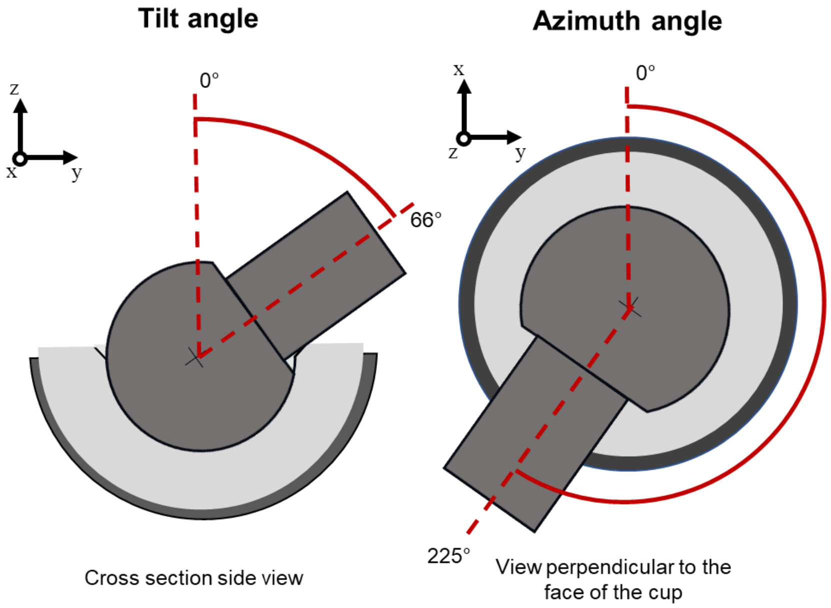

Figure 55 – Diagram detailing the defining angles used to describe total hip replacement femoral neck orientation Tilt and Azimuth angle.

5.2.1 Magnetic field responsivity to track magnet tilt angle

Lutz and Foletto (2019) investigated two methods for tracking the orientation of a joystick with a reference magnet and magnetic field sensor in a similar configuration to the present system (Figure 41). They described a simulated magnetic sensor enabled joystick. which had a ball joint of 10mm diameter, “air gap” (distance between the sensor and magnet) ranging from 0.9mm to 1.6mm and used a disc magnet of diameter 5.4mm, height 1mm and Br 1T, which could be tilted to a maximum of 25°.

Their first method which they called direct stick tracking which essentially returns a value **R,** representative of the distance the magnet is displaced in the XY direction and is represented as:

$$\boldsymbol{R} = \sqrt{{B_x}^2 + {B_y}^2}$$

A second method described by Lutz and Foletto (2019) is ratio stick tracking in which the B_x and B_y terms are replaced with $\frac{B_x}{B_z}$ and $\frac{B_y}{B_z}$ thus making the $\mathbf{R}_{\mathbf{ratio}}$ term:

$$R_{ratio} = \sqrt{\left(\frac{B_x}{B_z}\right)^2 + \left(\frac{B_y}{B_z}\right)^2}$$

The **R** and **R_{ratio}** values were evaluated over the tilt angle range of 0° to 66° for the present system and are shown in Figure 56 and Figure 57. Simulated data was used and produced using Magpylib Python package (Version: 4.0.0b2, Author: Michael Ortner) (the simulation method is described in further detail in Chapter 4) with the magnet configuration shown in (chapter 4). The simulated stem (and attached magnet) was incrementally rotated the by 1º over the full range of tilt angles (0° to 66°). The response of **R** is linear up to 25° (the maximum tilt angle Lultz and Foletto investigated) after which the trend becomes nonlinear. Direct stick tracking would not be suitable as above a tilt angle of 45° the **R** value reaches its peak and begins to decline. This means the system is non-unique as multiple tilt angle states produce the same responsivity value. Up to a tilt angle of 45° the **$\mathbf{R}_{\mathbf{ratio}}$** value is less than 1.0 and the trend is close to linear. For tilt angles greater than 45° the **$\mathbf{R}_{\mathbf{ratio}}$** is nonlinear and increases exponentially. This is a similar response to that reported by Lutz and Foletto who noted that for higher tilt angles i.e., >45° for the present system, the precision of the system is greater as the responsivity is steeper.

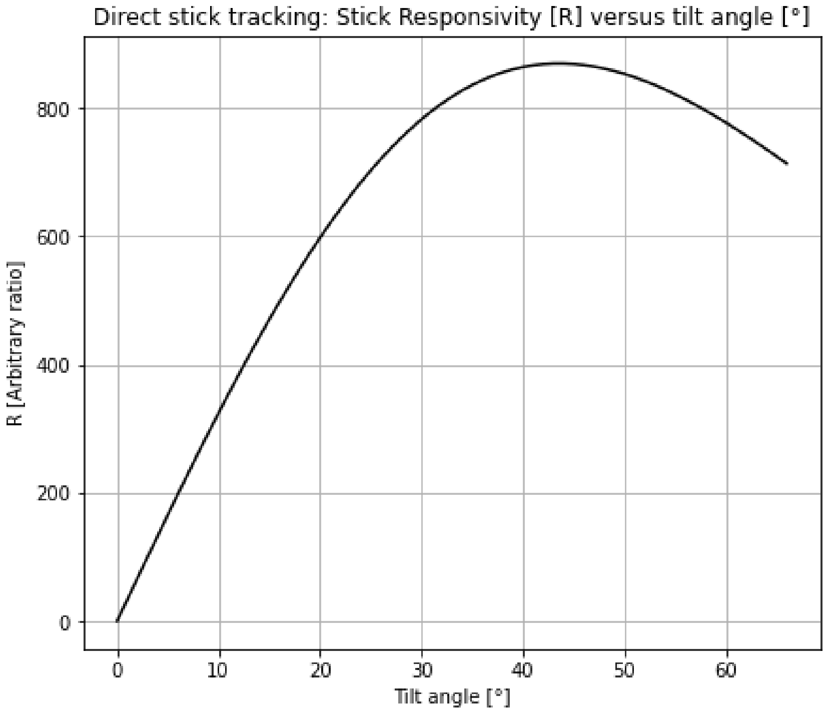

Figure 56 - Direct stick tracking method showing stick responsivity R versus tilt angle.

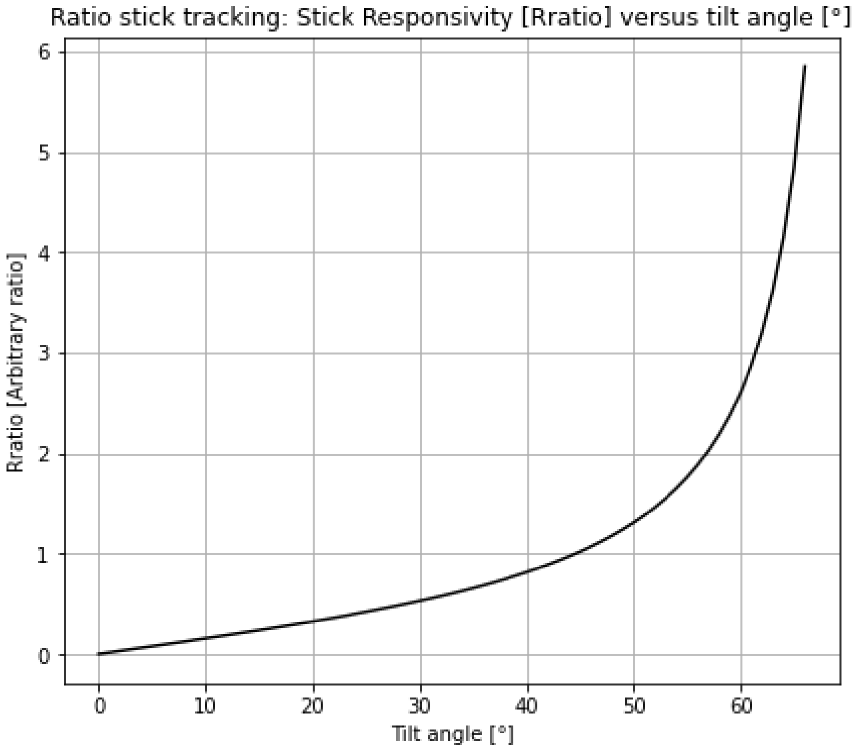

Figure 57 - Ratio stick tracking method showing stick responsivity R_{ratio} versus tilt angle.

As stem tilt angle increases the sensed signal in the Z direction (Bz) decreases additionally the distance the between the magnet and sensor increase which causes the magnitude of the magnetic field vector (|B|) to decrease. The Bz and |B| versus the full range of tilt angles (0° to 66°) are shown in Figure 58. Both the Bz and |B| have complete relationships over the full range of tilt angle making them suitable candidates for responsivity tracking methods. However, in the low tilt angle range <10° the gradient of the |B| and Bz slopes is comparatively low. Upon closer examination a 1° change in tilt angle from 0° to 1° elicits a change in Bz of 0.923 microT whereas the same step of 1° from 65° to 66° elicits a change in Bz of 27.6 microT. This difference in state separation means that the fidelity of the system, namely the system’s ability to differentiate between the tilt angle states, is higher at the top end of the tilt angle range >60° and reduced at the low tilt angle range <10°. This is an undesirable characteristic and instead it would be preferred that the states separation of the system be consistent over the full angle range which would be the case for a stick tracking method that returns a linear response.

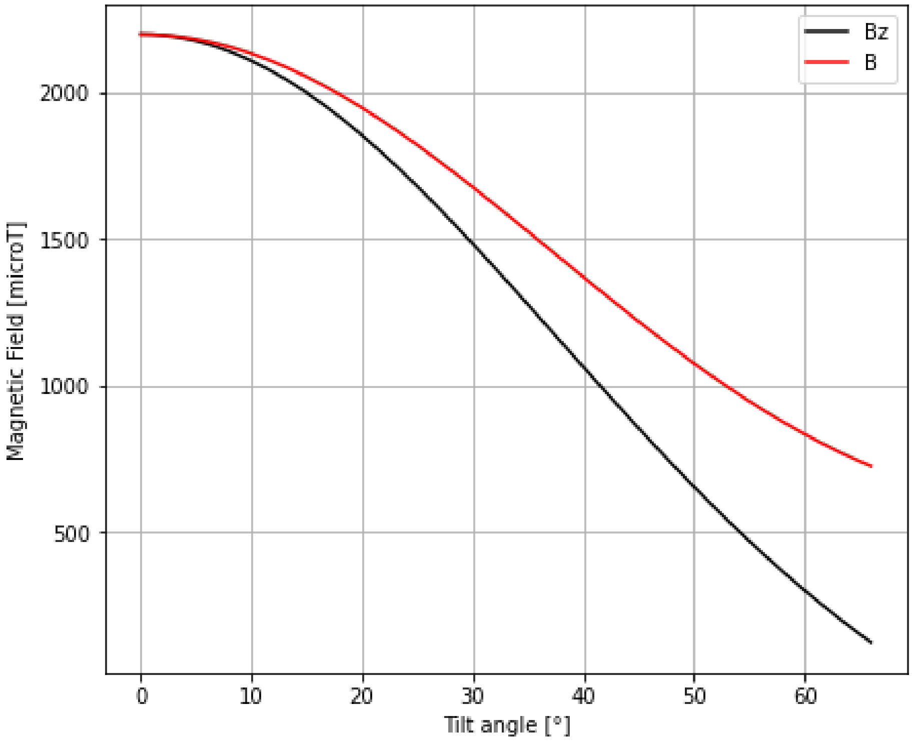

Figure 58 - Magnetic field strength in the Z axis and magnetic field vector versus tilt angle

An alternate method of calculating a ratio responsivity (not described by Lutz and Foletto) uses the |B| instead of Bz. This makes the responsivity term:

$$R_{ratioBMagnitude} = \sqrt{\left(\frac{B_x}{|B|}\right)^2 + \left(\frac{B_y}{|B|}\right)^2}$$

The ratio responsivity **$R_{ratioBMagnitude}$** versus the tilt angle range of (0° to 66°) for the present system is shown in Figure 59. The response is close to linear for the full range of tilt angles (0° to 66°) with the gradient beginning to slow after a tilt angle of 60°.

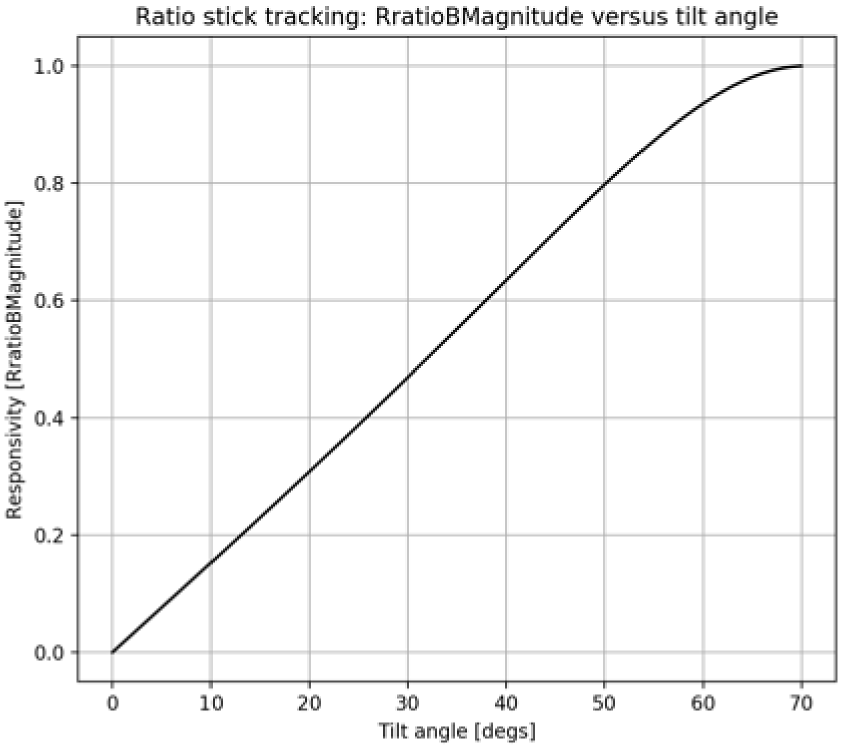

Figure 59 - Ratio stick tracking method showing stick responsivity $R_{ratioBMagnitude}$ versus tilt angle.

5.2.2 Responsivity tracking method selection

Lutz and Folletto performed an analysis to investigate the effect the "air gap" (the distance between their magnet and sensor) had on the values of **R** and $\mathbf{R_{ratio}}$ for their simulated joystick. They concluded that the superposition of the $\mathbf{R_{ratio}}$ curves at the different air gaps showed airgap had little effect on the response of $\mathbf{R_{ratio}}$ (Lutz. and Foletto., 2019). In their scenario air gap was a system parameter that could be varied in the present work this is a constrained variable. A similar analysis was performed for the present system but instead the change in distance between the magnet and sensor was replicating potential mounting errors of the components (magnet or sensor) or the femoral head component displacing out of the liner. If like Lutz and Foletto the responsivity curves show superposition (i.e. similarity) at different magnet displacements then

Simulations of the four responsivity methods including **Bz**, **|B|**, $\mathbf{R_{ratio}}$ and $\mathbf{R_{ratioBMagnitude}}$ were repeated with the magnet and centre of rotation being displaced in the X and Z axis by ± 1mm, 2mm & 3mm in turn. This replicates the stem’s centre of rotation being displaced away from the cup’s centre of rotation. The R method was not investigated as it was previously determined that it would be unsuitable as a tracking method as it returned and incomplete response.

The graphs of the four responsivity curves **Bz**, **|B|**, **R_{ratio}** and **$R_{ratioBMagnitude}$** for stem displacement in the Z axis and X axis are shown in Figure 60 a, b, c & d and Figure 61 a, b, c & d, respectively. The coefficient of determination (R2) was calculated to evaluate the agreement of the responsivity methods at the original stem location and at the subsequent stem displacements in the Z axis and X axis are shown in Table 9 and Table 10, respectively.

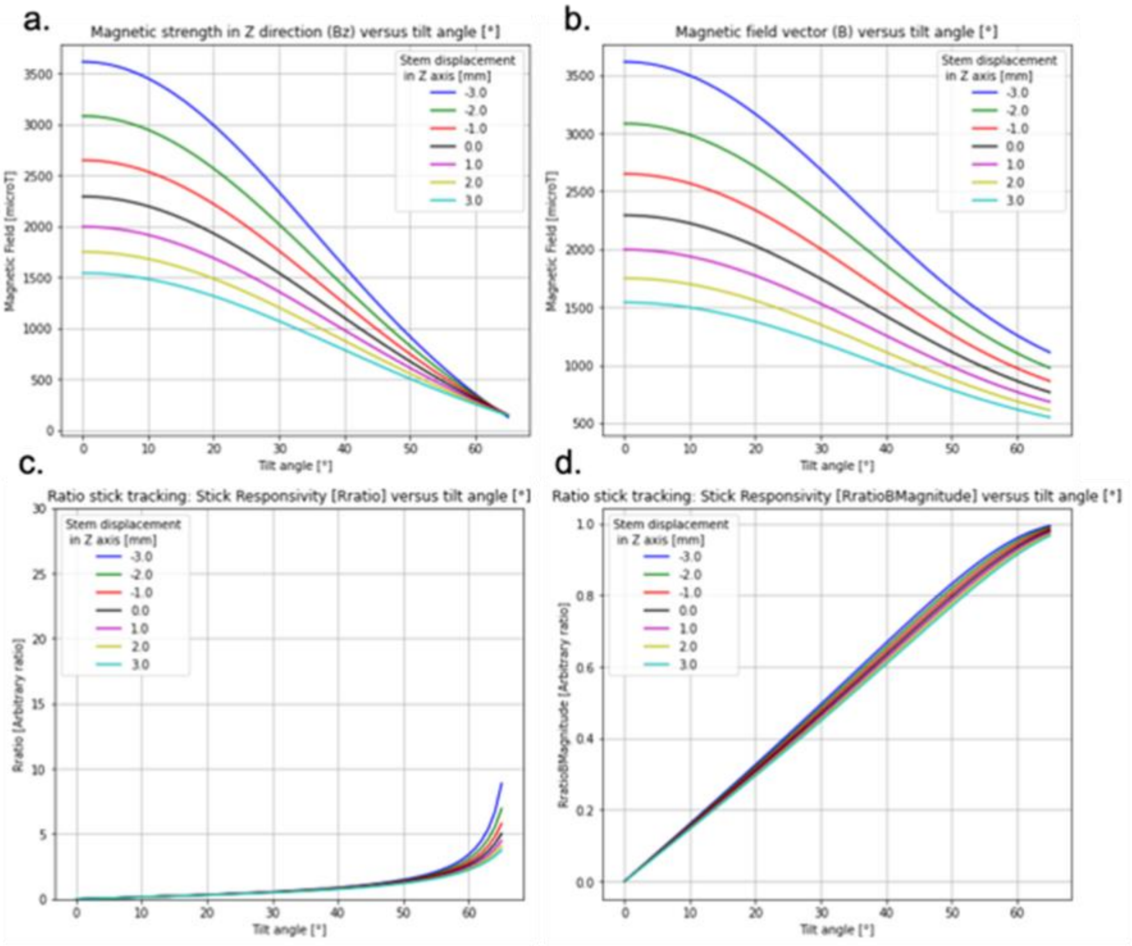

Figure 60 - Stick Responsivity of a. magnetic field strength in Z, b. magnetic field vector, c. R_{ratio} and d. $R_{ratioBMagnitude}$ versus tilt angle for stem displacements of -3mm, -2mm, -1mm, 0mm, 1mm, 2mm and 3mm in the vertical (Z axis) from the centre of rotation ((0mm,0mm,26.5mm).

Table 9 - R^2 for the Responsivities at the original stem position and Responsivities at -3mm, -2mm, -1mm, 0mm, 1mm, 2mm and 3mm in the vertical (Z axis) from the centre of rotation (0mm,0mm,26.5mm)

		R^2			
		Bz	**|B|**	**R_{ratio}**	**$R_{ratioBMagnitude}$**
Displacement in Z [mm]	-3	-0.4010	-2.355	0.6070	0.9935
	-2	0.4952	-0.2069	0.8920	0.9973
	-1	0.8963	0.7525	0.9814	0.9994
	0	1.0000	1.0000	1.0000	1.0000
	1	0.9276	0.8276	0.9895	0.9994
	2	0.7544	0.4157	0.9667	0.9979
	3	0.5272	-0.1239	0.9388	0.9956
Mean		0.6000	0.0443	0.9108	0.9976

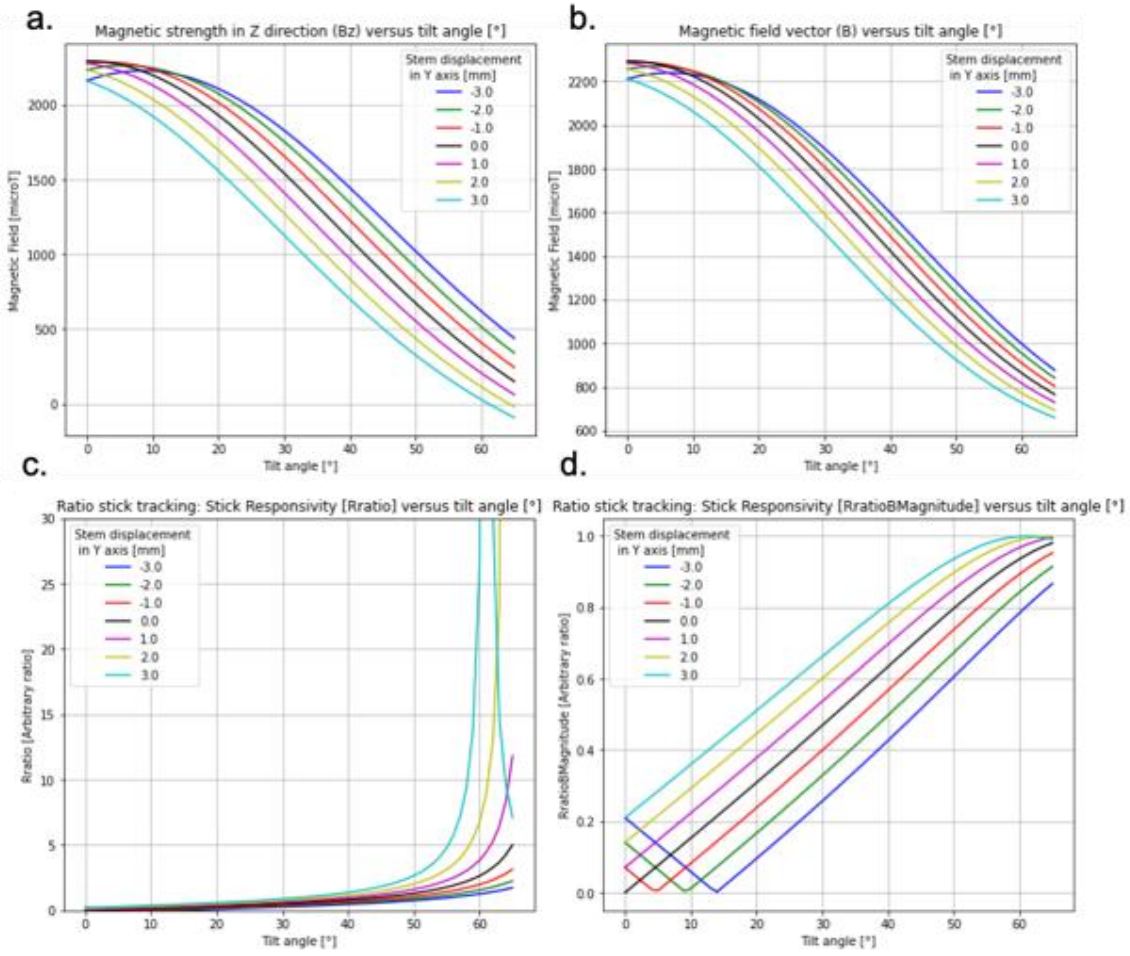

Figure 61 - Stick Responsivity of a. magnetic field strength in Z, b. magnetic field vector, c. R_{ratio} and d. $R_{ratioBMagnitude}$ versus tilt angle for stem displacements of -3mm, -2mm, -1mm, 0mm, 1mm, 2mm and 3mm in the Lateral (X axis) from the centre of rotation (0mm,0mm,26.5mm).

Table 10 – R^2 for the Responsivities at the original stem position and Responsivities at -3mm, -2mm, -1mm, 0mm, 1mm, 2mm and 3mm in the lateral (X axis) from the centre of rotation (0mm,0mm,26.5mm)

		R^2			
		Bz	**|B|**	**R_{ratio}**	**$R_{ratioBMagnitude}$**
Displacement in X [mm]	-3	0.8600	0.9369	0.4280	0.6274
	-2	0.9305	0.9670	0.6333	0.8298
	-1	0.9807	0.9903	0.8515	0.9565
	0	1.0000	1.0000	1.0000	1.0000
	1	0.9772	0.9873	-0.1355	0.9580
	2	0.9027	0.9428	-248	0.8413
	3	0.7701	0.8578	-1920	0.6643
Mean		0.9173	0.9546	-309.2672	0.8396

The Bz and the |B| stick responsivities are the most sensitive to errors induced by movements in the Z axis. $\mathbf{R_{ratio}}$ is robust up to a tilt angle of 45° but the exponential rise in value has led to a large amount of variation at the top angle range. The same can also be said of $\mathbf{R_{ratio}}$ when displacement occurs in the XY plane. $\mathbf{R_{ratioBMagnitude}}$ is the most robust to displacements in the Z axis with all tested displacements producing a linear relationship and the associated R^2 values all being over 0.9935. The |B| stick responsivity is the most robust to displacements in the lateral axis with a mean R^2 value of 0.9546 closely followed by the Bz responsivity with a mean R^2 value of 0.9173 and $\mathbf{R_{ratioBMagnitude}}$ at 0.8396. These results suggest that the $\mathbf{R_{ratioBMagnitude}}$ will be less effected by errors due to stem displacements and will be able to report stem tilt angle accurately when the femoral head is separated from the liner bearing surface.

5.2.3 Summary of direct and ratio stick tracking

The aim of these initial simulations was to find the more optimal stick tracking method for measuring stick tilt angle. The $\mathbf{R_{ratioBMagnitude}}$ function gives an almost linear response over the full angle range and was shown to be better (less susceptible to positioning errors in Z & X directions) than the previous responsivity tracking method described by Lutz and Foletto (2019). Therefore, it is hypothesised that the combination of the $\mathbf{R_{ratioBMagnitude}}$ function and the inverse tangent function will enable tracking two DoF tracking of stem orientation.

5.3 Implementation of numerical inversions of magnetic field approximations tracking methods

Previous MPO sensing systems have used tracking or inversion methods such as look-up tables (Lumetti et al., 2020), ratio responsivity tracking (Lutz. and Foletto., 2019), trigonometric functions to measure heading and orientation (Melexis, 2021), trigonometric functions to measure linear displacement (Ortner et al., 2018) and neural networks (Jones et al., 2020). Three unique tracking methods were investigated including Look Up Table, ratio stick tracking and a

Neural Network. The focus of investigation in this work has been characterising the accuracy of the tracking methods at returning the correct position and orientation state when compared to the ground truth. Computational efficiency is another important factor when considering real-time implementation on an embedded system. In particular, the memory or storage demands of each method and the speed at which the method can return the position and orientation value. These factors were not investigated in the present work but were hypothetically considered in tracking method evaluations. The theory and optimisation of responsivity tracking has been previously discussed in Section 5.2. The remainder of this section introduces the theory behind the other methods and gives a description of how each of the three method was practically implemented.

5.3.1 Look Up Table – practical implementation

A look up table is the simplest type of tracking method explored in this work. In essence, the output of the sensor is read, and an algorithm searches the reference dataset and finds the closest magnetic field value. The corresponding position and orientation state stored within the dataset is returned. In this work simulated data was produced to populate the reference datasets using Magpylib Python package (Version: 4.0.0b2, Author: Michael Ortner) (the simulation method is described in further detail in Chapter 4) with the magnet and sensor configuration shown in (Chapter 4). The input of the simulation was a dataset of all the possible orientation states within the sensing range ($States_n$) i.e. tilt angle from 0° to 65° in steps of 1° and azimuthal angles from 0° to 359° in steps of 1°. The output of the simulation was a dataset of B values at every orientation state (B_n). The magnetic field strength Bx, By & Bz, for each magnet position of the simulated data set is shown in Figure 62 where each colour corresponds to a particular tilt angle state. Angle increments are shown in steps of 5° for clarity.

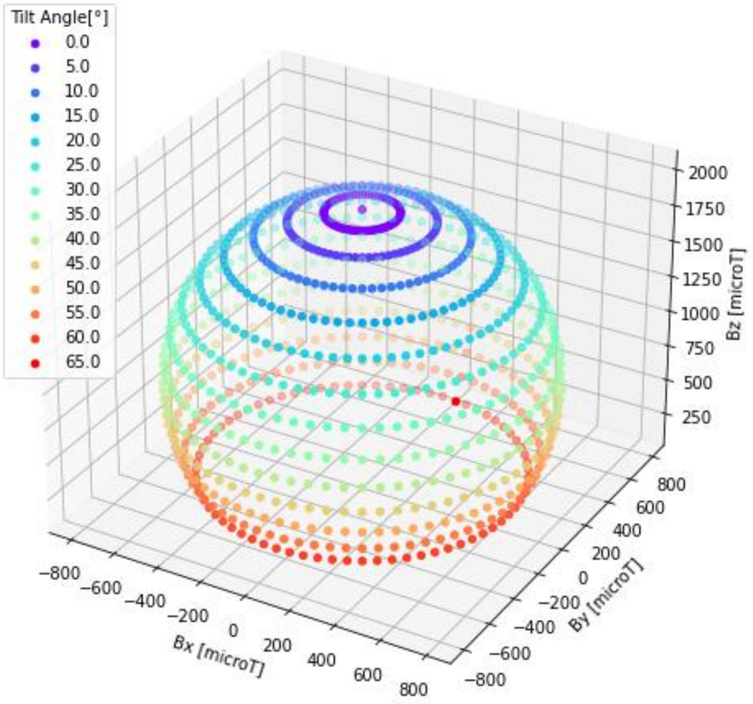

Figure 62 – Magnetic field strength Bx, By & Bz where each colour represents B over a full range of azimuthal angles at a given tilt angle. Tilt angle ranged from 0° to 65° with increments of 5° and Azimuthal angle ranged from 0° to 360° with increments of 5°.

Lumetti et al (2020) used a look up table as an inversion method for their three DoF multimedia control joystick which is a similar application to the present work. The computational efficiency of a look up table will progressively decrease as the size of the table increases. This is due to the speed it takes to run the algorithm (i.e. search the dataset) and the memory space required to store the reference data set B_n. The issue of operation speed and memory space may become more apparent with the addition of more degrees of freedom.

The look up table method was realised using a custom Matlab function, as shown in Appendix f). The function takes in the sensed magnetic field value and subtracts it from all the magnetic field values in the reference B_n dataset thus returning B_{diff} (which is the same length as the B_n and $States_n$ arrays). The index of the minimum difference is then found and used to return the corresponding position and orientation state stored in the $States_n$ array. Figure 62 shows that the data could be represented as a 3D curved surface which would allow estimation between the discrete simulated data values. The look up tables used throughout this work contained discrete values (e.g. angle step size of 1°) and so could only return discrete values. This would have affected the accuracy of the returned value however as the resolution of the look up table was comparable to the desired sensing resolution this was deemed sufficient for prototype development. Use of a parametric equation of a surface fitted to the B dataset could be explored in future work.

5.3.2 Ratio Stick Tracking – practical implementation

The ratio stick tracking (RST) method was realised using a look up table method like that described previously in section 5.3.1. The reference datasets had only 67 entries corresponding to the 67 degrees across the tilt angle range, hence the dataset was far smaller than the stand alone look up table. The azimuthal angle was then computed using the atan2(Y,X) function in Matlab where Y = By and X = Bx. This gave the the full 360° range of the azimuthal angle where if the stem azimuthal angle is 0° it is aligned with the positive X axis, when it is 90° it is aligned with the positive Y axis, when it is 180° it is aligned with the negative X axis and when it is 270° it is aligned with the negative Y axis.

5.3.3 Neural Network – practical implementation

Fitting the data using a neural network produced a function to relate magnetic field data B_n to the desired position and orientation state e.g. the tilt angle $[\theta]$ and azimuthal angle $[\psi]$. The resulting model required significantly less storage space when compared to look up table data set B_n and the model returning a value is likely to be faster than a look up table algorithm working with the sizes of B_n that are required for this work.

For tracking stem orientation to two DoF the MATLAB NNFit toolbox was used to train the neural network using a Levenberg-Marquardt backpropagation algorithm for training (Mathworks, 2021). The deep neural network structure included three hidden layers with 12, 12 & 12 neurons respectively and outputted tilt and azimuth angle a diagram of the NN structure is shown in Figure 63. The dataset was randomly divided amongst training 70% (samples), validation 15% (samples) and testing 15% (samples). This implementation of a neural network is similar to that used by (Jones et al., 2020) who developed a magnetic sensor enabled soft tactile force sensor. The chosen settings matched those suggested as standard by the MATLAB NNFit toolbox.

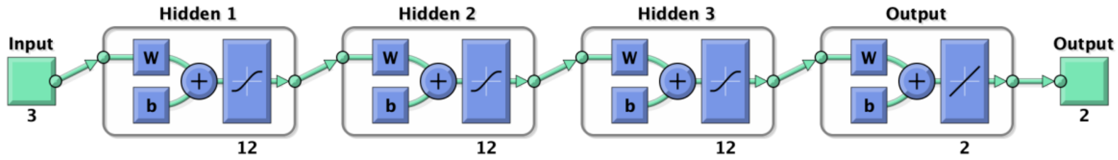

Figure 63 - Structure of the deep neural network with 3 neuron input layer (Bx, By, Bz), 12, 12 & 12 neuron hidden layers respectively and a 2 neuron output layer (tilt angle, azimuthal angle).

5.4 Simulated optimisation study 1: orientation tracking to two degrees of freedom magnet size and shape optimisation

The sensitivity of the magnetic sensing system is dependent on the step size between each state (which is a chosen system parameter) and the state separation (the extent to which the magnetic field values within the dataset are different). A system with a large state separation will be more adept at detecting changes in the position or orientation state of the magnet (Malagò et al., 2020).

Malago et al (2020) evaluated the minimum state separation of a MPO as a means of providing an estimation of the quality of a specific MPO implementation. They used this quality factor as a quantitative measure to guide the selection of the system parameters to optimise the performance of their MPO system. They affirm that a MPO system with a large quality factor is preferred as it is easier for the correct state or change in state to be determined and reduces the impact of background noise and other external factors. A similar optimisation approach was used in this work for the selection of the variable system parameters associated with each MPO implementation. For the MPO for 2DoF orientation tracking the system parameter being investigated is the size and shape of the reference magnet.

The working hypothesis presented here is that that the 8X2mm N42 Neodymium disc magnet (as used in the earlier in Section 4.7 Simulation method validation and sensor performance verification pilot study) would enable the best sensing performance. This is because the shape would mean the most amount of magnetic material is within the available space thus increasing the magnitude of the possible magnetic field. Additionally, the magnet is magnetised in the Z direction so the magnetised face of the magnet points toward the sensor. Both factors increase the magnetic field measured at the location of the sensor and are likely to directly increase the Q factor of this configuration. However, it is possible that an alternate magnet provides a greater Q factor and so warrants investigating.

5.4.1 Calculation of Quality Factor

To evaluate the minimum state separation or Qf_{min} of a B_n the nearest neighbour for each entry of the B_n is found. In simpler terms this takes each entry of the B_n and finds the closest other entry in the set, in terms of magnetic field vector distance this value will be referred to as the nearest neighbour magnetic field vector distance ($|_{NN}B|$). The Qf_{min} is then the minimum of the $|_{NN}B|$ evaluated for each entry of B_n. In this work the corresponding two closest orientation states were found, and the mean state separation (Qf_{mean}) was evaluated as the mean of $|_{NN}B|$ evaluated for each entry of B_n. This was achieved practically by using the scipy.spatial.KDTree nearest neighbour algorithm (Virtanen et al., 2020) which is the same as that described by Maneewongvatana and Mount (1999).

To validate the output of the algorithm the minimum nearest neighbour routine was performed on the B_n of the direct stick tracking from the magnetic field vector (B) previously described in Section 5.2.1. In this scenario for clarity, tilt angle states range from 0° to 65° in step of 5° and azimuthal angles range from 0° to 355° in steps of 5°. The magnetic field strength in the X, Y & Z direction (Bx, By & Bz) for each magnet position of the simulated data set is shown in Figure 62 where each colour corresponds to a particular tilt angle state. The result of the minimum nearest neighbour routine is a minimum magnetic field vector separation of 13.0μT which occurs between all states at a tilt angle of 5°. Inspection of Figure 62 shows that the spacing of the points at tilt angle of 5° is the smallest indicating that the minimum nearest neighbour of the B_n occurs when tilt angle is 5°. The difference in magnetic field vector between the orientation states s1 = [$\theta = 5°$, $\psi = 0°$] and s2 = [$\theta = 5°$, $\psi = 5°$] was computed using Equation 4, where B_{s1} = (0, 148.7, 1976.3) and B_{s2} = (-13.0, 148.1, 1976.3) were the magnetic field vectors when the magnet is in states s1 and s2 respectively. This returned a $|B_{diff}|$ value of 13.0µT thus confirming the function is working as expected.

$$|B_{diff}| = |B_{s1} - B_{s2}|$$

Equation 4

Jones et al (2020) used the arbitrary limit of 100 times earths latent magnetic field which equates to 6000µT (6mT) , as the lower bound for their sensing system. This was to limit errors to <1% when the orientation of the sensor changed. Ermakova et al. (2018) and Malago et al. (2020) developed systems with 5000µT (5mT) and 1000µT (1mT) state separations respectively. Initial simulations have shown that in the present scenario an MPO system with tilt angle step of 5° and azimuth angle step of 5°, results in Qf_{min} = 14.4 µT. Therefore, achieving comparable state separations seen in these examples is unlikely. This was expected as Ermakova et al. (2018) and Malago et al. (2020) had the magnet position closer to the sensor at an air gap of around 2 – 2.5mm. Therefore, the minimum alternative will be that Qf_{min} is greater than the sensitivity of the sensor i.e. 6µT in X&Y or 9.7 µT in Z.

5.4.2 Method: Simulated optimisations study 1

Optimisation study 1 investigated the effect of changing the reference magnet shape of the MPO for measuring orientation in two DoF. The magnet and sensor configuration used is the same as shown in Section 4.6.4. The simulated B_n data was produced by the same method described in Section 5.3.1 however, five angle step sizes (5º, 4º, 3º, 2º & 1º) were used to generate five B_n for each magnet with entries/sizes of 937, 1441, 2641, 5,941 & 23,761. A range of step sizes were used so that the effect of varying step size on Qf_{min} could be explored. Also, and more significantly it allowed evaluation of the level of sensitivity possible when given a predetermined Qf_{min} i.e. the sensitivity of the sensor being 6µT in X&Y or 9.7 µT in Z.

The array of magnets investigated were all able to fit within the maximum magnet space (12X4mm cylindrical region) and were selected from the stock of a supplier (Magnet Experts Ltd). Additionally, three hypothetical (hyp) magnets were also added to the array that were of conceivable shape and magnetisation direction. This included a N42 8X2mm diametrically magnetised (Di) disc magnet as the supplier stocked an N42 8X1mm (Di) disc magnet (which was included in the simulation) yet the larger magnet will have a stronger magnetic field due to the greater amount of magnetic material. The other two magnets where N42 7X7X2mm rectangle magnets the first magnetised in the Z direction the second in the X direction. These were selected as the 7X7X2mm dimension is the largest rectangle that can fit in the available space. Conceptually there are a few hypotheses that informed magnet selection for this investigation:

1. A disc magnet shape enables the most the most magnetic material to fit within the allowable space meaning the magnitude of the magnetic field will be the greatest. Therefore, the signal recorded by the sensor will be greater which could allow for better differentiation in the orientation states thus improving sensing performance.
2. For magnets magnetised in the Z direction, the magnetic field vector is pointing at the sensor meaning the magnetic field at the sensor location will be the greatest. Therefore, the signal recorded by the sensor will be greater which could allow for better differentiation in the orientation states thus improving sensing performance.
3. For magnets magnetised in the XY plane, the magnetic field is asymmetrical across the plane of the sensor this could allow for better differentiation of the orientation states rotating in that plane.

A summary of the investigated magnets, their dimensions, and the magnetisation direction, is shown in Table 11. For clarity the magnets will be referred to as M1 – M9.

Table 11 - Summary of the nine magnets investigated in the simulated optimisation studies where N42 is notation for the magnet material neodymium of grade 42, (Di) denotes the magnet is diametrically magnetised so in the X or Y direction and not along the central Z axis and (hyp) denotes the magnet was of hypothetical yet conceivable dimensions and magnetisation direction.

Magnet description	**Graphical display of magnet dimensions and direction of magnetisation**	**Magnet description**	**Graphical display of magnet dimensions and direction of magnetisation**
M1 Disc Magnet 8X2mm N42, Br 1300mT	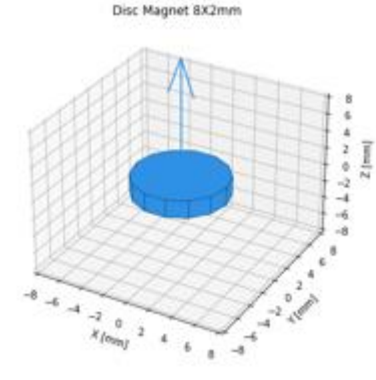	**M6** Rectangle magnet (DI) 2.5X7X2.5mm N42, Br 1300mT	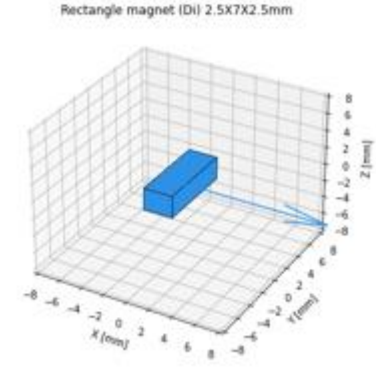
M2 Disc Magnet (Di) 8X1mm N42, Br 1300mT	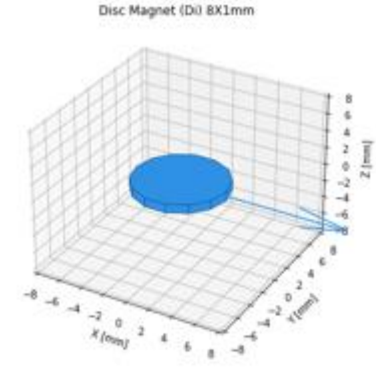	**M7** Rectangle magnet 10X3X2mm N42, Br 1300mT	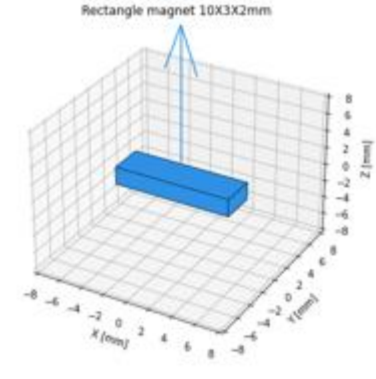
M3 Disc Magnet (Di)(hyp) 8X2mm N42, Br 1300mT	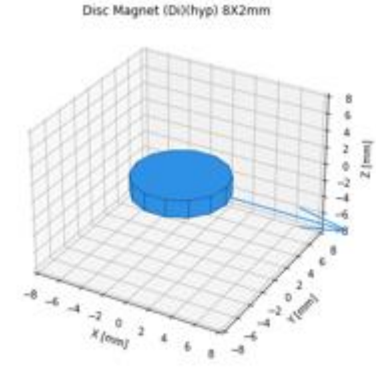	**M8** Rectangle magnet (hyp) 7X7X2mm N42, Br 1300mT	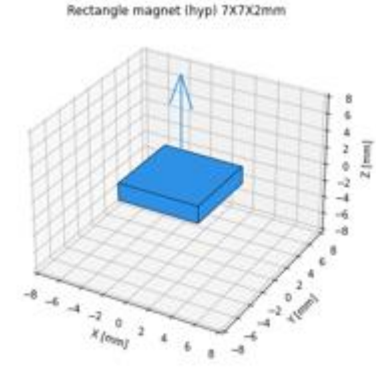

M4 Rectangle magnet 6X4X2mm N45H, Br 1340mT	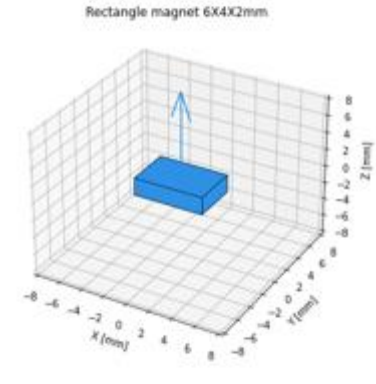	**M9** Rectangle magnet (Di)(hyp) 7X7X2mm N42, Br 1300mT	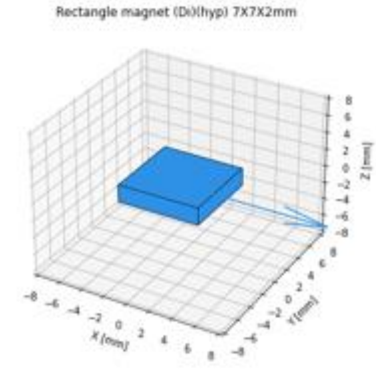
M5 Rectangle magnet 2.5X7X2.5mm N42, Br 1300mT	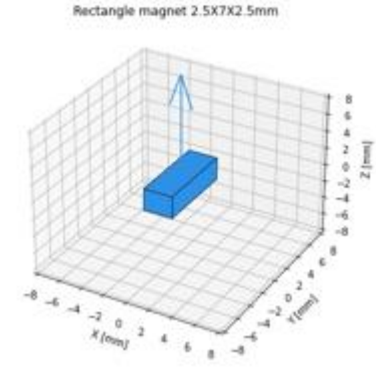		

5.4.3 Results: Simulated optimisations study 1

The Qf$_{\mathrm{mean}}$ and Qf$_{\mathrm{min}}$ evaluated from the B_n of the nine investigated magnets are shown in Figure 64 and Figure 65. The **M1** and **M8** magnet, had the two largest volumes of the investigated magnets at 100.5mm3 and 98mm3 respectively. When these two magnet shapes were magnetised so that the magnetised face of the magnet points towards the sensor the magnitudes of the magnetic field vector recorded at the sensor were the two largest values of all the investigated magnets at 1996.8μT and 1944.6μT respectively. This understandably resulted in the MPO implementations featuring these magnets returning the greatest Qf$_{\mathrm{mean}}$ of 10.4μT and 10.1μT, and Qf$_{\mathrm{min}}$ of 0.522 μT and 0.508 μT (at a step size of 1°) respectively. The **M8** magnet magnetised in the Z direction, cannot be selected for the prototype sensing system. Yet the inclusion in the optimisation study has confirmed the theory that the greater the magnetic field measured at the location of the sensor the greater the values of the resulting Qf$_{\mathrm{mean}}$ and Qf$_{\mathrm{min}}$.

A plot of the nearest neighbour magnetic field vector distances (|$_{\mathrm{NN}}$B|) when tilt angle increases by 1° starting at 0° for the M1 configuration is shown in Figure 66. The |$_{\mathrm{NN}}$B| when only azimuthal angle state changes from 0° to 1° at every tilt angle state is also shown in Figure 66. At every tilt angle state, $|_{NN}B|$ was constant across the full azimuthal angle range.

The key findings of this optimisation study are:

1. Decreasing the angle step size between the orientation states decreases the Qf_{mean} and Qf_{min}.
2. The **M1** magnet returned the greatest Qf_{mean} and Qf_{min} at every angle step size.
3. Magnets that were magnetised in the X direction (**M2, M3, M6** and **M9)** all returned the lowest Qf_{min}.
4. The $|_{NN}B|$ is constant when only azimuth angle changes yet varies when tilt angle is changed.

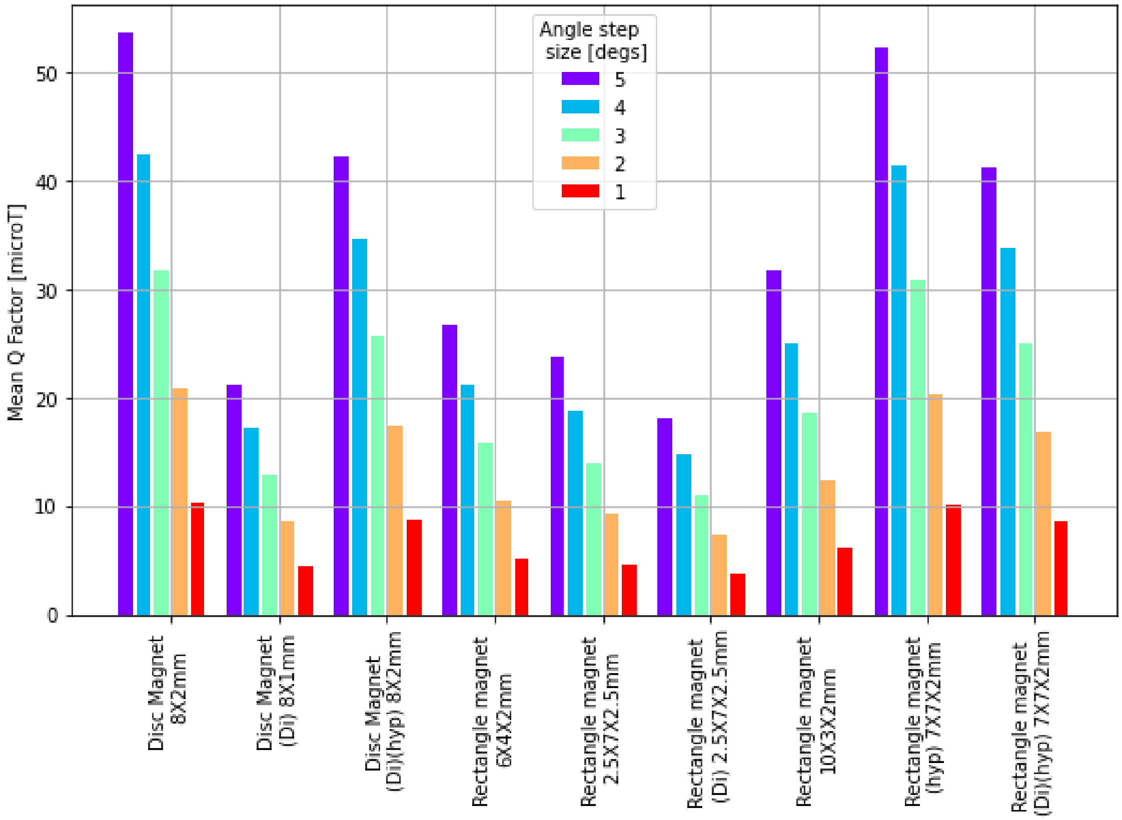

Figure 64 - Mean Q factor (Qf_{mean}) evaluated for optimisation study 1, orientation tracking to 2 DoF, magnet shape optimisation for the eight investigated magnets.

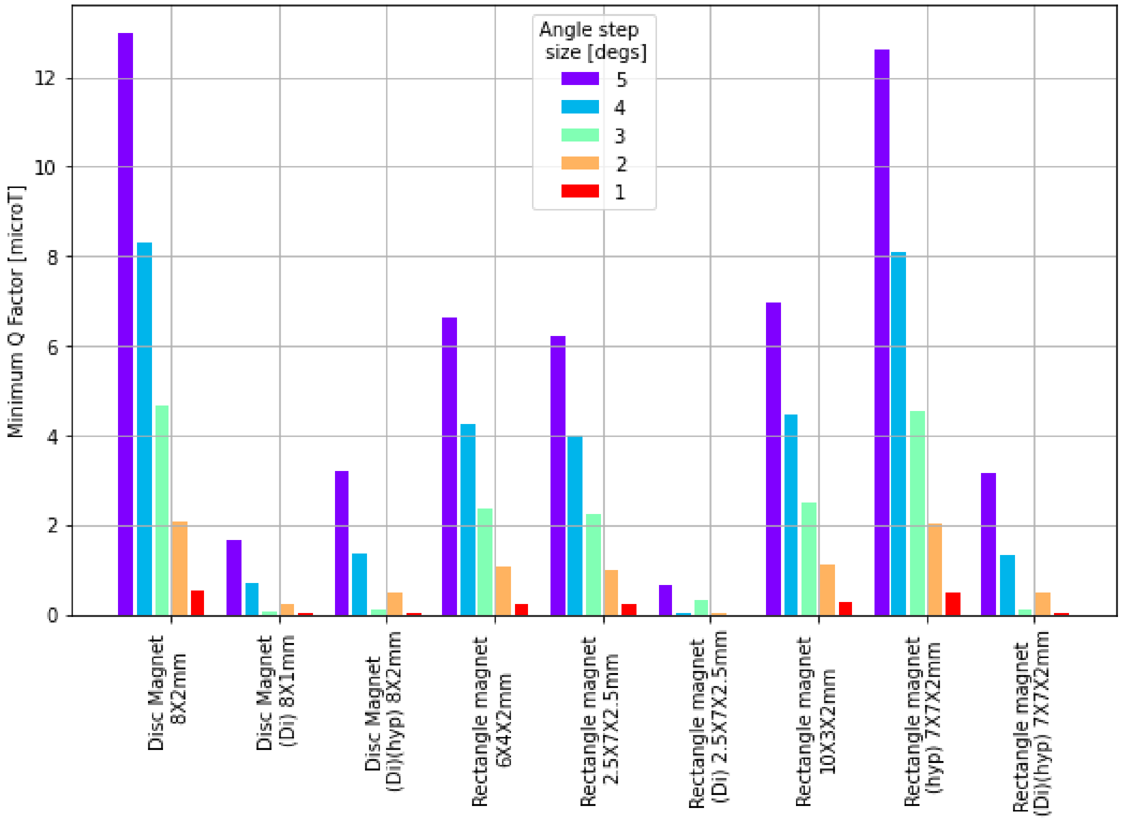

Figure 65 – Minimum Q factor (Qf_{min}) evaluated for optimisation study 1, orientation tracking to 2 DoF, magnet shape optimisation for the eight investigated magnets.

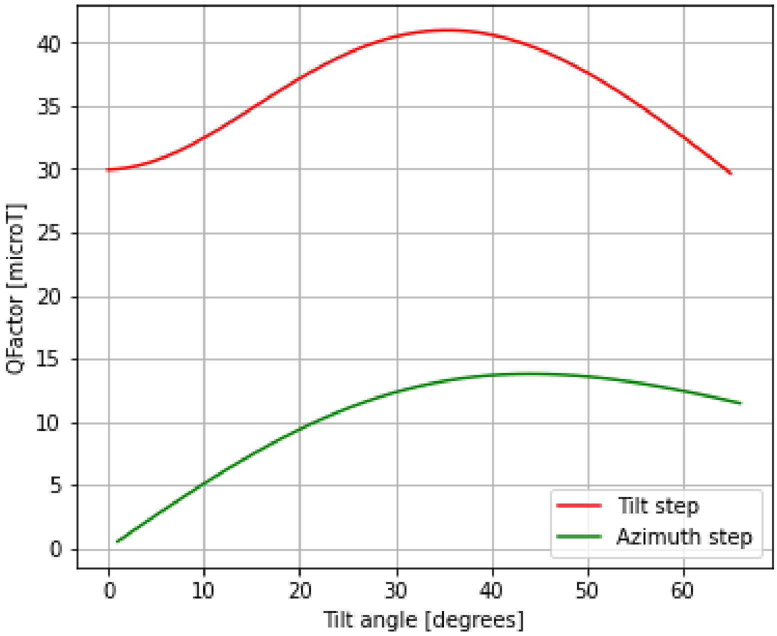

Figure 66 – The nearest neighbour magnetic field vector distances ($|_{NN}B|$) when tilt state increases by 1° starting at 0° (RED) and $|_{NN}B|$ when tilt angle is constant, and the azimuthal angle state goes from 0° to 1° (GREEN), data shown is for the M1 magnet configuration.

5.4.4 Discussion: Simulated optimisations study 1

The aim of this simulated optimisation study 1 was to investigate what effect changing the size and shape of the reference magnet had on the Qf_{mean} and Qf_{min} of the MPO implementations when measuring orientation to two DoF.

Increasing step size increases Q factor; this trend was expected as decreasing step size increases the number of possible orientation states within the angular range. Therefore, the B_n will be denser thus decreasing the state separation. This is an important trend to note when considering increasing the degrees of freedom i.e. adding more orientation states and when deciding the resolution of the system.

MPO implementations with magnets that were magnetised diametrically returned a comparatively low Qf_{min}. Figure 67 shows the magnetic field strength response for the **M1** and **M6** magnets during the simulation, only tilt angles at increments of 5° are shown for clarity. When the magnet is magnetised in the X direction change in orientation generates no change in the magnetic field strength in the Z direction. This created a smaller distribution of the magnetic field strength and so there is a smaller state separation between the orientation states resulting in a smaller Qf_{mean} and Qf_{min}. Similar responses are given by other magnets magnetised in the X direction. Additionally, MPO implementations with magnets that have symmetrical magnetic field distributions in the XY plane can measure tilt and azimuthal angle irrespective of stem rotation angle.

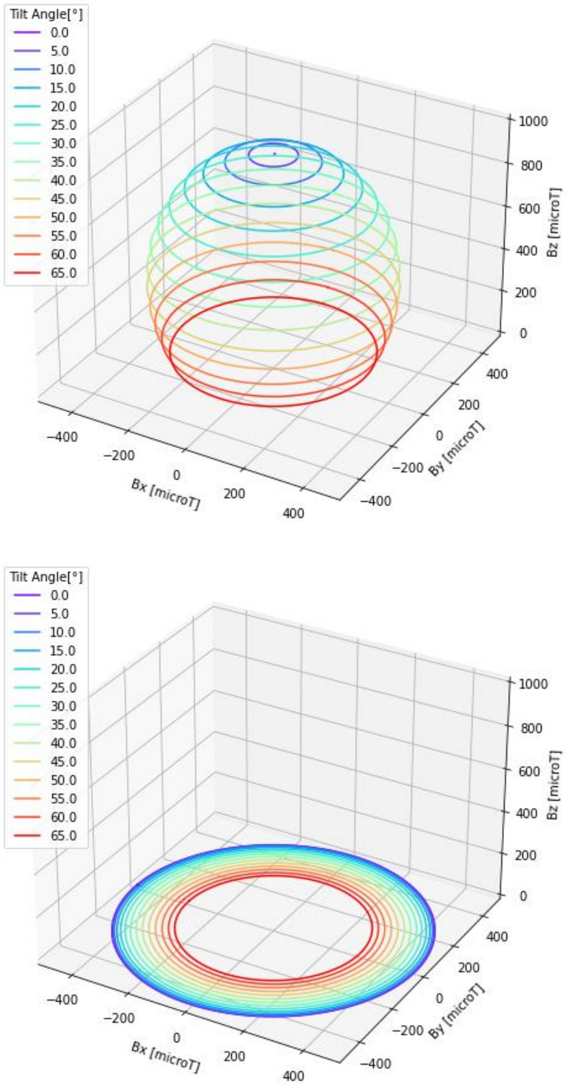

Figure 67 - Magnetic field strength in the X, Y & Z direction (Bx, By & Bz) for a 8X2mm Disc Magnet (magnetised in the Z direction and a 2.5X7X2.5mm rectangle magnet (magnetised in the X direction) where each colour represents B over a full range of azimuthal angles at a given tilt angle. Tilt angle ranged from 0° to 65° (with increments of 5° for clarity) and Azimuthal angle ranged from 0° to 360°.

The state separation was found to be constant when only azimuthal angle was varied. This is due to the distance between the magnet and sensor not changing when the stem is swept through the azimuth angle range. This creates symmetry in the magnetic field response demonstrated by the plotted coloured rings which each correspond to a particular tilt angle state (and thus full azimuth angle sweep), as shown in Figure 67. Figure 66 shows that for a MPO using an **M1** magnet and angle step size = 1° there is greater state separation in the tilt angle direction than in the azimuthal angle direction. In both angle directions the state separation is lowest in the low tilt angle region <20° and high tilt angle region >45°. This would indicate that these regions will be more susceptible to errors in orientation sensing. The impact of these higher error regions was explored further with simulations in Section 5.5 and experimental verification in Section 5.6.

The **M1** magnet can be considered the more optimal choice of magnet for an MPO sensing system measuring orientation to two DoF. However, at angle step sizes of <5° this MPO implementation did not meet the target Qf_{min}. i.e. the sensitivity of the sensor being 6µT in Bx & By or 9.7 µT in Bz. Although, Qf_{mean} values were greater than 10µT at all angle step sizes. So, it is hypothesised that an MPO configured with this implementation is feasible but there will likely be regions where sensing accuracy is poorer than others.

5.5 Simulated error study: Investigation of the impact component positioning errors had on the performance on the magnetic position and orientation sensing system tracking methods

The outcome of the sensor verification study presented in Chapter 4, showed that simulated and actual magnetic field of a magnetic sensing system would be sensitive to errors in the mechanical positioning of the components (magnet and sensor). A sensing system that is more robust to unavoidable errors like these would be more desirable. Lutz and Foletto (2019) performed an analysis in which they were exploring the robustness of two tracking techniques, namely direct and ratio responsivity tracking (as discussed in Section 5.2), for use in a magnetic sensor enabled joystick. They were investigating the impact of mounting precision and mechanical play in their joystick system by simulating parameter drifts in sensor position in the Z axis, magnet position in the Z axis and air gap variations from the reference value. They evaluated the percentage error between the original and drifted responsivities and used colour plots to show the location of the errors and highlight its asymmetrical distribution. A similar study was performed in the present work to compare the performance of three proposed MPO tracking methods namely ratio stick tracking with $\mathbf{R}_{\mathbf{ratioBMagnitude}}$, look up table and a Neural Network. However, instead of evaluating percentage error in the responsivities output this study reported error in the orientation prediction i.e. tilt and azimuth angle. This gave a better indication of how the simulated errors impacted the final orientation angle output and meant that the effect of the simulated errors on the azimuth angle prediction could be explored which was not previously considered by Lutz and Foletto (2019).

5.5.1 Method: Simulated error study

For this study the magnet (**M1**) and sensor configuration used is the same as shown in Section 4.6.4 and the simulated B_n data was produced by the same method described in Section 5.3.1. Firstly, a B_n dataset was generated with the magnet and sensor positioned as intended, Section 4.6.4. This B_n data was used as the Look Up table or **R$_{\textbf{ratioBMagnitude}}$** data and to train a Neural Network, see Section 5.3. The simulation was then repeated with either the magnet or sensor being positioned incorrectly, specifically translated from the intended position in the X, Y and Z direction in turn by 1mm and rotated from the desired position about the X, Y and Z axis in turn by 5° thus resulting in 12 specific test conditions. The simulation was then run using each tracking method in turn namely, ratio stick tracking with **R$_{\textbf{ratioBMagnitude}}$**, look up table and a neural network.

The erroneous B_n data outputted by the simulation was then inputted into the tracking method functions and the resulting orientation prediction (tilt angle, azimuth angle) were compared to the true orientation of the original simulation. At each orientation state the error between the original simulated orientation (expected) and the tracking method predicted orientation (observed) was computed for each angle direction using Equation 5. The sine and inverse sine function were used to remove the effect of crossing the azimuth angle singularity 360°/0°. The root mean squared error (RMSE) (Equation 3) was computed for each of the 12 specific test conditions for each method. The RMSE ± standard deviation (SD), minimum error, maximum error and range of error were computed across all test conditions for each tracking method.

$$Error = \sin^{-1}(\sin(Observed\ Value)) - \sin^{-1}(\sin(Expected\ Value))$$

Equation 5

$$RMSE = \sqrt{mean(Error^2)}$$

Equation 3

5.5.2 Results: Simulated error study

An array of colour plots showing the error in the stem tilt orientation and stem azimuth orientation, for each simulated error condition explored is shown in Figure 68 and Figure 69 respectively. The results shown in Figure 68 and Figure 69 are for the MPO implementation that used the Look Up Table tracking method, colour plots of the results when the other tracking methods were investigated are shown in the Appendix g). The colour bar range was set as twice the maximum standard deviation to the nearest ±5° for clarity and to prevent colour wash out. Bar charts of the RMSE in the tilt and azimuth angle direction for each of the 12 specific test conditions and for each tracking method are shown in Figure 70 and Figure 71. The values of the root mean squared error (RMSE) ± standard deviation (SD) of the predicted angle and the error in the stem orientation for each of the tracking methods are show in Table 12.

The key findings from this study were:

Key findings - Tilt angle direction:

1. Magnet or sensor rotation in the C direction incurred no error for look up table and $\mathbf{R}_{\mathbf{ratioBMagnitude}}$ method as the magnetic field of the magnet is symmetrical in the XY plane. Neural Network method did incur a small RMSE of 0.26° resulting from the systematic error in the Neural Network prediction.
2. All three methods showed little error when the magnet was translated in the X direction and rotated in the B direction. Whereas there was a high level of overestimation when the magnet was translated in the Y direction and rotated in the A direction.
3. Sensor translation in the X & Y direction and rotation in the A & B direction produced symmetrical responses showing under and over estimation dependent on the direction of the translation or rotation.

4. When the magnet or sensor was translated in the Z direction the Neural Network method performed worse with RMSE of 6.2° and 6.8° respectively. The look up table and $\mathbf{R_{ratioBMagnitude}}$ method had comparable RMSE values when the magnet was translated in the Z direction at 2.6° and 2.4°. Yet when the sensor was translated in the Z direction the RST method produced less error 0.7° when compared to the look up method 2.9°.

Key findings – Azimuth angle direction:

5. Magnet or sensor rotation in the C direction incurred no error for look up table and $\mathbf{R_{ratioBMagnitude}}$ method as the magnetic field of the magnet is symmetrical in the XY plane. Neural Network method did incur a small RMSE of 1.5° resulting from the systematic error in the Neural Network prediction.
6. All three methods showed little error when the magnet was translated in the Y direction and rotated in the A direction. Whereas there was a high level of overestimation when the magnet was translated in the X direction and rotated in the B direction.
7. Sensor translation in the X & Y direction and rotation in the A & B direction produced symmetrical responses showing under and over estimation dependent on the direction of the translation or rotation.
8. When the magnet or sensor was translated in the Z direction RMSE for the look up method was 4.5° and 4.2° respectively and RMSE for the Neural Network method was 18.9° and 31.1°. Whereas the $\mathbf{R_{ratioBMagnitude}}$ method incurred no errors.

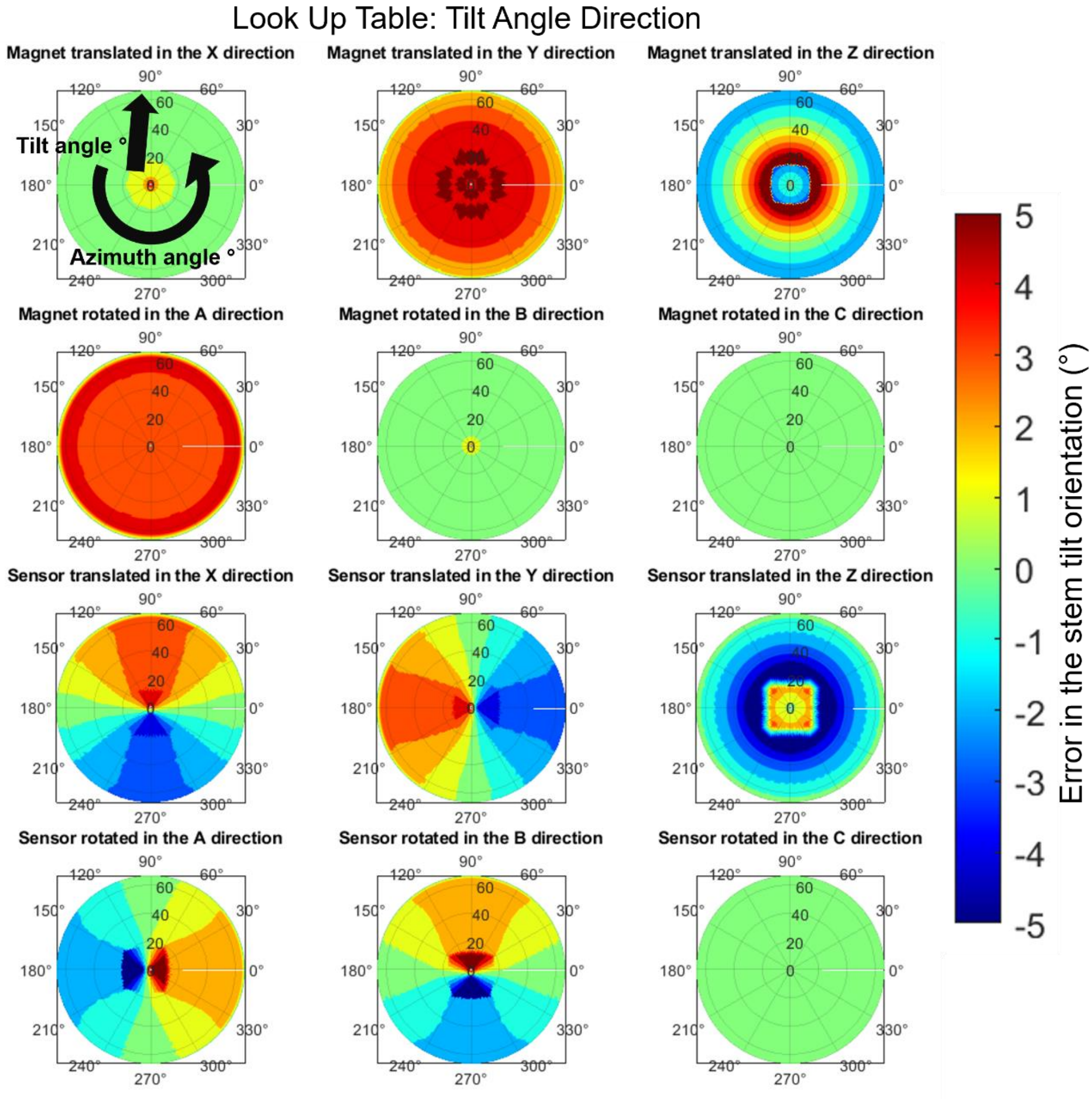

Figure 68 - Colour plots of the error in the stem tilt angle prediction made by the simulated MPO with the 8X2mm disc magnet using the look up table tracking method. The Azimuthal angle axis of the graph corresponds to the Azimuthal angle of the stem (0° - 360°) and the Radial axis of the graph corresponds to the tilt angle (0° - 66°). The colour bar range was set as twice the maximum standard deviation to the nearest ±5° for clarity and to prevent colour wash out.

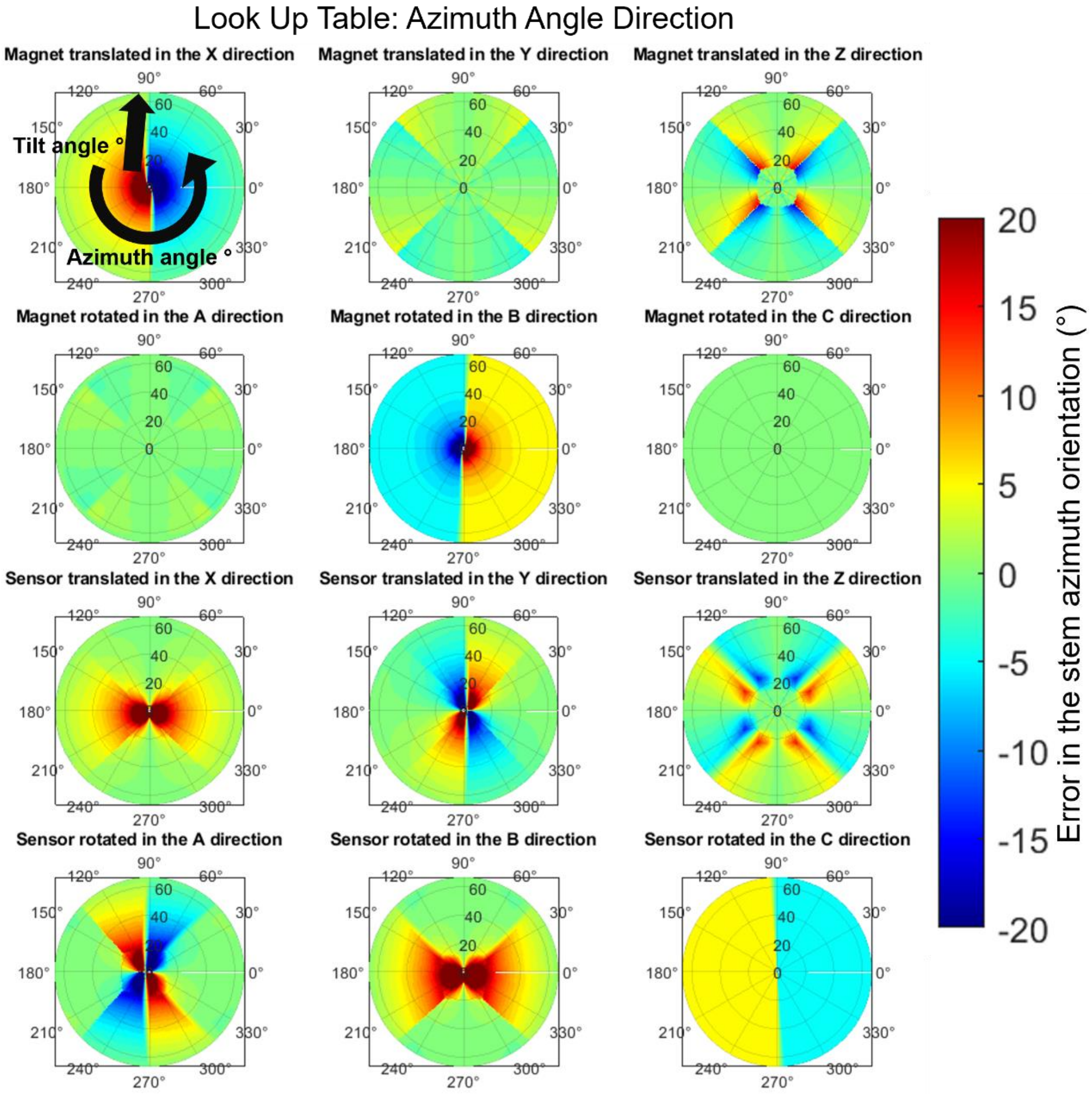

Figure 69 - Colour plots of the error in the stem azimuth angle prediction made by the simulated MPO with the 8X2mm disc magnet using the look up table tracking method. The Azimuthal angle axis of the graph corresponds to the Azimuthal angle of the stem (0° - 360°) and the Radial axis of the graph corresponds to the tilt angle (0° - 66°). The colour bar range was set as twice the maximum standard deviation to the nearest ±5° for clarity and to prevent colour wash out.

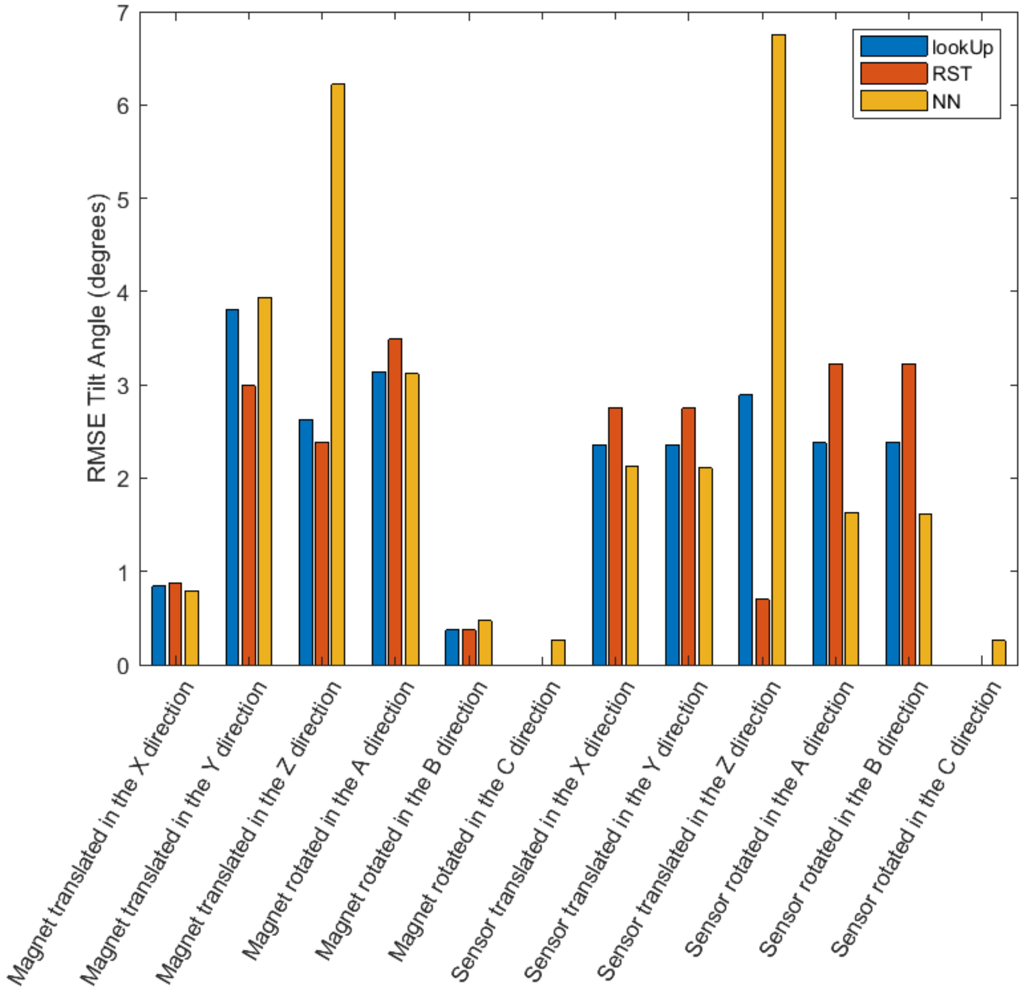

Figure 70 - Bar chart showing the RMSE in the tilt angle direction for each of the 12 specific test conditions and for each tracking method, performed in the simulated error analysis study.

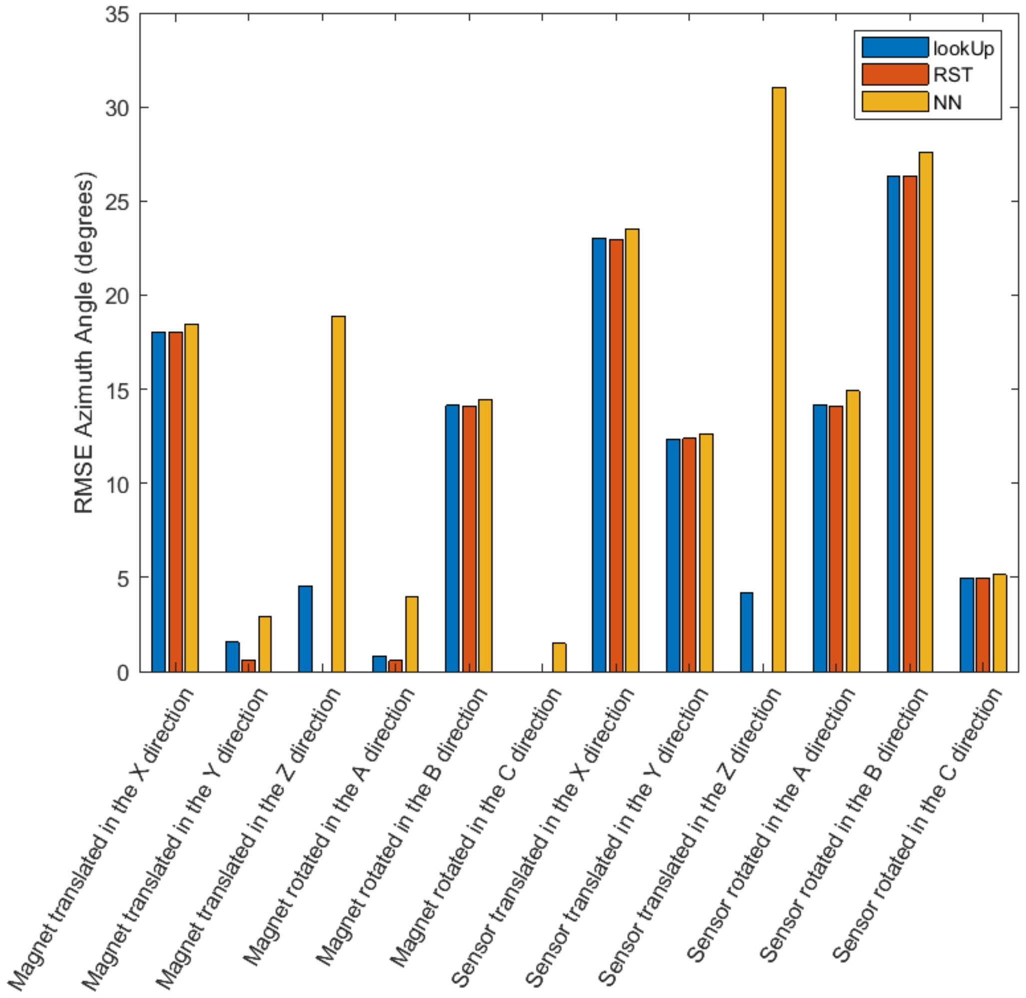

Figure 71 - Bar chart showing the RMSE in the azimuth angle direction for each of the 12 specific test conditions and for each tracking method, performed in the simulated error analysis study.

Table 12 - Root mean squared error, standard deviation and range values for the absolute error in the stem orientation for each tracking method, performed in the simulated error analysis study.

Tracking Method	***RMSE Tilt Angle ± SD [°]***	***Tilt Angle Error Range [°]***	***RMSE Azimuthal Angle ± SD [°]***	***Azimuthal Angle Error Range [°]***
Ratio stick tracking	2.3 ± 2.3	-6 to -6	13.3 ± 13.2	-90 to 180
Look up table	2.3 ± 2.2	-8 to 8	13.4 ± 13.3	-90 to 180
Neural Network	3.2 ± 3.2	--16.6 to 17.2	17.4 ± 17.3	-175 to 179

5.5.3 Discussion: Simulated error study

The aim of this simulated error study was to investigate the effect that errors in the positioning of the magnet and sensor (when they are embedded within the THR components) would have on the orientation of the stem reported by the three different tacking methods. The **R$_{\text{ratioBMagnitude}}$** and the look up table tracking methods showed comparable levels of performance whereas the Neural Network method reported higher levels of error. This suggests that the Neural Network model is not fully optimised. The training dataset size and the number and size of network layer were not altered and there was no examination into whether the model was over or under fitted. Future work can explore addressing these factors with the aim of improving the performance of the Neural Network thus reducing the error of the orientation prediction.

The results show that there was little error incurred in the Tilt angle direction across all the tested tracking methods. The largest errors occur in the Azimuthal angle prediction. Inspection of the colour plots shows that these discrepancies in Azimuthal angle prediction occur predominantly in the low Tilt angle region <20° this is in agreement with the findings of Section 5.5. This is because the state separation of the system in the azimuthal direction was found be lower than in the tilt direction and trended towards 0μT when tilt angle state decreased from 20° to 0°. Furthermore, inspection of the colour plots show there were no errors observed when the disc magnet is rotated about the Z axis. This is because the disc magnet is symmetrical in the XY plane and so rotation of the magnet in the C direction has no impact on the returned stem orientation.

Key findings 2 & 6 result from how the tilt and azimuth angle were defined in the magnetic field simulations. When azimuth angle is 0° the magnet is rotated in the A direction (about the X axis) so is in plane with the YZ plan. Therefore, further magnet rotation in the A direction essentially increases the tilt of the magnet thus leading to an overestimation. Magnet movement in the Y axis moves the magnet further from the central axis of the stem thus increasing the effective tilt angle and leading to an overestimation of tilt angle. Magnet movement in the X axis and rotation in the B axis misaligns the magnet with the YZ plane thus causing errors in the azimuth angle prediction.

Key finding 4 & 8 suggest that the $\mathbf{R}_{\mathbf{ratioBMagnitude}}$ method is more robust to in component positioning errors in Z direction. This was a similar finding to that reported by Lutz and Foletto (2019) and earlier during stick tracking optimisation presented in Section 5.2.2.

5.6 Experimental verification of tracking method performance for two degrees of freedom orientation tracking

An experimental method was developed to evaluate and compare the performance of the tracking methods for measuring stem component orientation to two DoF. The tracking methods being assessed include ratio stick tracking with $\mathbf{R}_{\mathbf{ratioBMagnitude}}$, look up table and a neural network.

5.6.1 Integration of magnetic field sensor into total hip replacement components

A magnetic field sensor board was pressed into a 3D printed disc that was then positioned in the introducer hole of the acetabular shell and potted in place with epoxy. The full method of positioning the sensor into the acetabular shell is in Appendix h) and image of the sensor in place is shown in Figure 72. A stem component was 3D printed and matched the geometry of a clinically available stem taper (as mentioned previously in Section 4.6) and included an extruded pocket, on the face of the stem taper, to hold the **M1** magnet, as shown in Figure 72.

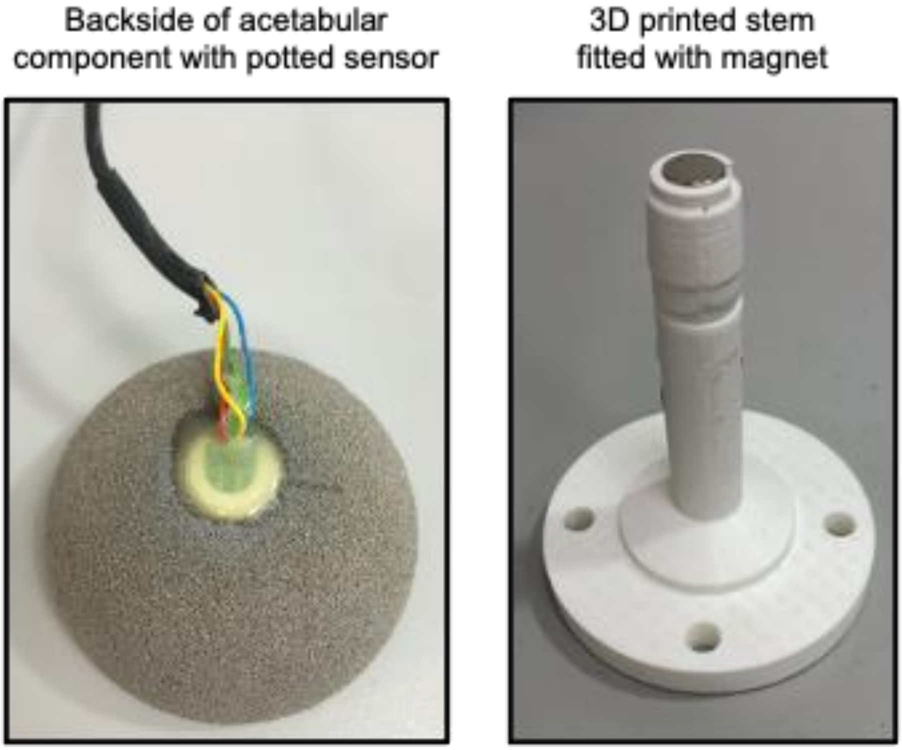

Backside of acetabular component with potted sensor

3D printed stem fitted with magnet

Figure 72 – Clinically available total hip replacement acetabular shell with mlx90393 sensor board potted into introducer hole.

To validate that the sensor had been positioned in the correct position (with respect to the magnet) a method was devised to use the output of the sensor to estimate the distance the magnet is from the sensor. The replica stem component was used to manually position the femoral head component into the acetabular shell and liner components. The sensor recorded 500 magnetic field readings whilst an operator manually positioned the replica stem to be approximately perpendicular with the face of the cup whilst also trying to position the stem to return the greatest Bz value. Once 500 values were recorded the reading with the greatest Bz value was found and inputted into a look up table function that was populated with values representative of the magnet being 17.5mm to 26.5mm (in steps of 0.1mm) from the sensitive spot of the sensor. The value the look up table returned was a prediction of the position of the magnet in the Z direction and could be compared with the intended magnet-to-sensor displacement of 20.5mm to see if correct sensor positioning had been achieved. Taking multiple (500) readings whilst the stem was moving and only returning the maximum, mitigated magnet or sensor positioning errors within the THR components. The magnet and sensor were designed to be perfectly perpendicular when the femoral head was located in the cup and the stem was at the neutral position (vertical). Therefore, the reading with the largest Bz value will return the shortest magnet-to-sensor displacement which should indicate that the magnet is positioned horizontally directly above the sensor.

The magnet-to-sensor displacement test was first performed immediately after the sensor was integrated into the THR components. The returned displacement was 21.5mm; 1mm greater than the intended displacement. All simulations were then repeated using the actual magnet-to-sensor displacement so that they were representative of the real system. After all testing with the THR components was complete the magnet-to-sensor displacement test was repeated, and it was found that estimated displacement had decreased to 21mm.

5.6.2 Method: Two degrees-of-freedom experimental motion study

The experimental setup was that described in 3.2.1. To test the performance of the tracking system at measuring stem orientation to two DoF the robot manipulated the stem from the neutral/vertical position to a tilted position and then rotated the stem through a full sweep of azimuthal angles 0° to 355°. The azimuthal sweep was repeated for a range of tilt angles from 5° to 60° with steps of 5°. The experimental run was performed three times for each of the tacking methods (ratio stick tracking with $\mathbf{R}_{\mathbf{ratioBMagnitude}}$, look up table and a neural network).

Stem orientation data was recorded by the magnetic sensing system and the robot arm. The timestamp of the data from the robot arm and sensing system was matched and temporally synched using the method described in Section 4.7.2. Data when stem azimuthal angle was >355° or <5° namely the period at the end of each azimuthal sweep to the start of a new stem tilt condition, at which the stem crossed the mathematical singularity at 0°/360°, was omitted to avoid mistaken errors. Data when stem tilt angle was <4° namely the very start of the test as the stem was moved to the first tilted position was also omitted as a stem tilt angle of 0° is at the azimuthal angle singularity.

To compare the sensing system tracking methods the error between the robot reported orientation (expected) and the sensing system predicted orientation (observed) was computed for each angle directions using Equation 5. The sine and inverse sine function were used to remove the effect of crossing the azimuth angle singularity 360°/0°. The RMSE (Equation 3) ± standard deviation (SD), minimum error, maximum error and range of error were computed for all the data across the three repeats.

$$Error = \sin^{-1}(\sin(\,Observed\ Value)) - \sin^{-1}(\sin(\,Expected\ Value))$$

Equation 5

$$RMSE = \sqrt{mean(Error^{2})}$$

Equation 3

5.6.3 Results: Two degrees-of-freedom experimental motion study

The plots of the robot arm stem angle and the $\mathbf{R_{ratioBMagnitude}}$, look up and neural network tracking method predicted stem angle, in the tilt angle direction and azimuthal angle direction, for the duration of motion study one, are shown in Figure 73 and Figure 74 respectively. The error between robot arm stem angle and predicted stem angle for the duration of motion study one is also shown in Figure 73 and Figure 74. The error made by the neural network tracking method was plotted on a separate axis to the error made by the $\mathbf{R_{ratioBMagnitude}}$ and look up table tracking method to aid comparison. The three repeats of each tracking method for motion study one, are shown on all the plots of Figure 73 and Figure 74. The values of the root mean squared error (RMSE) and standard deviation for actual robot arm stem angle versus tracking method predicted angle over the three repeats of the three tracking methods is shown in Table 13. The minimum, maximum and range of the error is also shown in Table 13**.**

The key findings from this study were:

- Errors in the Azimuthal angle were greater than in the tilt angle direction.

- Error in the Azimuthal angle was greater in the low tilt angle region i.e. <20°.
- Error in the tilt angle direction was greatest in low tilt angle region i.e. <20°and in the high tilt angle region >45°.
- Performance of the $\mathbf{R_{ratioBMagnitude}}$ responsivity tracking method and the Look Up table method are comparable, and in general performed better than the Neural Network method.

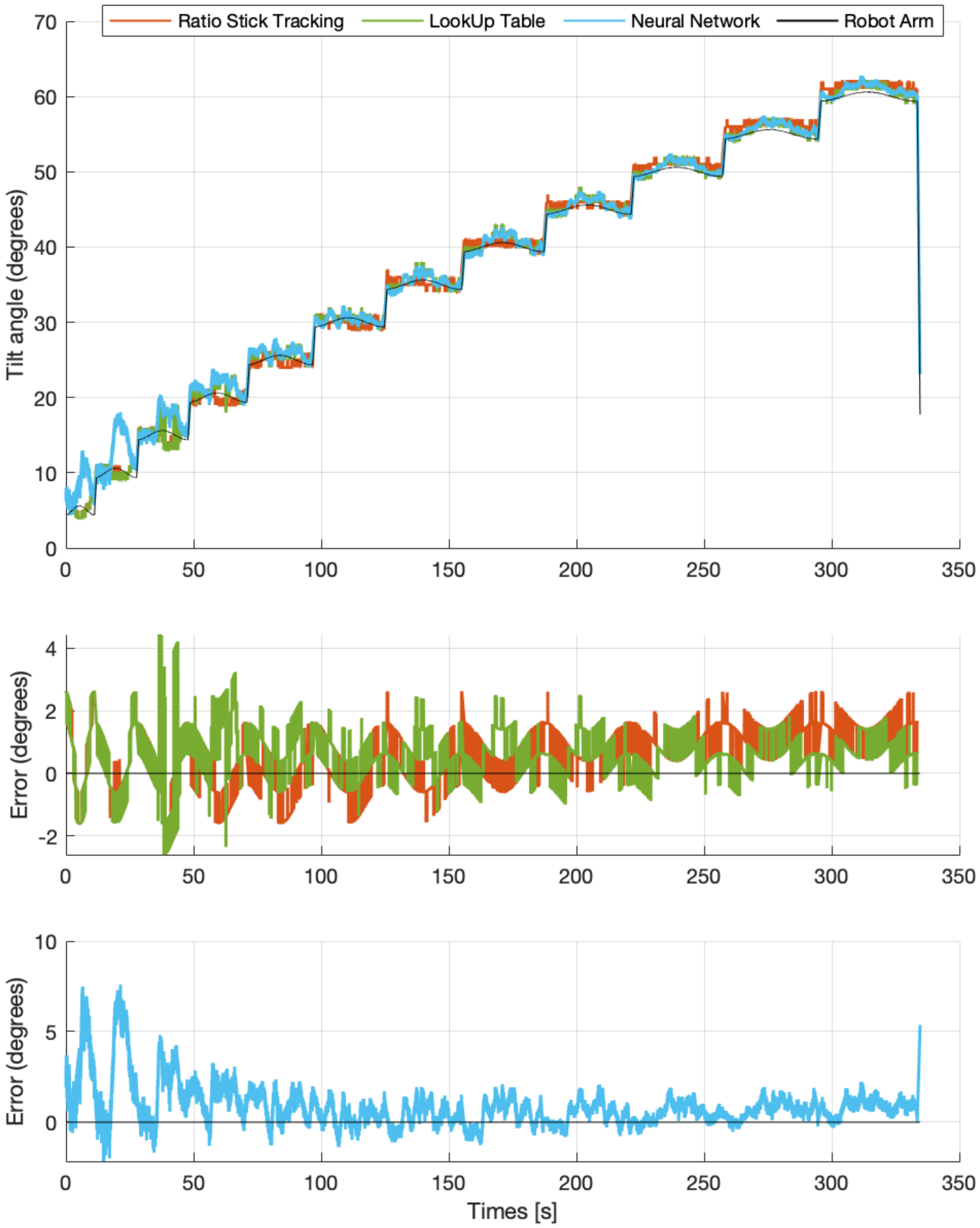

Figure 73 – Predicted versus actual (robot arm reported) stem angle in the tilt angle direction during motion study one made by the $R_{ratioBMagnitude}$, look up and neural network tracking methods. Error between the predicted and the actual (robot arm reported) stem angle in the tilt angle direction during motion study one. Error made by the neural network tracking method was reported on a separate axis to aid comparison.

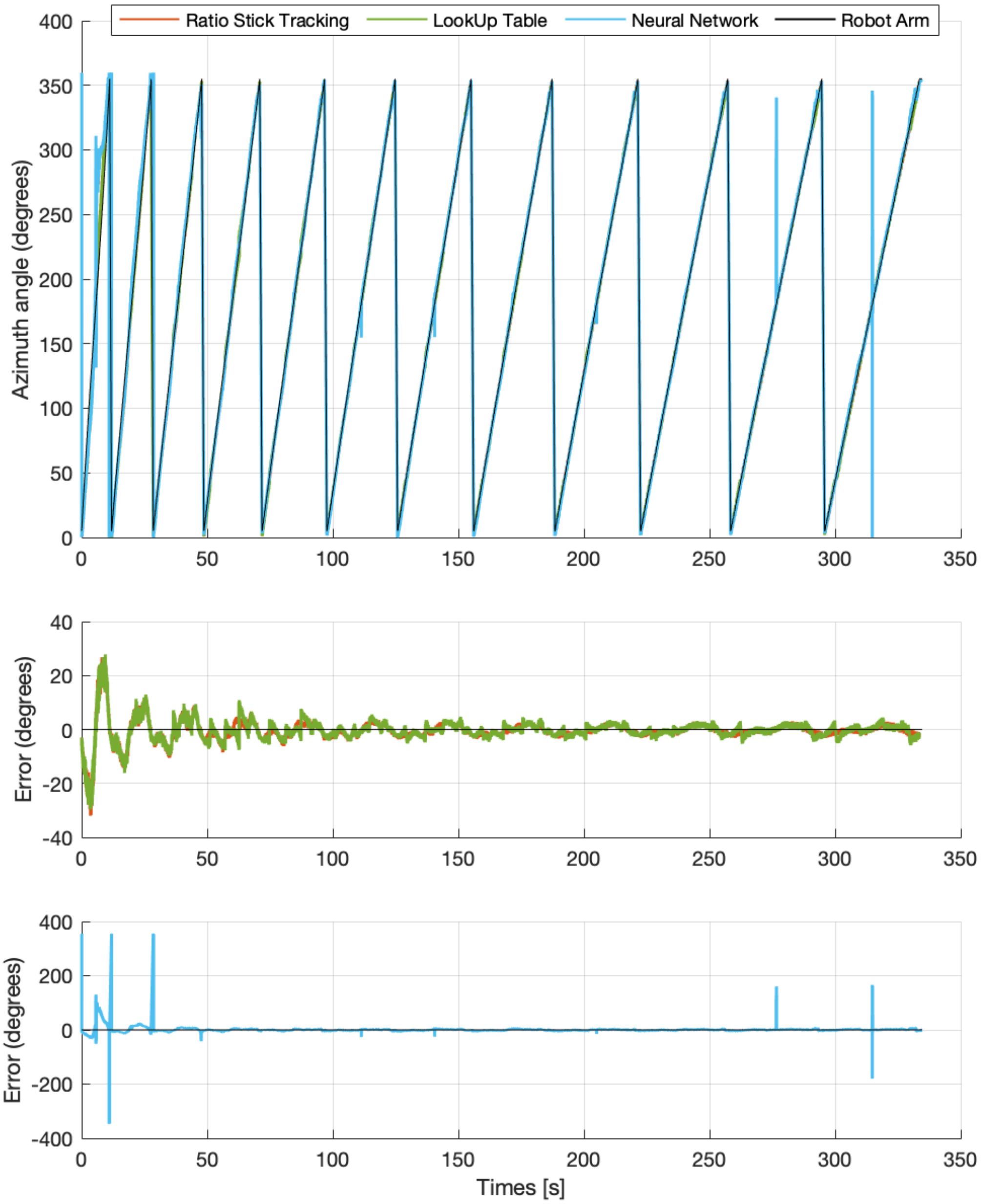

Figure 74 - Predicted versus actual (robot arm reported) stem angle in the azimuthal angle direction during motion study one made by the $R_{ratioBMagnitude}$, look up and neural network tracking methods. Error between the predicted and the actual (robot arm reported) stem angle in the tilt angle direction during motion study one. Error made by the neural network tracking method was reported on a separate axis to aid comparison.

Table 13 - Root mean squared error, standard deviation and minimum & maximum error for actual robot stem angle versus tracking method predicted angle across all repeats (n=3) for motion study 1

Tracking Method	*RMSE Tilt Angle ± SD [°] (n=3)*	*RMSE Azimuthal Angle ± SD [°] (n=3)*	*Min to Max, Range Tilt Angle Error [°] (n=3)*	*Min to Max, Range Azimuthal angle Error [°] (n=3)*
Ratio stick tracking	1.1 ± 0.9	3.9 ± 3.9	-2.5 to 2.6, 5.2	--25.2 to 31.6, 56.8
Look up table	1.0 ± 0.8	4.0 ± 4.0	-2.6 to 4.4, 7.0	-26.1 to 29.7, 55.8
Neural Network	1.5 ± 1.2	6.3 ± 6.2	-2.2 to 7.6, 9.8	-85.9 to 137.5, 137.5

5.6.4 Discussion: Two degrees-of-freedom orientation experimental motion study

The aim of this study was to explore if a magnetic position and orientation system can be used to track the orientation to two DoF, of a femoral head and stem whilst positioned in an acetabular cup component. A reference magnet and magnetic field sensor were integrated into clinically available total hip replacement components. Three separate methods for matching the magnetometer output to the position of the reference magnet attached to the stem were investigated.

When comparing the $\mathbf{R}_{\mathbf{ratioBMagnitude}}$ responsivity tracking method and the Look Up table method, statistically there is little difference in their performance apart from some comparatively higher levels of error in the tilt angle prediction made by the Look Up table method in the low angle (15° & 20°) region. The Neural Network method had the highest level of error in both the tilt angle and azimuthal angle directions. When error occurred in the higher angle range >20° the errors seemed to be extreme and sporadic. it may be that with further development and optimisation of the model that these occurrences could be omitted.

An explanation for the high level of Azimuthal angle prediction error when Tilt angle is <20° is that distance the stem translates when Tilt angle is <20° is less than when tilt angle is >20°. This inherently has the effect of decreasing the state separation thus making it harder for the system to distinguish between the separate states. A possible solution to this could be to stagger the Azimuthal angle steps across the range of Tilt angles. For example, when Tilt angle is <10° Azimuthal angles could have steps of 45° so 8 steps across the full 360° range and when tilt is >10° Azimuthal angles steps could remain at 1°. Additionally, the set of discrete orientation locations could be determined by mathematically selecting locations that are evenly separated across the full sensing region. This could be achieved using an algorithm like that of the Fibonacci sphere algorithm.

Following post processing of the robot orientation data an unexpected phenomenon was observed. During azimuth angle sweeps the robot arm tilt angle varied by approximately ±0.5° from the desired value. Typically starting below the intended value peaking above the intended value halfway through the azimuth sweep and then returning to below the intended value. In some instances, the sensing system was able to recognise the deviation from the expected values. This did however affect the computed error value as the look up table and RST method had effective resolutions of 1° which was greater than the observed deviations. The robot was not programmed to do this, and it is believed this was caused by component misalignment.

The tool centre point (TCP) of the UR3 was the intended to be the position of the centre of the femoral head with respect to the tool flange of the UR3. The TCP was used in all robot programs to define the position of the centre of the femoral head when the femoral head is located within the acetabular liner. In theory positioning the femoral head within the acetabular liner when the robot was in Freedrive mode would give a good estimation of the centre of the femoral head’s position (and so position of the TCP) when the femoral head is located in the acetabular liner. The TCP was the height of the centre of the femoral head when the femoral head component was positioned on the 3D printed stem component. The actual distance from the base of the 3D printed stem component to the top of the femoral head component minus half the diameter of the femoral head component was used as the TCP distance.

There may have been discrepancies between this measured TCP distance and the actual TCP location for example because the femoral head was not fully pressed onto the stem component or and more likely, because the connection between the base of the 3D printed stem component and the robot tool flange was not perfectly flush. This will have resulted in misalignment of the CoR of the femoral head and the acetabular liner during the experimental motion trials. In future experimental work the force transmitted through the tool flange could be recorded during the motion trials. Any spikes in the load could give an indication as to whether the CoRs are not at a coincidence. To be clear the UR3 can record the generalised forces through the tool flange however was not programmed to record this parameter during the experimental work presented in this thesis.

The difference between the intended magnet-to-sensor displacement and the observed displacement was deemed acceptable for this work and was a discrepancy that was removed with calibration. Initially the difference in magnet-to-sensor displacement would suggest that the sensor potting method was unsuitable as correct sensor position was not achieved. It was believed excess epoxy had been poured into the shell component preventing the liner from fully seating into the shell component. However, the decrease in magnet-to-sensor displacement following testing would suggest the liner recessed into the shell component. This could be a result of the liner not being correctly seated into the shell at the start of testing or that the loading during testing has naturally caused the liner to sink into the shell fully.

5.7 Measuring occurrence of an impingement event using two degrees-of-freedom orientation tracking

An impingement event in a THR occurs when the orientation of the components is at or beyond the maximum range of motion of the components. The femoral stem component contacts the rim of the liner component, a schematic of THR component impingement is shown in Figure 75. Component-component (primary) impingement is highly likely to be the most common cause of dislocation (Shon et al., 2005; Brown and Callaghan, 2008; Ghaffari et al., 2012). There is a need to further investigate the mechanics of impingement in-vitro including, what patient and surgical variables, and implant design factors, impact the prevalence and severity of impingement. However, current in-vitro total hip replacement simulation models (Ali et al., 2016) use a Gaiter filled of biological lubricant to surround the components. This means there is no line-of-sight view of the bearing or the components thus, making the identification of an impingement event challenging.

Experimental hip simulators offer no means of directly detecting impingement contact location therefore, impingement location can only be inferred from geometric models (Pryce et al., 2022; Williams, 2022) or predicted using simulator and component kinematics. Previous methods have used retrospective approaches examining the location of damage to the liner rim caused by repeated impingement contacts (Pryce et al., 2021; Williams, 2022). However, these methods aren’t real-time and will only highlight severe impingement events that cause detectable damage to the components and does not give indications of light contacts or near misses and cannot be translated to hard bearing materials (ceramics). A sensing system that integrates with THR components (without change to the component geometries), could be used in an experimental THR wear simulator (whilst the lubricant Gaiter is still in use) and can track the occurrence and report the location of a component-component impingement event, would be a useful tool for researchers.

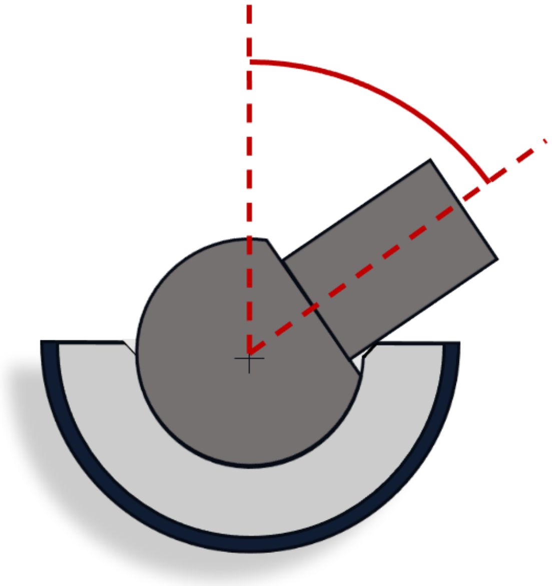

Figure 75 – Diagram of a component-component impingement event occurring between total hip replacement components.

The working hypothesis is that the MPO sensing system method of tracking orientation to two DoF would provide a means of measuring the occurrence and location of an impingement event between the THR components. The impingement event could be inferred as occurring when the tilt angle equals the maximum (or within a predetermined boundary) tilt angle of the components normal working ROM. The azimuthal angle can also be reported as it would give the inferred location on the rim of the liner where the impingement contact occurred. The $\mathbf{R}_{\mathbf{ratioBMagnitude}}$ tracking method was the only tracking method explored in this experiment as the findings of the previous study (Section 5.6) showed that it was the better performing tracking method.

5.7.1 Method: Impingement detection study

The objectives of this experiment were to recreate an impingement event between the THR components at several locations around the circumference of the rim of the liner. Then to characterise the accuracy and reliability of the sensing system when measuring the occurrence and the location of the impingement event between THR components.

The experimental setup was that described in Section 3.2.2, including the impingement continuity trigger system. The stem component began in a vertical orientation. The robot rotated the stem in the tilt direction until the components contacted. Once the continuity switch was triggered the robot arm was programmed to return to a tilt angle of 45° and then rotate in the azimuthal direction to the next impingement location. This was repeated 36 times around the full circumference of the rim at evenly spaced azimuthal angle steps of 10°, the protocol was then repeated five times.

Stem orientation data was recorded by the magnetic sensing system and the robot arm. The timestamp of the data from the robot arm and sensing system was matched and temporally synched using the method described in Section 4.7.2. Data when the stem azimuthal angle was >350° or <10°, namely the start and end of each test protocol, was omitted to avoid mistaken errors resulting from the stem crossing the mathematical singularity of 0°/360°.

To compare the sensing system tracking methods the error between the robot reported orientation (expected) and the sensing system predicted orientation (observed) was computed for each angle directions using Equation 2. The RMSE (Equation 3) ± standard deviation (SD) were computed for all the data across the five repeats.

An adapted version of the ratio stick tracking with $\mathbf{R}_{\mathbf{ratioBMagnitude}}$ tracking method was used for the MPO sensing system. Whenever stem tilt angle exceeded the threshold of 63° an impingement event was said to have occurred and a Boolean metric termed “impingementOccurence” was set to true. Additionally, the azimuthal angle of the stem was recorded as the term “impingementLocation” and the timestamp was also recorded.

5.7.2 Results: impingement detection study

A typical polar plot of robot arm recorded stem orientation and predicted stem orientation for the impingement detection test protocol is shown in Figure 76. Where the polar axis is the tilt angle and radial axis is the azimuth angle. The peaks in the robot recorded stem orientation indicate the azimuth location of the impingement point and the maximum tilt angle recorded at impingement point. The RMSE ± standard deviation and the for actual robot arm stem angle versus tracking method predicted angle across all five repeats were 2.9º ± 1.2º and 2.0º ± 2.0º in the tilt and azimuth angle respectively.

The key findings from this study were:

1. All the 36 impingement events created were detected by the MPO sensing system meaning occurrence detection was 100%.
2. The error in the azimuthal angle prediction was less than previously reported in Section 5.6.
3. The stem tilt angle prediction was typically overestimated.

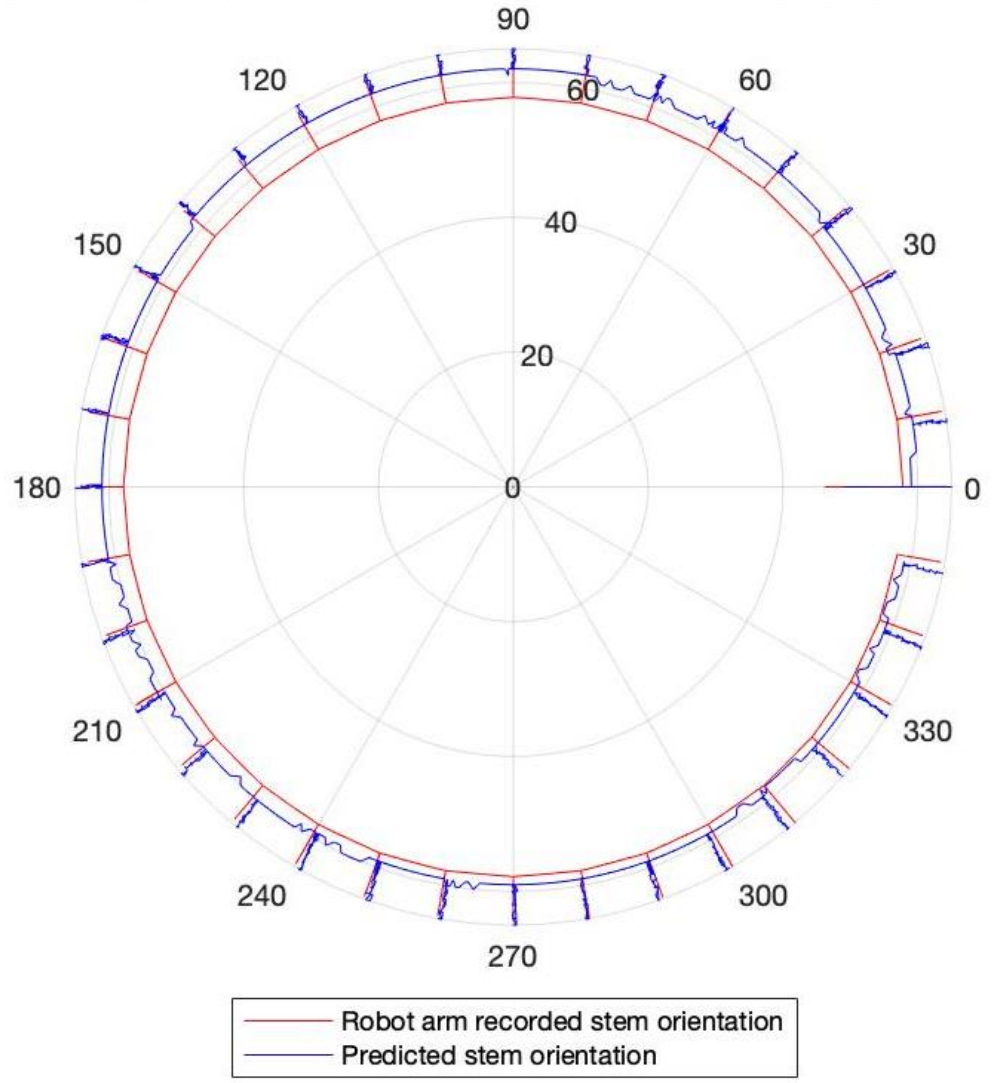

Figure 76 – A typical plot of the location of the impingement events during the impingement detection protocol including robot arm recorded stem orientation and predicted stem orientation in the Tilt angle direction and Azimuthal angle direction, repeat one of five. The Azimuthal angle axis of the graph corresponds to the Azimuthal angle of the stem (0° - 360°) and the Radial axis of the graph corresponds to the Tilt angle of the stem.

5.7.3 Discussion: impingement detection study

The aim of this study was to explore if a magnetic position and orientation system can be used to track the occurrence and location of an impingement event between the components of a THR.

The decrease in azimuth angle prediction error (when compared to that reported in Section 5.6) is likely because the impingement detection protocol had the stem positioned at a tilt angle >20° for the majority of the experimental run. The results of the simulated error analysis in Section 5.5, highlighted that azimuthal angle was harder to determine accurately when stem tilt angle was <20°. Hence the improved performance during the impingement detection protocol.

The overestimation of the stem tilt angle is a result of the magnetic field vector being read by the sensor being less than the magnitude of the simulated data. This would suggest that the magnet is further away from the sensor than it was designed to be. A possible explanation for this could be that during the impingement detection protocol run the femoral head component was not seated/located correctly into the liner component. This highlights that the system is sensitive to the positional accuracy of the THR components. Additionally, inspection of Figure 76 shows that tilt and azimuthal angle prediction varied around the circumference of the rim of the liner suggesting that the cup component was not perfectly level.

Inspection of the 3D geometry CAD of the THR components (through CAD files) showed that impingement between the components occurred at the point where stem tilt angle was 66° from the central axis of the liner component. Therefore, the tilt angle boundary dictating when an impingement event occurs was initially set at >65°. However, a pilot run of the impingement detection protocol showed that the impingement continuity switch was consistently triggered when robot arm stem angle was 64°. Therefore, the impingement occurrence boundary of the tracking system was reduced to >63°. The lower stem tilt angle at the point of impingement could be attributed to errors in the 3D printed component or because the thickness of the copper foil positioned on the components was not accounted for.

5.8 Summary work for femoral stem orientation tracking to two degrees-of-freedom, using a single sensor magnetic position & orientation tracking system

A magnetic position and orientation sensing system has been integrated into THR components and femoral stem orientation tracking to two degrees-of-freedom has been achieved. The design specifications that have been satisfied following completion of the work in this chapter are shown in Table 14.

Table 14 - Design specification evaluation for a sensing method for use in an instrumented THR prosthesis.

Requirement	Specification	Evaluation
Integration within implants	**Red** – Significant changes to implant geometry or bearing contact surface. **Green** – No change to implant geometry	**Green –** No change and sensor and magnet were integrated into pre-existing features on the THR components.
Power and data transfer	**Red** – Excessive wiring or positioning of the tether disrupts normal function of the implants. **Green** – Tether has no impact on the function of the components	**Green –** single tether (4 cable core) required and passes out the backside of the shell so does not disrupt the function of the components.
	Red – Requires additional power supply. **Green –** Can run on power supplied from PC or laptop	**Green –** Runs of PC.
	Red - Standardised gait cycle is 101 discrete data points per cycle so 50Hz to 101Hz would match monitoring 0.5cycle/s. **Green** - Standardised gait cycle is 101 discrete data points per cycle so 101Hz would match monitoring 1cycle/s.	**Red -** 50Hz achieved however sensor configuration was not optimised and sensor can achieve max frequency of 493Hz.
Measure the angle of the femoral stem relative to the acetabulum cup	**Red** – Can measure orientation over full angle range for one of the defined angle directions. **Green** – Can measure orientation over full angle range in all three defined angle directions.	**Red –** 2DoF achieved namely full tilt angle direction and full azimuth direction but not rotation angle direction.
	Red - Resolution 5º to 1º **Green –** Resolution <1º	**Red –** Resolution of 1º.
	Red - Accuracy 5º to 1º **Green –** Accuracy <1º	**Red –** 2DoF 1º error in Tilt direction and 4.2º error in azimuth direction. Impingement detection 2.9º error in Tilt direction and 2.0º error in azimuth direction.

All three of the considered tracking methods responsivity, look up table and neural network, have shown good agreement when compared to the actual stem angle manipulated by the robot arm. This was encouraging as the results of the optimisation study had shown that the minimum state separation (min Qf = 0.522 µT) of the selected MPO implementation was less than the sensitivity of the sensor (6µT in Bx & By or 9.7 µT in Bz). The $\mathbf{R_{ratioBMagnitude}}$ responsivity method is considered a more attractive tracking method as reducing tilt angle direction prediction to a singular trigonometric function improves computational and memory demands on the system. However, the drawback of this method is that it cannot be extended to measuring orientation to three degrees of freedom or measuring position.

The look up table method required access to a data set ($65 \times 359 = 23{,}335$ entries). Larger data sets will slow the speed of the searching function and so limit the frequency of the orientation sensing output. Operating speed was not an issue in this experimental testing yet if the system were to be adapted to include a third degree of freedom, then the data set would reach 8.4mil values ($65 \times 359 \times 359 = 8{,}377{,}265$) in which case computational performance may begin to impact sensing frequency. Training a Neural Network produces a single function making it more computationally efficient than a look up table. This advantage will become more apparent if additional degrees-of-freedom are added which would increase the size of the orientation or position states dataset. However, as the function is generated from a neural network there are inherent inconsistencies. Models trained using the same method and same dataset, may be slightly different which will make standardising the method challenging.

Two degrees-of-freedom orientation tracking showed utility as a means of measuring and reporting the occurrence of a component-component impingement event. Tilt angle at impingement and azimuth angle about the face of the cup is arguably a visually clearer way of reporting the location of a component-component impingement event. To the authors knowledge this work has been the first to integrate a magnetic position and orientation sensing system into total hip replacement components and one of the first to develop a sensing system method to detect the occurrence and location of a component-component impingement event in total hip replacement components.

Tracking orientation to two degrees-of-freedom (tilt angle and azimuth angle) is a limitation of this work as it does not capture the full orientation of the stem meaning orientation cannot be reported to the user in the clinical convention of flexion/extension, abduction adduction and internal/external rotation. The current MPO implementation using the M1 magnet has a symmetrical magnetic field distribution in the XY plane therefore rotation about the Z axis does not elicit a complete response and so the rotation angle of the stem cannot be determined using the present configuration. This suggests that deliberately creating magnetic field asymmetry may enable tracking of the additional required DoF. Previous groups (Ermakova et al., 2018; Lumetti et al., 2020; Malagò et al., 2020) developed three DoF orientation tracking MPOs in which they engineered asymmetry in their systems by using magnets magnetised laterally and having the magnet or sensor positioned asymmetrically. This enabled them to detect the stem rotation angle of their joysticks. The magnet and sensor positioning constraints (as specified in the design specification in Section 4.3) meant there was little scope to displace the magnet and sensor hence why configuring the MPO in such a way was not fully explored during this PhD project. Nevertheless, the theme of future work will be to extend the sensing capabilities of the system to measure orientation to three degrees-of-freedom.

Chapter 6 Development of a magnetic position and orientation sensing system for measuring bearing contact surface separation during an impingement driven subluxation event in total hip replacements

Total hip replacement bearing surface separation can occur during swing phase of gait cycle, edge loading, subluxation and dislocation (Amstutz et al., 1975; Scifert et al., 1999; Williams et al., 2003; Usrey et al., 2006). Furthermore, long term wear of the bearing surfaces can cause the femoral head to penetrate the surface of the liner. The quantification of this displacement is used to calculate/estimate linear/volumetric wear rates (Geerdink et al., 2008; Grillini and Affatato, 2013). Many of these phenomena have been investigated within experimental hip simulators (Williams et al., 2003; O'Dwyer Lancaster-Jones et al., 2018). Therefore, tracking the translation of the femoral head component with respect to the acetabular cup and liner would be an important aspect of monitoring the mechanical function of a THR and characterising adverse events in-vitro and in-vivo.

Ortner et al., (Ortner et al., 2018) previously presented a MPO sensing system for measuring absolute linear displacement using a permanent magnet and three axis magnetic field sensor. Jones et al., (Jones et al., 2020) developed a MPO sensing system for tactile force sensing. Their system featured a permanent magnet embedded in elastomer and positioned above a three-axis magnetic field sensor. Movement of the magnet in 3D space induced change in the sensed magnetic field which they calibrated (using a neural network) to the three DoF shear force applied to the elastomer protrusion of the sensing node. A similar method can be applied to the present system in which an MPO sensing system can be calibrated to output the 3D movement of a permanent magnet.

Impingement driven subluxation occurs following an impingement event in which the femoral head is levered out of the liner component, as shown in the schematic in Figure 77. Although a complex mechanical motion the working hypothesis is that impingement driven subluxation can be measured using an

MPO operating a Look Up table tracking method. The Look Up table could be populated with position and orientation states that correspond to the centre of the femoral head being at several discrete distances from the joint centre of rotation along a pathway that the centre of the femoral head would follow during a typical impingement driven subluxation event motion.

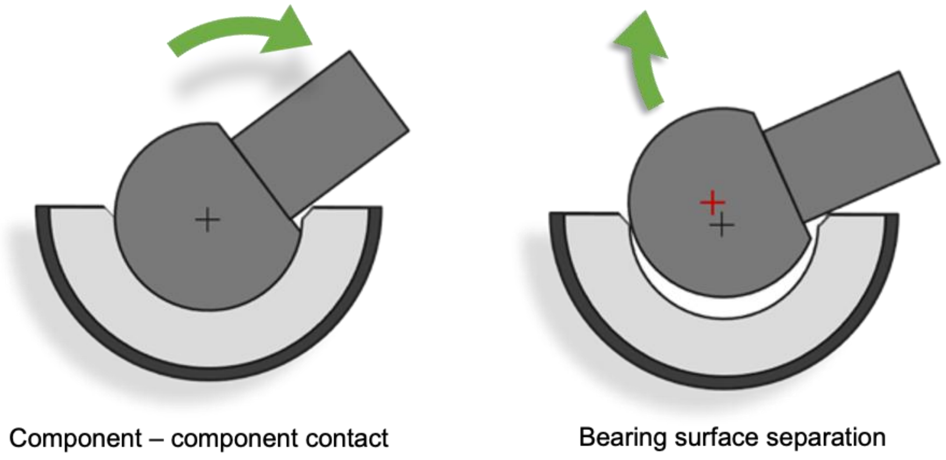

Figure 77 - Diagram of THR component - component impingement event progressing to an impingement driven subluxation event which results in the centre of the femoral head translating from the joint centre of rotation and the bearing contact surfaces to separating.

However, replicating the same method described in Chapter 5 in which magnet positions are defined through simulations, would be unsuitable as mathematically determining the path the centre of the femoral head would be complex due to the nature of a typical impingement driven subluxation motion. An alternate approach was to experimentally recreate an impingement driven subluxation event and use the recorded position and orientation data (that describes the translation of the centre of the femoral head) to produce the simulated magnetic field data for a look up table. The look up table tracking method then returned the distance the centre of the femoral head has translated from the joint centre of rotation thus giving an indication of the severity of the impingement driven subluxation event. Additionally, the location of the impingement point was predicted by returning the Azimuthal angle of the stem evaluated using the same direct trigonometry method described in Section 5.2. Arami et al. (2011) used a similar methodology in calibrating their instrumented knee implant which featured a permanent magnet) affixed to the femoral component) and three three-axis anisotropic magneto resistance sensors (embedded in the polyethylene insert). They used an optical motion capture system to record the orientation of the knee components (in flexion/extension and abduction/adduction) to train a neural network to map the recorded magnetic field data to the orientation of the components.

This section presents the work carried out to develop a MPO sensing system to measure the relative positions of THR components during a mechanical motion unique to THR components. This motion was replicating THR bearing surface separation because of impingement driven subluxation where component impingement causes the femoral head to leaver out of the cup. Development of this MPO sensing system was done experimentally and required a novel camera tracking system to measure bearing surface separation which was used to calibrate and later validate the performance of the sensing system experimentally.

6.1 Chapter Objectives

1. To recreate an impingement driven subluxation event between the THR components.
2. To record the distance the centre of the femoral head was displaced from the joint centre of rotation during an impingement driven subluxation event.
3. To characterise the accuracy and reliability of the sensing system when measuring THR bearing contact surface separation during the impingement driven subluxation event.

6.2 Experimentally generated magnet position and orientation data for generating magnetic field dataset for a magnetic position and orientation sensing system

The impingement driven subluxation motion was performed with the stem being rotated to a maximum angle of 74°. Using the method described in Section 3.2.3, the camera tracking system (CTS) recorded experimental data on the position of the centre of the femoral head, and the position and orientation of the reference magnet. A scatter plot of the inferred position of the centre of the femoral head and the inferred position of the magnet in the Z direction, is shown in Figure 78. The data presented is from the start of the impingement driven subluxation protocol to the peak displacement of the femoral head. The plot is centred at the centre of rotation of the joint. The initial peak of both values to 7mm was the verification motion programmed at the start of all impingement driven subluxation protocols performed on the robot arm. This was used to verify that the CTS was returning position values to a satisfactory level of accuracy. The first occurrence of component contact and so the beginning of the impingement driven subluxation event can be identified as the sudden increase in the position of the centre of the femoral head as this signifies the centre of the femoral head being displaced from the joint centre of rotation. The end of the impingement driven subluxation motion was defined as when the displacement peaked. Data values (of magnet position in the X and Z direction and magnet orientation in the tilt angle direction) over this period were extracted (using the method described in Chapter 3) and passed to the Magpylib script to generate simulated magnetic field data for the look up table. Twenty-five values were recorded during the subluxation event and used to populate the look up table. The range of position in the Z direction prediction was 0mm to 3.14mm, and the mean step size between values or effective resolution was 0.15mm. As the magnet position and orientation data is generated experimentally the effective resolution of the system cannot be controlled. The resulting resolution is determined by the distribution of the position data readings recorded during the full impingement driven subluxation motion. Furthermore, there were instances of repeated orientation and position values within the look up table data however these were deemed to have no effect on sensing performance.

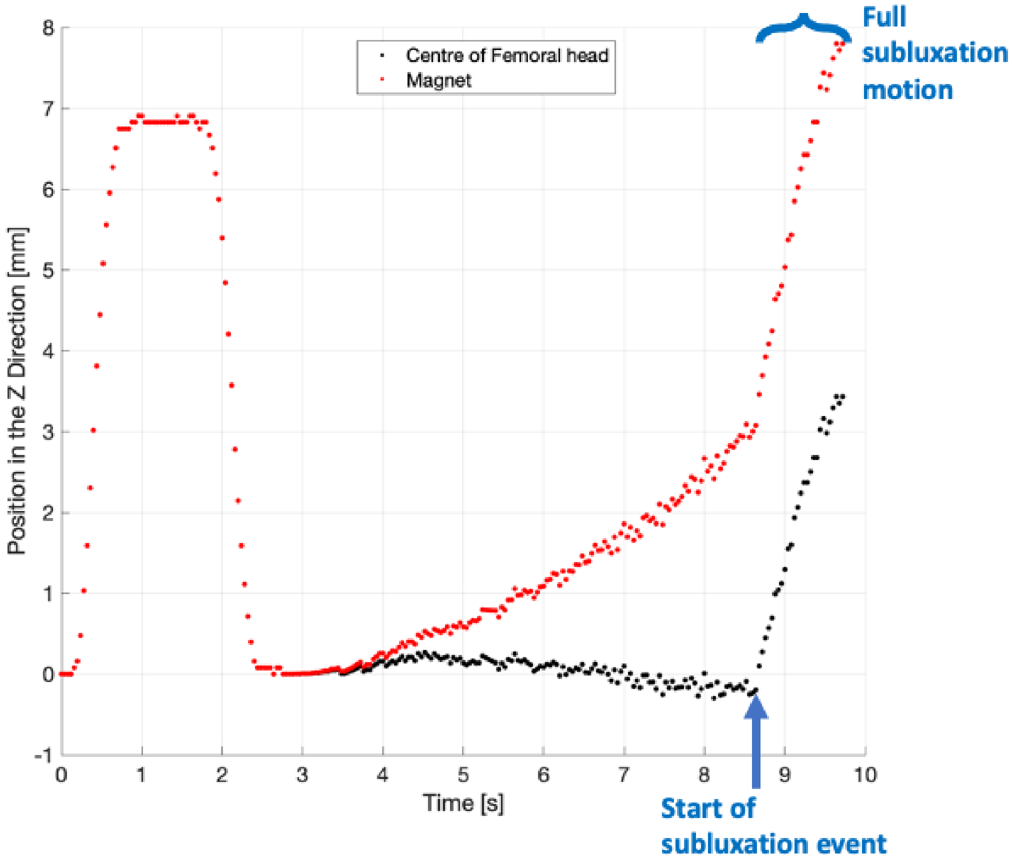

Figure 78 - Scatter plot of the inferred position of the centre of the femoral head and magnet during a single impingement driven subluxation event where the joint centre of rotation is at 0mm.

6.3 Method: Bearing contact surface separation study

The impingement driven subluxation motion test protocol began with the robot arm rotating the stem until the stem and liner components contacted. The continuity switch was used to detect the component contact and triggered the robot arm to return. This recreated an impingement event but no bearing surface separation so not an impingement driven subluxation event. The stem was then rotated to three angles beyond the normal working range of the components (beyond a tilt angle of 64°) namely, 70°, 72° and 74°. These angles were chosen as they created three distinct impingement driven subluxation events with evenly distributed levels of femoral head displacement. Following each impingement driven subluxation event, the stem was returned to a tilt angle of 45°. The full routine was repeated three times.

The sensing system recorded femoral head translation throughout the duration of the test and the robot arm recorded stem orientation and impingement continuity occurrence at their maximum sampling rates of 50Hz and 125Hz respectively. At the start of each test run the robot sent a trigger signal to the microcontroller which meant the data from the two sources could be synched. The recordings of the motion protocol were manually inspected frame by frame and the researcher judged the first occurrence of the femoral head moving out of the liner which indicated the start of the impingement driven subluxation. The camera recorded at a frame rate of 25 frames/s which resulted in the CTS recording position and orientation at 25Hz. To obtain datasets of the same size for statistical analysis timestamps of the extracted CTS coordinate data were matched to the closest timestamps of the sensor and robot data. The remaining sensor and robot data was omitted leaving datasets of the same size.

To evaluate the performance of the MPO sensing system four comparisons were made and error was computed using Equation 2:

1. The error between the robot reported (expected) and the CTS reported tilt angle (observed).
2. The error between the robot reported (expected) and the sensing system predicted tilt angle (observed).
3. The error between the CTS reported (expected) and the sensing system predicted tilt angle (observed).
4. The error between the CTS reported (expected) and the sensing system predicted position in the Z direction (observed).

The RMSE (Equation 3) ± standard deviation (SD) was computed from after the verification movement to the end of the test (i.e. after 2.5 seconds) across the three repeats.

6.4 Results: Bearing contact surface separation study

The plot of the robot arm recorded stem tilt angle, the CTS measured stem tilt angle and the MPO sensing system predicted stem angle, is shown in Figure 79. The data shown is for all three repeats of the subluxation protocol in turn. The RMSE (± standard deviation) of the reported stem tilt angle over full dataset, for the robot arm versus the CTS, the robot arm versus the MPO sensing system and the CTS versus the MPO sensing system were 3.0° ± 3.0°, 3.5° ± 3.3° and 1.1° ± 0.9° respectively.

The plot of the CTS recorded position and MPO sensing system predicted position of the centre of the femoral head in the Z axis with respect to the joint centre of rotation, is shown in Figure 80. The data shown is for all three repeats of the impingement driven subluxation protocol in turn. The RMSE (± standard deviation) of the reported position over full dataset for the CTS versus the MPO sensing system was 0.2mm ± 0.18mm.

The key findings from this study were:

1. The higher level of reported stem tilt angle error when the MPO sensing system and camera tracking system are compared to the robot arm. The CTS and MPO sensing system showed greater level of agreement and reported higher peak tilt angles than the robot arm.
2. The MPO sensing system was able to distinguish between the different severity levels of an impingement driven subluxation event and not report a false negative when only an impingement event occurred with no bearing surface separation.

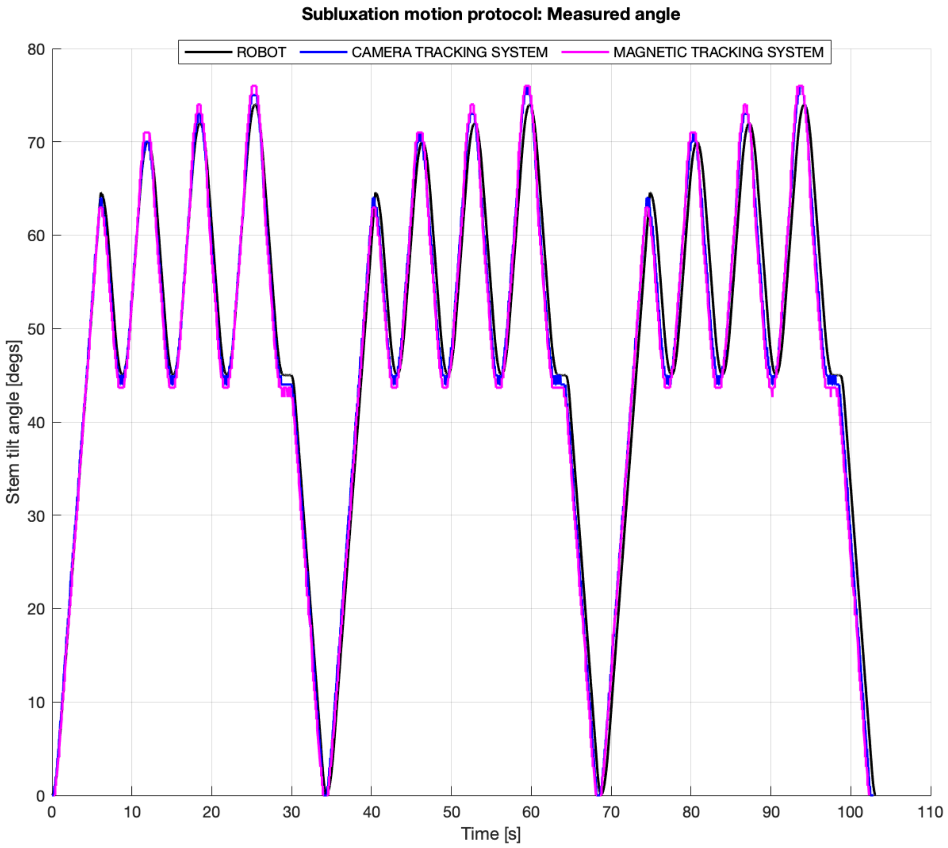

Figure 79 – Plot of the reported stem tilt angle, during the three repeats of the impingement driven subluxation motion protocol, by the robot arm, the camera tracking system and MPO sensing system.

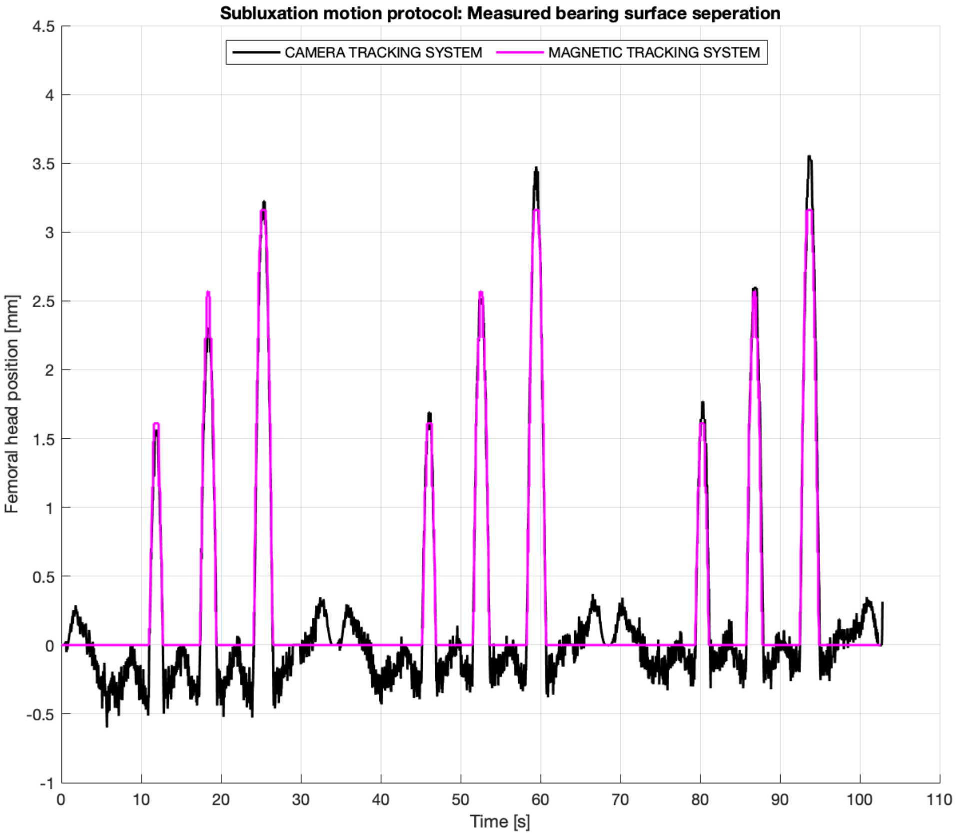

Figure 80 – Plot of the reported centre of the femoral head position, during the three repeats of the impingement driven subluxation motion protocol, by the camera tracking system and MPO sensing system.

6.5 Discussion: Bearing contact surface separation study

The aim of this study was to explore if a magnetic position and orientation system can be used to track the distance the centre of the femoral head was displaced from the joint centre of rotation during an impingement driven subluxation event.

The lower level of error between the CTS vs the MPO sensing system is because in this test the orientation measured by the CTS was used to calibrate the MPO sensing system. The CTS and the MPO sensing system reported greater tilt angles than the three peak angles the robot was programmed to reach. This is because the robot arm reports the orientation of the tool face and so if the stem component can flex or can move with respect to the tool face the true angle of the stem is not being reported. Whereas the CTS and the MPO sensing system were reporting the true angle of the stem hence why there was less error between the reported tilt angle of these systems.

The MPO sensing system reported position showed good agreement to the “ground truth” camera tracking system reported position. However, impingement driven subluxation was only assessed in one direction and in one plane. Theoretically the MPO sensing system could track the displacement of the centre of the femoral head and report the location of the stem in the azimuthal angle direction around the full circumference of the rim of the liner. Yet, the current experimental setup is not configured to verify the outcome of tracking subluxation at multiple locations around the rim of the cup so this capability could not be explored.

The level of error reported by the camera tracking system (RMSE ± Standard Deviation 0.26mm ± 0.24mm and 0.14mm ± 0.23mm in the X and Z direction respectively) was deemed sufficient for this work in Section 3.2.3. Yet, Figure 80 shows the camera tracking system reported a lot of noise (max >-0.5mm) when the femoral stem was located in the liner where displacement should have been 0mm. This will have been a result of the limitations discussed in Chapter 3. There is still potential for improving the camera tracking system method by sourcing a higher resolution camera or recording in monochrome with retro-reflective markers thus reducing the noise incurred from the coloured marker tracking. However, with the law of diminishing returns it may be more practical to use a commercially available system. Furthermore, in the future it is desired to progress from tracking femoral head movement during an impingement event subluxation event in a single plane to tracking position and orientation in 3D space. This will inherently increase the complexity of the system and might not be achievable with the current set up. Therefore, using a commercially available system like the OptiTrack which can achieve an error of <0.1mm in smaller measurement zone (OptiTrack, 2023), would be desired for future work.

When simulating an impingement driven subluxation event, the robot arm did not apply force axially the through the stem. This meant the femoral head was not pushed up the far side of the cup of the liner which typically happens during an impingement driven subluxation event (Usrey et al., 2006). Instead, displacement in the X axis was typically <0.8mm during an impingement driven subluxation event hence why only displacement in the Z axis was reported as this was the more significant contributor to the magnitude of the displacement. Therefore, the protocol used in this work was not a true recreation of an impingement driven subluxation event. However, what has been achieved is a method of replicating a unique mechanical motion with THR components and experimentally generating magnet position and orientation data to populate a look up table to form a MPO tracking method. Which can then be used to measure the position and orientation of the THR components when the unique motion is repeated. Therefore, it is hypothesised that if an alternate and more accurate method simulating an impingement driven subluxation event (and measuring the resulting femoral head displacement) is found, a MPO sensing system developed using the same methodology presented in this section would show a similar level of tracking performance.

6.6 Summary of femoral head position tracking using a single sensor magnetic position & orientation tracking system

Femoral head position tracking out of the liner during an impingement driven subluxation event has been achieved. This method was validated using a custom camera tracking system and was shown to accurately determine the occurrence and severity of an impingement driven subluxation event. However, the method of creating an impingement driven subluxation event was not biomechanically representative and the performance of the tracking system was only validated in a single plane. The design specifications that have been satisfied following completion of the work in this chapter are shown in Table 15.

Table 15 - Design specification evaluation for a prototype instrumented THR prosthesis CONTINUED.

Requirement	Specification	Evaluation
Measure component centre of rotation translation/separation of bearing contact surfaces	**Red** – Determine displacement of components to resolution >1mm. **Green** - Determine displacement of components to resolution <1mm.	**Green –** Effective resolution 0.15mm.
	Red - Accuracy 2mm to 1mm. **Green –** Accuracy <1mm.	**Green –** RMS **e**rror 0.2mm.

To the authors knowledge this work has been the first to integrate a sensing system within THR components to track impingement driven subluxation within THR components. This is a proof-of-concept prototype yet if this sensing system was integrated into an instrumented implant capable of in-vivo sensing the system could measure impingement driven subluxation events in real time. This could be used to inform the clinician on suggesting changes to the patient’s lifestyle, activity level or need for surgical intervention. The data gather in-vivo or in-vitro would help improve the understanding of the causes and mechanics of subluxation.

Chapter 7 Overall Discussion and Conclusions

7.1 Context of Research

The aim of this thesis was to integrate sensing systems into clinically available total hip replacement components to provide clinically relevant metrics related to performance. The challenges associated with developing an instrumented hip implant for clinical use were identified as choice of sensor, biocompatibility and integration within the implant, power, communication, and regulatory considerations. Choice of sensing method needed to be addressed first and so was the aspect of focus within the scope of this PhD. Development of this sensing system prototype required consideration of the following:

1. What phenomena should be detected?
2. What sensing method could be used?
3. Where can the sensing system components be positioned so as to not disrupt the function of the bearing?
4. How to test and validate the performance of the prototype?
5. Can the sensing system produce data to a clinically relevant degree of accuracy?

The majority of previous work relating to in-vivo sensing within hip implants had focused on measuring joint forces and moments (G Bergmann et al., 2001; Damm et al., 2010). Data gathered using these implants was later used to validate many computational and experimental models, improve component design and surgical technique. The direction chosen for the present study was to develop a sensing method to quantify the relative orientation and position of THR components. Tracking component kinematics is vital to the function of orthopaedic implants (Arami et al., 2011). Measuring joint forces and moments is needed to characterise joint kinetics yet, tracking component kinematics will be more important when determining metrics such as joint range of motion, step count, impingement and impingement driven subluxation. This explains why patient monitoring systems capable of recording joint kinematics and extracting objective metrics relating to patient recovery post orthopaedic surgery are starting to be used clinically for example, in wearable systems such as TracPatch (TracPatch Health, 2021) and MotionSense (Stryker, 2023). Furthermore, one of the most significant recent advancements in the field of arthroplasty has been the Personna IQ (Zimmer Biomet, 2023); the first in-vivo smart knee replacement enabled with an IMU capable of monitoring patient step count, cadence and functional range of motion (Orthopaedic Design & Technology, 2021; Zimmer Biomet, 2023). This uptake in smart sensor and telemetry enabled devices to monitor patient kinematics following joint replacement surgery has validated the decision/direction chosen for the present study.

7.2 Assessment of methods and developed sensing system

Experimental in-vitro hip simulators are used routinely in the pre-clinical testing of joint replacement components [for example, as specified by ISO 14242]. They are configured to replicate anatomical human hip angular movements, loading, speed and lubrication and are used to characterise implant component wear (Williams et al., 2003; Ali et al., 2016; Hadley et al., 2018; O'Dwyer Lancaster-Jones et al., 2018). Yet testing is burdensome in terms of time and these machines are costly >£300,000, in high demand and highly specialised. Therefore, it was apparent that such a simulator would not be suitable for the development of a novel sensing system. The use of robotic arms has seen a surge in uptake and is now considered a “gold standard” method for in-vitro biomechanical natural hip joint testing (Daou et al., 2019; Rychlik et al., 2023) and have been used previously in testing joint replacements (Herrmann et al., 2015; Kebbach et al., 2019; Maag et al., 2021). These systems all used industrial robotic arms capable of applying the cadaveric hip samples and joint replacement components with loads representative of anatomical joint force vectors. The robot arm used for this work was not capable of applying anatomically relevant loads consequentially loading was not introduced into the experimental testing methodologies. However, the focus of this work was on tracking component kinematics without consideration of the forces acting on the components. Therefore, the UR3 robot arm was a suitable method of simulating the kinematics of the simplified ball and socket hip joint model and recreating adverse events unique to THRs such as component impingement and bearing surface separation. To progress development of the prototype with further testing and validation an alternate hip simulation method (e.g. in-vitro experimental hip simulators or higher specification industrial robotic arms) would be needed to better simulate the mechanical environment of a human hip. This would allow further investigation into whether the sensing system can be used in tracking features of the human gait cycle and see if the results reported in Chapter 6 can be replicated when tracking femoral head position during impingement driven subluxation when the femoral stem is under physiologically relevant axial loading.

The accuracy, sensitivity and sensing range, of the magnetic position and orientation sensing system developed in this project cannot be directly compared to other magnetic position and orientation (MPO) sensing systems discussed in this work. Ermakova et al. (2018) Malago et al. (2020), Lumetti et al. (2020) and Lutz and Foletto (2019) all developed MPO enabled joysticks or multimedia control elements meaning the system configurations and design constraints were different from the present work. The work in this PhD built upon previous work on tracking methods and the methods of MPO system design and optimisation. Simulated optimisation studies were performed to maximise the minimum state separation of the MPO implementation similar to studies performed by Ermakova et al. (2018), Malago et al. (2020) and Lumetti et al. (2020). Magnet responsivity tracking methods were investigated using similar simulated error analysis studies to that performed by Lutz and Foletto (2019). However, the present work explored more comprehensive examples of component positioning errors and alternatively compared the simulated absolute angle error thus giving a clearer indication of the resultant error in angle prediction.

The most comparable study to the present work is that published by Arami et al. (2011; 2013; 2014) in which they integrated three magnetic field sensors and a permanent magnet into total knee replacement (TKR) components to track the component orientation to two degrees-of-freedom in the flexion/extension and abduction/adduction directions. They experimentally gathered magnetic field data from the sensor whilst the orientation of the TKR components were recorded by an optical tracking system. They then trained a neural network with the gathered data and evaluated the algorithms accuracy in relating magnetic field data back to the orientation of the components.

Therefore, there are similarities between the experimental methods used in this PhD work and the work conducted by Arami et al. They reported achieving a RMSE error in flexion/extension and abduction/adduction of 2.35° and 0.31° over the angle ranges of 138° to 192° and -8° to 4° respectively. This is comparable to the RMSE error achieved in this thesis namely 1° tilt angle direction and 4.2° in azimuth angle direction particularly when you consider that Arami et al. were measuring over a smaller sensing range. There is scope for the methods described in this PhD to be translated into a sensing system for use in a TKR prosthesis. When compared to the sensing system developed by Arami et al. it is anticipated that such a system would require a single three-axis magnetic field sensor thus simplifying the system, measure relative displacement between the TKR components and achieve a similar effective sensing range and level of error in orientation tracking.

7.3 Conclusion

This thesis is the first to show that a magnetic position and orientation sensing system can be used within a THR to measure the kinematics of the implant components. The output of the sensing system can measure the orientation and position of the components to a clinically relevant level of accuracy and detect the occurrence of adverse events unique to THRs including component impingement and bearing surface separation during impingement driven subluxation. The sensing system was integrated into the components without altering the geometry of the components and more importantly without disruption to the functional bearing surfaces therefore, there was no impact on the function of the implant. The sensing system is real-time, non-contact, low power (3.3v) and uses readily available off-the-shelf components. This preliminary development work has resulted in a functional engineering prototype. No other commercially available systems or published sensing methods known to the author, can be integrated into THRs in a similar manner, and detect THR bearing surface separation during impingement driven subluxation. This proof-of-concept prototype sensing system described in this thesis could be easily adapted and integrated within in-vitro experimental hip simulation testing methodologies. This would be a valuable research tool that investigators can use to further understand the mechanical environment of a hip implant. The data gathered can be used to inform new improvements in implant design, surgical technique and post operative care. With further development this sensing system could eventually be featured within a clinically available in-vivo sensing enabled THR prosthesis. This system would allow surgeons, healthcare workers and patients to continuously track the function of the implant and assess the ongoing risk or occurrence of adverse events e.g. component impingement or impingement driven subluxation. This data could be used to learn more about the function of THR components within patients and improve the convenience and quality of post-operative patient care.

7.4 Limitations

Some limitations of the work presented in this thesis were:

The chosen orientation representation created mathematical singularities.

The rotation, tilt, and azimuthal angle [φ, θ, ψ] notation AKA Y-notation (ZYZ Euler angles) was valuable for intuitively representing and visualising stem orientation in a clinically relevant way, describing the location of an impingement contact point and simplifying stem orientation to two degrees of freedom. A limitation of this mathematical representation is the occurrence of singularities in the azimuth angle. Firslty, when tilt angle was zero i.e. when the stem was in the neutral position and secondly, when the stem crossed the azimuth angle value of 0°/360°. Both instances led to high levels of noise in the reported azimuth angle (maximum theoretical error 360°) when the stem was in these regions. To mitigate the effect of singularities the recorded experimental data when stem tilt angle was <4° and when stem azimuthal angle was >355° or <5° was omitted which was necessary to avoid exaggerating the evaluated quantitative error.

A clinically available femoral stem component was not used throughout this project.

Clinically available CoCrMo femoral head, CoCrMo acetabular shell and a polyethylene liner were used throughout this PhD however a simplified 3D printed PLA spigot style stem was used. Additionally, the assembled THR components were simplified to a ball and socket joint. The justification for this was that it made development and testing more convenient. However, it does mean that an additional body of work will be needed to show that when a clinically available femoral stem component is used there is no change in the performance of the sensing method.

Stem orientation was only considered in two degrees-of-freedom throughout this work.

Configuring the developed MPO sensing system to predict stem orientation angle to three DoF was not fully explored. This did mean that the orientation of the stem could not be fully defined and so could not be presented using the common clinical notation i.e. Flexion/Extension, Abduction/Adduction and Internal/External rotation. Work lead by Michael Ortner including the publications (Ermakova et al., 2018; Lumetti et al., 2020; Malagò et al., 2020) has shown that orientation tracking to three DoF can be achieved with a single 3-axis magnetic field sensor MPO sensing system. Ortner's group were developing multimedia control elements/joysticks and so there was more flexibility in the mechanical design of their system. Therefore, there was scope for them to position the magnet and sensor asymmetrically with respect to the central axis of the joystick. The asymmetry of the system meant each individual orientation state elicited a unique magnetic field at the location of the sensor which allowed the creation of a complete 3 DoF MPO sensing system. In the present work the integration of the sensing system into the THR components was to incur no changes to the geometry of the components in particular the bearing contact surfaces as stipulated in the design specifications. This meant holes or recesses could not be drilled or machined into the components and so there was little opportunity to position the components asymmetrically within the components of the THR. Additionally, the maximum tilt angle used by Malago et al. (Malagò et al., 2020) was a third of that required in this work at 15° meaning that it was less demanding than that required by the present study. The greater required sensing range would be a more demanding system resulting in poorer sensing performance or a non-complete system.

Disparity between sensor output frequency and "ground truth measure" output frequency.

The difference in the polling rate of the sensor and the robot arm would have introduced time synching errors when comparing the outputs from the two systems. The impact of this disparity is minor nevertheless, an alternative would have been to evaluate the error between the outputs at defined locations whilst the robot is stationary. However, this would not allow analysis of the sensing systems performance whilst the robot was moving between locations hence why this method was not used.

7.5 Future work

7.5.1 Short-term future work

Future development, testing and validation should address the remaining design requirements and improve the underlying functionality of the technology and the sensing system. Specific areas to consider are as follows:

Satisfying remaining design specifications.

The design specifications pertaining to integrating the sensing system within the THR components were not fully satisfied. This included the sensing system being functional in all implant material combinations (metal-on-polyethylene, ceramic-on-polyethylene and ceramic-on-ceramic) and in all implant component sizes (head/cup size 22mm to 56mm) which were not explored due to time and component availability constraints. To investigate the impact of different THR component material combinations a similar approach described in Section 4.9 “Impact of metal (CoCr) total hip replacement components on magnetic field could be used. To show that the sensing method could be translated to alternate size components the simulations and experimental verification studies would need to be repeated to validate functionality and to see if component sizing impacts sensing error.

Improving the experimental impingement driven subluxation model.

A method of simulating a more biomechanically accurate impingement driven subluxation event is needed to repeat the bearing contact surface separation testing presented in Section 6.4. This will likely be achieved by using validated in-vitro experimental hip simulators (O’Dwyer Lancaster-Jones et al., 2018) or using a more capable robotic arm like that used (Herrmann et al., 2015; Daou et al., 2019). Additionally, improvements to the presented camera tracking system will need to be explored or alternatively a new method of characterising femoral head translation within a liner will be sourced, to improve the calibration and validation of the sensing system.

Optimisation of orientation states for improved state separation and sensing performance

The spacing of the orientation states included in the sensing range could be adapted and optimised to improve sensing performance. This could include reducing the range to reflect the maximum achievable ROM of a human hip joint i.e. Flexion/Extension 120º/30º, Abduction/Adduction 45º/35º and Internal/External rotation ±45º (Turley et al., 2011). The spacing of the orientation states could be optimised to create a more even distribution across the 1. effective translation of the magnet or 2. sensor read magnetic field at each orientation state. This spacing could be selected to reflect the desired state separation i.e. the sensitivity of the sensor. As previously stated, this could be achieved by staggering the azimuthal angle step size over the range of tilt angles. For example, when tilt angle is <10° azimuthal angles could have steps of 45° so 8 steps across the full 360° range and when tilt is >10° azimuthal angles steps could remain at 1°. Additionally, the set of discrete orientation locations could be determined by mathematically selecting locations that are evenly separated across the full sensing region. This could be achieved using an algorithm like that of the Fibonacci sphere algorithm.

Exploration into extending the sensing capabilities of the MPO sensing system to orientation tracking to three DoF.

Revoking the design requirement that there should be no alteration to the component geometries would allow more scope to position the magnet or sensor within the body of the liner, femoral head, or acetabular shell component. The magnet or sensor could then be positioned away from the central axis of the components thus creating the asymmetry needed to realise a complete MPO sensing system. Additionally, more 3-axis magnetic field sensors could be introduced into the system thus increasing the sensed magnetic field degrees-of-freedom. This could improve the performance of the current two DoF sensing performance but may also extend the sensing capabilities to three DoF or six DoF if position and orientation can be tracked simultaneously. Additional sensors will increase the complexity of the system yet if more sensing DoF are achieved then this would be a worthwhile trade-off.

Feature recognition for characterising THR kinematics, function and use during activities of daily living.

A higher-level approach could be employed for feature recognition and extracting metrics to characterise common activities of daily living (ADL) or adverse events that might occur within a THR e.g. steps, cadence, unusual gait cycle pattern or subluxation. Currently, the sensing system is configured to output the position and orientation of the components and so additional functionality will be needed to recognise common ADL or adverse events. Alternatively, the sensed magnetic field data could be matched directly to the magnetic field response when the implant components are put through the motion of for example a "normal" gait cycle or an adverse/abnormal gait cycle. The system could be trained on large data sets of patient gait data during ADL (e.g. (Khan and Badii, 2019; Luo et al., 2020; Ghorbani et al., 2021; Girase et al., 2021) and configured to output the activity recognised from the sensed magnetic field response and give a score depending on whether the motion was normal or abnormal.

Accounting for Earths Latent magnetic field

In-vivo the pelvis, femur and respective THR components will not remain at a fixed orientation with respect to the Earth. The Earth's latent magnetic field can vary between 25 microT to 65 microT depending on the location on the Earth's surface (NOAA - NCEI, 2024). This would have a significant impact on sensing performance as the upper bound of the Earth's latent magnetic field is greater than the minimum Q Factor of the MPO implementation for measuring orientation to two DoF. Figure 67 below from Section 5.4.3 Results of the simulated optimisation study shows the plot of the nearest neighbour magnetic field vector distances ($|_{NN}B|$) when tilt and azimuth angle increases by 1° starting at 0°. The $|_{NN}B|$ of the tilt angle varies meaning that the minimum and maximum error as a result of Earth's maximum magnetic field would be 1° to 2°. The $|_{NN}B|$ of the azimuth angle varies and tends to zero meaning that the minimum and maximum error would be 4° to 60°.

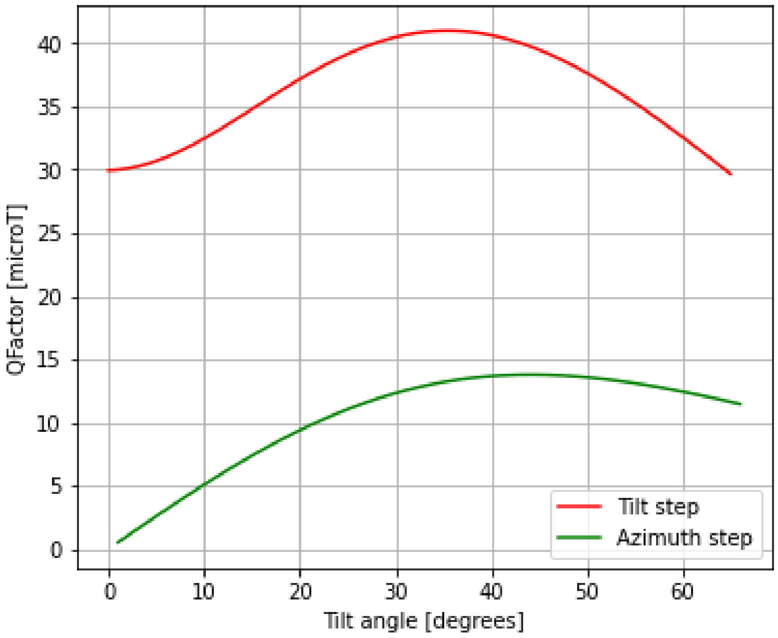

Figure 67 – The nearest neighbour magnetic field vector distances (|$_{NN}$B|) when tilt state increases by 1° starting at 0° (RED) and |$_{NN}$B| when tilt angle is constant, and the azimuthal angle state goes from 0° to 1° (GREEN), data shown is for the M1 magnet configuration.

So future version of the final sensing system will need to account for this. This could be achieved by using a secondary magnetic field sensor located outside the magnetic field of the reference magnet. In operation the resulting residual magnetic field could then be subtracted from the primary sensor's output. Alternatively, an IMU could be included within the system to provide a means of measuring pelvic or component orientation with respect to gravity. The output of the MPO sensing system could then be corrected algorithmically or the orientation measured could be reinforced by the output of the IMU.

Translation into experimental in-vitro hip simulation testing

This would show the utility of the prototype sensing system developed in this project as a research tool and provide additional opportunity for testing and validation. To achieve this additional design specification have been considered and are shown in Table 16. Testing could be initially done using protocols investigating component impingement within THRs for example (Pryce, 2019; Pryce et al., 2021; Williams, 2022). The ability of the sensing system to report the occurrence and location of an impingement point could be compared to the results in these studies. As previously stipulated, repeated validation and further testing of the bearing contact surface separation tracking could be performed following similar testing protocol to (O'Dwyer Lancaster-Jones et al., 2018).

Table 16 - Additional design specifications for instrumented hip implant to be used in experimental in-vitro hip simulator testing.

Requirement	Justification	Specification
Operate in Six dof experimental hip simulator	Hip replacements are contained in lubricant gaiters during testing so as to provide lubricant and mimic in-vivo environment during experimental testing (Williams et al., 2003; O'Dwyer Lancaster-Jones et al., 2018; Hadley et al., 2018). Without sufficient lubricant, hip replacements can only be run for approximately 1000 cycles.	**Red** – Has to be run out of gaiter (dry) **Green** – Fully waterproof and functional within lubricant filled gaiter.
	Wear test protocols for artificial hip joints should reach 5 million cycles as specified by ISO 14242-1, so sensing system will have to remain functional (but not necessarily record data continuously) for the full length of the test.	**Red** - 1k – 5mil **Green** - >5mil
	Adaptation or changes to current experimental simulators fixtures or test protocols will be an inconvenience to investigators and may impact results	**Red** – Requires new/adapted fixtures and fittings of simulator **Green** - Function within existing fixtures

7.5.2 Long-term future work to enable clinical use

The remaining challenges associated with developing the technology presented in this thesis to feature within an in-vivo sensing system for use within a THR include:

Biocompatibility and integration within the implant components

An alternate integration method is needed to satisfy the biocompatibility requirements for use of an in-vivo sensing system within a THR prosthesis. The possible sensor or magnet locations identified and used in this project included 1.) the region between the taper face and the femoral head face 2.) within the introducer hole and backside region of the THR shell. These regions were identified because they were existing features, were regions of comparatively low internal stresses, were surrounded by 'hard' material (i.e. metal CoCr not soft bearing material polyethylene) and were not near the functional bearing surfaces. However, the introducer hole region may not be suitable for all the accompanying electronics components needed for wireless powering and communication. Future work could look at positioning the electronic components within a chamber drilled or machined into the stem. A top plate could be welded to the top face of the taper thus creating a hermetically sealed chamber that is capable of separating the electronic components from the body’s tissue (Joung, 2013). This proposed method is similar to that used by Damm et al. (2010) and Bergmann et al. (2012). The magnet could also be sealed within a metal die (CoCr matching the material used for the rest of the component or medical grade stainless steel) with a thread that matches that of the introducer hole. The surgeon could then screw in the die during surgery once the acetabular shell has been positioned in the pelvis.

Regardless of the integration method the implant will need to pass appropriate biological and biochemical testing. This should include cytotoxicity testing, examination of the immunological and pathological effect on surrounding tissue and characterisation of the expected degradation of the implant’s material over the lifetime of the implant as per the recommendations of ISO 10993 or other such standards.

Power

The most appropriate battery to power the proposed in-vivo sensing system needs to be determined. A compact and high energy density battery e.g. lithium ion (Bock et al., 2012; Amar et al., 2015), would be the most suitable approach for powering an instrumented THR. This type of battery is already in clinical use in a similar application as the powering method used in the Persona IQ (Cushner et al., 2021; Zimmer Biomet, 2023). Battery selection is a multifactorial optimisation problem dependent on the size constraints of the implant package, and the power demands and power consumption of the combined telemetry and sensing system.

Once the design of the sensing and telemetry system has been finalised the power demands of the system will be known i.e. the magnetic field sensor used throughout this PhD has an operational voltage of 3.3v. The power consumption of the system will need to be quantified experimentally. A battery can then be selected that will satisfy the required size constraints and the capacity required to meet the power demands over the anticipated lifetime of the implant. A staggered data collection protocol could be adopted i.e. daily readings made <1yr post-operation then readings recorded at a lower frequency thereafter. This is the same approach used for the Persona IQ to conserve battery power (Cushner et al., 2021; Kelmers et al., 2022; Zimmer Biomet, 2023).

Communication

Further work is needed to select and test a method of wireless communication to transmit the data from the implant to out of the body. Using antenna-based radio frequency (RF) transceivers operating in the standardised Medical Device Radiocommunications Service (MedRadio) band of 401 – 406 MHz (FCC, 2017; Teshome et al., 2018) would be the most appropriate for an instrumented THR. The implant could autonomously send data to an external device at the patient's home that would then be uploaded to a secure cloud-based storage network accessible to the surgeon. This proposed external device is comparable to the base station used to collect data from the Personna IQ (Cushner et al., 2021; Zimmer Biomet, 2023).

There is typically greater soft tissue surrounding the human hip joint when compared to the knee joint. Therefore, work should be conducted to investigate RF signal attenuation from a source located in a THR implanted within a cadaveric human hip sample. The effect of the surrounding soft tissue has on the absorption of the RF signal should be characterised to see if data can be transmitted and received from out of the body to the location on the implanted THR using this wireless communication method. This study should also consider variation in the population and investigate the impact of how patient size and BMI affects the RF signal attenuation.

Regulatory considerations

Cadaveric testing whereby the final instrumented implant system is implanted into a human cadaveric hip to give an indication of expected performance in-vivo. Cushner et al. (2022) performed cadaveric testing in the pre-clinical testing of the Personna IQ instrumented TKR. The cadaveric study should aim to characterise the function of the sensing system at predicting component position and orientation. This could be validated by comparing values to measured angles of the joint segments (using protractor (Cushner et al., 2022) or image tracking system e.g. Vicon) or by taking plain radiograph or CT images. Additionally, a study should be performed to examine risk of implanting an THR with an affixed permanent magnet. Especially when an individual comes into proximity to a high-powered magnet for example during an MRI scan.

A THR enabled with an in-vivo sensing system would be categorised as a class III medical device thus requires stringent pre-clinical and clinical testing before it can be marketed and used. Further work will be needed to demonstrate compliance to the medical device directive 93/42/EEC on medical devices (EU MDD). This should include testing as specified by the following ISO standards covering general, particular and specific requirements:

1. ISO 14630:2012 non-active surgical implants — General requirements
2. ISO 21534:2007 non-active surgical implants — Joint replacement implants — Particular requirements
3. ISO 21535:2023 non-active surgical implants — Joint replacement implants — Specific requirements for hip-joint replacement implants

References

Abbott 2017. Press release: ABBOTT LAUNCHES THE FIRST AND ONLY SMARTPHONE COMPATIBLE INSERTABLE CARDIAC MONITOR IN THE U.S. [Accessed 15 June 2020]. Available from: abbott.mediaroom.com/.

Abdulkarim, A., Ellanti, P., Motterlini, N., Fahey, T. and O'Byrne, J.M. 2013. Cemented versus uncemented fixation in total hip replacement: a systematic review and meta-analysis of randomized controlled trials. *Orthopedic reviews*. **5**(1).

Albert, J.A., Owolabi, V., Gebel, A., Brahms, C.M., Granacher, U. and Arnrich, B. 2020. Evaluation of the pose tracking performance of the azure kinect and kinect v2 for gait analysis in comparison with a gold standard: A pilot study. *Sensors*. **20**(18), p.5104.

Ali, M., Al-Hajjar, M., Jennings, L.M. and Fisher, J. 2017. Wear and deformation of metal-on-polyethylene hip replacements under edge loading conditions due to variations in surgical positioning *In*: *Orthopaedic Proceedings*. The British Editorial Society of Bone & Joint Surgery, p.12.

Ali, M., Al-Hajjar, M., Partridge, S., Williams, S., Fisher, J. and Jennings, L.M. 2016. Influence of hip joint simulator design and mechanics on the wear and creep of metal-on-polyethylene bearings. *Proceedings of the Institution of Mechanical Engineers, Part H: Journal of Engineering in Medicine*. **230**(5), pp.389–397.

Almouahed, S., Gouriou, M., Hamitouche, C., Stindel, E. and Roux, C. 2011. The use of piezoceramics as electrical energy harvesters within instrumented knee implant during walking. *IEEE/ASME Transactions on Mechatronics*. **16**(5), pp.799–807.

Alshuhri, A.A., Holsgrove, T.P., Miles, A.W. and Cunningham, J.L. 2015. Development of a non-invasive diagnostic technique for acetabular component loosening in total hip replacements. *Medical Engineering and Physics*. **37**(8), pp.739–745.

Amar, A. Ben, Kouki, A.B. and Cao, H. 2015. Power approaches for implantable medical devices. *sensors*. **15**(11), pp.28889–28914.

Amstutz, H.C., Lodwig, R.M., Schurman, D.J. and Hodgson, A.G. 1975. Range of motion studies for total hip replacements. A comparative study with a new experimental apparatus. *Clinical orthopaedics and related research*. (111), pp.124–130.

AOA 2018. National Joint Replacement Registry: Hip, Knee & Shoulder Arthroplasty Annual Report 2018.

Arami, A., Aminian, K., Forchelet, D. and Renaud, P. 2014. Implantable and wearable measurement system for smart knee prosthesis *In*: *2014 IEEE Biomedical Circuits and Systems Conference (BioCAS) Proceedings*. IEEE, pp.240–243.

Arami, A., Simoncini, M., Atasoy, O., Ali, S., Hasenkamp, W., Bertsch, A., Meurville, E., Tanner, S., Renaud, P. and Dehollain, C. 2013. Instrumented knee prosthesis for force and kinematics measurements. *IEEE transactions on automation science and engineering*. **10**(3), pp.615–624.

Arami, A., Simoncini, M., Atasoy, O., Hasenkamp, W., Ali, S., Bertsch, A., Meurville, E., Tanner, S., Dejnabadi, H. and Leclercq, V. 2011. Instrumented prosthesis for knee implants monitoring *In*: *2011 IEEE international conference on automation science and engineering*. IEEE, pp.828–835.

Asif, Z. and Munir, M. 2005. Integrating the supply chain with RFID: A technical and business analysis. *Communications of the Association for Information Systems*. **15**(1), p.24.

Awal, M.R., Jusoh, M., Sabapathy, T., Kamarudin, M.R. and Rahim, R.A. 2016. State-of-the-art developments of acoustic energy transfer. *International Journal of Antennas and Propagation*. **2016**.

Balaban, A.L., Bakhvalov, Y.A. and Denisov, P.A. 2018. Review of methods for solving inverse problems in identifying permanent magnets of executive elements in dynamic devices *In*: *MATEC Web of Conferences*. EDP Sciences, p.4022.

Baumann, A.P., O'Neill, C., Owens, M.C., Weber, S.C., Sivan, S., D'Amico, R., Carmody, S., Bini, S., Sawyer, A.J. and Lotz, J.C. 2020. FDA Public Workshop: Orthopaedic Sensing, Measuring, and Advanced Reporting Technology (SMART) Devices. *Journal of orthopaedic research: official publication of the Orthopaedic Research Society*.

Bergmann, G, Deuretzbacher, G., Heller, M., Graichen, F., Rohlmann, A., Strauss, J. and Duda, G.N. 2001. Hip contact forces and gait patterns from routine activities. *Journal of Biomechanics*. **34**(7), pp.859–871.

Bergmann, G., Graichen, F., Dymke, J., Rohlmann, A., Duda, G.N. and Damm, P. 2012. High-tech hip implant for wireless temperature measurements in vivo. *PLoS One*. **7**(8), p.e43489.

Bergmann, G., Graichen, F., Jendrzynski, H. and Rohlmann, A. 1987. Long Term Animal Tests with Instrumented Hip Implants *In*: *Biomechanics: Basic and Applied Research*. Springer, pp.317–324.

Bergmann, G., Graichen, F. and Rohlmann, A. 1993. Hip joint loading during walking and running, measured in two patients. *Journal of biomechanics*. **26**(8), pp.969–990.

Bergmann, G., Graichen, F., Rohlmann, A., Verdonschot, N. and van Lenthe, G.H. 2001. Frictional heating of total hip implants, Part 1: measurements in patients. *Journal of Biomechanics*. **34**(4), pp.421–428.

Bergmann, G., Graichen, F., Siraky, J., Jendrzynski, H. and Rohlmann, A. 1988. Multichannel strain gauge telemetry for orthopaedic implants. *Journal of Biomechanics*. **21**(2), pp.169–176.

Beshchasna, N., Uhlemann, J. and Wolter, K.-J. 2006. Researching of biochemical degradation of electronic materials in fluid electrolytic mediums *In*: *2006 29th International Spring Seminar on Electronics Technology*. IEEE, pp.149–155.

Bluetooth.com 2020. Learn about Bluetooth. [Accessed 15 June 2020]. Available from: bluetooth.com.

Bock, D.C., Marschilok, A.C., Takeuchi, K.J. and Takeuchi, E.S. 2012. Batteries used to power implantable biomedical devices. *Electrochimica acta*. **84**, pp.155–164.

Bosker, B.H., Verheyen, C., Horstmann, W.G. and Tulp, N.J.A. 2007. Poor accuracy of freehand cup positioning during total hip arthroplasty. *Archives of orthopaedic and trauma surgery*. **127**(5), pp.375–379.

Bradley, P.D. 2011. Wireless medical implant technology—Recent advances and future developments *In*: *2011 Proceedings of the European Solid-State Device Research Conference (ESSDERC)*. IEEE, pp.54–58.

British Heart Foundation 2020. Life with a pacemaker: Two inspiring stories. [Accessed 15 June 2020]. Available from: bhf.org.uk.

Brown, T.D. and Callaghan, J.J. 2008. (ii) Impingement in total hip replacement: mechanisms and consequences. *Current orthopaedics*. **22**(6), pp.376–391.

Burns, A.J., Johnson, M.E. and Honeyman, P. 2016. A brief chronology of medical device security. *Communications of the ACM*. **59**(10), pp.66–72.

Camacho, J.M. and Sosa, V. 2013. Alternative method to calculate the magnetic field of permanent magnets with azimuthal symmetry. *Revista mexicana de física E*. **59**(1), pp.8–17.

Cao, H., Landge, V., Tata, U., Seo, Y.-S., Rao, S., Tang, S.-J., Tibbals, H.F., Spechler, S. and Chiao, J.-C. 2012. An implantable, batteryless, and wireless capsule with integrated impedance and pH sensors for gastroesophageal reflux monitoring. *IEEE Transactions on Biomedical Engineering*. **59**(11), pp.3131–3139.

Carlson, C.E., Mann, R.W. and Harris, W.H. 1974. A radio telemetry device for monitoring cartilage surface pressures in the human hip. *IEEE Transactions on Biomedical Engineering*. (4), pp.257–264.

Çelik, T. and Kisioglu, Y. 2019. Determination of The Hip Stem Loosening Using Vibration Method. *European Journal of Engineering and Natural Sciences*. **3**(1), pp.73–77.

Cheney, D. 2013. CBS 60 Minute: Dick Cheney's Heart. [Accessed 10 November 2020]. Available from: https://www.cbsnews.com/video/dick-cheneys-heart/.

Chung, J.K., Pratt, G.W., Babyn, P.S. and Poss, R. 1979. NEW DIAGNOSTIC-TECHNIQUE FOR THE EVALUATION OF PROSTHETIC FIXATION *In*: *IEEE Transactions on Biomedical Engineering*. IEEE-INST ELECTRICAL ELECTRONICS ENGINEERS INC 345 E 47TH ST, NEW YORK, NY …, p.532.

CIHI 2018. Hip and Knee Replacements in Canada, 2016–2017: Canadian Joint Replacement Registry Annual Report. *Ottawa, ON.*

Clearswift 2020. Infographic: Cybersecurity challenges in the UK healthcare sector. [Accessed 10 November 2020]. Available from: https://www.clearswift.com/blog/2020/01/22/infographic-cybersecurity-challenges-uk-healthcare-sector.

Conaty-Buck, S. 2017. Cybersecurity and healthcare records. *American Nurse Today*. **12**(9), pp.62–64.

Cushner, F., Schiller, P., Gross, J., Mueller, J.K. and Hunter, W. 2021. A total knee arthroplasty prosthesis capable of remote patient monitoring *In*: *Orthopaedic Proceedings*. The British Editorial Society of Bone & Joint Surgery, p.18.

Cushner, F.D., Schiller, P.J., Mueller, J.K.P., Gross, J.M. and Hunter, W.L. 2022. A cadaveric study addressing the feasibility of remote patient monitoring prosthesis for total knee arthroplasty. *The Journal of Arthroplasty*. **37**(6), pp.S350–S354.

Damm, P., Dymke, J., Ackermann, R., Bender, A., Graichen, F., Halder, A., Beier, A. and Bergmann, G. 2013. Friction in total hip joint prosthesis measured in vivo during walking. *PloS one*. **8**(11).

Damm, P., Graichen, F., Rohlmann, A., Bender, A. and Bergmann, G. 2010. Total hip joint prosthesis for in vivo measurement of forces and moments. *Medical engineering & physics*. **32**(1), pp.95–100.

Daou, H.E.L., Ng, K.C.G., Van Arkel, R., Jeffers, J.R.T. and y Baena, F.R. 2019. Robotic hip joint testing: Development and experimental protocols. *Medical engineering & physics*. **63**, pp.57–62.

Dargel, J., Oppermann, J., Brüggemann, G.-P. and Eysel, P. 2014. Dislocation following total hip replacement. *Deutsches Ärzteblatt International*. **111**(51–52), p.884.

Davies, J.P., Tse, M.-K. and Harris, W.H. 1996. Monitoring the integrity of the cement—metal interface of total joint components in vitro using acoustic emission and ultrasound. *The Journal of arthroplasty*. **11**(5), pp.594–601.

Davy, D.T., Kotzar, G.M., Brown, R.H., Heiple, K.G., Goldberg, V.M., Heiple, J.K.G., Berilla, J. and Burstein, A.H. 1988. Telemetric force measurements across the hip after total arthroplasty. *The Journal of bone and joint surgery. American volume*. **70**(1), pp.45–50.

Deyle, G. 2005. Diagnostic Imaging in Primary Care Physical Therapy. *Primary Care for the Physical Therapist*., pp.323-cp4.

DHSC 2018. Securing cyber resilience in health and care: October 2018 update. *Cyber Security Policy*.

DiGioia III, A.M., Jaramaz, B., Plakseychuk, A.Y., Moody Jr, J.E., Nikou, C., LaBarca, R.S., Levison, T.J. and Picard, F. 2002. Comparison of a mechanical acetabular alignment guide with computer placement of the socket. *The Journal of arthroplasty*. **17**(3), pp.359–364.

Disilvestro, M.R., Sherman, J.T. and Dietz, T.L. 2007. In vivo joint space measurement device and method.

Domas, S. 2019. Maybe Your Pacemaker Can’t Kill You. *InSecurity [PODCAST]*.

Domas, S. 2016. Protecting Medical Devices from Cyberharm. *Tedx Talks*. [Online]. [Accessed 13 August 2020]. Available from: https://www.youtube.com/watch?v=EyqwUFJKZo0.

Dorr, L.D., Wolf, A.W., Chandler, R. and Conaty, J.P. 1983. Classification and treatment of dislocations of total hip arthroplasty. *Clinical orthopaedics and related research*. (173), pp.151–158.

English and Kilvington 1979. In vivo records of hip loads using a femoral implant with telemetric output (a prelimary report). *Journal of biomedical engineering*. **1**(2), pp.111–115.

Ermakova, A., Ribeiro, M., Spitzer, D. and Ortner, M. 2018. Analytical Development of a Four-Axis Magnetic Multimedia Control Element. *IEEE Sensors Journal*. **18**(19), pp.7819–7825.

Ewald, H., Ruther, C., Mittelmeier, W., Bader, R. and Kluess, D. 2011. A novel in vivo sensor for loosening diagnostics in total hip replacement *In*: *SENSORS, 2011 IEEE*. IEEE, pp.89–92.

FCC 2017. Medical Device Radiocommunications Service. Available from: https://www.fcc.gov/medical-device-radiocommunications-service-medradio.

FDA 2015a. Class 2 Device Recall Merlinhome RF Remote Monitoring Transmitter, Model EX1150, with software versions 6.1M or 7.0.

FDA 2018a. Content of Premarket Submissions for Management of Cybersecurity in Medical Devices.

FDA 2013. Cybersecurity for Medical Devices and Hospital Networks: FDA Safety Communication. [Accessed 10 November 2020]. Available from: http://wayback.archive-it.org/7993/20170722144747/https:/www.fda.gov/MedicalDevices/Safety/AlertsandNotices/ucm356423.htm.

FDA 2018b. Cybersecurity Updates Affecting Medtronic Implantable Cardiac Device Programmers: FDA Safety Communication. [Accessed 10 November 2020]. Available from: https://www.fda.gov/medical-devices/safety-communications/cybersecurity-updates-affecting-medtronic-implantable-cardiac-device-programmers-fda-safety.

FDA 2015b. Cybersecurity Vulnerabilities of Hospira Symbiq Infusion System: FDA Safety Communication. [Accessed 10 November 2020]. Available from: https://web.archive.org/web/20170111070001/http:/www.fda.gov/MedicalDevices/Safety/AlertsandNotices/ucm456815.htm.

FDA 2014. GUIDANCE DOCUMENT Content of Premarket Submissions for Management of Cybersecurity in Medical Devices. [Accessed 10 November 2020]. Available from: https://www.fda.gov/regulatory-information/search-fda-guidance-documents/content-premarket-submissions-management-cybersecurity-medical-devices-0.

FDA 2018c. Medtronic Recalls Remote Controllers for MiniMed Insulin Pumps for Potential Cybersecurity Risks.

FDA 2020. SweynTooth Cybersecurity Vulnerabilities May Affect Certain Medical Devices: FDA Safety Communication.

FDA 2019. URGENT/11 Cybersecurity Vulnerabilities in a Widely-Used Third-Party Software Component May Introduce Risks During Use of Certain Medical Devices: FDA Safety Communication. [Accessed 10 November 2020]. Available from: https://www.fda.gov/medical-devices/safety-communications/urgent11-cybersecurity-vulnerabilities-widely-used-third-party-software-component-may-introduce.

Gabriel, S., Lau, R.W. and Gabriel, C. 1996. The dielectric properties of biological tissues: III. Parametric models for the dielectric spectrum of tissues. *Physics in medicine & biology*. **41**(11), p.2271.

Geerdink, C.H., Grimm, B., Vencken, W., Heyligers, I.C. and Tonino, A.J. 2008. The determination of linear and angular penetration of the femoral head into the acetabular component as an assessment of wear in total hip replacement: a comparison of four computer-assisted methods. *The Journal of Bone and Joint Surgery. British volume*. **90**(7), pp.839–846.

Georgiou, A.P. and Cunningham, J.L. 2001. Accurate diagnosis of hip prosthesis loosening using a vibrational technique. *Clinical Biomechanics*. **16**(4), pp.315–323.

Ghaffari, M., Nickmanesh, R., Tamannaee, N. and Farahmand, F. 2012. The impingement-dislocation risk of total hip replacement: Effects of cup orientation and patient maneuvers *In*: *2012 Annual International Conference of the IEEE Engineering in Medicine and Biology Society*. IEEE, pp.6801–6804.

Ghorbani, S., Mahdaviani, K., Thaler, A., Kording, K., Cook, D.J., Blohm, G. and Troje, N.F. 2021. MoVi: A large multi-purpose human motion and video dataset. *Plos one*. **16**(6), p.e0253157.

Girase, H., Nyayapati, P., Booker, J., Lotz, J.C., Bailey, J.F. and Matthew, R.P. 2021. Automated assessment and classification of spine, hip, and knee pathologies from sit-to-stand movements collected in clinical practice. *Journal of Biomechanics*. **128**, p.110786.

Goodin, D. 2011. Insulin pump hack delivers fatal dosage over the air. *theregister*. [Online]. [Accessed 10 November 2020]. Available from: https://www.theregister.com/2011/10/27/fatal_insulin_pump_attack/.

Graichen, F. and Bergmann, G. 1991. Four-channel telemetry system for in vivo measurement of hip joint forces. *Journal of biomedical engineering*. **13**(5), pp.370–374.

Graichen, F., Bergmann, G. and Rohlmann, A. 1999. Hip endoprosthesis for in vivo measurement of joint force and temperature. *Journal of biomechanics*. **32**(10), pp.1113–1117.

Gray, P. 2012. Pacemakers, defibrillators open to attack. *theregister*. [Online]. [Accessed 10 November 2020]. Available from: https://www.theregister.com/2012/10/17/pacemakers_open_to_wireless_attack/.

Grillini, L. and Affatato, S. 2013. How to measure wear following total hip arthroplasty. *Hip International*. **23**(3), pp.233–242.

Guevara-Valdivia, M.E. and Torres, P.I. 2011. *Remote Monitoring of Implantable Pacemaker, Cardioverter Defibrillator, and Cardiac Resynchronizer, Modern Pacemakers - Present and Future, Prof. Mithilesh R Das*.

Hadley, M., Hardaker, C., Isaac, G. and Fisher, J. 2018. Wear of different materials for total hip replacement under adverse stop-dwell-start in vitro wear simulation conditions. *Proceedings of the Institution of Mechanical Engineers, Part H: Journal of Engineering in Medicine*. **232**(12), pp.1261–1270.

Halperin, D., Heydt-Benjamin, T.S., Ransford, B., Clark, S.S., Defend, B., Morgan, W., Fu, K., Kohno, T. and Maisel, W.H. 2008. Pacemakers and implantable cardiac defibrillators: Software radio attacks and zero-power defenses *In*: *2008 IEEE Symposium on Security and Privacy (sp 2008)*. IEEE, pp.129–142.

Hammerberg, E.M., Wan, Z., Dastane, M. and Dorr, L.D. 2010. Wear and Range of Motion of Different Femoral Head Sizes. *The Journal of Arthroplasty*. **25**(6), pp.839–843.

Hassan, D.M., Johnston, G.H.F., Dust, W.N.C., Watson, G. and Dolovich, A.T. 1998. Accuracy of intraoperative assessment of acetabular prosthesis placement. *The Journal of Arthroplasty*. **13**(1), pp.80–84.

Henderson, D.M. 1977. *Euler angles, quaternions, and transformation matrices for space shuttle analysis*.

Herrmann, S., Kaehler, M., Grawe, R., Kluess, D., Woernle, C. and Bader, R. 2015. Physiological-like testing of the dislocation stability of artificial hip joints *In*: *New Trends in Mechanism and Machine Science: From Fundamentals to Industrial Applications*. Springer, pp.659–667.

Islam, M.N. and Yuce, M.R. 2016. Review of Medical Implant Communication System (MICS) band and network. *ICT Express*. **2**(4), pp.188–194.

Jantara, V.L. 2020. Wind turbine gearboxes: Failures, surface treatments and condition monitoring. *Non-Destructive Testing and Condition Monitoring Techniques for Renewable Energy Industrial Assets*., pp.69–90.

Jaramaz, B., Nikou, C., Simon, D.A. and DiGioia, A.M. 1997. Range of motion after total hip arthroplasty: Experimental verification of the analytical simulator *In*: *CVRMed-MRCAS'97*. Springer, pp.573–582.

Jones, D., Wang, L., Ghanbari, A., Vardakastani, V., Kedgley, A.E., Gardiner, M.D., Vincent, T.L., Culmer, P.R. and Alazmani, A. 2020. Design and evaluation of magnetic Hall effect tactile sensors for use in sensorized splints. *Sensors*. **20**(4), p.1123.

Joung, Y.-H. 2013. Development of implantable medical devices: from an engineering perspective. *International neurourology journal*. **17**(3), p.98.

Kebbach, M., Grawe, R., Geier, A., Winter, E., Bergschmidt, P., Kluess, D., D'Lima, D., Woernle, C. and Bader, R. 2019. Effect of surgical parameters on the biomechanical behaviour of bicondylar total knee endoprostheses–A robot-assisted test method based on a musculoskeletal model. *Scientific reports*. **9**(1), p.14504.

Kelmers, E., Szuba, A., King, S.W., Palan, J., Freear, S., Pandit, H.G. and van Duren, B.H. 2022. Smart Knee Implants: An Overview of Current Technologies and Future Possibilities. *Indian Journal of Orthopaedics*., pp.1–8.

Kennedy, J.G., Rogers, W.B., Soffe, K.E., Sullivan, R.J., Griffen, D.G. and Sheehan, L.J. 1998. Effect of acetabular component orientation on recurrent dislocation, pelvic osteolysis, polyethylene wear, and component migration. *The Journal of arthroplasty*. **13**(5), pp.530–534.

Khan, W. and Badii, A. 2019. Pathological gait abnormality detection and segmentation by processing the hip joints motion data to support mobile gait rehabilitation. *Research in C Medical & Engineering Sciences*. **7**(03).

Khokle, R., Esselle, K. and Bokor, D. 2018. Design, Modeling, and Evaluation of the Eddy Current Sensor Deeply Implanted in the Human Body. *Sensors*. **18**(11), p.3888.

Kilvington, M. and Goodman, R.M.F. 1981. In vivo hip joint forces recorded on a strain gauged 'English'prosthesis using an implanted transmitter. *Engineering in Medicine*. **10**(4), pp.175–187.

Kim, J.T. and Yoo, J.J. 2016. Implant design in cementless hip arthroplasty. *Hip & pelvis*. **28**(2), pp.65–75.

Kiourti, A., Costa, J.R., Fernandes, C.A. and Nikita, K.S. 2014. A broadband implantable and a dual-band on-body repeater antenna: Design and transmission performance. *IEEE transactions on antennas and propagation*. **62**(6), pp.2899–2908.

Kirsten, S., Uhlemann, J., Braunschweig, M. and Wolter, K.J. 2012. Packaging of electronic devices for long-term implantation *In*: *2012 35th International Spring Seminar on Electronics Technology*. IEEE, pp.123–127.

Knight, S.R., Aujla, R. and Biswas, S.P. 2011. Total Hip Arthroplasty-over 100 years of operative history. *Orthopedic reviews*. **3**(2).

Komistek, R.D., Dennis, D.A., Ochoa, J.A., Haas, B.D. and Hammill, C. 2002. In vivo comparison of hip separation after metal-on-metal or metal-on-polyethylene total hip arthroplasty. *JBJS*. **84**(10), pp.1836–1841.

Kotzar, G.M., Davy, D.T., Goldberg, V.M., Heiple, K.G., Berilla, J., Heiple Jr, K.G., Brown, R.H. and Burstein, A.H. 1991. Telemeterized in vivo hip joint force data: a report on two patients after total hip surgery. *Journal of Orthopaedic Research*. **9**(5), pp.621–633.

Lachiewicz, P.F., Soileau, E.S. and Martell, J.M. 2016. Wear and osteolysis of highly crosslinked polyethylene at 10 to 14 years: the effect of femoral head size. *Clinical Orthopaedics and Related Research®*. **474**(2), pp.365–371.

Lange, H.-E., Hohlfeld, D., Bader, R. and Kluess, D. 2020. A piezoelectric energy harvesting concept for an energy-autonomous instrumented total hip replacement. *Smart Materials and Structures*.

Learmonth, I.D., Young, C. and Rorabeck, C. 2007. The operation of the century: total hip replacement. *The Lancet*. **370**(9597), pp.1508–1519.

Ledet, E.H., Liddle, B., Kradinova, K. and Harper, S. 2018. Smart implants in orthopedic surgery, improving patient outcomes: a review. *Innovation and entrepreneurship in health*. **5**, p.41.

Lewinnek, G.E., Lewis, J.L., Tarr, R., Compere, C.L. and Zimmerman, J.R. 1978. Incidence of dislocation following hip arthroplasty for patients in the rehabilitation setting. *J Bone Joint Surg Am*. **60**(2), pp.217–220.

Li, P.L.S., Jones, N.B. and Gregg, P.J. 1996. Vibration analysis in the detection of total hip prosthetic loosening. *Medical engineering & physics*. **18**(7), pp.596–600.

Liu, Q., Cheng, X., Yan, D. and Zhou, Y. 2019. Plain radiography findings to predict dislocation after total hip arthroplasty. *Journal of Orthopaedic Translation*.

Lombardi Jr, A. V, Mallory, T.H., Dennis, D.A., Komistek, R.D., Fada, R.A. and Northcut, E.J. 2000. An in vivo determination of total hip arthroplasty pistoning during activity. *The Journal of Arthroplasty*. **15**(6), pp.702–709.

Lumetti, S., Malagò, P., Spitzer, D., Zaruba, S. and Ortner, M. 2020. Computationally Efficient Magnetic Position System Calibration *In*: *Engineering Proceedings*. Multidisciplinary Digital Publishing Institute, p.72.

Luo, Y., Coppola, S.M., Dixon, P.C., Li, S., Dennerlein, J.T. and Hu, B. 2020. A database of human gait performance on irregular and uneven surfaces collected by wearable sensors. *Scientific data*. **7**(1), p.219.

Lutz., C. and Foletto., A. 2019. *Joystick with Allegro Position Sensor IC*.

Maag, C., Metcalfe, A., Cracaoanu, I., Wise, C. and Auger, D.D. 2021. The development of simulator testing for total knee replacements. *Biosurface and Biotribology*. **7**(2), pp.70–82.

Maggs, J. and Wilson, M. 2017. The relative merits of cemented and uncemented prostheses in total hip arthroplasty. *Indian journal of orthopaedics*. **51**(4), p.377.

Malagò, P., Slanovc, F., Herzog, S., Lumetti, S., Schaden, T., Pellegrinetti, A., Moridi, M., Abert, C., Suess, D. and Ortner, M. 2020. Magnetic Position System Design Method Applied to Three-Axis Joystick Motion Tracking. *Sensors*. **20**(23), p.6873.

Malik, A., Maheshwari, A. and Dorr, L.D. 2007. Impingement with total hip replacement. *JBJS*. **89**(8), pp.1832–1842.

Maneewongvatana, S. and Mount, D.M. 1999. Analysis of approximate nearest neighbor searching with clustered point sets. *arXiv preprint cs/9901013*.

Marchetti, E., Krantz, N., Berton, C., Bocquet, D., Fouilleron, N., Migaud, H. and Girard, J. 2011. Component impingement in total hip arthroplasty: frequency and risk factors. A continuous retrieval analysis series of 416 cup. *Orthopaedics & Traumatology: Surgery & Research*. **97**(2), pp.127–133.

Marschner, U., Grätz, H., Jettkant, B., Ruwisch, D., Woldt, G., Fischer, W.-J. and Clasbrummel, B. 2009. Integration of a wireless lock-in measurement of hip prosthesis vibrations for loosening detection. *Sensors and Actuators A: Physical*. **156**(1), pp.145–154.

Matharu, G.S., Culliford, D.J., Blom, A.W. and Judge, A. 2022. Projections for primary hip and knee replacement surgery up to the year 2060: an analysis based on data from The National Joint Registry for England, Wales, Northern Ireland and the Isle of Man. *The Annals of The Royal College of Surgeons of England*. **104**(6), pp.443–448.

Mathworks 2021. Levenberg-Marquardt backpropagation. Available from: https://uk.mathworks.com/help/deeplearning/ref/trainlm.html.

MathWorks 2019. magcal. [Accessed 27 February 2024]. Available from: https://uk.mathworks.com/help/nav/ref/magcal.html.

Mavrogordato, M., Taylor, M., Taylor, A. and Browne, M. 2011. Real time monitoring of progressive damage during loading of a simplified total hip stem construct using embedded acoustic emission sensors. *Medical engineering & physics*. **33**(4), pp.395–406.

McCalden, R.W., Naudie, D.D., Yuan, X. and Bourne, R.B. 2005. Radiographic methods for the assessment of polyethylene wear after total hip arthroplasty. *JBJS*. **87**(10), pp.2323–2334.

McKellop, H.A. 2007. The lexicon of polyethylene wear in artificial joints. *Biomaterials*. **28**(34), pp.5049–5057.

McKellop, H.A. and D'Lima, D. 2008. How have wear testing and joint simulator studies helped to discriminate among materials and designs? *JAAOS-Journal of the American Academy of Orthopaedic Surgeons*. **16**, pp.S111–S119.

MDCG 2019. MDCG 2019-16 - Guidance on Cybersecurity for medical devices.

Melexis 2021. *How to use a magnetometer in a position sensor application*.

Melia, G. 2013. *Electromagnetic absorption by the human body from 1-15 GHz*. (Doctoral Dissertation, University of York).

Mentiplay, B.F., Banky, M., Clark, R.A., Kahn, M.B. and Williams, G. 2018. Lower limb angular velocity during walking at various speeds. *Gait & posture*. **65**, pp.190–196.

Mohammadbagherpoor, H., Ierymenko, P., Craver, M.H., Carlson, J., Dausch, D., Grant, E. and Lucey, J.D. 2019. An Implantable Wireless Inductive Sensor System Designed To Monitor Prosthesis Motion in Total Joint Replacement Surgery. *IEEE Transactions on Biomedical Engineering*.

Muro-De-La-Herran, A., Garcia-Zapirain, B. and Mendez-Zorrilla, A. 2014. Gait analysis methods: An overview of wearable and non-wearable systems, highlighting clinical applications. *Sensors*. **14**(2), pp.3362–3394.

Murray, D.W. 1992. Impingement and loosening of the long posterior wall acetabular implant. *The Journal of bone and joint surgery. British volume*. **74**(3), pp.377–379.

Murray, D.W. 1993. The definition and measurement of acetabular orientation. *The Journal of bone and joint surgery. British volume*. **75**(2), pp.228–232.

Nagymáté, G. and Kiss, R.M. 2018. Application of OptiTrack motion capture systems in human movement analysis: A systematic literature review. *Recent Innovations in Mechatronics*. **5**(1.), pp.1–9.

National Joint Registry 2020. 17th Annual Report 2020. [Accessed 13 November 2020]. Available from: https://reports.njrcentre.org.uk/Portals/0/PDFdownloads/NJR 17th Annual Report 2020.pdf.

Nelson, B.D., Karipott, S.S., Wang, Y. and Ong, K.G. 2020. Wireless Technologies for Implantable Devices. *Sensors*. **20**(16), p.4604.

NHS 2023. Osteoarthritis. Available from: https://www.nhs.uk/conditions/osteoarthritis/.

NJR 2018. NJR 15th Annual Report 2018.

NJR 2022. NJR Report 2022. Available from: https://www.njrcentre.org.uk/.

NOAA - NCEI 2024. Geomagnetism Frequently Asked Questions. Available from: www.ncei.noaa.gov/.

O’Dwyer Lancaster-Jones, O., Williams, S., Jennings, L.M., Thompson, J., Isaac, G.H., Fisher, J. and Al-Hajjar, M. 2018. An in vitro simulation model to assess the severity of edge loading and wear, due to variations in component positioning in hip joint replacements. *Journal of Biomedical Materials Research Part B: Applied Biomaterials*. **106**(5), pp.1897–1906.

OptiTrack 2023. OptiTrack for Movement Sciences. Available from: optitrack.com.

Orthload 2019. Loading of Orthopaedic Implants. [Accessed 30 January 2020]. Available from: https://orthoload.com/.

Orthopaedic Design & Technology 2021. First Knee Replacement Surgery with Persona IQ Smart Knee. [Accessed 2 June 2023]. Available from: https://www.odtmag.com/contents/view_breaking-news/2021-10-13/first-knee-replacement-surgery-with-persona-iq-smart-knee/.

Ortho-tag 2020. Ortho-tag. [Accessed 18 November 2020]. Available from: www.orthotag.com/.

Ortner, M., Ribeiro, M. and Spitzer, D. 2018. Absolute long-range linear position system with a single 3-D magnetic field sensor. *IEEE Transactions on Magnetics*. **55**(1), pp.1–4.

Otake, Y., Suzuki, N., Hattori, A., Hayashibe, M., Miki, H., Yamamura, M., Sugano, N., Yonenobu, K. and Ochi, T. 2005. Soft-Tissue Balance Evaluation System for Total Hip Arthroplasty by Intraoperative Contact Pressure Measurement at the Hip Joint. *Studies in health technology and informatics*. **119**, p.416.

Ozeri, S. and Shmilovitz, D. 2010. Ultrasonic transcutaneous energy transfer for powering implanted devices. *Ultrasonics*. **50**(6), pp.556–566.

Ozyagcilar, T. 2012. Calibrating an ecompass in the presence of hard and soft-iron interference. *Freescale Semiconductor Ltd*., pp.1–17.

Padgett, D.E. and Warashina, H. 2004. The unstable total hip replacement. *Clinical Orthopaedics and Related Research®*. **420**, pp.72–79.

Pancharoen, K., Zhu, D. and Beeby, S.P. 2014. A hip implant energy harvester *In*: *Journal of Physics: Conference Series*. IOP Publishing, p.12038.

Panero, E., Digo, E., Agostini, V. and Gastaldi, L. 2018. Comparison of different motion capture setups for gait analysis: Validation of spatio-temporal parameters estimation *In*: *2018 IEEE International Symposium on Medical Measurements and Applications (MeMeA)*. IEEE, pp.1–6.

Parvizi, J., Kim, G.K., Parvizi, J. and Kim, G.K. 2010. Bone Scan. *High Yield Orthopaedics*., pp.66–67.

Pounds, G. 2023. *Development of a Novel Motion-Capture Methodology to Assess Medial Meniscus Displacement during Cadaveric Gait Simulation [IN PRINT]*. University of Leeds.

Pryce, G., Al-Hajjar, M., Thompson, J., Wilcox, R., Board, T. and Williams, S. 2021. AN IN VITRO METHOD TO INVESTIGATE IMPLANT IMPINGEMENT OF HIP ARTHROPLASTIES *In*: *Orthopaedic Proceedings*. The British Editorial Society of Bone & Joint Surgery, p.21.

Pryce, G.M. 2019. *PhD: Polyethylene acetabular liner rim damage in total hip replacements*. University of Leeds, White Rose eTheses Online.

Pryce, G.M., Sabu, B., Al-Hajjar, M., Wilcox, R.K., Thompson, J., Isaac, G.H., Board, T. and Williams, S. 2022. Impingement in total hip arthroplasty: A geometric model. *Proceedings of the Institution of Mechanical Engineers, Part H: Journal of Engineering in Medicine*. **236**(4), pp.504–514.

Puers, R., Catrysse, M., Vandevoorde, G., Collier, R.J., Louridas, E., Burny, F., Donkerwolcke, M. and Moulart, F. 2000. A telemetry system for the detection of hip prosthesis loosening by vibration analysis. *Sensors and Actuators A: Physical*. **85**(1–3), pp.42–47.

Rieger, J.S., Jaeger, S., Schuld, C., Kretzer, J.P. and Bitsch, R.G. 2013. A vibrational technique for diagnosing loosened total hip endoprostheses: An experimental sawbone study. *Medical engineering & physics*. **35**(3), pp.329–337.

Rittmeister, M. and Callitsis, C. 2006. Factors influencing cup orientation in 500 consecutive total hip replacements. *Clinical Orthopaedics and Related Research®*. **445**, pp.192–196.

Roithmayr, C.M., Hodges, D.H. and Cross, P. 2016. *Dynamics: Theory and Application of Kane's Method* [Online]. Cambridge University Press. Available from: https://books.google.co.uk/books?id=dKizCwAAQBAJ.

Roques, A., Browne, M., Thompson, J., Rowland, C. and Taylor, A. 2004. Investigation of fatigue crack growth in acrylic bone cement using the acoustic emission technique. *Biomaterials*. **25**(5), pp.769–778.

Rosenstein, A.D., McCoy, G.F., Bulstrode, C.J., McLardy-Smith, P.D., Cunningham, J.L. and Turner-Smith, A.R. 1989. The differentiation of loose and secure femoral implants in total hip replacement using a vibrational technique: an anatomical and pilot clinical study. *Proceedings* *of the Institution of Mechanical Engineers, Part H: Journal of Engineering in Medicine*. **203**(2), pp.77–81.

Rowland, C., Browne, M., Taylor, A. and Leatherhead, U.K. 2004. Dynamic health monitoring of metal on metal hip prostheses using acoustic emission *In*: *26th European conference on acoustic emission testing*. Citeseer, pp.465–467.

Rowlands, A., Duck, F.A. and Cunningham, J.L. 2008. Bone vibration measurement using ultrasound: Application to detection of hip prosthesis loosening. *Medical engineering & physics*. **30**(3), pp.278–284.

Ruther, C., Ewald, H., Mittelmeier, W., Bader, R. and Kluess, D. 2010. Localization of uncemented hip Stem loosening with a novel in-vivo sensor system based on vibration analysis *In*: *6th World Congress of Biomechanics (WCB 2010). August 1-6, 2010 Singapore*. Springer, pp.620–623.

Ruther, C., Gabler, C., Ewald, H., Ellenrieder, M., Haenle, M., Lindner, T., Mittelmeier, W., Bader, R. and Kluess, D. 2014. In vivo monitoring of implant osseointegration in a rabbit model using acoustic sound analysis. *Journal of Orthopaedic Research*. **32**(4), pp.606–612.

Ruther, C., Timm, U., Ewald, H., Mittelmeier, W., Bader, R., Schmelter, R., Lohrengel, A. and Kluess, D. 2012. Current possibilities for detection of loosening of total hip replacements and how intelligent implants could improve diagnostic accuracy *In*: *Recent advances in arthroplasty*. IntechOpen.

Rychlik, M., Wendland, G., Jackowski, M., Rennert, R., Schaser, K.-D. and Nowotny, J. 2023. Calibration procedure and biomechanical validation of an universal six degree-of-freedom robotic system for hip joint testing. *Journal of Orthopaedic Surgery and Research*. **18**(1), p.164.

Rydell, N.W. 1966. Forces acting on the femoral head-prosthesis: a study on strain gauge supplied prostheses in living persons. *Acta Orthopaedica Scandinavica*. **37**(sup88), pp.1–132.

Sample, A.P., Yeager, D.J., Powledge, P.S., Mamishev, A. V and Smith, J.R. 2008. Design of an RFID-based battery-free programmable sensing platform. *IEEE transactions on instrumentation and measurement*. **57**(11), pp.2608–2615.

Sauer, S., Kirsten, S., Storck, F., Grätz, H., Marschner, U., Ruwisch, D. and Fischer, W.-J. 2013. A medical wireless measurement system for hip prosthesis loosening detection based on vibration analysis. *Sensors & Transducers*. **18**(1), p.134.

Scifert, C.F., Brown, T.D. and Lipman, J.D. 1999. Finite element analysis of a novel design approach to resisting total hip dislocation. *Clinical Biomechanics*. **14**(10), pp.697–703.

Sejdić, E., Rothfuss, M.A., Stachel, J.R., Franconi, N.G., Bocan, K., Lovell, M.R. and Mickle, M.H. 2013. Innovation and translation efforts in wireless medical connectivity, telemedicine and eMedicine: a story from the RFID Center of Excellence at the University of Pittsburgh. *Annals of biomedical engineering*. **41**(9), pp.1913–1925.

Semlitsch, M. and Willert, H.G. 1997. Clinical wear behaviour of ultra-high molecular weight polyethylene cups paired with metal and ceramic ball heads in comparison to metal-on-metal pairings of hip joint replacements. *Proceedings of the Institution of Mechanical Engineers, Part H: Journal of Engineering in Medicine*. **211**(1), pp.73–88.

Shadid, R. and Noghanian, S. 2018. A literature survey on wireless power transfer for biomedical devices. *International Journal of Antennas and Propagation*. **2018**.

SHAR 2017. Swedish Hip Arthroplasty Register Annual Report 2017.

Shon, W.Y., Baldini, T., Peterson, M.G., Wright, T.M. and Salvati, E.A. 2005. Impingement in total hip arthroplasty: a study of retrieved acetabular components. *The Journal of arthroplasty*. **20**(4), pp.427–435.

Siciliano, B., Khatib, O. and Kröger, T. 2008. *Springer handbook of robotics*. Springer.

Silva, N.M., Santos, P.M., Ferreira, J.A.F., dos Santos, M.P.S., Ramos, A., Simões, J.A.O., Reis, M. and Morais, R. 2013. Power management architecture for smart hip prostheses comprising multiple energy harvesting systems. *Sensors and Actuators A: physical*. **202**, pp.183–192.

Singh, J.A., Yu, S., Chen, L. and Cleveland, J.D. 2019. Rates of total joint replacement in the United States: future projections to 2020–2040 using the national inpatient sample. *The Journal of rheumatology*. **46**(9), pp.1134–1140.

Soares dos Santos, M.P., Ferreira, J.A.F., Ramos, A., Simões, J.A.O., Morais, R., Silva, N.M., Santos, P.M., Reis, M.C. and Oliveira, T. 2014. Instrumented hip joint replacements, femoral replacements and femoral fracture stabilizers. *Expert review of medical devices*. **11**(6), pp.617–635.

Soares dos Santos, M.P., Ferreira, J.A.F., Ramos, A., Simões, J.A.O., Morais, R., Silva, N.M., Santos, P.M., Reis, M.J.C.S. and Oliveira, T. 2013. Instrumented hip implants: Electric supply systems. *Journal of Biomechanics*. **46**(15), pp.2561–2571.

Southampton, U.H. 2018. Press release: Doctors implant and programme pacemaker using Bluetooth technology. [Accessed 15 June 2020]. Available from: uhs.nhs.uk/.

Souto, G., Muralter, F., Arjona, L., Landaluce, H. and Perallos, A. 2019. Protocol for Streaming Data from an RFID Sensor Network. *Sensors*. **19**(14), p.3148.

Stryker 2023. MotionSense with OrthoLogIQ. Where innovation meets recovery.

Sugiyama, H., Whiteside, L.A. and Kaiser, A.D. 1989. Examination of rotational fixation of the femoral component in total hip arthroplasty. A mechanical study of micromovement and acoustic emission. *Clinical orthopaedics and related research*. (249), pp.122–128.

Sundfeldt, M., V Carlsson, L., B Johansson, C., Thomsen, P. and Gretzer, C. 2006. Aseptic loosening, not only a question of wear: a review of different theories. *Acta orthopaedica*. **77**(2), pp.177–197.

Teeter, M., Lam, K., Howard, J., Lanting, B. and Yuan, X. 2016. RADIOSTEREOMETRIC ANALYSIS USING CLINICAL RADIOGRAPHIC VIEWS: MEASURING TOTAL HIP CUP POSITION AND WEAR *In*: *Orthopaedic Proceedings*. The British Editorial Society of Bone & Joint Surgery, p.5.

Temmerman, O.P.P., Raijmakers, P., Berkhof, J., Hoekstra, O.S., Teule, G.J.J. and Heyligers, I.C. 2005. Accuracy of diagnostic imaging techniques in the diagnosis of aseptic loosening of the femoral component of a hip prosthesis: a meta-analysis. *The Journal of bone and joint surgery. British volume*. **87**(6), pp.781–785.

Teshome, A.K., Kibret, B. and Lai, D.T.H. 2018. A review of implant communication technology in WBAN: Progress and challenges. *IEEE reviews in biomedical engineering*. **12**, pp.88–99.

Tesla, N. 1900. System of transmission of electrical energy.

TracPatch Health 2021. TracPatch.

Turley, G.A., Ahmed, S.M.Y., Williams, M.A. and Griffin, D.R. 2011. Establishing a range of motion boundary for total hip arthroplasty. *Proceedings of the Institution of Mechanical Engineers, Part H: Journal of Engineering in Medicine*. **225**(8), pp.769–782.

Uhlemann, J., Schindler, S., Schlottig, G., Drechsler, M., Starcke, S., Vollmer, G. and Wolter, K.-J. 2005. Cytotoxicity of COB materials *In*: *Proceedings Electronic Components and Technology, 2005. ECTC'05.* IEEE, pp.593–596.

Usrey, M.M., Noble, P.C., Rudner, L.J., Conditt, M.A., Birman, M. V, Santore, R.F. and Mathis, K.B. 2006. Does neck/liner impingement increase wear of ultrahigh-molecular-weight polyethylene liners? *The Journal of arthroplasty*. **21**(6), pp.65–71.

Varga, M. and Wolter, K.-J. 2014. Sensors and imaging methods for detecting loosening of orthopedic implants—a review *In*: *2014 IEEE 20th International Symposium for Design and Technology in Electronic Packaging (SIITME)*. IEEE, pp.333–335.

Vena, A., Sorli, B., Charlot, B. and Naudi, S. 2015. An RFID-based implant for identification and pressure sensing of orthopedic prosthesis *In*: *2015 1st URSI Atlantic Radio Science Conference (URSI AT-RASC)*. IEEE, p.1.

Vickers, O.G., Culmer, P.R., Isaac, G.H., Kay, R.W., Shuttleworth, M.P., Board, T. and Williams, S. 2021. Is in vivo sensing in a total hip replacement a possibility? A review on past systems and future challenges. *Progress in Biomedical Engineering*. **3**(4), p.42004.

Virtanen, P., Gommers, R., Oliphant, T.E., Haberland, M., Reddy, T., Cournapeau, D., Burovski, E., Peterson, P., Weckesser, W. and Bright, J. 2020. SciPy 1.0: fundamental algorithms for scientific computing in Python. *Nature methods*. **17**(3), pp.261–272.

Wageningen, D. van and Waffenschmidt, E. 2018. Basic principle of inductive power transmission. [Accessed 14 June 2020]. Available from: http://www.wirelesspowerconsortium.com/.

Wevers and Surgeon 2000. Acoustic Emission and Composites. *Comprehensive Composite Materials*., pp.345–357.

WHO 1993. *Electromagnetic fields (300 Hz to 300 GHz / published under the joint sponsorship of the United Nations Environment Programme, the International Radiation Protection Association, and the World Health Organization*. World Health Organization.

Williams, S., Butterfield, M., Stewart, T., Ingham, E., Stone, M. and Fisher, J. 2003. Wear and deformation of ceramic-on-polyethylene total hip replacements with joint laxity and swing phase microseparation. *Proceedings of the Institution of Mechanical Engineers, Part H: Journal of Engineering in Medicine*. **217**(2), pp.147–153.

Williams, S.P. 2022. *PhD: Impingement in total hip replacements*. University of Leeds, White Rose eTheses Online.

Wooley, P.H. and Schwarz, E.M. 2004. Aseptic loosening. *Gene therapy*. **11**(4), p.402.

Xiao, Z., Tan, X., Chen, X., Chen, S., Zhang, Z., Zhang, H., Wang, J., Huang, Y., Zhang, P. and Zheng, L. 2015. An implantable RFID sensor tag toward continuous glucose monitoring. *IEEE journal of biomedical and health informatics*. **19**(3), pp.910–919.

Yao, M. 2017. Your Electronic Medical Records Could Be Worth $1000 To Hackers. *Forbes*. [Online]. [Accessed 9 November 2020]. Available from: www.forbes.com/.

Zimmer Biomet 2023. Persona IQ, The Smart Knee.

Appendix

a) Matlab function for processing robot recorded orientation data

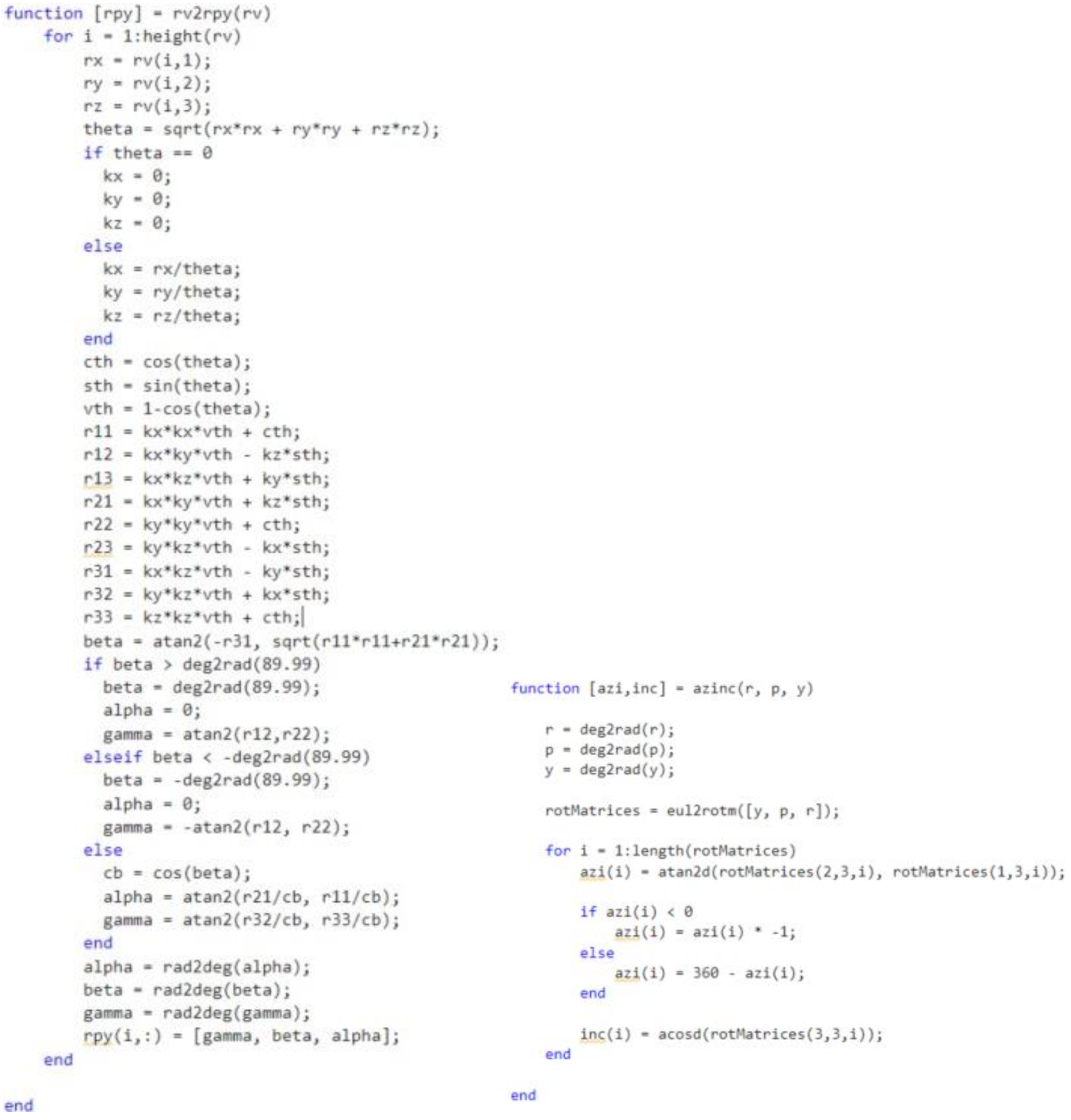

```
function [rpy] = rv2rpy(rv)
    for i = 1:height(rv)
        rx = rv(i,1);
        ry = rv(i,2);
        rz = rv(i,3);
        theta = sqrt(rx*rx + ry*ry + rz*rz);
        if theta == 0
          kx = 0;
          ky = 0;
          kz = 0;
        else
          kx = rx/theta;
          ky = ry/theta;
          kz = rz/theta;
        end
        cth = cos(theta);
        sth = sin(theta);
        vth = 1-cos(theta);
        r11 = kx*kx*vth + cth;
        r12 = kx*ky*vth - kz*sth;
        r13 = kx*kz*vth + ky*sth;
        r21 = kx*ky*vth + kz*sth;
        r22 = ky*ky*vth + cth;
        r23 = ky*kz*vth - kx*sth;
        r31 = kx*kz*vth - ky*sth;
        r32 = ky*kz*vth + kx*sth;
        r33 = kz*kz*vth + cth;
        beta = atan2(-r31, sqrt(r11*r11+r21*r21));
        if beta > deg2rad(89.99)
          beta = deg2rad(89.99);
          alpha = 0;
          gamma = atan2(r12,r22);
        elseif beta < -deg2rad(89.99)
          beta = -deg2rad(89.99);
          alpha = 0;
          gamma = -atan2(r12, r22);
        else
          cb = cos(beta);
          alpha = atan2(r21/cb, r11/cb);
          gamma = atan2(r32/cb, r33/cb);
        end
        alpha = rad2deg(alpha);
        beta = rad2deg(beta);
        gamma = rad2deg(gamma);
        rpy(i,:) = [gamma, beta, alpha];
    end

end
```

```
function [azi,inc] = azinc(r, p, y)

    r = deg2rad(r);
    p = deg2rad(p);
    y = deg2rad(y);

    rotMatrices = eul2rotm([y, p, r]);

    for i = 1:length(rotMatrices)
        azi(i) = atan2d(rotMatrices(2,3,i), rotMatrices(1,3,i));

        if azi(i) < 0
            azi(i) = azi(i) * -1;
        else
            azi(i) = 360 - azi(i);
        end

        inc(i) = acosd(rotMatrices(3,3,i));
    end

end
```

Figure 81 - Rv2rpy Matlab function for converting the robot recorded rotation vectors into Euler angles and azinc function for converting Euler angles to azimuth and inclination/tilt angles.

b) Calculation of effective orientation resolution achieved by UR3

The maximum effective orientation resolution will occur when the UR3 translates by the smallest distance to rotate the components in the tilt and azimuth direction i.e. sensitive zone. For the tilt angle direction this will be when the stem rotates (in the tilt angle direction) form the neutral position i.e. tilt = 0°. For the azimuth angle direction this will be when the stem rotates (in the azimuth angle direction) when the stem is at the smallest tilt angle that isn't zero i.e. tilt = 5°. This minimum distance will be constant for the entire angle range. The UR3 has a pose repeatability of ±0.1mm [UR3 user manual]. Therefore, estimating what effect the UR3 having a positional error of 0.1mm when orientating in these sensitive zones will give the maximum effective orientation resolution. A diagram detailing the calculation made to estimate the maximum effective orientation resolution in the tilt angle direction is shown in Figure 82. Diagrams detailing the calculations made to estimate the maximum effective orientation resolution in the azimuth angle direction are shown in Figure 83.

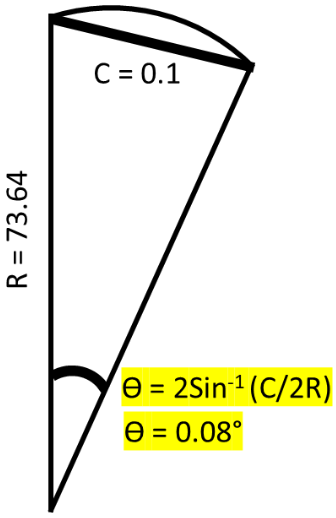

Figure 82 - Diagram of the circular segment calculation made to estimate the maximum effective orientation resolution in the tilt angle direction (ϴ) where R = TCP distance (distance from robot tool flange to THR component centre-of-rotation) and C = UR3 pose repeatability.

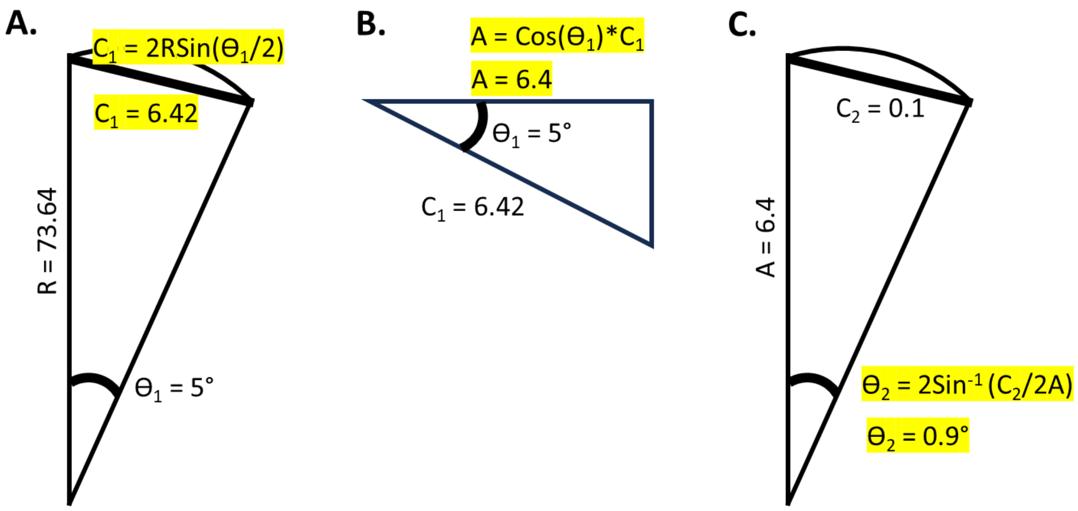

Figure 83 - Diagram of the circular segment and trigonometry calculations made to estimate the maximum effective orientation resolution in the azimuth angle direction (Θ_2) where R = TCP distance (distance from robot tool flange to THR component centre-of-rotation) and C_1 = distance robot tool flange translates when tilt = Θ_2 = 5°, A = distance robot tool flange translates in the XY plane and C_2 = UR3 pose repeatability.

c) Conversion of rotation angle, tilt angle and azimuthal angle or Euler ZYZ to flexion/extension, abduction/adduction and internal and external rotation or Euler XYZ

An example of a 3D rotation matrix is shown in Equation 6.

$$R = \begin{bmatrix} R_{1,1} & R_{1,2} & R_{1,3} \\ R_{2,1} & R_{2,2} & R_{2,3} \\ R_{3,1} & R_{3,2} & R_{3,3} \end{bmatrix}$$

Equation 6

The corresponding rotation matrix for the Euler sequence ZYZ is shown in Equation 7 from (Roithmayr et al., 2016).

$$R = Z(\alpha), Y(\beta), Z(\gamma)$$

$$ZYZ = \begin{bmatrix} c_1c_2c_3 - s_1s_3 & -c_3s_1 - c_1c_2c_3 & c_1s_2 \\ c_1s_3 + c_2c_3s_1 & c_1s_3 - c_2s_1s_3 & s_1s_2 \\ s_2s_3 & c_3s_2 & c_2 \end{bmatrix}$$

$Where\ s_1, s_2\ and\ s_3\ is\ \sin(\alpha), \sin(\beta)\ and\ sin(\gamma), and\ c_1, c_2\ and\ c_3\ is\ \cos(\alpha), \cos(\beta)\ and\ cos(\gamma).$

Equation 7

The angles for α, β and γ which correspond to the angles of the Euler sequence XYZ, can then be calculated from elements of the rotation matrix show in Equation 7 using Equation 8 from (Henderson, 1977).

$$\alpha = \arctan\left(\frac{-R_{2,3}}{R_{3,3}}\right)$$

$$\beta = \arcsin(R_{1,3})$$

$$\gamma = \arctan\left(\frac{-R_{1,2}}{R_{1,1}}\right)$$

Equation 8

d) Schematic of the selected magnetic field sensor

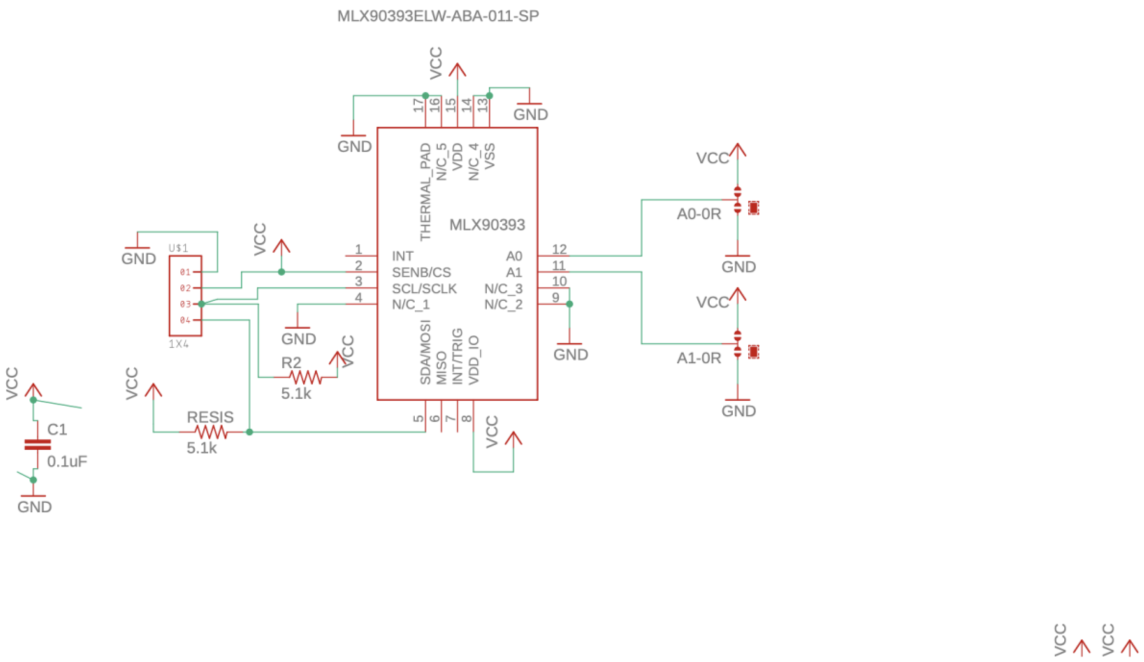

Figure 84 - Magnetic field sensor (mlx90393) board schematic as per the manufacturers recommended application diagram.

e) Adafruit_mlx90393 library configuration settings

Details of the Adafruit_mlx90393 library configuration settings are shown in TABLE. In some cases, the settings were set to the same values recommended in the demo script accompanying the Adafruit_mlx90393 library and in some cases the levels were altered. Gain was changed to GAIN_5X and resolution was changed to RES_19 in all directions (XYZ). This was to decrease the effect of residual background noise at the expense of sensitivity. Digital filtering was changed to FILTER_3 to increase the data output rate or sensing frequency.

Table 17 – Summary of the Adafruit_mlx90393 library configuration parameters, descriptions from [ref data sheet], the recommended values from the Adafruit_mlx90393 library demo script {REF} and the values chosen for all testing with the magnetic field sensor.

Parameter	Details	Recommended	Chosen
Gain [GAIN_SEL]	Analog chain gain setting. (Range: 1X, 1.33X, 1.67X, 2X, 2.5X, 3X, 4X, 5X)	GAIN_2.5X	GAIN_5X
Resolution [RES_XYZ]	Selects 16-bit output value from 19-bit analog to digital converter. (Range: Res_16 to Res_19)	X = Res_19 Y = Res_19 Z = Res_16	X = Res_19 Y = Res_19 Z = Res_19
Oversampling [OSR]	Magnetic sensor analog to digital converter oversampling ratio. (Range: OSR_0 to OSR_3)	OSR_2	OSR_2
Digital filtering [DIG_FILT]	Digital filter applicable to analog to digital converter. (Range: Filter_0 to Filter_7)	FILTER_6	FILTER_3

f) MATLAB Look up table function

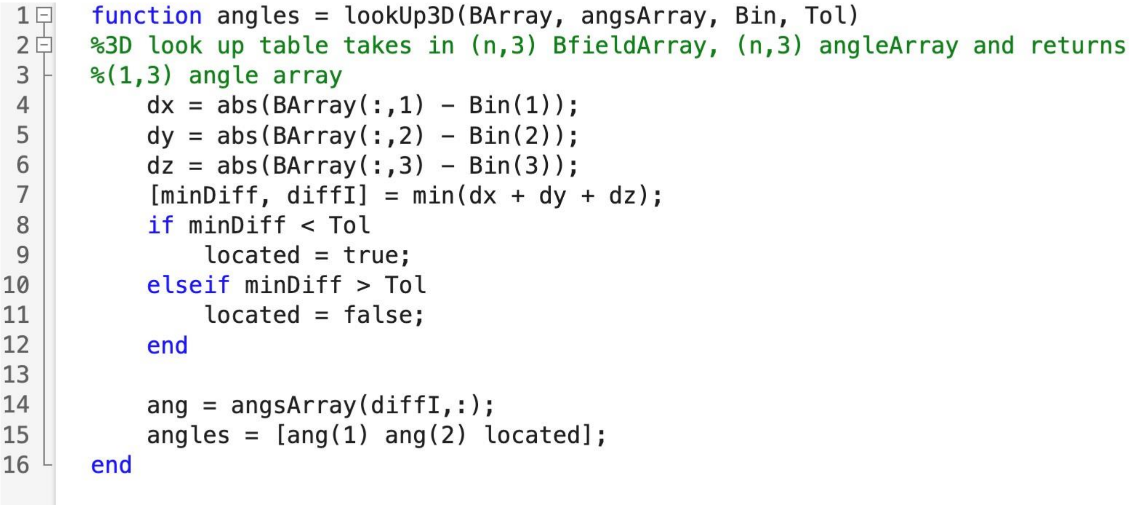

```matlab
function angles = lookUp3D(BArray, angsArray, Bin, Tol)
%3D look up table takes in (n,3) BfieldArray, (n,3) angleArray and returns
%(1,3) angle array
    dx = abs(BArray(:,1) - Bin(1));
    dy = abs(BArray(:,2) - Bin(2));
    dz = abs(BArray(:,3) - Bin(3));
    [minDiff, diffI] = min(dx + dy + dz);
    if minDiff < Tol
        located = true;
    elseif minDiff > Tol
        located = false;
    end

    ang = angsArray(diffI,:);
    angles = [ang(1) ang(2) located];
end
```

Figure 85 – MATLAB look up table function used to implement look up table tracking method in experimental testing. The function accepts an array of magnetic field data (BArray), an array of orientation states (angsArray), the sensed magnetic field in the form [Bx,By,Bz] (Bin) and a tolerance value that was used to see how far out of the look up table the sensed value was (Tol).

g) Simulated error study 1: Additional results

Arrays of colour plots showing the error in the stem tilt orientation and stem azimuth orientation, for each simulated error condition explored for the ratio stick tracking with $\mathbf{R}_{\mathbf{ratioBMagnitude}}$ and the neural network MPO tracking methods, are shown in Figure 86, Figure 87, Figure 88 and Figure 89. The colour bar range was set as twice the maximum standard deviation to the nearest ±5 for clarity and to prevent colour wash out.

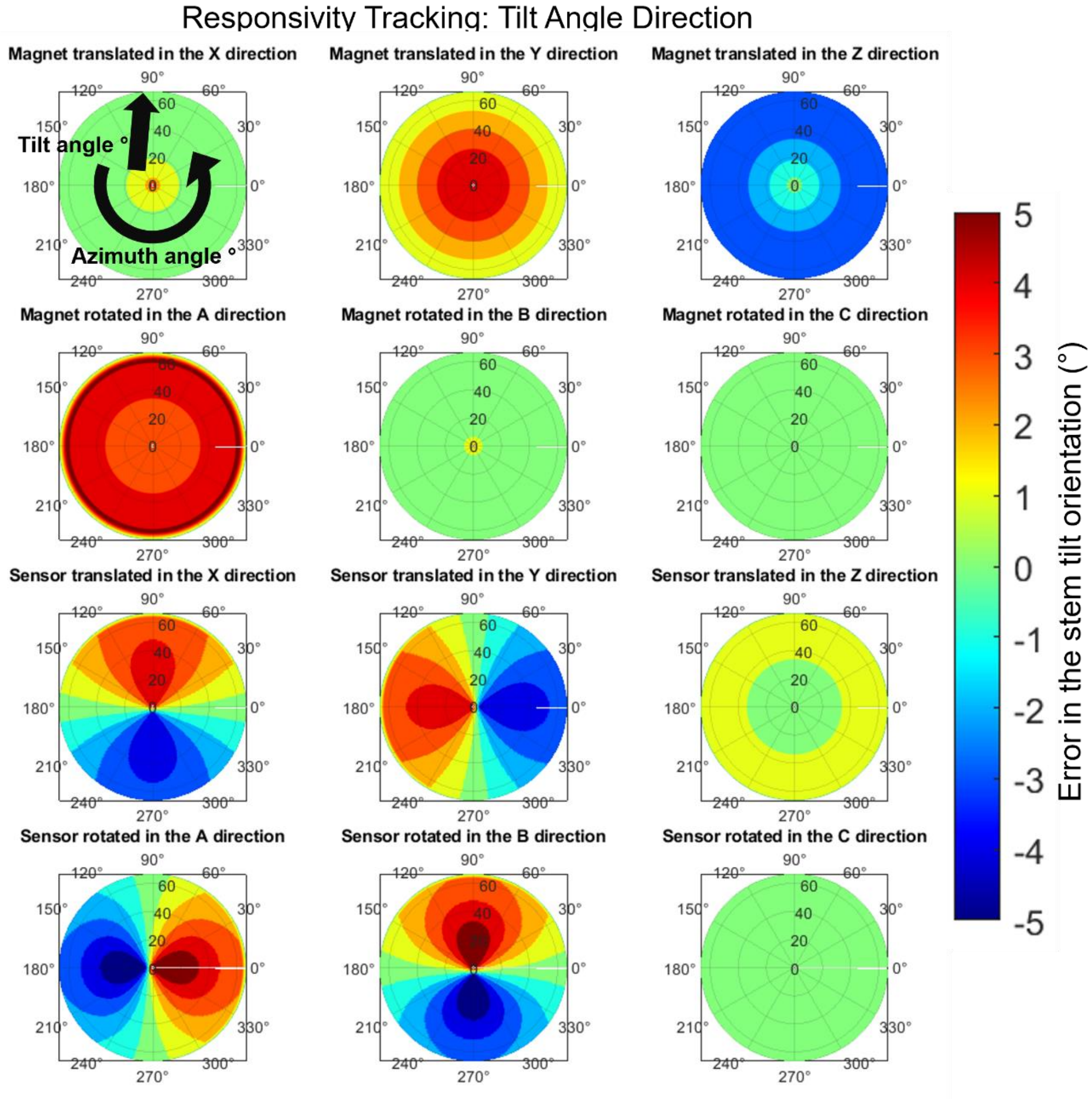

Figure 86 - Colour plots of the error in the stem tilt angle prediction made by the simulated MPO with the 8X2mm disc magnet using the or RratioBMagnitude tracking method. The Azimuthal angle axis of the graph corresponds to the Azimuthal angle of the stem (0° - 360°) and the Radial axis of the graph corresponds to the tilt angle (0° - 66°). The colour bar range was set as twice the maximum standard deviation to the nearest ±5° for clarity and to prevent colour wash out.

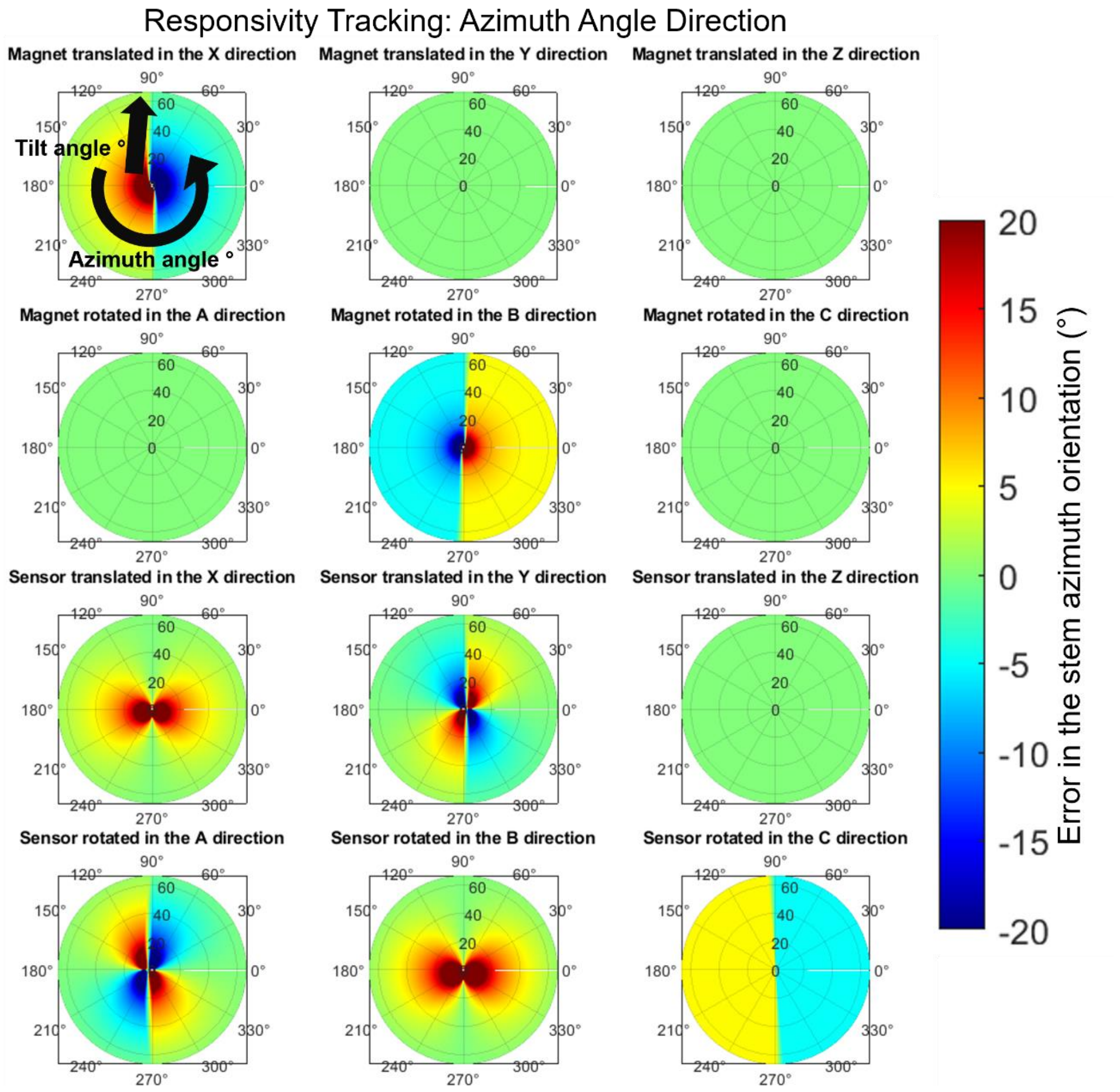

Figure 87 - Colour plots of the error in the stem azimuth angle prediction made by the simulated MPO with the 8X2mm disc magnet using the or $R_{ratioBMagnitude}$ tracking method. The Azimuthal angle axis of the graph corresponds to the Azimuthal angle of the stem (0° - 360°) and the Radial axis of the graph corresponds to the tilt angle (0° - 66°). The colour bar range was set as twice the maximum standard deviation to the nearest ±5° for clarity and to prevent colour wash out.

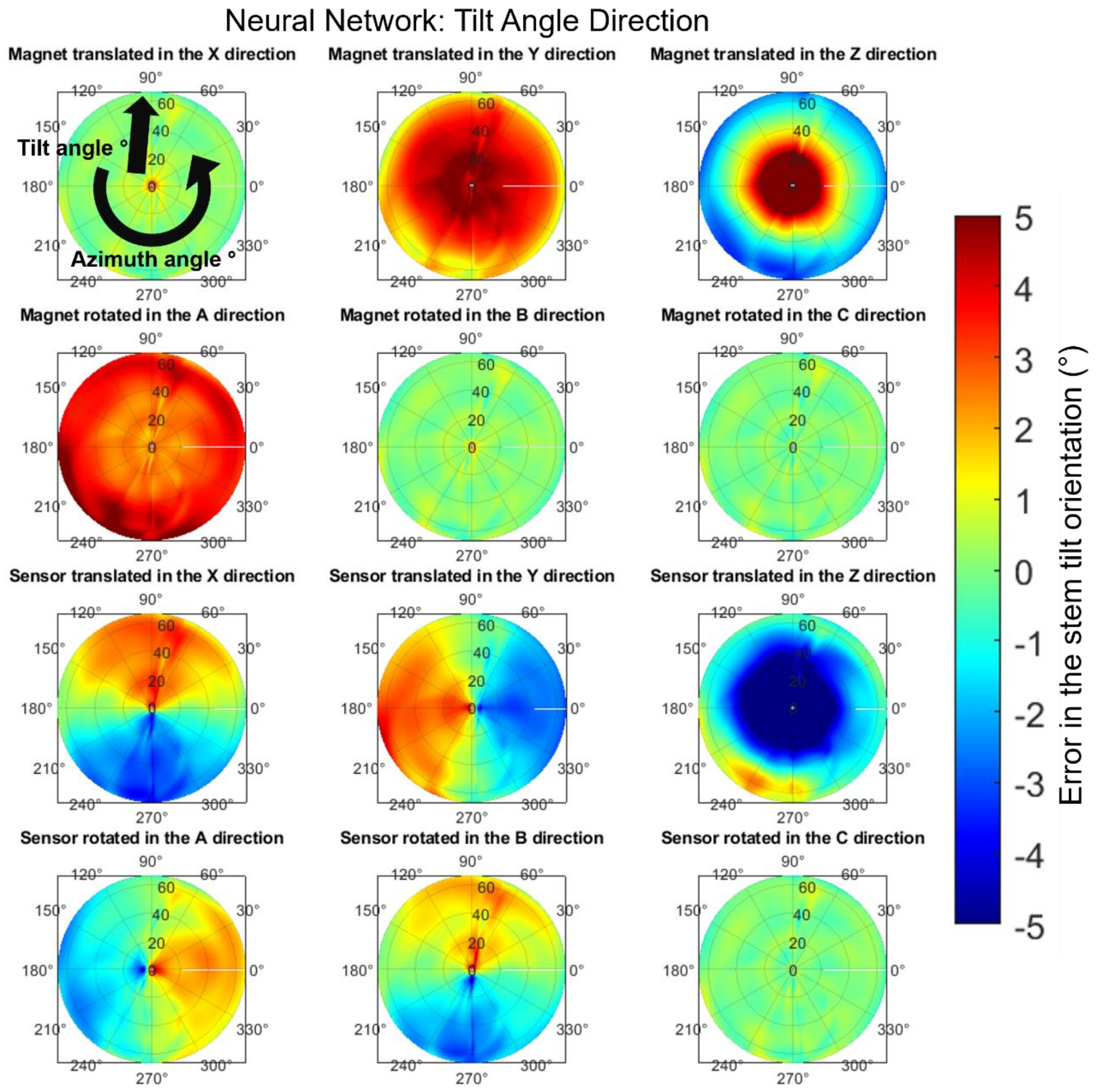

Figure 88 - Colour plots of the error in the stem tilt angle prediction made by the simulated MPO with the 8X2mm disc magnet using the Neural Network tracking method. The Azimuthal angle axis of the graph corresponds to the Azimuthal angle of the stem (0° - 360°) and the Radial axis of the graph corresponds to the tilt angle (0° - 66°). The colour bar range was set as twice the maximum standard deviation to the nearest ±5° for clarity and to prevent colour wash out.

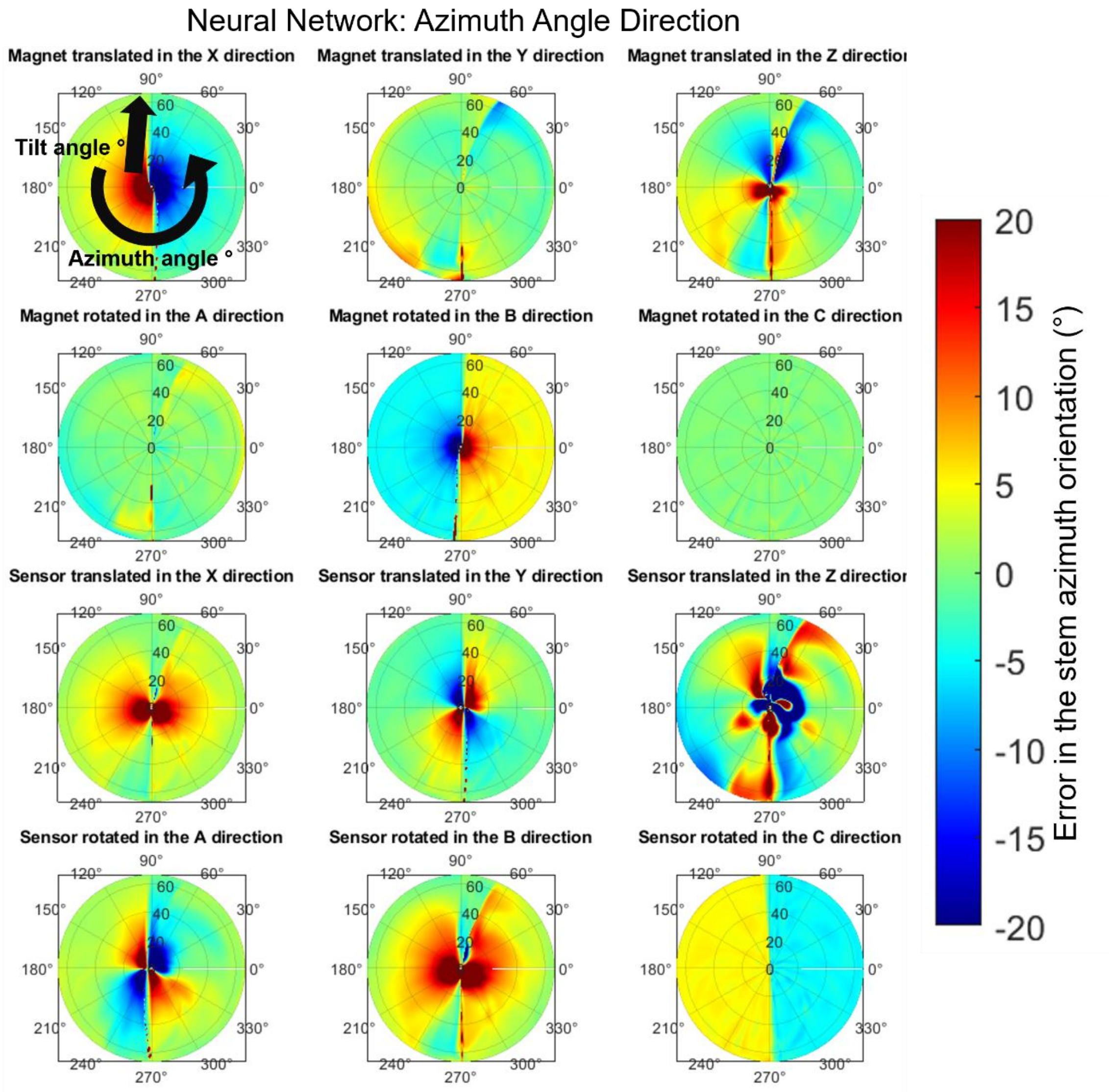

Figure 89 - Colour plots of the error in the stem azimuth angle prediction made by the simulated MPO with the 8X2mm disc magnet using the Neural Network tracking method. The Azimuthal angle axis of the graph corresponds to the Azimuthal angle of the stem (0° - 360°) and the Radial axis of the graph corresponds to the tilt angle (0° - 66°). The colour bar range was set as twice the maximum standard deviation to the nearest ±5° for clarity and to prevent colour wash out.

h) Method of potting sensor into acetabular shell component

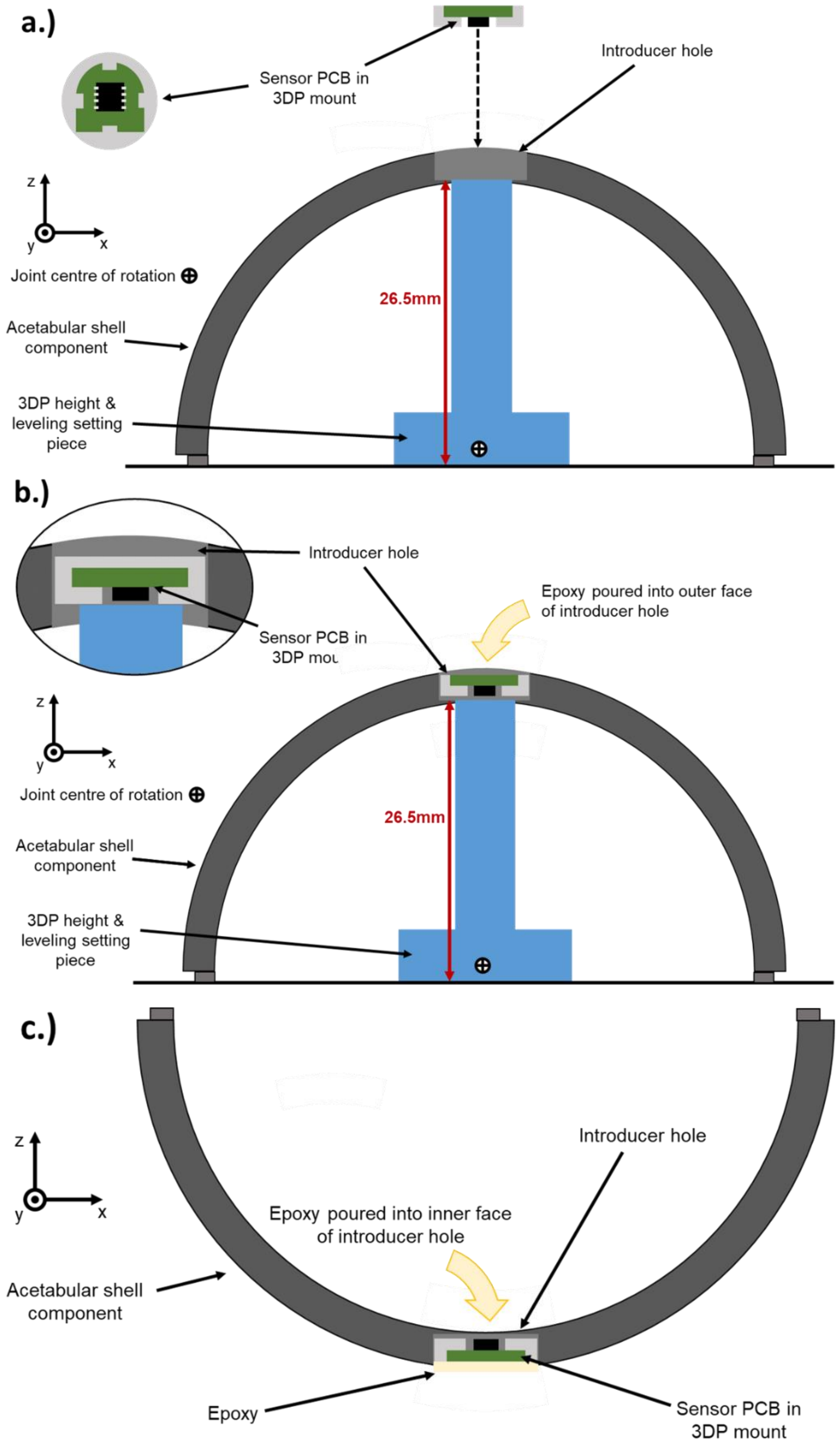

Figure 90 - Diagram detailing the method used to pot the sensor into the acetabular shell component using a setting piece to control the height and level of the sensor.

The sensor PCB was pressed and then superglued into a 3D printed mount that was 2mm thick and centred the sensitive spot of the magnetometer chip 0.5mm from the bottom face of the mount (Figure 90a). The sensor mount was then pressed into the acetabular hole using the setting piece to position the mount at the correct height. The centre of rotation of the acetabular shell component was 0.5mm from the face of the rim. This meant the setting piece was 26.5mm to position the sensitive spot of the magnetometer chip at the intended location of 26.5mm from the joint centre of rotation. Epoxy was then poured into the backside of the introducer and left to cure (Figure 90b). Once the epoxy had cured the shell could be flipped over and epoxy poured into the introducer hole from the other direction (topside) thus encapsulating the sensor ensuring a water-tight seal (Figure 90c).

i) Conference Proceedings

Chapter 5 of this thesis is based on the publication at the Orthopaedic Research Society 2022 Conference titled: **Development of a non-contact real-time method of tracking position and orientation of total hip replacement components.**

Authors: Oliver G. Vickers, Matthew P. Shuttleworth, Graham H. Isaac, Tim Board, Peter R. Culmer, Sophie Williams, Robert W. Kay

Introduction: Adverse mechanical mechanisms such as impingement, subluxation and edge loading, can lead to total hip replacement (THR) failure therefore, a better understanding of how the mechanical environment coupled with other factors like range of motion, are affected by patient and surgical design variables is required. Existing in-vitro experimental methods cannot continuously identify or assess these events in real time. Therefore, a sensing system that could track metrics such as femoral stem angle and femoral head position within an acetabular cup component would be an attractive proposition if incorporated within an experimental hip simulator, particularly during adverse testing regimes. Magnetic sensing technology employing permanent magnets coupled with a magnetic field sensor can provide a contact free method for position, proximity, and angle measurement, and have been used previously to track the position of a joystick (Ermakova et al., 2018; Malagò et al., 2020). Furthermore, magnetic field integrated circuit sensors are typically low-cost, have a small form factor and high sensing frequency and resolution thus making a magnetic sensing system a viable method for use in THR component tracking. The objectives of this work were to explore the use of a magnetic position and orientation system for tracking femoral stem angle and femoral head position within an acetabular cup component of a THR.

Methods: A tri-axis magnetometer (mlx90393, Melexis) and a disc magnet (N42 Neodymium, Magnet Experts Ltd) were integrated into clinically available THR components along with a cable tether. Simulated magnetic field data representative of the movement of the magnet and sensor when attached to the THR components was produced. This data was then used to calibrate the sensor and match the position and orientation state of the femoral head to the magnetic field output of the sensor. A robot arm (UR3, Universal Robots) was used to move the THR components through two representative motion profiles to verify the performance of the sensing system, a photo of the experimental setup is shown in Figure 1. Motion study 1, had the femoral head moved sinusoidally in the Roll (flexion/extension) plane and then Pitch (abduction/adduction) plane by ±50° for 5 cycles. Motion study 2, had the head raised out of the cup component (by distances of 2, 4, 6, 8, 10, 14 and 18mm) and translated in the +X, -X, +Y and -Y directions sequentially, until the head contacted the rim of the cup replicating an edge loading scenario. During the motion study experiments angular and position data were recorded by the magnetic sensing system and the robot arm at their maximum sampling rates of 50Hz and 125Hz respectively.

Results: The addition of the sensor and magnet required no changes to the THR component geometries resulting in no impact to the function of the articulating surfaces. To examine the accuracy of the magnetic sensing system, the predicted femoral stem angle and head position were compared to the actual stem angle and head position of the robot arm. The plot of actual stem angle versus predicted stem angle from motion study 1 is shown in Figure 2 where error in the Roll and Pitch planes was found to be similar with (root mean squared errors) RMSEs of 1.17° and 1.16° respectively. The plot of actual head position versus predicted head position from motion study 2 is shown in Figure 3 where RMSEs in the X, Y and Z direction was found to be 0.68mm, 0.7mm and 0.31mm respectively.

Discussion: The aim of this study was to explore whether a magnetic position and orientation sensing system can be used as a non-contact method of tracking the angle and position of a femoral head and stem within an acetabular cup in real-time. Close agreement was shown between the output of the magnetic sensing system and the ground truth (actual stem angle and head position of the robot arm). In the current configuration the magnetic sensing system can only measure orientation in two degrees of freedom and position of the head can only be determined when the stem is perpendicular to the face of the cup. Future work will extend these sensing capabilities to tracking orientation in three degrees of freedom and measuring the position of the head during adverse motions such as subluxation caused by the stem levering out the head.

Significance: This preliminary study has shown that a magnetic sensing system can be used to track the position and orientation of THR components. This method could be used as a research tool to better understand the function of a THR and provide data that could inform implant design or surgical approach.

Images:

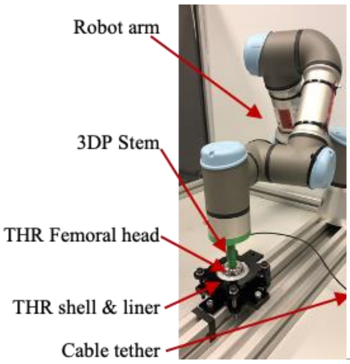

Figure 1 – Annotated photo of the experimental setup

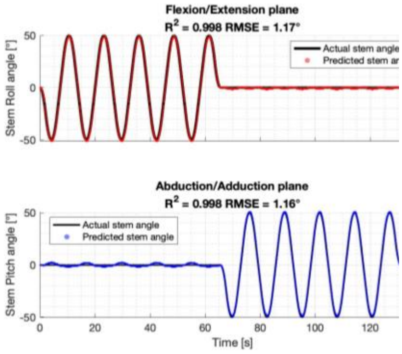

Figure 2 – Motion study 1: actual stem angle versus predicted stem angle

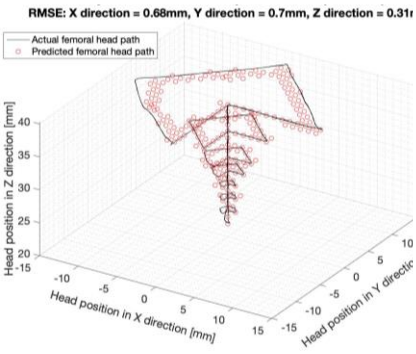

Figure 3 – Motion study 2: actual femoral head position versus predicted position

Chapter 6 of this thesis is based on the publications at the Wrightington John Charnley Gold Medal Research Day 2022 and the International Society for Technology in Arthroplasty 2022 Conference titled: **A non-contact method for measuring separation during subluxation events in total hip replacements**.

Authors: Oliver G. Vickers, Matthew P. Shuttleworth, Graham H. Isaac, Peter R. Culmer, Robert W. Kay, Tim Board, Sophie Williams

Introduction: Subluxation in total hip replacements (THRs) can lead to liner damage, cause patient discomfort and be a precursor to dislocation. Therefore, there is a need to further investigate the mechanism of subluxation, yet current in-vitro methods do not allow for a line-of-sight view and are often not feedback driven making studying this phenomenon challenging. Previous work has shown that magnetic sensing technology can track the position of a joystick and the angle and position of a THR femoral head within an acetabular liner. The aim of this work is to see if the same approaches can measure displacement of the femoral head during a re-creation of subluxation.

Methods: A tri-axis magnetometer (mlx90393, Melexis) and a magnet (N42 Neodymium, Magnet Experts Ltd) were integrated into clinically available components. The metal femoral head was positioned onto a 3D printed polymer stem and whilst the femoral head was located in an acetabular shell and liner a robot arm (UR3, Universal Robots) was used to rotate the stem. The stem was rotated to the maximum inclination angle of 66° (impingement occurrence only) and then three angles beyond the working range of the THR components (70°, 72° & 74°) in turn and thus levering the femoral head out of the cup. The stem was returned to an inclination of 45° between each angle and the motion profile was repeated (n=3). To validate the magnetic tracking system (MTS) a camera (Lumix GF6, Panasonic) and Computer Vision Toolbox (MATLAB, MathWorks) acted as a camera tracking system (CTS) and was used to track the position and orientation of the femoral head.

Results: When comparing inclination angle measured by the robot with that of the CTS and MTS (Figure 1), error when the stem had not impinged (i.e. robot arm angle at 66° and 45°) was 0.86°±0.30° (mean±SD) and 1.47°±0.27° for the CTS and MTS respectively.

This underestimation of stem angle meant that the MTS did not detect the occurrence of the initial impingement contact as impingement was inferred as whenever the stem angle was >66°. Closer agreement was seen when comparing angle measured by the CTS and MTS over the entire dataset with error of 0.61°±0.92°. This was expected as the 3D printed stem appeared to flex during subluxation. The estimated femoral head position in the z axis showed good agreement to that of the CTS with error of -0.06mm±0.18mm. A plot of impingement occurrence measured by the robot and MTS, and subluxation distance in the z axis measured by the CTS and MTS is shown in Figure 2.

Conclusion: This preliminary work has shown that magnetic sensing technology can track the position and orientation of a femoral head within an acetabular cup during complex adverse motions. Future, work will further develop the method to improve accuracy of impingement occurrence detection. Additionally, a more representative re-creation of a subluxation event is needed in which anatomical loads are included.

Acknowledgements: Oliver Vickers' studentship is funded by the EPSRC CDT in Tissue Engineering and Regenerative Medicine (Grant number EP/L014823/1)

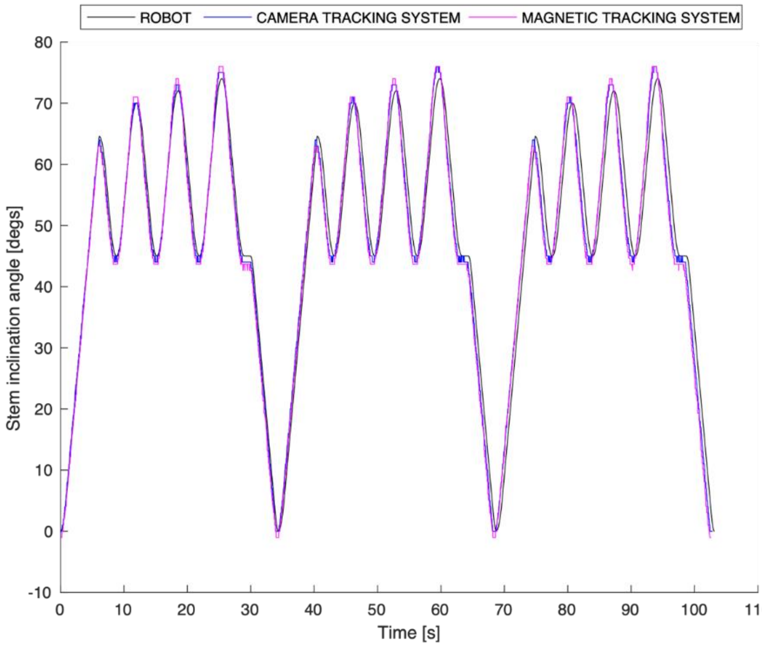

Figure 1 – Stem inclination angle measured by the robot arm, camera tracking system and magnetic sensing system when the robot arm is rotated to 66°, 70°, 72° and 74° (returning to 45° in between each angle) where component impingement first occurs at 66°.

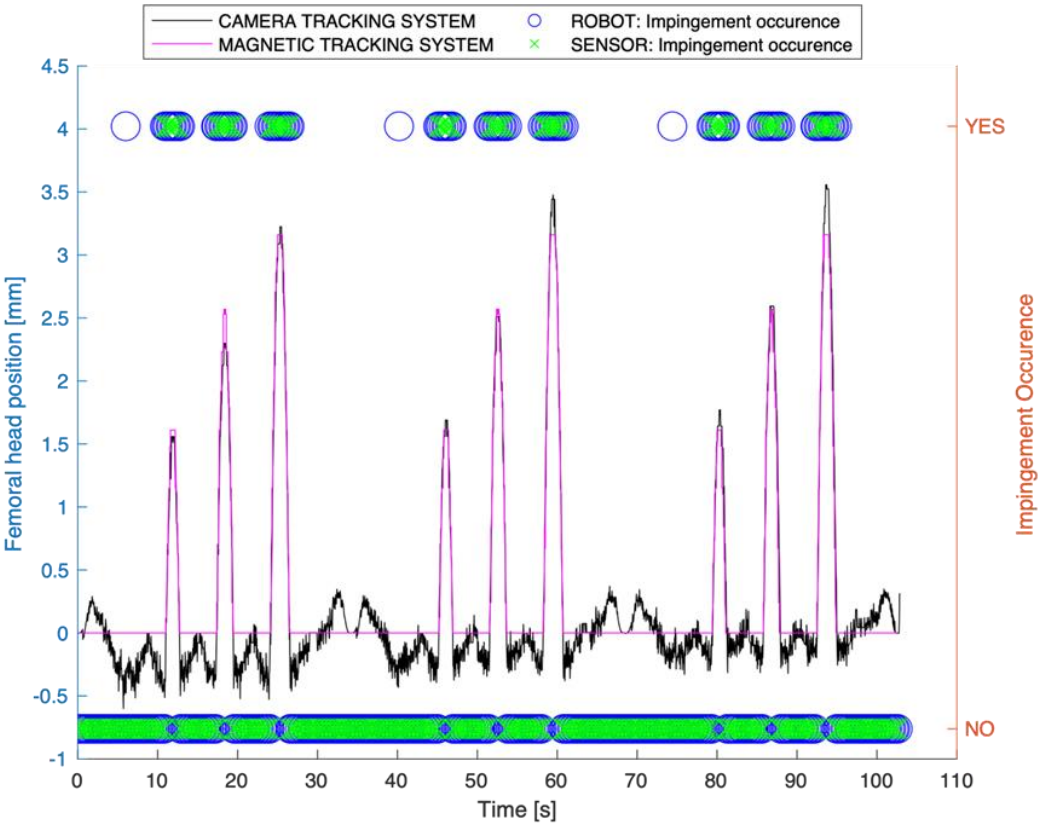

Figure 2 – Sensor reported impingement occurrence and estimated femoral head position in the z axis along with the impingement occurrence measured by the robot arm and the femoral head position measured by the camera tracking system.

j) Publications

See below a full copy of the publication contributing to this thesis:

Vickers, O.G., Culmer, P.R., Isaac, G.H., Kay, R.W., Shuttleworth, M.P., Board, T. and Williams, S. 2021. **Is in vivo sensing in a total hip replacement a possibility? A review on past systems and future challenges.** Progress in Biomedical Engineering. 3(4), p.42004.

The primary author completed all literature searching and reviewing, and preparation of the publication. All remaining authors contributed to proofreading the article before publication.